Cytosolic Ca^{2+}, a master regulator of vacuolar ion conductance and fast auxin signaling in *Arabidopsis thaliana*

Zytosolisches Ca^{2+}, ein zentraler Regulator der vakuolären Ionenleitfähigkeit und der schnellen Auxin-Signaltransduktion in *Arabidopsis thaliana*

Dissertation

for a doctoral degree in natural sciences
at the Julius-Maximilians-University Würzburg

by

Julian Dindas
born in Schlema

Würzburg, 2017

Cytosolic Ca^{2+}, a master regulator of vacuolar ion conductance and fast auxin signaling in *Arabidopsis thaliana*

Zytosolisches Ca^{2+}, ein zentraler Regulator der vakuolären Ionenleitfähigkeit
und der schnellen Auxin-Signaltransduktion in *Arabidopsis thaliana*

Dissertation
for a doctoral degree in natural sciences
at the Julius-Maximilians-University Würzburg

by

Julian Dindas
born in Schlema

Würzburg, 2017

Date of submission:

<u>Members of the promotion committee</u>

Chairperson:

Primary referee: Prof. Dr. Rainer Hedrich

Secondary referee: Prof. Dr. Erhard Wischmeyer

Date of public defence:

Date of Receipt of Certificates:

Acknowledgment

This work would not have been possible without the supervision, the advice and the support from many people.

First, I would like to thank **Prof. Dr. Rainer Hedrich** for giving me the opportunity to work in his group and for the two interesting topics presented in this work I was able to work on. Especially, I want to thank him for the supervision, fruitful discussions and helpful input during my experimental work on auxin transport and signaling. Additionally, I am grateful for the advice and the opportunities concerning my professional future.

I thank **Prof. Dr. Erhard Wischmeyer** for being the second referee of this work.

I am also greatly appreciative to **PD Dr. Rob Roelfsema**, who supervised my research during the past years and who always had biological as well as technical advice. Without him, I never would have successfully impaled a single root hair cell. He wrote the software applications that enabled us to perform important ion flux measurements and to analyse them in an efficient way. I also thank him for spending a lot of time to look through my thesis and help to improve my scientific writing.

Important for the successful completion of this work was also **Prof. Dr. Dirk Becker**, who always had an open ear and was always able to make time to discuss results. He suggested useful experimental ideas to this work and also critical read parts of this thesis and provided helpful modifications to it.

Dr. Sönke Scherzer deserves my appreciation for his continuous help and discussions around ion flux measurements and performing the crucial ion flux measurements with the *tir1* mutants.

Thankfully, **Heike M. Müller** and **Pamela Korte** extracted RNA and performed qPCR measurements on the little plant material I provided them with. **Katharina von Meyer** performed the first proton flux measurements shown in this work.

Prof. Dr. Malcolm Bennett, **Prof. Dr. Klaus Palme** and **Dr. Melanie Krebs** provided important mutant and reporter lines that were used in this work.

I would also like to extend my thanks to **all other members of the Botany I** who supported me during the last 4 ¾ years.

During all these years of my education, **my family** has been supporting me a lot and deserves my deepest gratitude for all their support. My partner **Irene** accompanied me during the ups and downs of my roller coaster ride as a PhD student. She deserves my deepest gratitude for what she means to me.

Zusammenfassung

Das Phytohormon Auxin erfüllt wichtige Funktionen bei der Initiierung von pflanzlichen Geweben und Organen, wie auch in der Steuerung des Wurzelwachstums im Zusammenspiel mit äußeren Reizen wie Schwerkraft, Wasser- und Nähstoffverfügbarkeit. Diese Funktionen basieren dabei vor allem auf der Auxin-abhängigen Regulation von Zellteilung und -streckung. Wichtig für letzteres ist dabei die Kontrolle des Zellturgors durch die Vakuole. Als Speicher für Nährstoffe, Metabolite und Toxine sind Vakuolen von essentieller Bedeutung. Vakuolär gespeicherte Metabolite und Ionen werden sowohl über aktive Transportprozesse, als auch passiv durch Ionenkanäle, über die vakuoläre Membran mit dem Zytoplasma ausgetauscht. In ihrer Funktion als *second messenger* sind Kalziumionen wichtige Regulatoren, aber auch Gegenstand vakuolärer Transportprozesse. Änderungen der zytosolischen Kalziumkonzentration wirken nicht nur lokal, sie werden auch mit einer Signalweiterleitung über längere Distanzen in Verbindung gebracht. Im Rahmen dieser Arbeit wurden elektrophysiologische Methoden mit bildgebenden Methoden kombiniert um Einblicke in das Zusammenspiel zwischen zytosolischen Kalziumsignalen, vakuolärer Transportprozesse und der Auxin-Physiologie im intakten pflanzlichen Organismus zu gewinnen.

Kalziumsignale sind an der Regulierung vakuolärer Ionenkanäle und Transporter beteiligt. Um dies im intakten Organismus zu untersuchen wurden im Modellsystem junger Wurzelhaare von *Arabidopsis thaliana* Messungen mit intrazellulären Mikroelektroden durchgeführt. Mittels der Zwei-Elektroden-Spannungsklemm-Technik konnte bestätigt werden, dass die vakuoläre Membran der limitierende elektrische Wiederstand während intravakuolärer Messungen ist und so gemessene Ionenströme in der Tat nur die Ströme über die vakuoläre Membran repräsentieren. Die bereits bekannte zeitabhängige Abnahme der vakuolären Leitfähigkeit in Einstichexperimenten konnte weiterhin mit einer einstichbedingten, transienten Erhöhung der zytosolischen Kalziumkonzentration korreliert werden. Durch intravakuoläre Spannungsklemmexperimente in Wurzelhaarzellen von Kalziumreporterpflanzen konnte dieser Zusammenhang zwischen vakuolärer Leitfähigkeit und der zytosolischen Kalziumkonzentration bestätigt werden.

Die Vakuole ist jedoch nicht nur ein Empfänger zytosolischer Kalziumsignale. Da die Vakuole den größten intrazellulären Kalziumspeicher darstellt, wird seit Langem diskutiert, ob sie auch an der Erzeugung solcher Signale beteiligt ist. Dies konnte in intakten Wurzelhaarzellen bestätigt werden. Änderungen des vakuolären Membranpotentials wirkten sich auf die zytosolische Kalziumkonzentration in diesen Zellen aus. Während depolarisierende Potentiale zu einer Erhöhung der zytosolischen Kalziumkonzentration führten, bewirkte eine Hyperpolarisierung der vakuolären Membran das Gegenteil. Thermodynamische Überlegungen zum passiven und aktiven Kalziumtransport über die vakuoläre Membran legten dabei den Schluss nahe, dass die hierin beschriebenen Ergebnisse das Verhalten von vakuolären H^+/Ca^{2+} Austauschern wiederspiegeln, deren Aktivität durch die protonenmotorische Kraft bestimmt wird.

Im Rahmen dieser Arbeit stellte sich weiterhin heraus, dass zytosolisches Kalzium ebenso ein zentraler Regulator eines schnellen Auxin-induzierten Signalweges ist, über den der polare Transport des Hormons reguliert wird.

Im gleichen Modellsystem junger Wurzelhaare konnte gezeigt werden, dass die externe Applikation von Auxin eine sehr schnelle, Auxinkonzentrations- und pH-abhängige Depolarisation des Plasmamembranpotentials zur Folge hat. Synchron zur Depolarisation des Plasmamembranpotentials wurden im Zytosol transiente Kalziumsignale registriert. Diese wurden durch einen von Auxin aktivierten Einstrom von Kalziumionen durch den Ionenkanal CNGC14 hervorgerufen. Experimente an Verlustmutanten als auch pharmakologische Experimente zeigten, dass zur Auxin-induzierten Aktivierung des Kalziumkanals die Auxin-Perzeption durch die F-box Proteine der TIR1/AFB Familie erforderlich ist. Durch Untersuchungen der Auxin-abhängigen Depolarisation wie auch des Auxin-induzierten Einstroms von Protonen in epidermale Wurzelzellen von Verlustmutanten konnte gezeigt werden, dass die sekundär aktive Aufnahme von Auxin durch das hochaffine Transportprotein AUX1 für die schnelle Depolarisation verantwortlich ist. Nicht nur die zytosolischen Kalziumsignale korrelierten mit der CNGC14 Funktion, sondern ebenso die AUX1-vermittelte Depolarisation von Wurzelhaaren. Eine unveränderte Expression von *AUX1* in der *cngc14* Verlustmutante legte dabei den Schluss nahe, dass die Aktivität von AUX1 posttranslational reguliert werden muss. Diese Hypothese erfuhr Unterstützung durch Experimente, in denen die Behandlung mit dem Kalziumkanalblocker Lanthan zu einer Inaktivierung von AUX1 im Wildtyp führte.

Die zytosolische Beladung einzelner epidermaler Wurzelzellen mit Auxin hatte die Ausbreitung lateraler und acropetaler Kalziumwellen zur Folge. Diese korrelierten mit einer Verschiebung des Auxin-Gradienten an der Wurzelspitze und unterstützten somit eine hypothetische Kalziumabhängige Regulation des polaren Auxin Transports. Ein Model für einen schnellen, Auxin induzierten und kalziumabhängigen Signalweg wird präsentiert und dessen Bedeutung für das gravitrope Wurzelwachstum diskutiert. Da die AUX1-vermittelte Depolarisation in Abhängigkeit von der externen Phosphatkonzentration variierte, wird die Bedeutung dieses schnellen Signalwegs ebenso für die Anpassung des Wurzelhaarwachstums an eine nicht ausreichende Verfügbarkeit von Phosphat diskutiert.

Summary

The phytohormone auxin performs important functions in the initiation of plant tissues and organs, as well as in the control of root growth in conjunction with external stimuli such as gravity, water and nutrient availability. These functions are based primarily on the auxin-dependent regulation of cell division and elongation. Important for the latter is the control of the cell turgor by the vacuole. As storage for nutrients, metabolites and toxins, vacuoles are of vital importance. Vacuolar stored metabolites and ions are exchanged across the vacuolar membrane with the cytoplasm via active transport processes as well as passively through ion channels. In their function as second messenger, calcium ions are important regulators but also subject to vacuolar transport processes. Changes in the cytosolic calcium concentration not only act locally, but are also associated with signal transduction over longer distances. In this work, electrophysiological methods were combined with imaging techniques to gain insights into the interaction between cytosolic calcium signals, vacuolar transport processes and auxin physiology in the intact plant organism.

Calcium signals are involved in the regulation of vacuolar ion channels and transporters. In order to investigate this in the intact organism, intracellular microelectrode measurements were performed in the model system of bulging *Arabidopsis thaliana* root hairs. By means of the two-electrode voltage-clamp technique, it could be confirmed that the vacuolar membrane is the limiting electrical resistance during intravacuolar measurements and thus measured ion currents actually represent only the currents across the vacuolar membrane. The already known time-dependent decrease of vacuolar conductivity during intravacuolar experiments could be further correlated with an impalement-related, transient increase of the cytosolic calcium concentration. Intravacuolar voltage-clamp experiments in root hair cells of calcium reporter plants confirmed this relationship between vacuolar conductivity and the cytosolic calcium concentration.

However, the vacuole is not just a recipient of cytosolic calcium signals. Since the vacuole represents the largest intracellular calcium reservoir, it has long been argued that it is also involved in the generation of such signals. This could be confirmed in intact root hair cells. Changes in the vacuolar membrane potential affected the cytosolic calcium concentration in these cells. While depolarizing potentials led to an increase of the cytosolic calcium concentration, hyperpolarization of the vacuolar membrane caused the opposite. Thermodynamic considerations of passive and active calcium transport across the vacuolar membrane suggested that the results described herein reflect the behaviour of vacuolar H^+/Ca^{2+} exchangers whose activity is determined by the proton motive force.

In addition, cytosolic calcium has been shown to be a key regulator of a rapid auxin-induced signaling pathway that regulates polar transport of the hormone.

In the same model system of bulging root hairs it could be shown that the external application of auxin results in a very fast, auxin concentration- and pH-dependent depolarization of the plasma membrane potential. Synchronous with the depolarization of the plasma membrane potential, transient calcium signals were recorded in the cytosol. These were caused by an auxin-activated influx of calcium ions through the ion channel CNGC14. Experiments on loss-of-function mutants as well as pharmacological experiments showed that the auxin-induced activation of the calcium channel requires auxin-perception by the F-box proteins of the TIR1/AFB family.

Investigations of auxin-dependent depolarization as well as the auxin-induced influx of protons into epidermal root cells of loss-of-function mutants showed that the secondary active uptake of auxin by the high-affinity transport protein AUX1 is responsible for the rapid depolarization

Not only the cytosolic calcium signals correlated with CNGC14 function, but also the AUX1-mediated depolarization of root hairs. An unchanged expression of *AUX1* in the *cngc14* loss-of-function mutant suggested that the activity of AUX1 must be post-translationally regulated. This hypothesis was supported by experiments in which treatment with the calcium channel blocker lanthanum led to inactivation of AUX1 in the wild type.

The cytosolic loading of individual epidermal root cells with auxin resulted in the spread of lateral and acropetal calcium waves. These correlated with a shift of the auxin gradient at the root apex and thus supported a hypothetical calcium-dependent regulation of polar auxin transport. A model for a rapid, auxin-induced and calcium-dependent signaling pathway is presented and its importance for gravitropic root growth is discussed. Since AUX1-mediated depolarization varied with external phosphate concentration, the importance of this rapid signaling pathway is also discussed for the adaptation of root hair growth to an inadequate availability of phosphate.

Table of Contents

1. Introduction

1.1. How plants regulate root growth

Roots are essential for plants since they supply the aerial organs with water and essential mineral nutrients like potassium (K^+), phosphate (PO_4^{2-}, P_i), and nitrate (NO_3^-). In return, the photosynthetically active tissues supply the root system with the energy needed for growth.
In general, growth in plants, including their roots, is mostly achieved through cellular elongation. However, rather than through an energetically costly expansion of the cytosol, plant cells elongate via the passive uptake of water for which the high concentration of osmotically active substances in the vacuolar lumen provides the driving force (Taiz 1992; Marty 1999).
Root growth and thus the architecture of the whole root system of a plant is shaped by the interplay of external stimuli like gravity, water, nutrient availability and microbial interactions with internal determinants, foremost the hormone auxin, which is a key regulator of plant growth and development (Malekpoor Mansoorkhani *et al.* 2014). For example, auxin determines the direction of gravity-guided root growth by maintaining a defined local auxin gradient in the root apex (a detailed description of auxin transport and physiology is given below in **Chapter 1.3**). Any deviation from a vertical growth direction leads to a spatial shift of the auxin gradient resulting in a differential cell elongation and reorientation of root growth to a vertical direction (Ottenschläger *et al.* 2003). The link between auxin and tugor-driven cellular elongation is provided by the acid growth theory (Kutschera 1994). Since plant cells are enclosed in mechanically rigid cell walls, those must be weakened to yield to the hydrostatic pressure from the vacuole. Based on observations that auxin promoted growth is accompanied by an acidification of the cell wall (Rayle and Cleland 1977), the acid growth theory states that auxin stimulates the activity of adenosine triphosphate (ATP)-driven proton (H^+) pumps at the plasma membrane (PM) (Takahashi *et al.* 2012). The ensuing acidification of the extracellular space subsequently activates hydrolytic enzymes therein, called expansins, which contribute to cell wall weakening and, ultimately, growth (McQueen-Mason *et al.* 1992). Since vacuoles and auxin fulfill such essential functions during growth, they are subject of intensive studies. In the case of auxin, its directional transport, which is unique among plant hormones, and its perception and signaling mechanisms are of particular interest. Analysing the transport processes across the vacuolar membrane (VM) that exchange organic and inorganic solutes between the cytosol and the vacuole, on the other hand, is essential for a comprehensive understanding of the physiological functions of the vacuole.

1.2. The plant vacuole

1.2.1. Physiological functions of the vacuole

Vacuoles fulfill a diverse set of functions, as they occupy around 90% of a plant cells volume and store high amounts of osmolytes. The central vacuoles in mature plant cells develop from many small provacuoles in young, not terminally differentiated cells. The endoplasmic reticulum (ER) is their main membrane source. During maturation of the cell, the provacuoles fuse and increase their volume by solute and water uptake (Viotti 2014).

Vacuoles balance the ion homeostasis of the cytosol and thus support many cellular functions, like the assembly of the cytoskeleton and the regulation of enzyme activity, which are sensitive to changes in pH, the cytosolic free calcium concentration ($[Ca^{2+}]_{cyt}$) and heavy metals (Casey *et al.* 2010; Yadav 2010; Qin *et al.* 2012; Ranty *et al.* 2016). The cytosolic pH of around pH 7 to 7.5 is *inter alia* maintained by the energized sequestration of H^+ into the vacuolar lumen and by the release of buffering dicarboxylates like malate into the cytosol (Hurth *et al.* 2005; Li *et al.* 2005; Krebs *et al.* 2010; Rienmüller *et al.* 2012). The vacuolar lumen is also the main Ca^{2+} storage in a plant cell, since the luminal concentration of free Ca^{2+} exceeds cytosolic levels by approximately three to four orders of magnitude (Bethmann *et al.* 1995; Marty 1999; Roelfsema and Hedrich 2010; Schönknecht 2013). It can thus be assumed that the vacuole is an important regulator of $[Ca^{2+}]_{cyt}$ and of significance for Ca^{2+}-related signalling events (Schönknecht 2013). Plants do not have a secretory system to excrete toxic substances, neither are they able to change their location in case of a contamination. Instead, plants sequester toxic heavy metals like cadmium or mercury into the vacuole to overcome these disadvantages. Vacuoles also function in homeostasis of essential metals like copper (Cu) and iron (Fe) (Sharma *et al.* 2016).

The vacuole represents an essential storage compartment of primary and secondary metabolites. Carbohydrates, like sucrose in taproots of sugar beet (Jung *et al.* 2015) or an organic acid, like malic acid in crassulacean acid metabolism (CAM-) plants (White and Smith 1989) are accumulated in vacuoles as a reservoir of energy and CO_2, respectively. Among secondary metabolites are the various phenolic and alkaloidic substances used in defence strategies against herbivores and microbial pathogens (Hatsugai and Hara-Nishimura 2010; Mithofer and Boland 2012). Flavonoids like anthocyanins accumulate in vacuoles as a protection against photodamage (Pourcel *et al.* 2010). Specialized vacuoles can function as nutrient sources for growth and development of the plant embryo (Herman and Larkins 1999), or protein degradation (Carter *et al.* 2004).

1.2.2. Transport across the vacuolar membrane

1.2.2.1. Thermodynamics of vacuolar membrane transport

The above-described functions, like tugor regulation, ion homeostasis, intracellular signaling and carbohydrate storage rely on the ability of the vacuole to retain high concentrations of solutes. Uptake of those solutes, however, is often against the respective electrochemical gradient. In general, the energy, required for membrane transport against such a gradient, is provided by the chemical and the electrical component of the proton motive force (pmf). In the case of the VM, the chemical component is the ΔpH across the VM (ΔpH_{VM}) between the acidic vacuolar lumen and the neutral cytosol. In *Arabidopsis thaliana* (henceforth *A. thaliana*) root cells the ΔpH_{VM} is around one to two pH units (Bibikova *et al.* 1998; Bassil *et al.* 2011), but it can reach extreme values like 5 pH units in citrus fruits (Taiz 1992) or 6 pH units in the brown algae *Desmeresti*a (McClintock *et al.* 1982). The ΔpH_{VM} is established by VM-localized H^+-ATPases and H^+-PPases, which hydrolyse cytosolic ATP or pyrophosphate (PP_i), respectively (**Fig. 1.1**). Both proteins are primary active H^+-pumps, which use the energy that is liberated during hydrolyzation to translocate protons with a rate of 10^0 to 10^3 s^{-1} against the electrochemical gradient into the vacuole (Li *et al.* 2005; Lodish *et al.* 2008; Krebs *et al.* 2010; Rienmüller *et al.* 2012). Apart from H^+-pumps, specific primary transporters at the VM were described to be involved in the luminal accumulation of Ca^{2+}, heavy metals and secondary metabolites (Martinoia *et al.* 2012).

The electrical component of the pmf is the VM potential, which is formed by the unequal distribution of charges between the cytosolic and luminal site of the membrane due to the combined action of pumps, transporters, and ion channels. The VM potential is assumed to be around -30 mV to -40 mV (Martinoia *et al.* 2007; Martinoia *et al.* 2012). This potential difference is relatively low when compared to the hyperpolarized PM which transporters and channels operate at a PM potential well negative of -110 mV (Hedrich 2012). Both the PM potential and the VM potential are negatively charged on the cytosolic side of the membrane and are thus given as negative values according to the sign convention proposed by Bertl *et al*. (1992).

The pmf generated at the VM can be used by secondary active transporters, which includes symport- and antiport-carriers (**Fig. 1.1**). Both types of transporters are membrane-localized and can use the pmf to achieve the electrochemical uphill (i.e. into the vacuolar lumen) transport of solutes with a rate of 10^2 to 10^4 s^{-1} by coupling it to the downhill (i.e. into the cytosol) transport of H^+ (Lodish *et al.* 2008). If, for example, a ΔpH_{VM} of 2 pH units and a VM potential of -30 mV are assumed, then, application of **Equation 1.1** (Christensen 1975) at 20°C yields 14.1 kJ of potential energy stored in one mole of H^+. This energy can be used by H^+-coupled antiporters to establish high luminal/cytosolic concentration gradients of ions like Ca^{2+} or uncharged solutes like sucrose as given in **Tab. 1.1**.

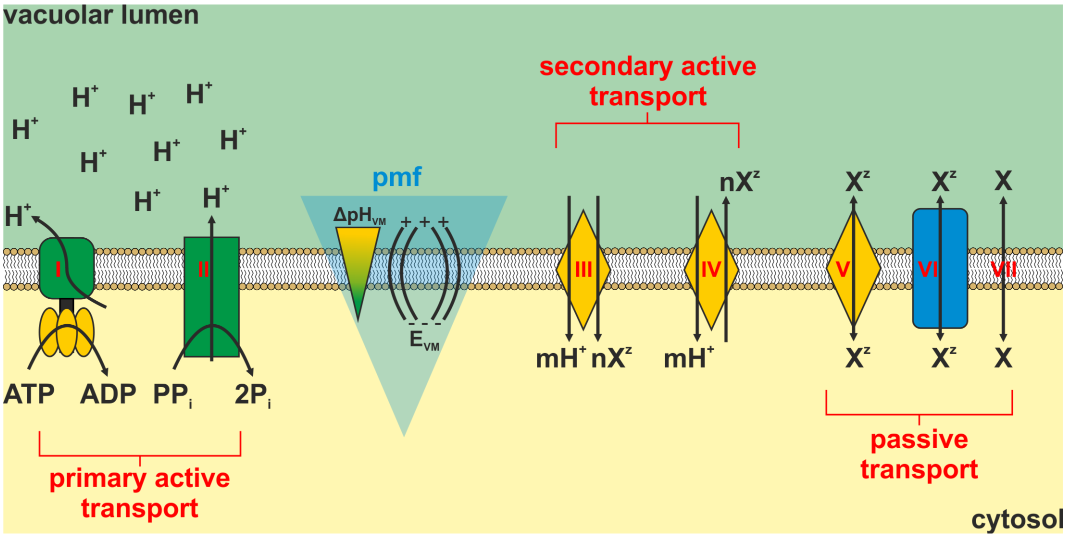

Fig. 1.1: Principal vacuolar transport components. Membrane transport can be divided into primary active, secondary active and passive transport. At the VM, the constituents of primary active transport are the H^+-translocating ATPase (**I**) and PPase (**II**). Their H^+-pump activity establishes a ΔpH_{VM}, which together with the VM potential (E_{VM}) forms the pmf (light blue triangle). **Secondary active transporters** utilize the pmf and are either symporters (**III**) or antiporters (**IV**). Symporter translocate *n* molecules of solute *X* with valenz *z* by unidirectional coupling to *m* molecules of H^+. An antiporter translocates the solute into the vacuole. **Passive transport** combines carrier-mediated transport through uniporters (**V**) and the flow of ions through channel proteins (**VI**). Both of which facilitate diffusion along the electrochemical gradient. Passive diffusion of uncharged molecules (**VII**) is with the chemical gradient across the membrane.

$$G = R * T * ln\left(\frac{[X^z]_{lumen}}{[X^z]_{cytsol}}\right)^n + n * z * F * E_{VM}$$

Equation 1.1: Calculation of the pmf. G: free energy; **R**: universal gas constant (8,314 (kg m²)/(s² mol K)) ; **T**: absolute temperature; **X**: ion species; **z**: ionic valenz; **n**: stoichiometry; **F**: Faraday constant (96485 s A/mol); **E$_{VM}$**: VM potential

Ion species	Luminal accumulation
X	~300
X^-	~1000
X^{2-}	~3500
X^+	100
X^{2+}	~30

Tab. 1.1: **Possible luminal/cytosolic concentration gradients** established by proton-coupled antiporters at a reversal potential of -30 mV, a ΔpH of two units and with an assumed 1:1 transport stoichiometry.

Besides primary active pumps and secondary active transporters, uniporter and ion channels passively contribute (i.e. without being energized by ATP or the pmf) to a selective ion or molecule transport across the VM (**Fig. 1.1**; (Hedrich and Neher 1987)). Ion channels show the highest molecule translocation rate with 10^7 to 10^8 s^{-1} (Lodish *et al.* 2008). Due to the passive nature of transport via channels it is strictly dependent on the electrochemical gradient of the particular ion. The membrane potential, at which the direction of flow of a specific ion is changed is referred to as "the reversal potential" (E_{rev}). For example, the luminal/cytosolic Ca^{2+} gradient is typically in the order of 10^4 (10^{-3} M luminal against 10^{-7} M cytosolic) due to the role of primary active Ca^{2+}-ATPases and secondary active Ca^{2+}/H^+-exchanger (Felle 1988b; Bethmann *et al.* 1995; Felle and Hepler 1997; Wymer *et al.* 1997; Bose *et al.* 2011; Martinoia *et al.* 2012). In this case, a derivative of the Nernst equation (**Equation 1.2**; (Schwarz and Rettinger 2003)) gives a reversal potential of +116 mV. Therefore, passive Ca^{2+} fluxes directed into the vacuole are not possible at a physiological VM potential of -30 mV, Ca^{2+} release from the vacuole via ion channels, however, is facilitated.

$$E_{rev} = \frac{R * T}{z * F} * ln\left(\frac{[X^z]_{lumen}}{[X^z]_{cytosol}}\right)$$

Equation 1.2: Calculation of the reversal potential. Symbols are as for **Equation 1.1**.

Anions cannot only be luminal enriched via H^+-coupled transport, but also via passive transport through ion channels, based on the VM potential as the responsible driving force. If the potential difference is -30 mV, monovalent anions, like chloride (Cl^-) or NO_3^-, can be enriched in the vacuolar lumen by a factor of 3 and divalent anions like malate^{2-} or sulphate (SO_4^{2-}) by a factor of 10. Additionally, organic anions might get trapped in the vacuole due to a change in their valence caused by the change in pH when they move from the neutral cytosol to the acidic vacuole.

1.2.2.2. Cation transporter

Two cations are of a main importance for plant physiology: K^+ and Ca^{2+}. K^+ is an important macronutrient for plants and a limiting factor of crop yield and quality (Leigh and Jones 1984). It can account for 2 to 10% of a plant's dry weight due to concentrations in the order of 10^{-1} M in both the cytosol and the vacuole (Sharma *et al.* 2013; Wang and Wu 2013). The functions that K^+ fulfills in plants can be classified into two groups. The first group includes cellular functions for which the high and stable cytosolic K^+-concentration is an essential prerequisite. Among those functions are its involvement in protein biosynthesis and enzyme activation (Sharma *et al.* 2013).

The second group includes functions which rely on the movement of highly mobile K^+ ions between cellular compartments or its long-distance transport in the plant. These functions include tugor-regulation during cell elongation and stomatal movement, acting as counter-ion, and contributing, together with H^+, to the generation of the PM potential (Armengaud *et al.* 2004; Sharma *et al.* 2013; Wang and Wu 2013). K^+ serves an additionally important function in the phloem, where its gradient was proposed to function as an alternative energy source for phloem loading in case of a local ATP depletion (Gajdanowicz *et al.* 2011).

The functions K^+ fulfils in plant physiology dependent on K^+ uptake by root epidermal cells of which root hair cells increase the total resorptive surface. K^+ must be taken up by root hair cells against an average cytosol/soil concentration gradient of 10^3 (Sharma *et al.* 2013). Two transport systems can be found in *A. thaliana* root hairs which guarantee an efficient K^+-uptake under varying external concentrations (Epstein *et al.* 1963). The high-affinity transport system is represented by HAK5, whose homolog was recently shown to be a K^+/H^+-antiporter in the glands of the Venus flytrap *Dionaea muscipula* (Scherzer *et al.* 2015). The low-affinity transport system, on the other hand, is represented by AKT1, an inward rectifying K^+-channel of the Shaker family (Hirsch *et al.* 1998; Gierth *et al.* 2005; Nieves-Cordones *et al.* 2010; Wang and Wu 2013). However, besides an efficient uptake system at the PM, the exchange of K^+ between the cytosol and vacuole is also of crucial importance to maintain a stable cytosolic concentration (Walker *et al.* 1996; Sharma *et al.* 2013; Wang and Wu 2013).

Vacuolar K^+-transporters and channels - The uptake of K^+ against the electrochemical gradient into the vacuole is executed by the cation/H^+-antiporters NHX1 and NHX2, which were localized to root tips, the vascular tissue, guard cells, flowers and all seedling tissues (Barragan *et al.* 2012). Together with NHX3 and NHX4, they belong to the class of VM-localized NHXs and are described to transport both K^+ and Na^+ ions *in planta* (Apse *et al.* 1999; Venema *et al.* 2002; Leidi *et al.* 2010; Bassil *et al.* 2011; Barragan *et al.* 2012). *A. thaliana nhx1nhx2* double loss-of-function mutants displayed defects in flower development, stomatal movement, cell expansion, tugor regulation, pH-regulation, and growth because of their lost ability to efficiently transport K^+ into the vacuole (Bassil *et al.* 2011; Barragan *et al.* 2012; Andres *et al.* 2014). The ability of NHX1/2 to carry Na^+ besides K^+ would point towards a significant role of these transporters in plant salt tolerance. However, although it is excepted that vacuolar Na^+ sequestration is necessary for plant salt tolerance, loss-of-function mutants of vacuolar NHXs were not consistently reported to show an increased salt sensitivity (Jiang *et al.* 2010; Barragan *et al.* 2012; Martinoia *et al.* 2012). Much more consistently described was their importance for stomatal movement. The loss of an efficient K^+

uptake into the vacuole of *nhx1nhx2* mutants was shown to result in impaired stomatal movement, acidified vacuoles and a loss of vacuolar dynamics in guard cells (Barragan *et al.* 2012; Andres *et al.* 2014).

While loading of the vacuole with K^+ is apparently facilitated by K^+/H^+-symport, the release of K^+ from the vacuole, on the other hand, is mediated by ion channels with the electrochemical gradient as the driving force. These ion channels are the VM-localized members of the TANDEM-PORE K^+ (TPK)-family TPK1/2/3/5 including the K^+ INWARD RECTIFIER-LIKE (K_{ir}-like) channel KCO3 (Sharma *et al.* 2013). Another ion channel that is discussed to contribute to vacuolar K^+-release is the TWO-PORE CHANNEL1 (TPC1) which was found to represent the slow vacuolar (SV)-channel found with the earliest vacuolar patch-clamp measurements (Hedrich *et al.* 1986). The best characterized TPKs to date, are the vacuolar TPK1 and TPK3 (Voelker *et al.* 2006; Gobert *et al.* 2007) as well as the pollen tube PM-localized TPK4 (Becker *et al.* 2004). TPK3 was suggested to have an additional function in regulation of the thylakoid pmf during the light-dependent reaction of photosynthesis (Carraretto *et al.* 2013). Hence, TPK3 might serve a dual function as a K^+ channel in the VM and in the thylakoid membrane of chloroplasts as well. Members of the *TPK* gene family are expressed in roots (*TPK1/2/3*), leaves (*TPK1/2/3/5*), flowers (*TPK1/2/5*), and senescent leaves (*TPK3/5*). The activity of these non-rectifying channels seems to be independent of the membrane voltage, but regulated by pH and Ca^{2+}-dependent phosphorylation, which leads to subsequent interaction with 14-3-3 proteins (Becker *et al.* 2004; Gobert *et al.* 2007; Latz *et al.* 2007; Carraretto *et al.* 2013; Latz *et al.* 2013).

The TPC1 channel, a special case - In contrast to the K^+-selective TPK channels, TPC1 is a slowly activating, voltage-dependent, Ca^{2+}-regulated and non-selective cation channel (Hedrich *et al.* 1986; Hedrich and Neher 1987; Peiter *et al.* 2005; Hedrich and Marten 2011). It is permeable to mono- and divalent cations and is broadly expressed in *A. thaliana* tissues and conserved among other plant species (Furuichi *et al.* 2001; Hedrich and Marten 2011). The TPC1 channel was described to be closed under a physiological VM potential. Only a shift to positive potentials activates the channel and allows, in the absence of a gradient, the permeation of K^+ into the vacuole (Hedrich *et al.* 1986; Jaslan *et al.* 2016). The activation voltage of TPC1 shifts to more negative, i.e. more physiological, membrane voltages, in case the cytosolic K^+ concentration is lowered (Hedrich and Marten 2011; Hedrich 2012). The steeper electrochemical gradient allows a TPC1-dependent release of K^+ from the vacuole, which suggests a role for this channel in K^+ homeostasis (Hedrich and Marten 2011).

Ca^{2+} transport across the vacuolar membrane - In its function as the main Ca^{2+} storage of plant cells, the vacuole maintains high luminal concentrations by the activity of the two Ca^{2+}-ATPases, ACA4 and ACA11 and that of the secondary active Ca^{2+}/H^+ exchanger of the CATION EXCHANGER (CAX) family (Martinoia *et al.* 2012). Both transport systems achieve import of Ca^{2+} against the membrane polarization and a steep luminal/cytosolic concentration gradient of up to 10^4. As it was described above, primary active transporters show the lowest transport rate, however, this is compensated through the high substrate affinity of, e.g. Ca^{2+}-ATPases. *Vice versa*, the co-transporter of the CAX-family show a much greater transport rate but are less affine to their substrate Ca^{2+} (Shigaki and Hirschi 2006; Roelfsema and Hedrich 2010; Bose *et al.* 2011). This differential transport behavior led to the proposition of a housekeeping function for Ca^{2+}-ATPases in maintaining a low $[Ca^{2+}]_{cyt}$, while the much faster CAX transporters might act in the reduction of $[Ca^{2+}]_{cyt}$ after elevations during signaling processes (Roelfsema and Hedrich 2010; Bose *et al.* 2011). In contrast to the knowledge of Ca^{2+} storage mechanisms, much less is known about the Ca^{2+} release transporters in the VM (Schönknecht 2013). However, the involvement of TPC1 in salt stress- and wounding-induced long-distance Ca^{2+}-signaling has recently been demonstrated ((Choi *et al.* 2014; Kiep *et al.* 2015); a detailed description is provided in **Chapter 1.4.1.**).

1.2.2.3. Anion transport

Both inorganic and organic anions play important roles in plant physiology. The bioavailability of soil nutrients like NO_3^-, SO_4^{2-}, and P_i determines growth and agricultural productivity (Lopez-Bucio *et al.* 2003). Cl^-, like K^+, is osmotically active and involved in diverse processes like tugor regulation during stomatal movement (De Angeli *et al.* 2013), in the regulation of photosynthesis (Herdean *et al.* 2016) and pollen tube growth (Gutermuth *et al.* 2013). Carboxylates like malate and citrate are intermediates of primary metabolism and also fulfill functions as osmotica and in pH-homeostasis. Moreover, organic acids, like citrate and malate, help to release soil bound nutrients, protect plants from toxic heavy metals through complexation and in the case of malate serve as a temporary carbon storage in CAM plants. Furthermore, plants provide symbiotic microorganisms with carboxylates in exchange for NO_3^- and P_i (Meyer *et al.* 2010; Hedrich 2012).

ClC anion transporters - Once anions are taken up from the soil, or being synthesized, the vacuole serves as their main storage compartment. In the case of NO_3^- and Cl^-, accumulation in the vacuole seems to be realized by the anion/H^+ antiporter of the misleadingly named CHLORIDE CHANNEL (ClC) family. In *A. thaliana*, four of this seven members containing family were localized to the VM, namely ClCa, b, c and ClCg (De Angeli *et al.* 2006; Jossier *et al.* 2010; von der Fecht-Bartenbach *et al.* 2010; Nguyen *et al.* 2016). To date, the mechanistically best described members of this family are ClCa and ClCb. ClCa was the first plant ClC to which a function could be assigned through the observation of a reduced NO_3^- accumulation in *clca* knock-out mutants, while Cl^-, SO_4^{2-} and P_i levels remained unaltered (Geelen *et al.* 2000). Patch-clamp experiments later confirmed ClCa as a $2NO_3^-/H^+$-antiporter with a selectivity for NO_3^- over Cl^- and which is negatively regulated by ATP binding (De Angeli *et al.* 2006; De Angeli *et al.* 2009). Heterologous expression in *Xenopus laevis* oocytes demonstrated a NO_3^-/H^+-antiporter mechanism for ClCb, which seems to have a selectivity sequence of NO_3^- > Br^- > Cl^- > malate^{2-} > I^- (von der Fecht-Bartenbach *et al.* 2010). However, a physiological role of ClCb *in planta* has yet to be shown as anion levels remained unaltered in *clcb* mutants (von der Fecht-Bartenbach *et al.* 2010). From another class of transporters, NRT2.7 was identified as a putative vacuolar NO_3^- transporter as well, seemingly regulating NO_3^- accumulation in seeds (Chopin *et al.* 2007). While *ClCb* was shown to be expressed in the seedling root and hypocotyl, as well as in the leaves and flowers of mature plants (von der Fecht-Bartenbach *et al.* 2010), the expression of *ClCc* was reported, apart from a weak expression in roots, to be restricted to pollen tubes and guard cells (Jossier *et al.* 2010). While KNO_3 was shown to be able to restore impaired stomatal movement in *clcc* loss-of-function mutants, KCl was reported to be unable to do so (Jossier *et al.* 2010). Those results suggest a role of ClCc as a putative Cl^-/H^+-antiporter, in tugor regulation during stomatal movement in addition to a part in Cl^--sequestration during salt stress (Jossier *et al.* 2010). The closest homolog to *ClCc* is the last vacuolar ClC-family member *ClCg*. Those two putative Cl^-/H^+-antiporter were reported to act non-redundantly in tolerating excess Cl^- (Nguyen *et al.* 2016).

AMLT and MATE-encoded anion channels - The second important group of vacuolar anion transporters constitutes from the members of the again often misleadingly named ALUMINUM-ACTIVATED MALATE TRANSPORTER (ALMT) family. Two of its members, ALMT6 and ALMT9, were reported to be localized to the VM (Kovermann *et al.* 2007; Meyer *et al.* 2011). Together with *ALMT3*, *ALMT4,* and *ALMT5,* they form a separate phylogenetic clade within their gene family (Kovermann *et al.* 2007). ALMT5 was reported to be localized to the ER (Kovermann *et al.* 2007), suggesting a role in vesicle transport. However, the function of ALMT3 and 4 , as well as their localization, has yet to be demonstrated. The two best characterized members, ALMT6 and 9, show distinct functions. ALMT6 functions as an ion channel that conducts both malate and fumarate into the vacuole of guard cells. The channel could only be activated by micromolar $[Ca^{2+}]_{cyt}$ and seems to be regulated by the luminal pH and cytosolic malate concentration (Meyer *et al.* 2011). ALMT9

was as well initially described to be a malate and fumarate conducting ion channel in mesophyll cells (Kovermann *et al.* 2007). However, ALMT9 was later reported to be a carboxylate activated Cl^- channel, which acts independently from $[Ca^{2+}]_{cyt}$ to conduct Cl^- into the vacuole of guard cells where it is required for stomatal opening (De Angeli *et al.* 2013).
Recently, two proteins of the class of DETOXIFICATION EFFLUX CARRIER/MULTIDRUG AND TOXIC COMPOUND EXTRUSION (DTX/MATE) transporters were reported to constitute functional Cl^- channels at the VM of *A. thaliana* (Zhang *et al.* 2017a). *DTX33* and *DTX35* are among the 56 members of their gene family. Diverse functions in multidrug detoxification, in flavonoid, carboxylate and hormone transport, as well as in pathogen defence have been suggested for this transporter family (Li *et al.* 2002; Durrett *et al.* 2007; Marinova *et al.* 2007; Serrano *et al.* 2013; Zhang *et al.* 2014; Dobritzsch *et al.* 2016). Both channels are expressed in diverse tissues and organs, including roots, mesophyll cells, guard cells, stems, and flowers, and were shown to positively influence stomatal opening, pollen tube growth and root hair elongation (Zhang *et al.* 2017a).
SO_4^{2-} and P_i **transport** - Other anions essential for plant growth are SO_4^{2-} and P_i. The vacuolar transport system for SO_4^{2-} is partially known. While the transporter facilitating vacuolar SO_4^{2-} influx is still unknown (Gigolashvili and Kopriva 2014), SULTR4.1 has been identified as a vacuolar SO_4^{2-} efflux transporter (Kataoka *et al.* 2004). Although the vacuole is an important storage and sequestration compartment for P_i under limiting as well as under excess conditions, the responsible transporters for P_i accumulation in this compartment only have been recently identified in *A. thaliana. The* gene family of *PHOSPHATE TRANSPORTER 5*/*VACUOLAR PHOSPHATE TRANSPORTER* (*PHT5*/*VPT*) was reported to contain three members of the long sought-after transporters (Liu *et al.* 2015; Liu *et al.* 2016). However, only *pht5.1* (*vpt1*) loss-of-function mutant plants displayed a severe growth retardation phenotype under low, standard and high P_i conditions as well as a reduced ability to accumulate P_i. PHT5.1 (VPT1) was identified as an ion channel which is responsible for vacuolar PO_4^{2-} accumulation, but also conducts to lesser extents other anions like, SO_4^{2-}, NO_3^- and Cl^- (Liu *et al.* 2015). Moreover, the results of Liu *et al*. (2015) highlight the importance of this channel for vacuolar storage of P_i, when phosphate nutrition is growth limiting and sequestration when high P_i concentrations become toxic.

1.3. Transport and physiology of the plant hormone auxin

The ability of plants to sense the direction of light as well as gravity and to alter growth of shoot and root organs accordingly (phototropism and gravitropism) are among the best observable responses of plants.

In 1880 Charles Darwin and his son Francis published observations, which ultimately lead to the discovery of auxin. They could show that phototropism of canary grass coleoptiles (*Phalaris canariensis*) depends on light absorption by a part of the coleoptile that is well above and distinct from the side of bending. They concluded, "*[…] when seedlings are freely exposed to a lateral light, some influence is transmitted from the upper to the lower part, causing the latter to bend*" (Darwin *et al.* 1880).

Its directional transport in plants led to the identification of auxin as indole-3-acteic acid (3-IAA) as a promotor of plant growth. Peter Boysen-Jensen could demonstrate in 1913 that there is indeed a mobile, basipetally traveling signal in oat hypocotyls (Boysen-Jensen 1913). The physiological nature of it was elucidated independently by Nicolai Cholodny and Fritz Went as a growth promoting plant hormone (Went 1926; Cholodny 1927). The identification of its chemical nature began when three plant growth promoting substances, among them 3-IAA, were isolated from human urine and were called auxins (Kögl *et al.* 1934). Synthetically produced 3-IAA was later shown to be an active promotor of root formation (Thimann and Koepfli 1935). Finally, 3-IAA was discovered *in planta* in developing kernels of *Zea mays* (Haagen-Smit *et al.* 1946).

Auxin regulates the growth of plant tissues i.e. cell division, growth, elongation, and differentiation, distinctively depending on the tissue examined. For example, in the shoot and the root high auxin concentrations inhibit cell elongation, whereas low auxin levels promote cell elongation (Thimann 1938). The distinction between shoot and root tissues, however, are the different bell-shaped auxin sensitivities as they were first described by Thimann, (1938). While micromolar concentrations of externally applied auxin still induce cell elongation in shoot tissues, concentrations in the nanomolar range already inhibit root cell elongation (Thimann 1938; Dela Fuente and Leopold 1970; Evans *et al.* 1994).

Tropic responses provide examples for those different auxin sensitivities between the root and the shoot. Hypocotyls respond to light and gravity with bending towards and away from the source, respectively. The reason is a differential cell elongation. In the shoot, a higher auxin response in cells at the shaded side of the curvature than in cells at the illuminated side was reported (Friml *et al.* 2002b). Hence, high auxin levels promote cell elongation in the shoot. In the gravitropic response of the root, however, high auxin levels at the physiological lower side inhibit root cell elongation (Ottenschläger *et al.* 2003).

Besides the tropic responses to light and gravity, also the initiation of new organs, like lateral roots, is regulated by auxin (Benkova *et al.* 2003). Thereby, the process of lateral root primordia initiation from pericycle cells provides an example for a cell-specific auxin sensitivity. At low auxin concentrations, pericycle cells are arrested in the G2 phase of the cell cycle (Ferreira *et al.* 1994). The cell cycle arrest in the G2 phase enables them to commence mitosis after an increase of the local auxin concentration. The cell cycles of epidermal and cortical cells, however, are terminally arrested in the G0 phase. These cells are thus insensitive to auxin and do not commence mitosis and do not develop into primordia when auxin is applied externally (Blakely and Evans 1979; Benkova *et al.* 2003).

As explained above, cell elongation and division are strongly dependent on auxin and are controlled in intact plants through the formation of local hormone gradients. In turn, the formation of auxin gradients is highly dependent on auxin synthesis and transport mechanisms.

1.3.1. Transport routes of auxin *in planta* and physiological implications

Auxin is synthesized either via a tryptophane-dependent, or -independent pathway and transported from its main source tissues in the shoot apex and young leaves, to sink tissues in the apical parts of primary and lateral roots (Ljung *et al.* 2001; Woodward and Bartel 2005; Petrasek and Friml 2009). Based on the expression of auxin biosynthesis genes, auxin is probably produced in all cells of the shoot apical meristem (SAM; (Cheng *et al.* 2006; Pinon *et al.* 2013)). Additionally, significant auxin biosynthesis was also demonstrated to occur especially in the tips of primary and the lateral roots (Ljung *et al.* 2005).

Two forms of auxin transport can be differentiated *in planta*. Experiments in which radiolabeled auxin was fed to mature leaves of *Pisum sativum* showed that the major transport route over long distances occurs as bulk flow via the phloem (**Fig. 1.2;** (Morris and Kadir 1972)) . The second form of transport is the polar cell-to-cell transport of auxin (polar auxin transport, PAT) in shoot and root tissues (**Fig. 1.2B and C**). The latter form of auxin tranport was discovered by application of radiolabeled auxin to the shoot tip of *Pisum sativum*. In this experimental system, auxin transport was observed in the vascular cambium, but not in the phloem (Morris and Thomas 1978). While the phloem flow is relatively fast with 5-20 cm/h, PAT is at least ten times slower (Michniewicz *et al.* 2007a). Nevertheless, PAT is of particular importance for auxin distribution on a cellular scale, as it regulates the establishment of auxin gradients required for tropic responses to light and gravity. Auxin gradients are also involved in organ initiation and development of lateral roots, leaves, and flowers. Moreover, meristem formation and maintenance during reproductive and vegetative growth as well as shade avoidance in leaves depend on gradients of this omnipotent phytohormone (Cambridge and Morris 1996; Casimiro *et al.* 2001; Swarup *et al.* 2001; Friml *et al.* 2002a; Friml *et al.* 2002b; Benkova *et al.* 2003; Ottenschläger *et al.* 2003; Reinhardt *et al.* 2003).

PAT is already of importance during early embryogenesis, when the vascular system is not yet established. As soon as after the first zygotic division, an auxin gradient can be detected that helps to define the apical-basal body axis (Friml *et al.* 2003). Later during embryogenesis, auxin maxima initiate the formation of tissues and organs like the cotyledons and the root apex (Friml *et al.* 2003; Petrasek and Friml 2009). Moreover, PAT through the inner embryonic cell layers is described to be involved in the specification of the future vascular tissues (Hardtke and Berleth 1998; Friml *et al.* 2003).

In the mature root, the phloem bulk flow transports auxin towards the root tip. From the site of phloem unloading in the root tip, PAT is responsible for auxin accumulation in root apical tissues that include the cells of the quiescent center, the columella initials, and the columella cells (Swarup *et al.* 2001; Friml *et al.* 2002a). In the quiescent centre, auxin is essential in maintaining the mitotic silence (Kerk and Feldman 1995; Sabatini *et al.* 1999). Within the root tip, auxin reaches a relatively high concentration and is transported to the cells of the lateral root cap, in which PAT becomes basipetal, transporting auxin via epidermal cells towards the elongation zone (Müller *et al.* 1998; Swarup *et al.* 2001). This transport route is of primary importance for root gravitropism. If roots are stimulated by a shift of the gravitational vector from perpendicular to a lateral orientation, this signal is transduced by the columella cells, which signal to the elongation zone, by alteration of PAT. As a result, auxin levels increase at the new physiological lower site of the root where they inhibit cell elongation and thus lead to a differential elongation of the root until the root apex and gravitational vector are aligned again (Ottenschläger *et al.* 2003). The model of PAT in the root tip was named *the fountain model*, whereas its counterpart in the shoot apices was denoted as *the reverse fountain model* (**Fig. 1.2B and C**; (Benkova *et al.* 2003)). In the latter model, auxin is supplied by local biosynthesis and flows acropetally through the outermost epidermal cell layer towards newly formed leaf, or flower, primordia at the shoot apical meristem. Thereafter, it is redirected from inner cell layers and into the basipetal flow directed to the root (Benkova *et al.* 2003).

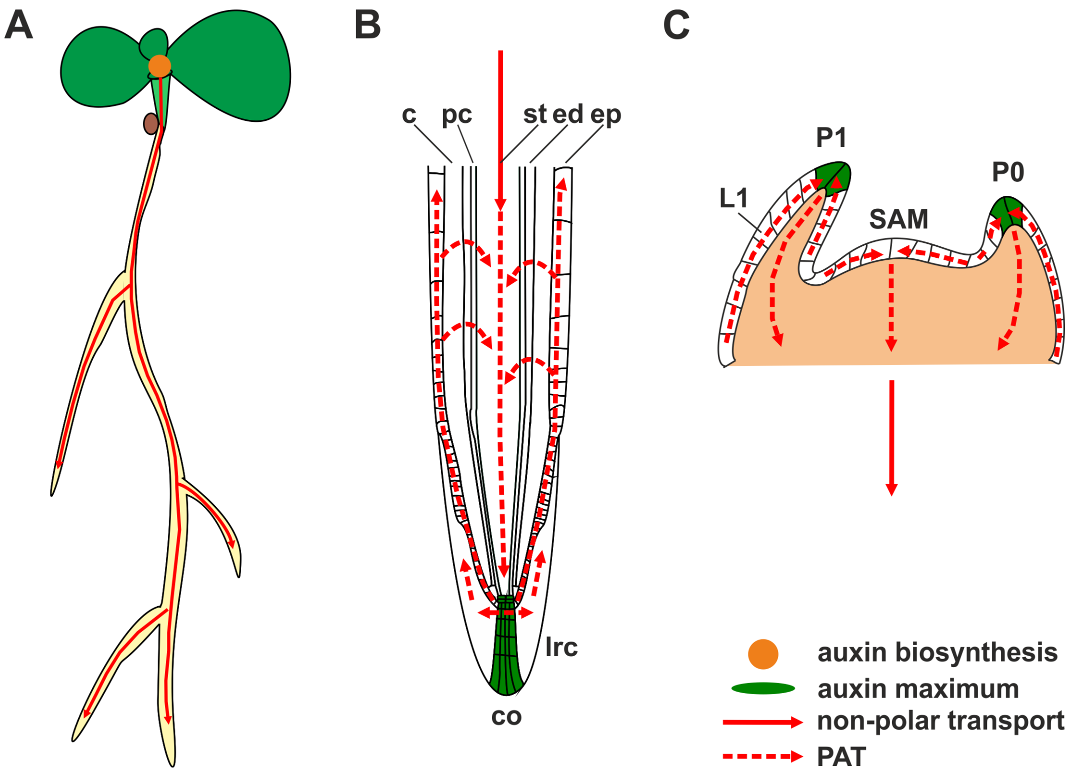

Fig 1.2: Auxin transport routes in *Arabidopsis thaliana*. (**A**) Auxin is produced in shoot apical tissues. Via the bulk flow of the phloem, auxin reaches sink tissues in the tips of primary and lateral roots. (**B**) Fountain model of auxin transport in the root. Auxin is unloaded from the phloem and distributed throughout various root tissues through polar auxin transport. The hormone is supplied from the root apex and flows through the lateral root cap and epidermal cells. Note that lateral transport of auxin in cortex cells leads to recycling of the hormone via the ploem. **lrc** lateral root cap; **ep** epidermis; **ed** endodermis; **st** stele; **co** columella; **pc** pericycle; **c** cortex. (**C**) Reversed fountain model of auxin transport in the shoot apical meristem. Polar transport of auxin in the epidermal cell layer **L1** transports auxin into the tips of leaf or flower primordia **P1** and **P0** and towards the shoot apical meristem. Redirection of auxin transport to inner cell layers channels the auxin flux into a basipetal direction, which ultimately enters into the developing vascular tissue.

1.3.2. Diffusion vs. carrier-mediated auxin transport

Auxin can move between cells either in its protonated form (IAAH) by passive membrane diffusion or in its anionic form (IAA^-) by carrier-mediated transport. The IAAH permeability of the PM of tobacco protoplasts was estimated to be around 0.18 cm/h (Delbarre *et al.* 1996). However, passive diffusion is not the predominant form of auxin transport at the cellular level. When analysing auxin transport in tobacco suspension cells and roots of *Vicia faba* and *A. thaliana,* carrier-mediated transport was found to exceed diffusion by a factor of 10 to 15 (Tsurumi and Ohwaki 1978; Delbarre *et al.* 1996; Yamamoto and Yamamoto 1998; Swarup *et al.* 2005; Kramer and Bennett 2006). To explain the directionality of auxin-transport the chemiosmotic polar diffusion model of auxin transport was proposed (Rubery and Sheldrake 1974; Raven 1975; Goldsmith 1977). These early models considered the electrical potential across the PM, the pH-difference (ΔpH), and the different auxin concentrations between cytosol and apoplast, to explain how passive diffusion of auxin, the presence of an auxin influx carrier and the asymmetric distribution of efflux carriers in the PM account for PAT.

Auxin is a weak organic acid, and therefore both forms of movement of auxin, diffusion and carrier-mediated, depend on the pH in the respective cellular compartment. In the case of *A. thaliana* root cells, the pH in the apoplast is in the range of pH 5.0 to 5.5 and pH 7.0 to 7.5 in the cytosol (Swarup and Peret 2012). The equilibrium of the dissociation reaction of IAAH is at the site of the anion in both compartments because the pK_a of IAAH (4.75) is below both pH ranges (**Fig. 1.3A**). Nevertheless, the acidic apoplastic pH allows a considerable fraction of IAAH to passively diffuse along its concentration gradient into the cell, where it dissociates at the neutral pH in the cytosol leading to an enrichment of IAA^- in this compartment.

Besides the disability of the charged auxin anion IAA^- to diffuse across the hydrophobic bilayer of the PM, also electrochemical restraints call for a specific PM-localized auxin transport machinery (**Fig. 1.3B**). The electrical PM potential of -160 to -180 mV for root cells ((Wang *et al.* 2015); own data), together with its outward directed concentration gradient (complete deprotonation of IAAH in the cytosol, **Fig. 1.3A**) prevents a passive influx of IAA^-. Hence, the influx of IAA^- across the PM and against its electrochemical gradient requires an active transport mechanism. As it was described above for the transport across the VM, the driving force for such a transport mechanism is stored in the pmf composed of the PM potential and the ΔpH between cytosol and apoplast.

The same considerations regarding the electrochemical gradient, however, act in favor for a passive carrier-mediated efflux of IAA^-, which would thus not be against but along (downhill) its electrochemical gradient across the PM.

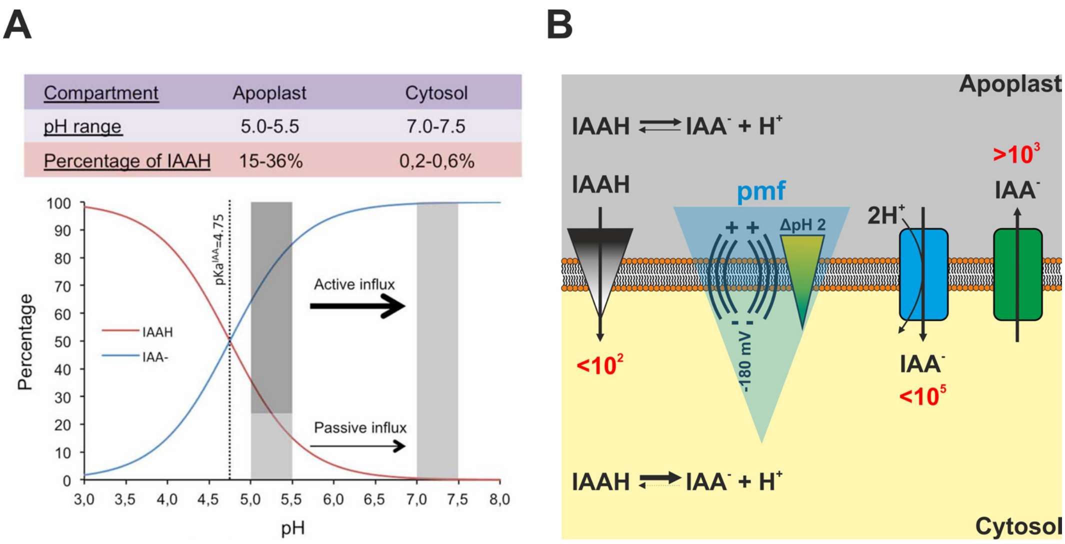

Fig. 1.3: Diffusion versus carrier-mediated auxin transport across the PM. (**A**) The dissociation of auxin at apoplastic and cytosolic pH-values (gray bars). The passive influx of IAAH is possible by diffusion along its concentration gradient. The influx of IAA^- can only be achieved through active transport against its gradient. (reproduced from and © by Swarup and Peret, (2012, originally published under the terms of the creative commons attribution license) (**B**) Electrochemical model of auxin transport at a PM potential of -180 mV and a ΔpH of two units. Auxin can enter the cytosol via diffusion along its concentration gradient of the protonated form (black to white triangle) or via carrier-mediated proton-coupled influx of its anion (blue box). Efflux via diffusion is not possible, but rather relies on the presence of efflux carriers (green box) which facilitate IAA^- efflux along the electrochemical gradient. Theoretical ideal enrichment factors are shown in red.

The following calculations exemplify the magnitude of cytosolic IAA^- enrichment that is driven by carrier-mediated influx, in comparison to passive diffusion, given a PM potential of -180 mV and a ΔpH of two units.

If, in the case of passive diffusion of IAAH, the dissociation of auxin in the apoplast and the cytosol is considered through the law of mass action with

$$\frac{[IAA^-]_{apoplast} * [H^+]_{apoplast}}{[IAAH]_{apoplast}} = \frac{[IAA^-]_{cytosol} * [H^+]_{cytosol}}{[IAAH]_{cytosol}}$$

Equation 1.3: Law of mass action applied to auxin dissociation in the apoplast and cytosol.

it follows with a ΔpH across the PM of two pH units, that

$$10^2 * \frac{[IAA^-]_{apoplast}}{[IAAH]_{apoplast}} = \frac{[IAA^-]_{cytosol}}{[IAAH]_{cytosol}}$$

Equation 1.4: Transformation of Equation 1.3 with a ΔpH of two units.

which gives a cytosolic enrichment factor for IAA^- of < 10^2, because IAAH should still be at a considerable concentration in the apoplast but not in the cytosol (Goldsmith 1977).

For a carrier-mediated and H^+-coupled auxin influx, the PM potential as well as the ΔpH must be considered as driving forces. Transformation of **Equation 1.2** gives the H^+ gradient that is equivalent to a given PM potential. **Equation 1.5** thus shows that a PM potential of -180 mV is equivalent to a ΔpH of three units.

$$-0.180\ V = 0{,}059\ V * log\frac{[H^+]_{in}}{[H^+]_{out}}$$

Equation 1.5: Transformation of Equation 1.2 to obtain the H^+ gradient equivalent to a PM potential of -180 mV.

Together with a ΔpH of two units, this results in a pmf in the order of 10^5. Since H^+-coupled auxin uptake must be electrogenic to fully benefit from the pmf a transport stoichiometry must be assumed that couples the influx of at least two H^+ to the influx of each IAA^- molecule. A pmf of 10^5 is thus equivalent to a theoretical upper border for the cytosolic enrichment of auxin via electrogenic IAA^- influx if a net movement of one positive charge is assumed. Hence, cytosolic IAA^- accumulation via an active carrier-mediated influx exceeds the accumulation by passive diffusion of IAAH 1.000-fold.

Since the carrier-mediated efflux of IAA^- is passively posible, the driving force is determined by the electrochemical gradient of IAA^-. If, again, a PM potenial of -180 mV is assumed this alone would result in a theoretical apoplastic enrichment factor for IAA^- in the order of 10^3.

The above-described examples show that carrier-mediated auxin transport represents an effective way for uptake and release of the hormone.

1.3.3. Auxin transporters in *A. thaliana*

Four predominant classes of auxin transporters have been identified in *A. thaliana* so far. The efflux facilitators of the PIN-FORMED (PIN) family (Okada *et al.* 1991; Gälweiler *et al.* 1998; Müller *et al.* 1998; Friml *et al.* 2002a; Friml *et al.* 2003) and influx facilitators of the AUXIN1/AUX1-LIKE (AUX/LAX) family (Bennett *et al.* 1996; Swarup *et al.* 2001; Bainbridge *et al.* 2008). The P-GLYCOPROTEINS (PGP) belong to the class of ATP-binding (ABC) transporters and are involved in influx and efflux (Noh *et al.* 2001; Noh *et al.* 2003; Geisler *et al.* 2005). The fourth class constitutes from members of the PIN-LIKES (PILS; (Barbez *et al.* 2012)). Additionally, with WALLS ARE THIN1 (WAT1) an auxin transporter localized to the vacuolar membrane (VM) has been recently identified as well (Ranocha *et al.* 2013). Moreover, with experimental evidence pointing towards an auxin influx function of the NO_3^- transporter NRT1.1 a link between auxin-controlled root development and the nutrient availability in the soil is provided (Krouk *et al.* 2010).

1.3.3.1. The AUX/LAX family of auxin influx carriers

The existence of a saturable auxin influx carrier with an influx optimum at a weakly acidic pH was first shown by Rubery and Sheldrake, (1974) in grown gall suspension culture cells. Further experimental data obtained from zucchini membrane vesicles revealed that auxin influx exceeds values predicted for a passive carrier-mediated transport, favoring a putative H^+-symport mechanism (Lomax *et al.* 1985). Later, loss-of-function mutations of the *A. thaliana AUX1* gene were found to be responsible for agravitropism and resistance against auxin-induced root growth inhibition (Bennett *et al.* 1996). A wild type-like auxin-responsiveness could be successfully restored by cloning of the gene and subsequent complementation of *aux1* mutants (Bennett *et al.* 1996).

The amino acid sequence of *AUX1* shows similarities to the *AMINO ACID PERMEASE I* (*AAPI*) of *A. thaliana*. Since auxin is a derivative of the amino acid tryptophane, and moreover, since plant amino acid permeases like AAPI are known to act as H^+-symporters, the conclusion was drawn that AUX1 is the previously proposed H^+-driven auxin influx carrier (Bennett *et al.* 1996). Additionally, *in situ* hybridization showed *AUX1* expression specifically in the root apex of *A. thaliana* seedlings, further highlighting the functional connection between *AUX1* and root growth (Bennett *et al.* 1996).

The first direct mechanistic evidence for AUX1 being the IAA^-/H^+ influx carrier was provided by heterologous expression of *AUX1* in *Xenopus leavis* oocytes (Yang *et al.* 2006). Via uptake experiments of radiolabeled auxin (^{3}H-IAA), AUX1 was characterized as a high affinity (K_m=800 nM), saturable and pH-dependent (optimum at an external pH of 6) auxin transporter (Yang *et al.* 2006). Moreover, the binding capacity of purified AUX1 protein for its substrate IAA was found to be half saturable at 2.6 µM IAA with a pH optimum at pH 5.5 (Carrier *et al.* 2008), which is slightly more acidic than the value found by Yang *et al*. (2006) for auxin uptake.

The above-described observation that *AUX1* expression is restricted to the root apex was later refined. **Fig. 1.4A** illustrates AUX1 localization in the PM of protophloem cells, in the gravity sensing columella cells, in the lateral root cap, and in epidermal cells as they emerge from under the root cap (Swarup *et al.* 2001; Swarup and Peret 2012). Except for the protophloem cells, where it shows a basal localization, AUX1 is more or less symmetrically distributed in the PM (Swarup *et al.* 2001).

The basal AUX1 localization in protophloem cells supports phloem unloading and acropetal auxin transport into the root apex. *AUX1* expression in the lateral root cap and epidermal cells is believed to be involved in basipetal transport of auxin from the apex, where a gravity stimulus is sensed, to the elongation zone, in which cells respond to the stimulus by differential elongation (Swarup *et al.* 2001).

Besides the founding member *AUX1*, the phylogenetic tree of the *AUX/LAX* gene family is composed of the close homologs *LAX1* to *3*, with which it shares sequence similarities between 70 and 80% (**Fig. 1.4B** and **C**). In addition to *AUX1, LAX1* and *LAX3* were shown to encode functional auxin influx carrier located to the PM (Yang *et al.* 2006; Swarup *et al.* 2008; Peret *et al.* 2012; Swarup and Peret 2012).

The expression of *LAX1* is restricted to the mature vascular tissue of the primary root, and LAX1 was shown to facilitate auxin uptake when expressed in oocytes (Peret *et al.* 2012). *LAX2* is involved in the formation of the vascular tissue in cotyledons of *A. thaliana* and is expressed in developing vascular tissues of the plant embryo and in the quiescent center and columella cells of seedlings (Peret *et al.* 2012). *LAX3* is expressed in the *A. thaliana* seedling root stele and columella cells and additionally in cortical and epidermal cells overlaying emerging lateral root primordia. A *lax3* loss-of-function mutant was reported to show a reduced number of lateral roots, similar to *aux1* mutants (Swarup *et al.* 2008). Another similarity emerged through the characterisation of LAX3 in oocytes. Uptake experiments with ^{3}H-IAA resulted in the similar saturable kinetics as described for AUX1 (Swarup *et al.* 2008).

It is noteworthy that from all *AUX/LAX* family members only *aux1* loss-of-function mutants displays an agravitropic and auxin-induced root growth inhibition resistant phenotype (Peret *et al.* 2012). Furthermore, quadruple *aux1lax1lax2lax3* loss-of-function mutant plants show severe developmental defects like multiplied and clustered shoot primordia and a spiral phyllotaxis with irregular angles between leaves, suggesting that *AUX/LAX* genes have overlapping functions in various cell types (Bainbridge *et al.* 2008).

A

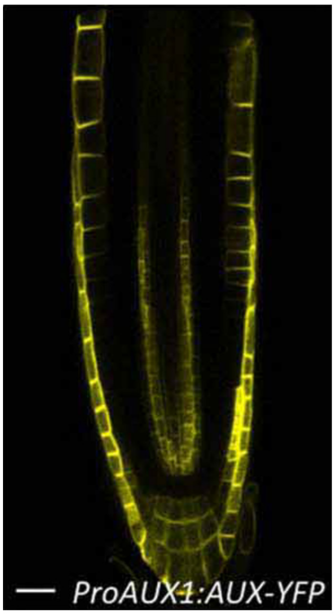

B

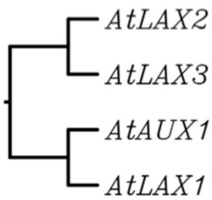

C

	AUX1	LAX1	LAX2
LAX3	76.4%	77.2%	81.3%
LAX2	75.4%	74.3%	
LAX1	80.8%		

Fig. 1.4. The *AUX/LAX* gene family of *A. thaliana*. (**A**) Localization of YFP tagged AUX1 in the root tip of *A. thaliana***.** Scale bar is 20 µm**.** (**B**) Phylogenetic tree of the *AUX/LAX* family. (**C**) The sequence similarity between *AUX/LAX* gene family members. Reproduced from and © Swarup and Peret, (2012, originally published under the terms of the creative commons attribution license).

1.3.3.2. PINs, PILS, and PGPs

Of particular significance for PAT is the PIN family of efflux carriers. The chemiosmotic model for PAT predicted the existence of auxin efflux carriers, which provoke a directional auxin transport due to their asymmetrical distribution within the PM (Rubery and Sheldrake 1974). The existence of such carriers remained obscure until the founding member of the *PIN* gene family was identified after the first isolation of an *A. thaliana pin1* loss-of-function mutant (Okada *et al.* 1991; Gälweiler *et al.* 1998). This mutant is virtually unable to develop any lateral organs at its stem and shows defects in the development of the vascular tissue (Okada *et al.* 1991). These phenotypes could be mimicked by growing plants in the presence of auxin efflux inhibitors like naphthylphthalamic acid (NPA; (Okada *et al.* 1991; Gälweiler *et al.* 1998)). PIN1 was found to localize specifically to the basal side of cells in the vascular tissue of stems in *A. thaliana* (Gälweiler *et al.* 1998) . The proof that PAT and thus root gravitropism depends on the polar localization of PINs has been provided by ectopic expression of GFP or hemagglutinin-tagged pPIN2:PIN1 in the *pin2* background. Only if PIN1 was localized to the basal side of root epidermal cells, a wild type-like response to a gravity stimulus was observed (Wisniewska *et al.* 2006). The *pin1* mutant is devoid of lateral stem organs, because in wild type PIN1 directs the flow of auxin through epidermal cells of an organ primordium towards

its tip (Petrasek and Friml 2009). Inner cell files, which show a localization of PIN1 at the basal site, drain auxin from the tip (Benkova *et al.* 2003; Reinhardt *et al.* 2003; Heisler *et al.* 2005). This reversed fountain model (Benkova *et al.* 2003) generates auxin concentration maxima at the tip of each primordium in the SAM. Hence the loss of *PIN1* disrupts primordium and organ development.
In roots, with PIN2 another member of the PIN family was found to be an important efflux carrier for PAT during the gravitropic response (Müller *et al.* 1998). PIN2 localizes to the basal part of the PM of epidermal cells and on the apical side of the cortical cells at the root apex (Müller *et al.* 1998; Blilou *et al.* 2005). With PIN3 yet another member of the PIN family was found to be important for the root gravitropic response. PIN3 was demonstrated to localize to the apical side of the PM of gravity sensing columella cells in the root tip. It was further shown that PIN3 is redistributed to the lateral PM site of these cells after a gravity stimulus was applied from this direction (Friml *et al.* 2002b).
Besides PIN1, PIN2, and PIN3, also PIN4 and PIN7 were shown to localize to the PM (Müller *et al.* 1998; Friml *et al.* 2002a; Friml *et al.* 2002b; Friml *et al.* 2003). The latter two transporters are involved in developmental processes during plant embryo development. PIN1, PIN4, and PIN7 were reported to play crucial roles in the formation of auxin gradients just after the first cell division. Those gradients ensure the formation of the apical-basal body axis, shoot and root apices, cotyledons and the vascular tissue (Friml *et al.* 2002a; Benkova *et al.* 2003; Friml *et al.* 2003). All PM-localized PIN proteins contribute to maintaining the activity of the root apical meristem (RAM) from germination on by establishing a circulating auxin flow (see **Fig. 1.2B**) through which fractions of the hormone are redeployed to the root apex (Blilou *et al.* 2005). Later in development, PIN1, PIN3 and PIN7 are involved in post-embryonic organogeneses like the formation of lateral roots or shoot-derived organs (Benkova *et al.* 2003).
Both PIN6 and PIN8 were reported to show a dual localization to the membrane of the ER and the PM. Additionally, they facilitated auxin efflux in tobacco suspension cells (Petrasek *et al.* 2006; Ganguly *et al.* 2010; Dal Bosco *et al.* 2012; Ding *et al.* 2012; Simon *et al.* 2016). The remaining PIN5 was found to be solely localized to the ER membrane where it seems to fulfill auxin loading of the ER (Mravec *et al.* 2009).
Together with the ubiquitously expressed transporters of the PILS family (Barbez *et al.* 2012) PIN5, 6 and 8 are not described to contribute significantly to PAT but rather to fulfill functions in maintaining intracellular auxin homeostasis by compartmentalization of the hormone and fine-tuning signaling by withdrawing auxin from the cytosol (Mravec *et al.* 2009; Dal Bosco *et al.* 2012; Ding *et al.* 2012). The importance of intracellular auxin transporters is highlighted by the defects

that follow loss or overexpression of PILS transporters. Those defects encompass dwarfed growth, sterility, short hypocotyls and higher lateral root density (Barbez *et al.* 2012).
Four out of 21 members of the *A. thaliana* P-GLYCOPROTEIN/MULTIDRUG-RESISTANCE/ATP BINDING CASSETTE B (PGP/MDR/ABCB) subfamily of ABC proteins were described to transport auxin actively across the PM energized by ATP hydrolysis. In *A. thaliana* loss-of-function *abcb1* and *abcb19* mutants showed auxin-related growth and developmental defects like dwarfed growth, a reduced apical dominance, and enhanced tropic responses (Noh *et al.* 2001; Noh *et al.* 2003). Lack of ABCB1 and 19 leads to a disturbed basal localization of PIN1 in hypocotyl cells, which seems to represent the underlying mechanism of the phenotype, as it results in a reduced basipetal but increased lateral flow of auxin (Noh *et al.* 2001; Noh *et al.* 2003). ABCB1 and 19 were further characterized as auxin efflux facilitators in heterologous expression systems and *abcb1* mutant mesophyll protoplasts (Geisler *et al.* 2005). The transport characteristics of the remaining ABCBs 4 and 21 are not yet clearly resolved, due to contradictory results obtained in heterologous and homologous expression systems (Cho *et al.* 2007; Yang and Murphy 2009; Kamimoto *et al.* 2012).

1.3.4. The auxin perception mechanism

Mechanistically, auxin shares its main perception and signal transduction pathway with the other phytohormones jasmonic acid and gibberellic acid. The core component of this mechanism is an SCF-E3-type ubiquitin ligase. This complex is composed of an RING-BOX PROTEIN1 (RBX1), which transfers ubiquitin to the substrate, and the scaffolding component CULLIN1 (CUL1). The adaptor protein ARABIDOPSIS SKP1 HOMOLOG1 (ASK1) connects the CUL1 to a hormone and substrate specific F-box protein as the high-affinity hormone receptor. In case of auxin, the F-box proteins are the redundant receptors TRANSPORT INHIBITOR RESPONSE1 (TIR1) and AUXIN SIGNALING F-BOX PROTEIN1-3 (AFB1-3) (Gray *et al.* 1999; Dharmasiri *et al.* 2005a; Dharmasiri *et al.* 2005b; Kepinski and Leyser 2005; Santner *et al.* 2009; Lavy and Estelle 2016).
Nuclear auxin perception results in physiological responses mainly by modulating gene expression (Guilfoyle and Key 1986; Theologis 1986; Abel and Theologis 1996). Two classes of transcription factors provide the link between perception and transcription. Proteins of the family of Aux/INDOLE-3 ACETIC ACID (Aux/IAAs, 29 members in *A. thaliana*) repress the function of AUXIN RESPONSE FACTORS (ARFs, 23 members in *A. thaliana*; (Kim *et al.* 1997; Ulmasov *et al.* 1997a; Ulmasov *et al.* 1997b; Tiwari *et al.* 2001; Guilfoyle and Hagen 2007)). ARFs were shown to directly bind auxin response elements (AuxRE) within the promotor regions of auxin-responsive genes

(Ulmasov *et al.* 1997a). Depending on their structure, ARFs can either fulfill activating or a repressing function on transcription (Guilfoyle and Hagen 2007). Repression involves the recruitment of TOPLESS (TPL) and TPL-related (TPR) co-repressors by Aux/IAAs (Szemenyei *et al.* 2008). Through the interaction with histone deacetylases, they seem to promote chromatin condensation, resulting in transcriptional repression (Long *et al.* 2006; Kagale and Rozwadowski 2011). Those interactions, however, are only persistent in the absence of auxin. The hormone mediates the recruitment of Aux/IAAs as substrates to the ubiquitin ligase $SCF^{TIR1/AFB}$ (Gray *et al.* 2001; Dharmasiri *et al.* 2005a; Kepinski and Leyser 2005). Marked by polyubiquitin, Aux/IAAs are degraded by the 26S-proteasome (Gray *et al.* 2001). Hence, ARFs are no longer functionally repressed, and transcription is altered. The expression of Aux/IAA repressors, however, is itself under control of auxin. Auxin stimulates Aux/IAA expression thereby generating a negative feedback loop within the signal transduction pathway (Abel and Theologis 1996).

1.3.5. Auxin and its role in nutrient foraging

Roots supply the aerial tissues with essential elements like potassium, nitrogen, phosphorus, iron and sulfur. The chemical cross-reactivity between these nutrients and other soil components, their solubility in water and competition with neighboring plants, however, will limit nutrient availability (Lopez-Bucio *et al.* 2003; Lynch 2011; Peret *et al.* 2011). P_i is among the nutrients for which starvation induces a postembryonic remodeling of the architecture of plant root systems for better nutrient exploitation (Lynch and Brown 2001; Lopez-Bucio *et al.* 2003).

In *A. thaliana*, P_i starvation (< 10 µM) leads to growth inhibition of the primary root, because of loss of meristematic identity. At the same time, a lack of P_i supply was described to causes an increased initiation, growth and branching of lateral roots especially at zones near the shoot (Williamson *et al.* 2001; Lopez-Bucio *et al.* 2002; Al-Ghazi *et al.* 2003; Sanchez-Calderon *et al.* 2005).

In P_i starved soils, plants also develop longer root hairs with higher density, thus contributing to an increased root surface for nutrient resorption (Bates and Lynch 1996; Ma *et al.* 2001). The larger number and length of root hairs was shown to be further augmented with an enhanced P_i uptake capacity of root hairs (Bates and Lynch 2000).

Auxin is one of the main factors that determines the root architecture and it is therefore likely that P_i starvation affects root growth by altering auxin gradients which were shown to be necessary for RAM maintenance and initiation of lateral root development (Friml *et al.* 2002a; Benkova *et al.* 2003; Friml *et al.* 2003).

In P_i-starved *A. thaliana* plants, the expression levels of the auxin receptor encoding gene *TIR1* and of the transcriptional auxin response reporter pDR5:GUS showed increased basal auxin responses in root meristems and especially in pericycle cells (Nacry *et al.* 2005; Perez-Torres *et al.* 2008; Perez Torres *et al.* 2009). In line with these results, the *tir1* mutant is insensitive to P_i starvation with respect to lateral root formation, although it still shows starvation-dependent inhibition of primary root elongation (Perez-Torres *et al.* 2008). Based on these results, it was suggested that low P_i-dependent growth inhibition of the primary root is due to the increased auxin response in the RAM (Nacry *et al.* 2005). This is believed to cause the differentiation of meristematic cells, loss of quiescent center identity and a stop in cell elongation (Sanchez-Calderon *et al.* 2005). Shootwards, however, a higher auxin level or sensitivity promotes lateral root initiation and growth from pericycle cells (Nacry *et al.* 2005).

As already mentioned, P_i starvation also promotes root hair growth. Under non-starving conditions, differentiation of epidermal cells into root hair cells starts at the basal end of the elongation zone. However, under P_i starvation, also non-hair cells develop root hairs, and because the meristematic identity at the primary root is lost and cells are differentiated root hair growth is already visible at much more apical positions (Müller and Schmidt 2004; Stetter *et al.* 2015).

1.4. Ca^{2+} signaling in plants

The sessile lifestyle of plants implies a high flexibility of growth and development to adapt to an ever-changing environment. The perception of environmental stimuli like water availability, light, wounding, mechanical cues, herbivory and pathogens, often triggers long-range signals transmitted to distal parts of the plant, where they trigger transcriptional, biochemical and metabolical alterations leading up to changes in growth and development (Choi *et al.* 2016). Those signals were shown to include small RNAs (Yoo *et al.* 2004), peptides (Reid *et al.* 2011), proteins (Corbesier *et al.* 2007), hormones like auxin (Darwin *et al.* 1880), sugars (Mason *et al.* 2014), volatile compounds (Baldwin *et al.* 2006), hydraulic signals (Farmer *et al.* 2014), electrical signals (Zimmermann *et al.* 2009), reactive oxygen species (ROS; (Alvarez *et al.* 1998)) and Ca^{2+} (Choi *et al.* 2014). For this plethora of signals three main routes through plant tissues are described by Gilroy *et al*. (2014): (**i**) the symplastic route connects the cytosol of nearby cells via plasmodesmata; (**ii**) signals which take the apoplastic route are transmitted in the space between adjacent cells and (**iii**) the vascular route allows the long-range transmission of signals between cells, tissues and plant organs which are connected via the vasculature. Among all those signals, Ca^{2+} stands out as an universal second messenger in plant physiology (Choi *et al.* 2016; Gilroy *et al.* 2016).

1.4.1. Cytosolic Ca^{2+} influx

Across plant species, the basal $[Ca^{2+}]_{cyt}$ was shown to be maintained at a low level of approximately 200 nM (Felle 1988b; Bethmann *et al.* 1995; Felle and Hepler 1997; Wymer *et al.* 1997). The free Ca^{2+} concentrations in storage compartments, foremost the vacuole, the ER, and the apoplast, however, are believed to be in the low millimolar range (Bose *et al.* 2011). Together with the cytosolic negative electrical polarization of the plasma- and organelle membranes, these steep gradients allow a very fast release of Ca^{2+} into the cytosol. Ca^{2+} signals are observed as transient changes of $[Ca^{2+}]_{cyt}$. This requires at least two separate transport systems: while Ca^{2+}-permeable ion channels with their high transport rates account for a very fast and passive Ca^{2+} influx along the steep electrochemical gradients, primary and secondary active Ca^{2+} transporters are speculated to decrease the $[Ca^{2+}]_{cyt}$ during a subsiding signal and to maintain the low basal $[Ca^{2+}]_{cyt}$ in between signals (Tuteja and Mahajan 2007; Roelfsema and Hedrich 2010).
In the case of Ca^{2+} influx across the PM, the experimental evidence points towards the existence of voltage-dependent, voltage-independent, and ligand- as well as osmotically activated Ca^{2+}-permeable channels. Except for the ligand-activated channels, the genetic identities of those Ca^{2+}-permeable channels are, however, largely unknown (Roelfsema and Hedrich 2010; Jammes *et al.* 2011; Hedrich 2012; Swarbreck *et al.* 2013). Hyperpolarisation-activated Ca^{2+}-permeable channels are described in acting on stomatal movement in guard cells (Grabov and Blatt 1998; Köhler and Blatt 2002; Stoelzle *et al.* 2003), in pollen tubes (Qu *et al.* 2007) and to co-exist with voltage-independent Ca^{2+}-permeable channels in roots, where both types seem to be involved in cell elongation (Very and Davies 2000; Demidchik *et al.* 2002; Foreman *et al.* 2003). Discussed to be among the ligand-activated Ca^{2+} channels are the CYCLIC NUCLEOTIDE-GATED CHANNELS (CNGCs) and the amino acid-gated GLUTAMATE RECEPTOR-LIKEs (GLRs) (Dietrich *et al.* 2010; Hedrich 2012). Members of the CNGC family were shown to be functional Ca^{2+}-permeable channels involved in the formation of Ca^{2+} signals needed for pollen tube growth and guidance, immune responses, auxin-regulated root gravitropism and nuclear Ca^{2+} spiking events preceding root symbiosis in *Medicago truncatula* (Yoshioka *et al.* 2006; Zhou *et al.* 2014; Charpentier *et al.* 2016; DeFalco *et al.* 2016; Gao *et al.* 2016). Concerning *A. thaliana* GLRs, several members of this family were shown to mediate Ca^{2+} influx associated with long-range transmission of wound-induced electrical signals,

root gravitropism, pollen tube growth and immune responses (Qi *et al.* 2006; Miller *et al.* 2010; Michard *et al.* 2011; Vincill *et al.* 2012; Li *et al.* 2013; Manzoor *et al.* 2013). To date, with REDUCED HYPEROSMOLALITY INDUCED $[Ca^{2+}]_{cyt}$ INCREASE 1 (OSCA1) and Ca^{2+} PERMEABLE STRESS GATED CATION CHANNEL1 (CSC1) two PM-localized osmotically activated Ca^{2+} channels have been identified in *A. thaliana* (Hou *et al.* 2014; Yuan *et al.* 2014). Patch-clamp experiments confirmed OSCA1 as a voltage-independent and hyperosmolarity-activated cation channel with a selectivity for K^+ over Ca^{2+} (Yuan *et al.* 2014). Analysis of a loss-of-function mutant revealed OSCA1 to function as an osmo-sensor by mediating osmolarity-induced Ca^{2+} signaling in guard cells and roots with implications on stomatal closure and root growth in response to osmotic stress (Yuan *et al.* 2014). CSC1 lead to hyperosmolarity-induced transient Ca^{2+} siganls when expressen in Chinese Hamster Ovary cells (Hou *et al.* 2014). Heterologous expression of CSC1 in oocytes revealed channel characteristics similar to OSCA1. CSC1 showed a voltage-independent as well as a hyperosmolarity-activated behaviour and channel-deactivation was shown to dependent on the presence of Ca^{2+} in the bath (Hou *et al.* 2014).

In the case of Ca^{2+} influx from the vacuole, TPC1 is so far the only vacuolar ion channel for which a possible role in Ca^{2+} release has been brought forward (Ward and Schroeder 1994). However, the ability of TPC1 to conduct Ca^{2+} at physiological conditions has not unequivocally been demonstrated. Nevertheless, both luminal and cytosolic Ca^{2+} levels regulate the gating properties of TPC1, albeit with opposing effects. While a rise in the luminal Ca^{2+} concentration shifts the voltage-threshold to depolarizing potentials, increasing $[Ca^{2+}]_{cyt}$ causes a change to more hyperpolarized, i.e. to more physiological potentials (Hedrich and Marten 2011). The latter response, together with a Ca^{2+} permeability of the TPC1 channel, lead to the theory that TPC1 facilitates Ca^{2+}-induced Ca^{2+} release (CICR) from the vacuole (Ward and Schroeder 1994; Bewell *et al.* 1999). A direct proof of the physiological relevance of TPC1 for CICR, however, remained elusive (Hedrich and Marten 2011; Hedrich 2012). In recent years TPC1 was demonstrated to be essential for the long-range and systemic transmission of Ca^{2+} signals induced by salt stress and mechanical wounding. The rapid shootward propagation of a salt stress-induced Ca^{2+} wave in the root, as well as the transmission of a local wound-induced Ca^{2+} signal to neighboring leaves, were both impaired in the *tpc1* loss-of-function mutant (Choi *et al.* 2014; Kiep *et al.* 2015).

As outlined below, long range Ca^{2+} signaling is likely to be interwoven with the propagation of an ROS wave. TPC1 might provide a mechanistic link between the two messenger molecules (Gilroy *et al.* 2014), as ROS were shown to suppress vacuolar Ca^{2+} release and the activity of the TPC1 channel (Pottosin *et al.* 2009). Moreover, TPC1 was shown to be essential for the formation of a salt stress induced apoplastic ROS wave in roots of *A. thaliana* (Evans *et al.* 2016). The sensitivity of TPC1 against ROS, combined with the apparent requirement of TPC1 for the long-range propagation of Ca^{2+} and ROS signals, point to an important role of TPC1 in the propagation of systemic signals.

1.4.2. Function and propagation Ca^{2+} signals in plants

Apart from stress signalling, cytosolic Ca^{2+} signals were described to play pivotal roles in the movement of stomata (Allen *et al.* 2000; Allen *et al.* 2001), the apical growth of pollen tubes and root hairs (Pierson *et al.* 1996; Bibikova *et al.* 1997), the control of the circadian rhythm (Love *et al.* 2004), tropic responses (Toyota *et al.* 2008) and fertilization (Denninger *et al.* 2014). As described above, Ca^{2+} signals are of a transient nature. The kinetics of the signal, however, were found specific for each stimulus and the subsequent response. The different kinetic patterns or "signatures" (Webb *et al.* 1996) of alterations of the $[Ca^{2+}]_{cyt}$ are defined by waveform, frequency, amplitude as well as their spatiotemporal transmission in plant tissues. Ca^{2+} signatures are discussed to encode stimulus-specific information, which is integrated to evoke specific physiological responses (Dodd *et al.* 2010; Kudla *et al.* 2010; Hashimoto and Kudla 2011; Batistic and Kudla 2012; Gilroy *et al.* 2014). For example, in *A. thaliana* roots the wave-like shootward propagation of a Ca^{2+} signal was triggered after a local salt stress was applied (Choi *et al.* 2014). In *Medicago truncatula* and *Alfalfa* root hairs, however, the exposure to nodulation factors, leads to the induction of cyosolic and nuclear Ca^{2+} spiking events (Ehrhardt *et al.* 1996; Miwa *et al.* 2006; Charpentier *et al.* 2016). The different Ca^{2+} signals, triggered by salt stress or Nod factors seem to have a specific influence on gene expression. This correlation was shown for the induction of nodulation-specific gene expression in *M. truncatula* root hairs, which required a minimal number of 36 consecutive Ca^{2+} spikes (Miwa *et al.* 2006), as well as in *A. thaliana*, for which different Ca^{2+} signatures were shown to result in correspondingly different transcriptional changes (Whalley *et al.* 2011).

In order to act as a specific signal, $[Ca^{2+}]_{cyt}$ must be sensed by Ca^{2+} binding proteins which integrate Ca^{2+} signals into physiological processes depending to their diverse subcellular localizations, Ca^{2+} affinities, and target proteins. ELONGATION FACTOR (EF)-hand motifs contain a Ca^{2+} binding α-helix-loop-α-helix structure and are responsible for the Ca^{2+}-sensitivity of many proteins. Ca^{2+} sensors can be divided into those which unite a Ca^{2+} binding function with a protein kinase activity and those proteins, which have no kinase function and relay the signal via Ca^{2+}-dependent protein-

protein interactions. To the first group belong the plant-specific Ca^{2+}-DEPENDENT PROTEIN KINASES (CDPKs or CPKs) and the Ca^{2+} specific interaction between CALCINEURIN B-LIKE (CBL) and CBL-INTERACTING PROTEIN KINASES (CIPKs) in which CBLs act as the Ca^{2+} sensors activating the kinase function of the interacting CIPKs. The second group contains the conserved CALMODULIN (CaM) and the plant-specific CaM-like (CML) proteins that alter downstream processes by Ca^{2+}-dependent protein-protein interactions (Sanders *et al.* 2002; Hashimoto and Kudla 2011; Mao *et al.* 2016; Ranty *et al.* 2016).

Although a link between Ca^{2+} signatures and a specific response seems to be well described, less is clear about how long-range Ca^{2+} signals are transmitted in plant tissues. The experimental evidence points towards Ca^{2+} signals being intertwined with other long-range signal transduction mechanisms, most notably electrical signals and ROS (Gilroy *et al.* 2014; Choi *et al.* 2016; Choi *et al.* 2017). Well studied examples for electrical signals which spread through plant tissues are the fast and self-propagating action potentials (APs) (Fromm and Lautner 2007). APs are tightly linked to the movement of Ca^{2+} (Fromm and Lautner 2007). For example, APs of the giant green algae *Chara* occur simultaneously with the release of Ca^{2+} from internal stores (Plieth *et al.* 1998) and three consecutive APs induce a transient Ca^{2+} signal in the gland cells of *Dionaea muscipula* (Escalante-Perez *et al.* 2011). APs are believed to start with the initial influx of Ca^{2+} through e.g. a mechanosensitive channel resulting in the subsequent Ca^{2+}-dependent activation of anion channels resulting in the fast depolarization phase of the AP (Fromm and Lautner 2007; Choi *et al.* 2016). Moreover, the systemic propagation of AP-like wound-induced PM potential changes in *A. thaliana*, recorded by either surface potential electrodes or phloem-penetrating aphids, depends on the presence of the two putative Ca^{2+} channels GLR3.3 and GLR3.6 (Mousavi *et al.* 2013; Salvador-Recatala *et al.* 2014; Salvador-Recatala 2016).

The second example of a wave-like signal transmitted over long distances *in planta* and which is also linked to Ca^{2+} signaling are ROS (Miller *et al.* 2009; Mittler *et al.* 2011; Gilroy *et al.* 2014; Choi *et al.* 2016). In *A. thaliana,* the apoplastic generation of ROS and their systemic propagation was shown to dependent on the presence of the PM-localized NADPH oxidases RESPIRATORY BURST HOMOLOGS (RBOHs) (Sagi and Fluhr 2001; Miller *et al.* 2009). The activity of these enzymes depends on the $[Ca^{2+}]_{cyt}$ at multiple levels, for which regulatory features present in the N-terminal domain are responsible (Choi *et al.* 2016; Choi *et al.* 2017). The presence of EF-hand motifs allows an immediate level of Ca^{2+}-dependent regulation. N-terminal phosphorylation through CPKs and CBL/CIPK complexes together with Ca^{2+}-dependent accumulation of phosphatidic acid that binds to the N-terminal region of RBOHs mediate indirect integrations of Ca^{2+} signals into ROS production

(Ogasawara *et al.* 2008; Zhang *et al.* 2009; Kimura *et al.* 2012; Dubiella *et al.* 2013; Gilroy *et al.* 2014; Choi *et al.* 2016; Choi *et al.* 2017). The functional interdependence of Ca^{2+} and ROS signals has been reported in several studies. Experiments on guard cells of the *A. thaliana rbohdrbohf* double losss-of-function mutant, for example, have shown that the abscisic acid (ABA)-dependent activation of PM-localized Ca^{2+} channels and thus Ca^{2+} influx, in turn, dependents on the production of ROS (Kwak *et al.* 2003). A comparable effect was reported for *A. thaliana* roots where RBOHC produced ROS stimulate the activity of hyperpolarization-activated Ca^{2+} channels essential for root hair elongation (Foreman *et al.* 2003). Additionally, the Ca^{2+} binding protein CPK5 was shown to target RBOHD for activation through its N-terminal phosphorylation directly, and the *cpk5* mutant was reported to consequently lack the ability for the systemic propagation of an ROS signal to distal leaves upon a local flagellin treatment (Dubiella *et al.* 2013). Moreover, the salt stress-induced shootward propagating Ca^{2+} wave in *A. thaliana* roots, which was already mentioned above, enhances the expression of ROS-induced marker genes like *ZAT12* in the shoot (Choi *et al.* 2014) and was recently shown to be abolished when roots were treated with the ROS scavenger ascorbate (Evans *et al.* 2016). Those findings led to the development of a positive feedback model, in which the production of ROS by RBOHs stimulate the activity of Ca^{2+} channels. The subsequent elevation of the $[Ca^{2+}]_{cyt}$ then feeds back on the activity of RBOHs through the above described regulatory mechanisms including Ca^{2+} binding and Ca^{2+}-dependent phosphorylation (Kwak *et al.* 2003; Mittler *et al.* 2011; Kimura *et al.* 2012; Dubiella *et al.* 2013; Gilroy *et al.* 2014; Evans *et al.* 2016). Gilroy *et al*. (2014) described that this model, however, cannot be applied to the long-range transmission of Ca^{2+} signals without problems. The cytosol, with its low basal Ca^{2+} level and the connection of adjacent cells via plasmodesmata, is a suitable transmission medium for Ca^{2+} signals, but due to the abundance of essential processes sensitive to oxidative damage therein, the more appropriate transmission compartment for ROS is the apoplast. However, the high Ca^{2+} buffering capacity of the cytosol in concert with the apoplastic scavenging of ROS might limit the long-range transmission of a combined signal. The limited range and slow diffusion velocities of both Ca^{2+} and ROS signals might be compensated by simultaneously propagating electrical signals. Those were shown to be associated with Ca^{2+} signals, and the same might be true for ROS signals since the propagation of surface potential changes to distal leaves of *A. thaliana* in response to a local heat, or excess light stimulus was reported to depend on the presence of RBOHD (Suzuki *et al.* 2013). Therefore a model is discussed in which the mutual maintenance of Ca^{2+}, ROS, and electrical signals accounts for the systemic propagation of those signals in plants (Steinhorst and Kudla 2013; Suzuki *et al.* 2013; Gilroy *et al.* 2014; Choi *et al.* 2016; Gilroy *et al.* 2016; Choi *et al.* 2017).

1.4.3. The role of Ca^{2+} in auxin physiology

Externally applied auxin triggers fast cytosolic Ca^{2+} signals in various cell types and plant species, like mesophyll protoplasts from wheat (Shishova and Lindberg 2004), coleoptiles and roots of maize (Felle 1988a; Gehring *et al.* 1990) and roots of *A. thaliana* (Monshausen *et al.* 2011). The apoplast and internal Ca^{2+} stores contribute to an auxin-induced Ca^{2+} release, which is most likely independent from transcriptional changes induced by the $SCF^{TIR1/AFB}$ signaling cascade, based on the speed of the emerging signal (Vanneste and Friml 2013). So far, the only Ca^{2+}-permeable channel identified to be involved in auxin-induced cytosolic Ca^{2+} signals in *A. thaliana* is the PM-localized CNGC14 (Shih *et al.* 2015). Within their study, the authors propose that CNGC14-dependent Ca^{2+} signals are likely elicited through apoplastic perception of the gravitational redirected auxin flow. These $[Ca^{2+}]_{cyt}$ elevations should further be necessary for apoplast alkalization and the subsequent reduction of cell elongation, which leads to realignment of the root growth direction with the gravitational vector. With this model, the work by Shih *et al*. (2015) drove a mechanistic explanation forward concerning earlier findings which showed that Ca^{2+} moves asymmetrically through gravity-stimulated roots and that Ca^{2+} chelators have an inhibitory effect on root gravitropism (Lee *et al.* 1983a, b; Bjorkman and Leopold 1987).

As it was described above, it has long been known that auxin has a concentration-dependent effect on cell elongation. Ca^{2+} signaling was shown to be integrated into cell elongation through the regulation of the activity of the PM H^+-ATPase AHA2 (**Fig. 1.5A**). This H^+ pump is apparently regulated by the phosphorylation status of its C-terminus within minutes after auxin application (Takahashi *et al.* 2012; Fendrych *et al.* 2016). While phosphorylation of the penultimate threonine residue (Thr-947 of AHA2) enables the interaction with 14-3-3 proteins and the subsequent activation of AHA2, phosphorylation of the Ser-931 residue has the opposite effect (Fuglsang *et al.* 1999; Fuglsang *et al.* 2007; Takahashi *et al.* 2012). Mechanistically, low auxin concentrations stimulate AHA2 activity through the stabilization of the phosphorylated Thr-947 by SMALL AUXIN UP RNA19 (SAUR19)-dependent inhibition of the PP2C-D1 phosphatase (Spartz *et al.* 2014). Higher auxin concentrations, on the other hand, lead to the Ca^{2+}-dependent phosphorylation of Ser-931 through the Ca^{2+} sensing protein CBL2 and its interacting protein kinase CIPK11 (Fuglsang *et al.* 2007).

Although the Ca^{2+}-dependent alterations of AHA2 activity have an indirect effect on cellular auxin transport via pmf modulation, there also exists experimental evidence that $[Ca^{2+}]_{cyt}$ regulates the activity of auxin transporters directly via Ca^{2+} binding proteins. In fact, the general importance of Ca^{2+} availability for PAT has long been known (Dela Fuente and Leopold 1973; Dela Fuente 1984). **Fig. 1.5B** summarizes the current knowledge of the impact of auxin-induced Ca^{2+} signals on auxin influx and efflux. So far, it has gotten clear that members of two sub-families of AGCVIII class protein kinases interact with PIN and ABCB auxin efflux facilitators. The first subfamily constitutes of the serine/threonine kinase PINOID (PID) and its close homologs WAVY ROOT GROWTH1 and 2 (WAG1/2; (Christensen *et al.* 2000; Dhonukshe *et al.* 2010)). PID/WAGs-dependent phosphorylation of PIN1 and PIN3 was reported to enhance auxin-efflux in the *Xenopus* oocyte expression system, as well as *in planta* and to interfere with PIN polarity (Michniewicz *et al.* 2007b; Kleine-Vehn *et al.* 2009; Dhonukshe *et al.* 2010; Zourelidou *et al.* 2014). The influence of PID on ABCB1 depends on its interaction with the Immunophilin-like TWISTED DWARF1 (TWD1) (Henrichs *et al.* 2012; Wang *et al.* 2013a). The integration of Ca^{2+} signals seems to occur via the Ca^{2+}-dependent interaction of PID with the Ca^{2+} binding proteins PID BINDING PROTEIN1 (PBP1) and TOUCH3 (TCH3) (Benjamins *et al.* 2003). The second subfamily of AGCVIII kinases contains four functional redundant D6 PROTEIN KINASEs (D6PKs), which were also found to positively regulate auxin efflux *in planta* as well as in oocytes (Zourelidou *et al.* 2009; Barbosa *et al.* 2014; Zourelidou *et al.* 2014).

Because of the close relationship between D6PKs and PID/WAGs, a Ca^{2+}-dependent regulation of D6PKs is discussed, however, not yet confirmed (Vanneste and Friml 2013). Both, *pid/wag* and *d6pk* loss-of-function mutants show phenotypes, like defects during embryogenesis, defects in the SAM, and in lateral root formation similar to those of *pin* mutants, thus highlighting their importance for a proper PIN-dependent auxin transport (Willige and Chory 2015). Concerning auxin influx, only the putative NO_3^--regulated auxin influx carrier NRT1.1 (Krouk *et al.* 2010) has been shown to be phosphorylated by the Ca^{2+}-dependent kinase CIPK23 (Cheong *et al.* 2007; Ho *et al.* 2009). This phosphorylation enhances the affinity of NRT1.1 for its primary substrate NO_3^-, thus reducing its auxin transport capacity.

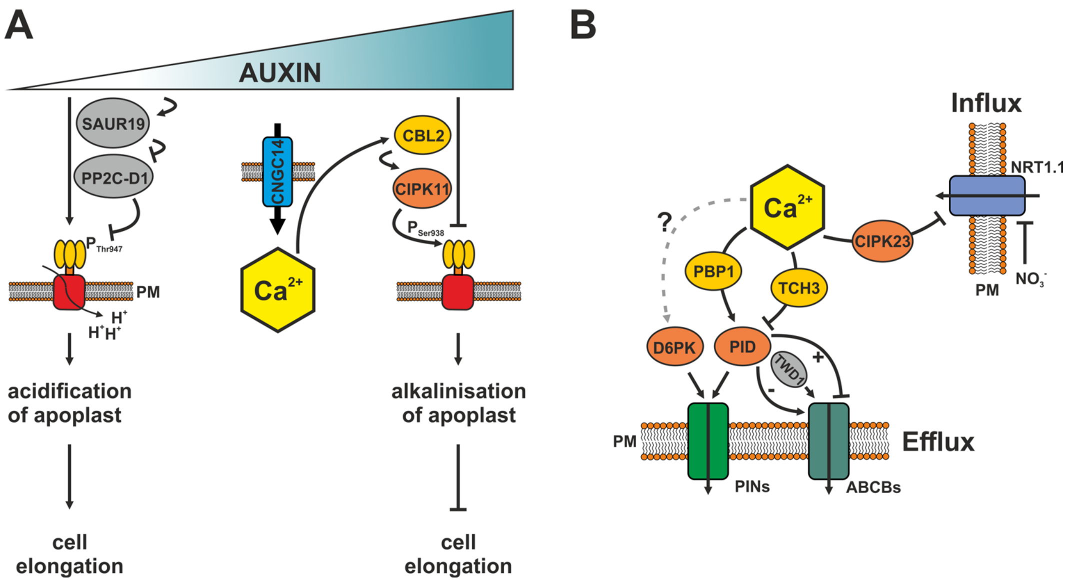

Fig. 1.5: Integration of Ca^{2+} signals into auxin physiology. (**A**) Low auxin concentrations stimulate apoplastic acidification, and in return cell elongation, through stabilization of the Thr-947 phosphorylation of AHA2. High auxin levels are thought to lead to a Ca^{2+}-induced activation of CBL2/CIPK11 that phophorylates of Ser-938 in AHA2 and inhibits the activity of this H^+-ATPase. The figure was updated and expanded after Vanneste and Friml, (2013). (**B**) The Ca^{2+}-dependent interaction of PID with PBP1 and TCH3 regulates the activity of PIN and ABCB efflux transporters. PID interaction with ABCB depends on TWD1, which also stimulates ABCB, independently from PID. A Ca^{2+}-dependent regulation of D6PK is still elusive (doted gray arrow). CIPK23 regulates the auxin influx capacity of NRT1.1).

1.5. *A. thaliana* root hair cells – an attractive *in planta* system to study vacuoles and auxin transport

The intracellular localization of vacuoles complicates their analysis *in planta*. Before the patch-clamp technique was available, intracellular microelectrodes were used for *in planta* analysis of vacuolar properties including the VM potential (Spanswick and Williams 1964), luminal pH (Penny and Bowling 1975) and abundance of different ions (Spanswick and Williams 1964; Dunlop and Bowling 1971). Also the electrical conductance of the VM has been probed *in vivo* before in *Avena* coleoptiles, maize suspension culture cells and mostly in giant algae of the *Characeae* family like *Nitella* and *Chara* (Goldsmith and Cleland 1978; Tester *et al.* 1987; Holdaway-Clarke *et al.* 1996). The development of the patch-clamp technique (Neher *et al.* 1978) and its first application to isolated plant vacuoles (Hedrich *et al.* 1986), however, was key to gain detailed insights into the electrophysiological characteristics of vacuolar transport and its genetic background (Gobert *et al.* 2007; Schulz *et al.* 2011; Rienmüller *et al.* 2012; Jaslan *et al.* 2016). The patch-clamp technique, together with experimental approaches that employed heterologous expression systems such as oocytes or yeast cells (Kovermann *et al.* 2007; Latz *et al.* 2007; Klemens *et al.* 2013), advanced the knowledge of how individual transporters and ion channels work and are being regulated. *In planta* approaches to probe the electrical properties, however, benefit from the presence of a nearly undisturbed cytoplasm, including regulatory proteins like the aforementioned Ca^{2+} binding CPKs and CBL/CIPKs. The undisturbed connection between the VM and the cytoplasm is important to probe the modulations of vacuolar transport processes in response to external chemical or mechanical cues that trigger local or systemic signaling events.

At the experimental site, root hair cells of *A. thaliana* display important characteristics that make them an optimal model system, both for the analysis of the electrical properties of vacuoles and auxin transport and signaling *in planta*. Root hair cells have the advantage that they are easily accessible for microelectrodes and imaging approaches at hydroponically grown plants (Lew 2004; Jeworutzki *et al.* 2010). Additionally, the root hair tip is typically devoid of the vacuole, which allows for the differentiation of cytoplasmic against vacuolar microelectrode impalement. Moreover, root hair cells were demonstrated to tolerate the impalement with two individual microelectrodes, thus enabling the simultaneous observation of the electrical properties of the VM and those of the PM (Lew 2004).

At the physiological site, the VM of root hair cells seems to contain nearly all important transporters and channels described earlier in this work. **Fig. 1.6A** shows the gene expression of known vacuolar active and passive transporters, as well as of ion channels in *A. thaliana* root epidermal cells extracted from data published by Lan *et al*., (2013) and Birnbaum *et al*., (2003). Additionally, **Fig. 1.6B** provides an overview of the functions and the so far known transport mechanisms of some relevant transporters. Among the highly expressed genes are *TPC1*, *CAX2* and *ACA11*, which are putatively important for vacuolar Ca^{2+} release and uptake during Ca^{2+} signaling events (Roelfsema and Hedrich 2010; Bose *et al.* 2011; Choi *et al.* 2014). Moreover, transport proteins for essential nutrients like P_i (PHT5.1), NO_3^- (ClCa), Cl^- (ClCc, ALMT9, DTXs), K^+ (TPC1, NHX1, TPKs), as well as for Zn^{2+} and Mg^{2+} (MTP1, MGT2, MHX1), seem to be present in the VM of root epidermal cells (Martinoia *et al.* 2012; Liu *et al.* 2015; Zhang *et al.* 2017a). ESL1, TMT1, and SWEET16 represent the capacity to store and release sugars from root cell vacuoles (Yamada *et al.* 2010; Schulz *et al.* 2011; Klemens *et al.* 2013). The different ABCCs, together with heavy metal transporters like COPT5 and NRAMP4 confer the ability to sequester xenobiotics, secondary metabolites and heavy metals (Martinoia *et al.* 2012; Klemens *et al.* 2013).

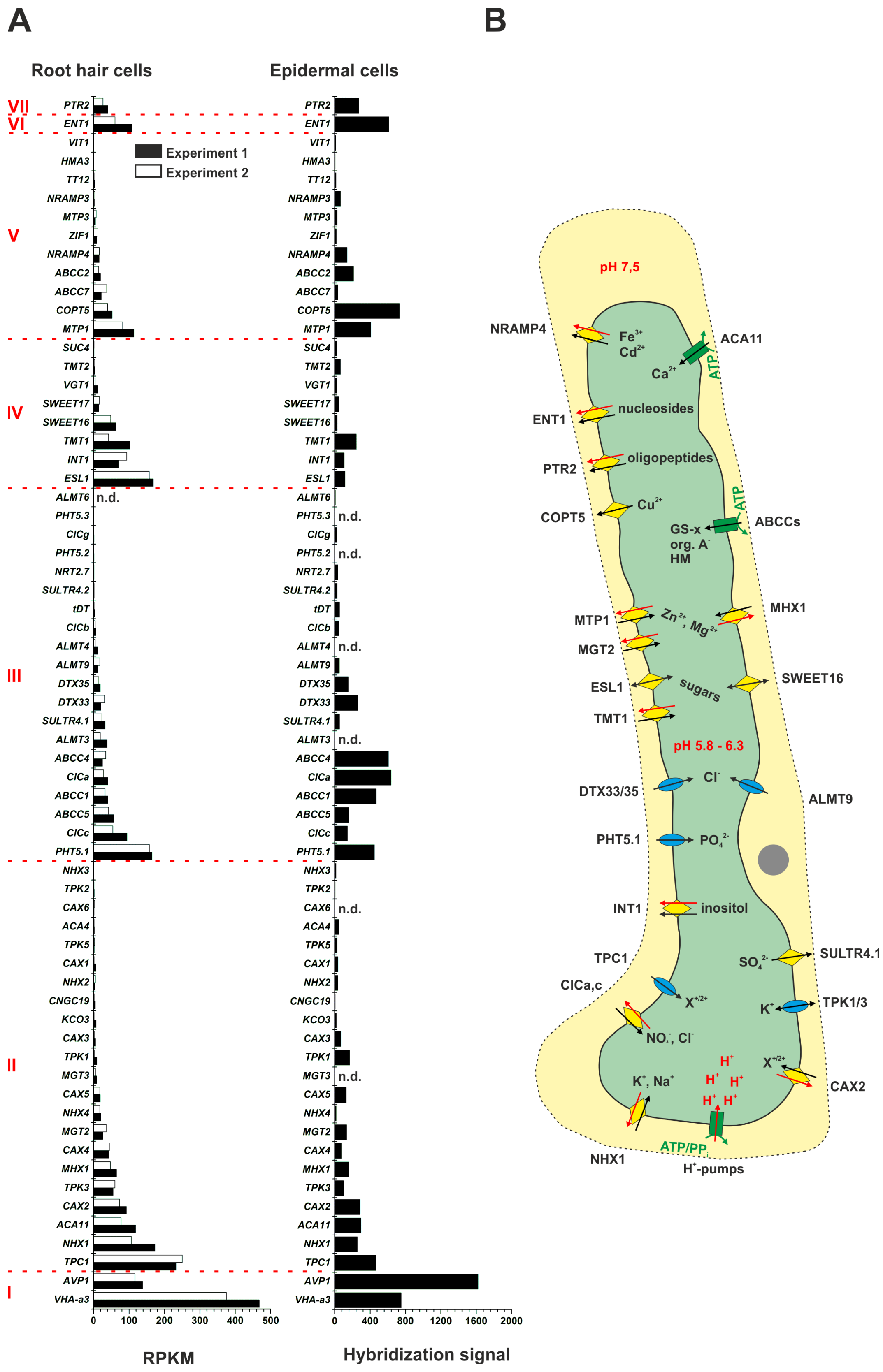
A
B
Root hair cells
Epidermal cells
Experiment 1
Experiment 2
VII
VI
V
IV
III
II
I
PTR2
ENT1
VIT1
HMA3
TT12
NRAMP3
MTP3
ZIF1
NRAMP4
ABCC2
ABCC7
COPT5
MTP1
SUC4
TMT2
VGT1
SWEET17
SWEET16
TMT1
INT1
ESL1
ALMT6
PHT5.3
ClCg
PHT5.2
NRT2.7
SULTR4.2
tDT
ClCb
ALMT4
ALMT9
DTX35
DTX33
SULTR4.1
ALMT3
ABCC4
ClCa
ABCC1
ABCC5
ClCc
PHT5.1
NHX3
TPK2
CAX6
ACA4
TPK5
CAX1
NHX2
CNGC19
KCO3
CAX3
TPK1
MGT3
CAX5
NHX4
MGT2
CAX4
MHX1
TPK3
CAX2
ACA11
NHX1
TPC1
AVP1
VHA-a3
n.d.
0
100
200
300
400
500
800
1200
1600
2000
RPKM
Hybridization signal
pH 7,5
NRAMP4
Fe3+
Cd2+
ACA11
Ca2+
ATP
ENT1
nucleosides
PTR2
oligopeptides
COPT5
Cu2+
ABCCs
GS-x
org. A-
HM
MHX1
MTP1
Zn2+, Mg2+
MGT2
SWEET16
ESL1
sugars
TMT1
pH 5.8 - 6.3
DTX33/35
Cl-
ALMT9
PHT5.1
PO42-
INT1
inositol
TPC1
SULTR4.1
SO42-
ClCa,c
X+/2+
K+
TPK1/3
NO3-, Cl-
H+
CAX2
K+, Na+
ATP/PPi
NHX1
H+-pumps

Fig. 1.6: Expression profiles and functions of vacuolar pumps, ion channels and transporters in root epidermal cells extracted from data published by Lan *et al*. (2013) and Birnbaum *et al*. (2003). (**A**) The selection of genes and the categorization on the left regarding the transported substrates corresponds to Martinoia *et al*. (2012). Categorization is as follows. **I**: H^+-pumps; **II**: cation transporter; **III**: anion transporter; **IV**: carbohydrate transporter; **V**: heavy metal transporter; **VI**: nucleoside transporter; **VII**: oligopeptide transporter. In addition to Martinoia *et al*. (2012), H^+-pumps were added due to their importance by providing the trans-tonoplast H^+-gradient. *SWEET16 and 17* were shown to encode vacuolar sugar transporters (Chardon *et al.* 2013; Klemens *et al.* 2013; Guo *et al.* 2014). *KCO3* encodes a putative vacuolar K^+-channel (Rocchetti *et al.* 2012). *ALMT3* is a putative vacuolar member of the *ALMT* family (Kovermann *et al.* 2007) and the *PHT* family was recently shown to include the vacuolar P_i channel PHT5.1 (Liu *et al.* 2015; Liu *et al.* 2016). **The left bar chart** shows expression data from two independent RNA-sequencing experiments (as indicated by the black and white bars) on *A. thaliana* root hair protoplasts published by Lan *et al*. (2013). Protoplasts were isolated from the first 10 mm of roots from 5d old seedlings. Root hair protoplasts were isolated from other cells, based on their expression of the green fluorescent protein (GFP) under the root hair-specific promotor of *EXPANSIN 7*. Expression data are shown in reads per kilobase per million mapped reads (RPKM). **The right bar chart** shows expression data of the same genes but extracted from microarray data published by Birnbaum *et al*. (2003). This data shows the expression profiles (as the average of three replicates) of epidermal cell protoplasts (tricho- and atrichoblasts) of roots from 5d old *A. thaliana* seedlings. From three developmental stages published, the latest stage is displayed. Its lower border from the root tip up was defined by Birnbaum *et al*. (2003) by the start of the longitudinal expansion, and fully elongated root hairs defined the upper border of stage 3. GFP marker lines were used for isolation of protoplasts from specific tissues (pGLABRA2::GFP for epidermal cells). Expression data are shown as the microarray hybridization signal. Genes of which expression profiles could not be retrieved from the data sets are marked with not detectable (n.d.). (**B**) A functional representation of transport processes between the cytosol (beige) and the vacuolar lumen (green) of *A. thaliana* root hair cells of each category from (A). Transporter names are shown outside the root hair cell and substrates inside in the vacuolar lumen. Ion channels are depicted in blue, secondary active and passive transporters are depicted in yellow and primary active transporters are green. Black arrows represent substrate transport routes, and in cases of H^+ co- or antiport the cytosolic influx of H^+ is represented by red arrows. The depicted pH values are according to Bibikova *et al*. (1998) and Bassil *et al*. (2011) for growing root hair cells. Abbreviations are: $\mathbf{X^{+/2+}}$ mono- or divalent cation; **HM** heavy metal; **GS-x** glutathione conjugate

Just like root hairs are a perfect system to study the vacuole, they are equally suitable to study auxin transport in real time with electrophysiological methods. Auxin is regarded as the main regulator of primary and lateral root growth. Moreover, it is also believed to be essential for root hair development (Masucci and Schiefelbein 1994; Pitts *et al.* 1998). Both, the auxin transport mutants *pin2* and *aux1*, as well as the auxin quadruple receptor mutant *tir1afb1afb2afb3*, display a short root hair phenotype (Dharmasiri *et al.* 2005b; Jones *et al.* 2009; Rigas *et al.* 2013). AUX1 was recently shown to be important for the promotion of root hair growth during P_i-starvation in *A. thaliana* and *Oryza sativa* (Bhosale *et al.* 2017; Giri *et al.* 2017). Root hair-specific expression of any PM-localized *PIN* resulted in shorter root hairs (Ganguly *et al.* 2010). The enhancement of auxin sensitivity of root hair cells by overexpressing *TIR1* resulted in longer root hairs compared to wild-

type (Ganguly *et al.* 2010). Further, a constitutive shut-down of auxin signaling by expressing degradation resistant Aux/IAA mutants inhibited root hair growth (Fukaki *et al.* 2002).
Out of the main transporter classes contributing to PAT, transcriptomic analysis showed that *PIN2* and *AUX1* are the only genes expressed in root hair cells of *A. thaliana* (**Fig. 1.7**; (Birnbaum *et al.* 2003; Lan *et al.* 2013)). It should be noted here that experiments, using fluorescently labeled proteins, localized the efflux carrier PIN2 to the basal PM site of both root hair and non-hair cells (Jones *et al.* 2009). The main influx carrier AUX1, however, was not detectable in root hair cells with such an approach (Jones *et al.* 2009). A possible explanation of this contradiction might be a much higher sensitivity of the transcriptomic approaches.

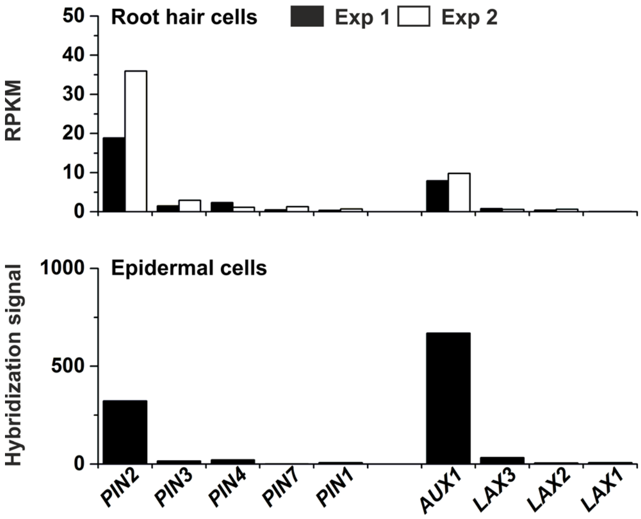

Fig. 1.7: Expression of auxin transporter in *A. thaliana* root epidermal cells. The upper panel shows expression data from two independent RNA-sequencing experiments (black and white bars) on *A. thaliana* root hair protoplasts published by Lan *et al*. (2013). refer to lower graph for X-axis labels. Data were obtained as described for **Fig. 1.6**. Expression data are shown in reads per kilobase per million mapped reads (RPKM). **The lower panel** shows expression data of the same genes but extracted from microarray data published by Birnbaum *et al*. (2003). From three developmental stages published, the latest stage is displayed. Its lower border from the root tip up was defined by Birnbaum *et al*. (2003) by the start of the longitudinal expansion, and fully elongated root hairs defined the upper border of stage 3. Data was obtained as described for **Fig. 1.6**.

1.6. Experimental work that preceded this thesis

Regarding an *in planta* analysis of the electrical properties of plant vacuoles Dr. Yi Wang (Wang *et al.* 2015) performed initial experiments in which root epidermal cells of *A. thaliana* seedlings were impaled with sharp microelectrodes (**Fig. 1.8A** and **B**). The fluorescent dye Lucifer yellow (LY) was injected into the cells to report the intracellular localization of the electrode tip. Cytosolic impalement was found to be associated with time-independent currents of high amplitude that correlated to a PM conductance of 97 nS. The electrical conductance measured after impalement of the vacuole, however, was approximately five-fold lower, with a value of 19 nS. In contrast to an average PM potential of -172 mV, electrodes localized in the vacuole measured considerably more positive potentials, with a value of -141 mV. The difference of 31 mV between the two compartments matches the previously reported values for the VM potential (Martinoia *et al.* 2007; Martinoia *et al.* 2012). In subsequent experiments, Dr. Florian Rienmüller found the VM conductance to decrease with time after microelectrode impalement (Wang *et al.* 2015). Since $[Ca^{2+}]_{cyt}$ elevations are likely to be triggered through impalement, experiments were performed in which the Ca^{2+} indicator dye FURA-2 was iontophoretically injected into the cytosol of bulging *A. thaliana* root hair cells. Simultaneously the VM conductances of the same root hair cells were probed to test the possibility that the total VM conductance is sensitive to changes of $[Ca^{2+}]_{cyt}$. Thereby, it could be shown that sudden transient $[Ca^{2+}]_{cyt}$ elevations are associated with likewise transiently increases of the VM conductance (**Fig. 1.8C** and **D;** (Wang *et al.* 2015)).

Bulging root hair cells are well suited to study the transport of the plant growth hormone auxin with electrophysiological methods. In initial experiments, Dr. Elżbieta Król could show that auxins externally applied to whole seedlings trigger a concentration and pH-dependent depolarization of the PM potential of root hair cells of *A. thaliana* seedlings. This membrane response was further shown to be absent in *aux1* mutant plants when they were challenged with external 3-IAA.

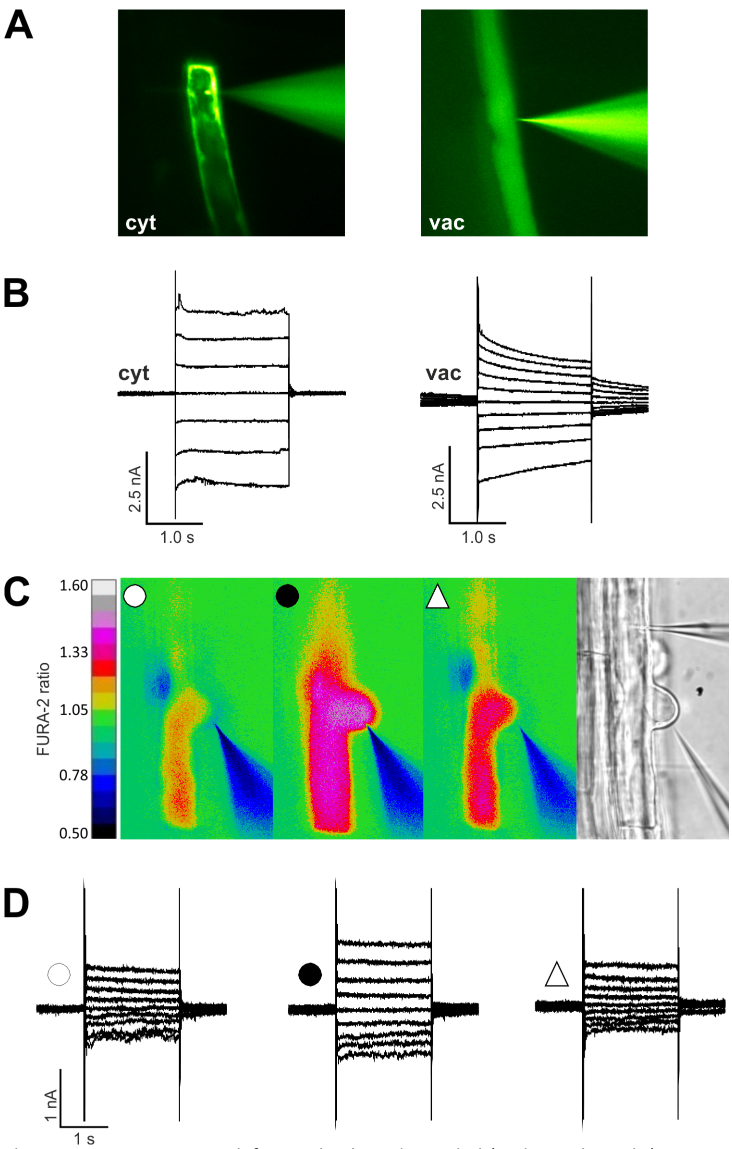

Fig. 1.8: Electrical properties of the VM of *A. thaliana* root epidermal cells and their connection to cytosolic Ca^{2+}. Modified from Wang *et al.* (2015). With permission for reuse from Elsevier. Data obtained by Dr. Yi Wang (A and B) and Dr. Florian Rienmüller (C and D). (**A**) Impalement of root epidermal cells by triple-barrelled microelectrodes. The fluorescent dye Lucifer yellow was used to determine the intracellular position of the electrode tip in either the cytosol (left panel) or within the vacuolar lumen (right panel). (**B**) Typical electrical currents measured at the corresponding electrode positions shown in (A). (**C**) Ratiometric live-cell imaging of the Ca^{2+} indicator FURA-2 iontophoretically injected into the cytosol of bulging root hair cells, which were impaled by two microelectrodes (brightfield picture on the right). FURA-2 was injected via a microelectrode impaled through the root hair tip and a second microelectrode impaled into the vacuole was used for voltage-clamp experiments. From left to right the color-coded (scale on the right) images indicate $[Ca^{2+}]_{cyt}$ before (white circle), during (black circle) and after a peak in the cytosolic Ca^{2+} level (white triangle). (**D**) Vacuolar currents corresponding to the images from (C). Note the transient increase in membrane current during the Ca^{2+} peak.

1.7. Aim of this work

The interplay of cytosolic Ca^{2+} with the electrical conductance of the vacuolar membrane as well as its integration in the earliest auxin-induced signaling events were the focal points of this work. Bulging root hair cells of *A. thaliana* were chosen as a suitable model system that allows the investigation of both aims *in planta* through the combination of electrophysiological with live-cell imaging techniques.

The first part is dedicated to the electrical properties of vacuoles, which fulfil a role in turgor regulation and serve as intracellular storages for nutrients, metabolites, and toxins. These functions depend on the transport processes across the VM. Since the patch-clamp technique and techniques of molecular biology became available the transport mechanisms, regulation and physiological impact of many vacuolar transporters and channels have been characterized (Martinoia *et al.* 2012). However, as the patch-clamp technique requires the isolation of vacuoles only limited experimental data on the *in vivo* regulation of vacuolar transport processes is available. Therefore, the aim of the first part of this work was to gain deeper knowledge of the role of vacuoles for ion homeostasis in those cells. Since individual VM conductances are known to be Ca^{2+}-dependently regulated or to be involved in the exchange of Ca^{2+} between the cytosol and the vacuole, the relationship between the VM conductance and $[Ca^{2+}]_{cyt}$ had to be investigated.

The second part of this work aimed at the analysis of the earliest auxin-induced responses in root cells of *A. thaliana*. Among those fast responses are the depolarization of the PM potential, apoplastic alkalinisation as well as cytosolic Ca^{2+} signals mediated by a PM-localized putative Ca^{2+} channel (Felle *et al.* 1991; Monshausen *et al.* 2011; Shih *et al.* 2015). A model has recently been brought forward that integrates auxin-induced Ca^{2+} signals into the root gravitropic response (Shih *et al.* 2015). However, the role and interaction of single components in fast auxin siganling, for example auxin perception or the H^+-conductance responsible for apoplastic alkalinistaion, remain largely elusive. Moreover, the depolarization of the PM potential has long been speculated to represent electrogenic H^+-coupled auxin influx (Felle *et al.* 1991), and a Ca^{2+} dependent regulation of auxin efflux is at least discussed (Vanneste and Friml 2013). For those reasons, this work analyses the integartion of known constituents of polar auxin transport, auxin perception and Ca^{2+} influx in fast auxin signaling in the root of *A. thaliana*.

2. Material and Methods

2.1. Plant material and growth conditions

Seeds of various *A. thaliana* lines (**Tab. 2.1**) were sterilized for five minutes by application of 6% NaOCl (Roth, Germany) supplemented with 0.05% Triton-X 100 (AppliChem, Germany). Three to six washing steps with deionized water removed the sterilizing solution. Single seeds were placed in a row on the surface of 1 ml of plant growth medium (**Tab. 2.2**) filled within small Petri-dishes (Ø 35 mm, Sarstedt, Germany) to enable root accessibility for microelectrodes (**Fig. 2.1A**). The Petri-dishes were placed vertically (**Fig. 2.1B**) in a growth chamber (KBWF 720, Binder, Germany) with controlled environmental conditions (12h day vs. 12h night; 21°C at day vs. 16°C at night; 120 µmol photons m^{-2} s^{-1}) three to five days before experiments.

Tab. 2.1: Lines of *A. thaliana* used in this work. R-GECO1 and GFP expressing lines were kindly provided by Melanie Krebs (University of Heidelberg). DII-Venus, *aux1* and *tir/afb* mutants were kindly provided by Malcolm Bennett (University of Nottingham), and *abp1* mutants were kindly provided by Klaus Palme (University of Freiburg).

Line	Background	Description	Reference
Col-0	-	wild type, *Columbia 0*	-
Ler	-	wild type, *Landsberg erecta*	-
Ws	-	wild type, *Wassilewskija*	-
R-GECO1 NES YC3.6	*Col-0*	Cytosolic Ca^{2+}-reporter line	(Keinath *et al.* 2015)
UBQ10:GFP	*Col-0*	Cytosolic GFP line	-
DII-VENUS	*Col-0*	Auxin perception reporter line	(Brunoud *et al.* 2012)
aux1-2	*Ler*	*AUX1* ethyl methanesulfonate (EMS) mutant	(Mirza *et al.* 1984)
aux1-7	*Col-0*	*AUX1* EMS mutant	(Pickett *et al.* 1990)
aux1-22	*Col-0*	*AUX1* diepoxybutan (DEB) mutant	(Roman *et al.* 1995)
aux1-T	*Ws*	*AUX1* T-DNA insertion line	(Swarup *et al.* 2004)
wav5-33	*Ler*	*AUX1* EMS mutant	(Okada and Shimura 1990)
abp1-c1	*Col-0*	*ABP1* CRISPR/CAS line	(Gao *et al.* 2015)
abp1-TD1	*Col-0*	*ABP1* T-DNA insertion line	(Gao *et al.* 2015)
pin2 (eir1-1)	*Col-0*	*PIN2* DEB mutant line	(Roman *et al.* 1995)
cngc14-2	*Col-0*	*CNGC14* T-DNA insertion line	(Shih *et al.* 2015)
tir1-1	*Col-0*	*TIR1* EMS mutant	(Parry *et al.* 2009)
tir1-1afb2-3afb3-4	*Col-0*	Triple mutant of *TIR1* and *AFB2/3*	(Parry *et al.* 2009)

Tab. 2.2: Composition of plant growth media.

Component	Final concentration
Murashige & Skoog (MS)-medium (basal salt mixture incl. MES; Duchefa; Netherlands)	0.12% (equals ¼ strength)
Sucrose (AppliChem; Germany)	0.5%
TRIS (AppliChem)	Adjusting pH 5.8
Agarose (Bio&Sell, Germany)	1%
For *PO_4^{2-} nutrition experiments the MS-medium was replaced by the following nutrients (µM)*	
NH_4NO_3	5200
KNO_3	4700
$CaCl_2$	600
$MgSO_4$	200
H_3BO_4	25.1
Na_2EDTA	25
$FeSO_4$	25
MnO_4	19
$ZnSO_4$	13.3
KI	1.7
Na_2MoO_4	0.386
$CoCl_2$	0.030
$CuSO_4$	0.025
KCl	- (P_i final conc. = 312 µM)
	281 (P_i final conc. = 31 µM)
	309 (P_i final conc. = 3 µM)
	312 (P_i final conc. = 0.3 µM)
KH_2PO_4	312 (P_i final conc. = 312 µM)
	31 (P_i final conc. = 31 µM)
	3 (P_i final conc. = 3 µM)
	0.3 (P_i final conc. = 0.3 µM)

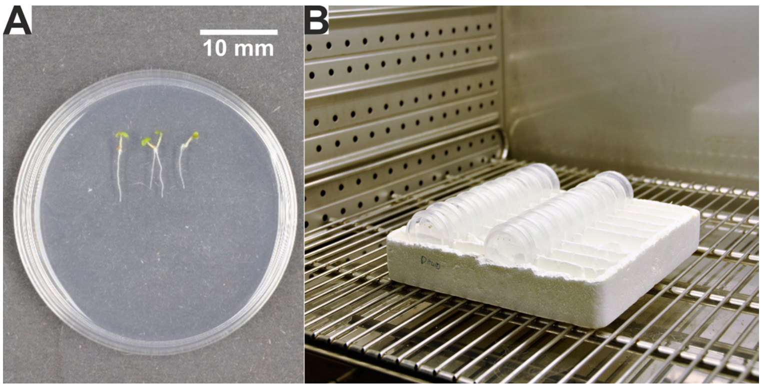

Fig. 2.1: Sterile *A. thaliana* seedling growth. (**A**) Seedlings grown on the surface of the medium**.** (**B**) Petri-dishes placed vertically in a styrofoam tray within the growth chamber.

2.2. Experimental set-up for electrophysiological measurements on root epidermal cells of *A. thaliana*

2.2.1. Intracellular measurements on bulging root hair cells

2.2.1.1. The two-electrode voltage-clamp technique

Electrical currents across the VM were recorded with the two-electrode voltage-clamp (TEVC) technique. **Fig. 2.2** shows a simplified electrical circuit model of intravacuolar measurements at a bulging root hair cell. In principle, this technique uses two electrodes, a voltage-, and a current electrode impaled into a single cell. The membrane potential, measured with the voltage electrode, connected to a microelectrode amplifier (A_1), is forwarded to a differential amplifier (A_2). Here the input voltage V_{in} is compared with the command voltage V_{cmd}. If there is a difference between V_{in} and V_{cmd}, a current is injected through the second microelectrode until V_{in} equals V_{cmd}. For the experiments described in this work, both electrodes were made of thin glass capillaries which were fused at their tip to a double-barrelled microelectrode.

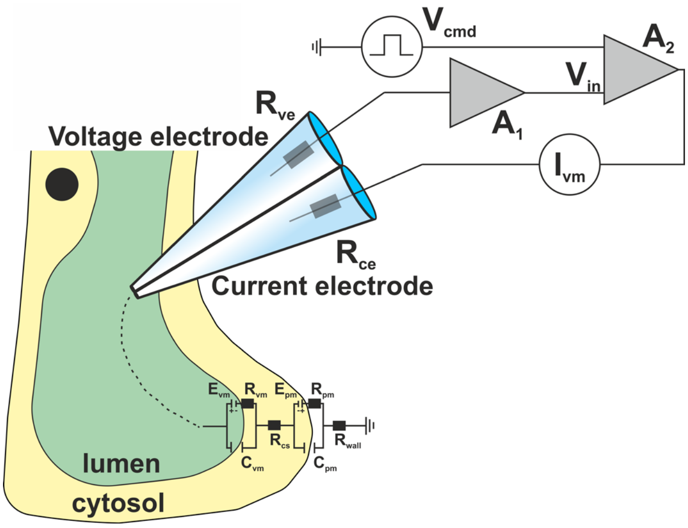

Fig. 2.2: Two-electrode voltage-clamp technique. An electrode with the resistance R_{ve}, connected to an input amplifier (A_1) records the voltage across both membranes (E_{pm} and E_{vm}) as V_{in}. A differential amplifier (A_2) compares V_{in} with a given voltage (V_{cmd}). A difference results in a current (I_{vm}) injected into the cell by a second electrode. This equals the membrane current (dashed line) at V_{cmd}. The PM, VM, cytosol, and cell wall are shown with their respective resistances (R_{pm}, R_{vm}, R_{cs}, R_{wall}), capacities (C_{pm}, C_{vm}) and potentials (E_{pm} and E_{vm}).

2.2.1.2. Preparation of microelectrodes and application pipettes

Thin microelectrodes were prepared from borosilicate glass capillaries ($Ø_{out}$ 1 mm, $Ø_{in}$ 0.58 mm, w/ filament, Hilgenberg, Germany). Single-barrelled microelectrodes used for PM potential recordings and preparation of application pipettes were pulled from capillaries with a P-2000 horizontal laser puller (Sutter Instruments, USA). Double-barrelled microelectrodes used for intravacuolar voltage-clamp experiments were prepared by fusing two glass capillaries through successively heating, turning them by 360° and pre-pulling them using an L/M-3P-A customized vertical puller (List-Medical-Electronic, USA). Thereafter the double-barrelled microelectrodes were pulled with the horizontal laser puller (P2000, Sutter). Auxin was locally applied to bulging root hair cells via application pipettes prepared from single-barrelled microelectrodes, of which tips were manually broken off to an approx. 20 to 40 µm wide opening.

2.2.1.3. Experimental set-up for intracellular measurements

Seedlings of *A. thaliana* were accustomed to the bath solutions (**Tab. 2.3**) before the start of the experiment. In the case of vacuolar measurements, this was carried out overnight. For this purpose, two milliliters of sterile bath solution were applied, and the Petri-dishes were sealed and put in a vertical (upright) position in the growth chamber again. For measurements of the auxin response, the bath solution was applied at least 20 min before the experiment. If needed, the bath solutions was supplemented with various auxin perception and transport inhibitors given in **Tab. 2.3.** Before measurement, the seedling containing Petri-dishes were placed on the table of an upright microscope (Axioskop 2FS, Zeiss AG, Germany; **Fig. 2.3**). Microelectrodes were mounted on micromanipulators (MM3A-LMP, Kleindiek Nanotechnik, Germany, or Triple Axis Micromanipulator, Sensapex Oy, Finland) to impale them into bulging root hair cells. The bath solution was connected to ground with reference electrodes made from the same glass capillaries as the microelectrodes, which were backfilled with 300 mM KCl and sealed with an agarose plug (2% agarose in 300 mM KCl). All barrels of the microelectrodes were backfilled with 300 mM KCl and connected via custom build Ag/AgCl half-cells to HS180 head stages with 100 GΩ input resistance (Bio-Logic, France). The head stages were connected to microelectrode amplifiers (VF-102; Bio-Logic). During voltage clamp experiments the membrane potential was manipulated by using a differential amplifier (CA-100, Bio-Logic). For online acquisition, data were filtered with a four-pole low-pass Bessel filter (LPF 202A, Warner Instruments, USA) at 200 Hz and sampled at 1 kHz (voltage-clamp experiments on vacuoles) or 0.1 kHz (potential measurements) using either the PULSE software (v. 8.74, HEKA, Germany) or the WinWCP software (University of Strathlyclyde, UK) with an LIH-1600 interface (HEKA) or an NI USB 6259 interface (National Instruments, USA).

Tab. 2.3: Bath solutions used for impalement experiments. Auxinole, IAA derivatives, and pABA were kindly provided by Klaus Palme (University of Freiburg)

Component	Concentration (mM)
Bath solution for vacuolar measurements	
$CaCl_2$	5
KCl	4
$MgCl_2$	0.25
NaCl	0.5
HEPES (MP Biomedicals, France)	1
KOH	Adjusting pH to 7
Bath solution for auxin-response measurements	
$CaCl_2$	1
KCl	0.1
MES	5
BTP (Sigma-Aldrich)	Adjusting pH to 5.5
Inhibitors of PAT and auxin perception with solvent (µM)	
Triiodobenzoic acid (TIBA; Sigma-Aldrich; MeOH)	20
Naphthylphthalamic acid (NPA; Sigma-Aldrich; MeOH)	20
Auxinole (DMSO)	10 and 20
PEO-IAA (phenylethyl-2-oxo-IAA; DMSO)	10
N-ethyl-PEO-IAA (DMSO)	10
N-ethoxy-ethyl-PEO-IAA (DMSO)	10
p-Aminobenzoic acid (pABA; DMSO)	10

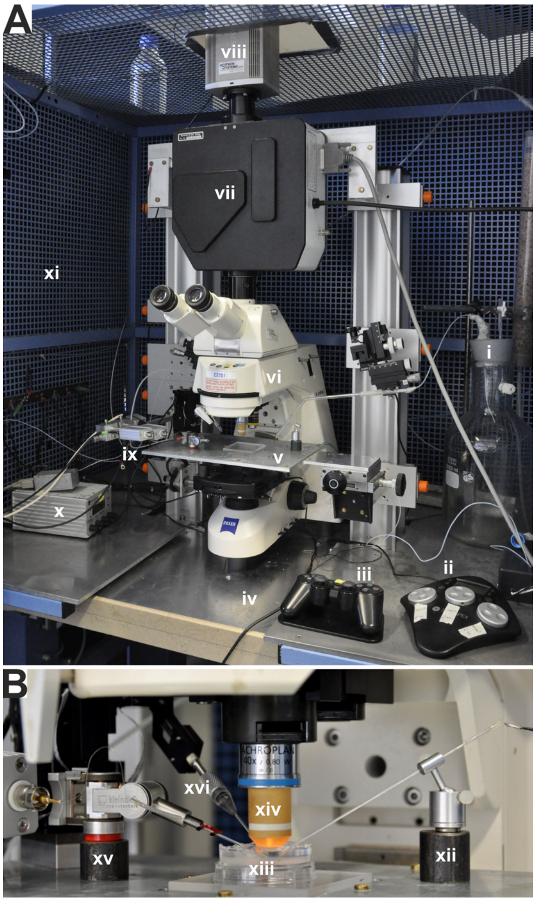

Fig. 2.3: Set-up for root hair impalement measurements and live-cell imaging. (**A**) (**i**) Waste bottle of perfusion system**;** (**ii**) control unit of the Sensapex micromanipulator**;** (**iii**) controller of the Kleindiek micromanipulator**;** (**iv**) vibration isolating table**;** (**v**) custom made microscope table**;** (**vi**) Zeiss Axiokop 2FS**;** (**vii**) CARV2 confocal imager; (**viii**) QuantEM 512SC CCD camera; (**ix**) headstages for microelectrodes; (**x**) control unit of Kleindiek micromanipulator**;** (**xi**) faraday cage. (**B**) Close up of measuring set-up (**xii**) ground-connected reference electrode with manipulator; (**xiii**) Petri-dish with sterile-grown seedlings; (**xiv**) Achroplan 40x/0.80w objective; (**xv**) Kleindiek micromanipulator with single-barrelled microelectrode**;** (**xvi**) Sensapex micromanipulator (background) with application pipette

2.2.1.4. Cytosolic application of Bapta, Ca^{2+}, and auxin

In Experiments in which the cytosolic Ca^{2+} homeostasis of the cytosol was changed through iontophoretic injection of the Ca^{2+}-chelator BAPTA (Sigma-Aldrich) and Ca^{2+}, single-barrelled electrodes were tip filled with 10 mM BAPTA or backfilled with 1 M $CaCl_2$. Cytosolic auxin application was achieved by using single- and double-barrelled microelectrodes impaled through the tips of bulging root hair cells. The tips of those electrodes were filled with the mixtures listed in **Tab. 2.4**, which contained the fluorescent dye Lucifer Yellow CH (Fluka/Sigma, Germany) and either 3-IAA (Sigma-Aldrich) or 2-NAA (2-naphthaleneacetic acid; Merck, Germany). The pH of both mixtures was adjusted to pH 7 to achieve complete deprotonation of the auxins ($pK_a \approx 4.7$). The common negative charge of 3-IAA/2-NAA and of the fluorescent dye allowed LY to serve as a loading control for current injection. Exogenous application of auxins (3-IAA; 5F-IAA (5-fluoro acetic acid; Sigma-Aldrich); 1-NAA (1-naphthaleneacetic acid; Duchefa); 2-NAA; 2,4-D (2,4-

Dichlorophenoxyacetic acid; Merck) and benzoic acid (BA, Sigma-Aldrich/Fluka)) was achieved by using application pipettes which were filled with auxin-containing bath solution, mounted on a Sensapex micromanipulator and positioned approx. 150 µm from the impaled root hair cells. The pipettes were connected to a Picospritzer II microinjection dispense system (General Valve, USA) operating at 20 kPa to apply 1 s back pressure pulses.

Tab. 2.4: Tip-filling solutions used for cytosolic auxin injection.

Component	Concentration (mM)
3-IAA mixture	
3-IAA	6.66
LY	0.5
HEPES	0.83
TRIS	Adjusting pH to 7
2-NAA mixture	
2-NAA	3.33
LY	0.5
HEPES	0.83
TRIS	Adjusting pH to 7

2.2.1.5. The sign convention for electrical measurements on endomembranes

In 1992, a convention for electrical measurements on endomembranes was proposed (Bertl *et al.* 1992). In the proposal, the cytosol was regarded as the reference point for electrical measurements treating the lumen of the organelles equivalent to the extracellular space. **Fig. 2.4** illustrates the conditions with voltage electrodes either located in the cytosol, or lumen of the vacuole and shows how the voltage gradients are arranged across the VM and PM. If the microelectrode only penetrates the PM, it is located in the cytosol of the cell and will record the potential across the PM (E_{pm}) (**Fig. 2.4A**). For a viable root hair cell, this potential will have a negative sign. However, in the case of vacuolar impalement, two membrane potentials are measured in series (**Fig. 2.4B**). Just as for the PM, a negative membrane potential, relative to the cytosol, excists across the VM (Martinoia *et al.* 2012). As a result, the relation between the VM potential (E_{vm}), the PM potential (E_{pm}) and the total potential (E_t) can be written as

$$E_t = E_{pm} - E_{vm}$$

and consequently

$$E_{vm} = E_{pm} - E_t$$

Equation 2.1: Calculation of the VM potential from membrane potential measurements.

The above-described convention (Bertl *et al.* 1992) has its implications on ion currents across the VM. In the case of cations, a positive current is equal to a flux of cations from the cytosol into the vacuolar lumen. However, a microelectrode impaled through both membranes will record the VM potential with the reversed polarity (**Fig. 2.4B**). As a result, the ion currents will be recorded with a reversed sign and a post measurement sign correction is necessary for a correct interpretation of the currents across the VM.

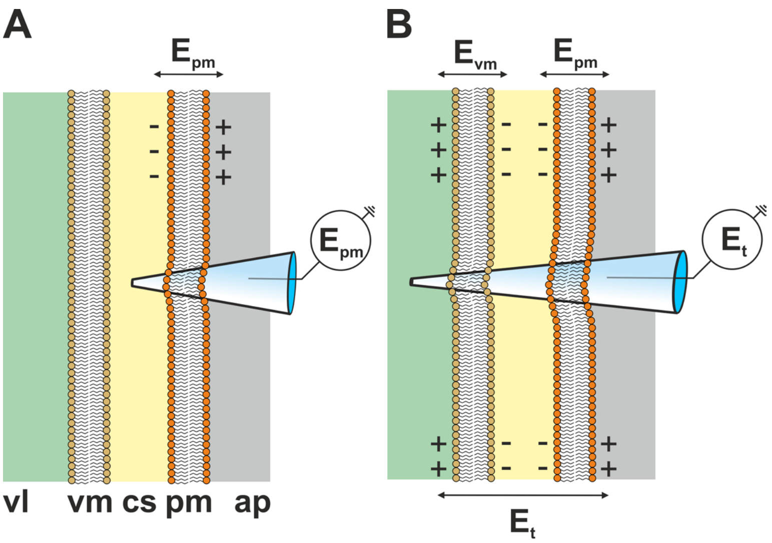

Fig. 2.4: Illustration of potentials measured with intracellular electrodes. Adapted after Wang et al. (2015). With permission for reuse from Elsevier. (**A**) A microelectrode impaled through the PM will measure the voltage E_{pm} between the cytosol (yellow) and the apoplast (gray). **ap:** apoplast; **pm**: plasma membrane; **cs:** cytosol; **vm:** vacuolar membrane; **vl:** vacuolar lumen. (**B**) A microelectrode of which the tip is within the vacuolar lumen (green) has penetrated both the PM and the VM and will, therefore, record the total voltage E_t composed of E_{pm} and the voltage across the VM E_{vm}.

2.2.1.6. Analysis of intracellular measurements

Bipolar voltage pulse protocols were applied, to deduce the current-voltage (I/V) relationship of the VM (**Fig. 2.5A**). To this purpose, vacuolar membranes were clamped from the resting potential, in 2 s pulses to more positive and negative voltages with 20 mV increments. The steady-state currents (I_{SS}, **Fig. 2.5B**) at the end of each voltage pulse were plotted against the voltage difference relative to the resting potential. For experiments in which the relationship between the VM potential and $[Ca^{2+}]_{cyt}$ was analysed, voltage pulses of a duration of 30 s were applied. These protocols are shown with the individual experiments in **Chapter 3.1.3.**

Either the amplitude of the depolarization or the peak depolarization velocity was used to analyze the auxin-induced PM response. **Fig. 2.5C** illustrates how the amplitude was determined as the difference between a stable pre-auxin potential (at least 30 s) and the peak response. The maximum rate of depolarization was deduced manually in Excel (Microsoft, USA) from differentiated (transformation into the 1st derivative) PM potential recordings which were post-filtered by averaging 1 s intervals. After transformation, the trace shows that auxin-triggers a rapid change in the membrane potential of which the velocity peaks approximately 10 to 20s after application of the stimulus. (**Fig. 2.5D**). The OriginPro (OriginLab Corporation, USA) software was used to produce graphics and calculate curve fittings.

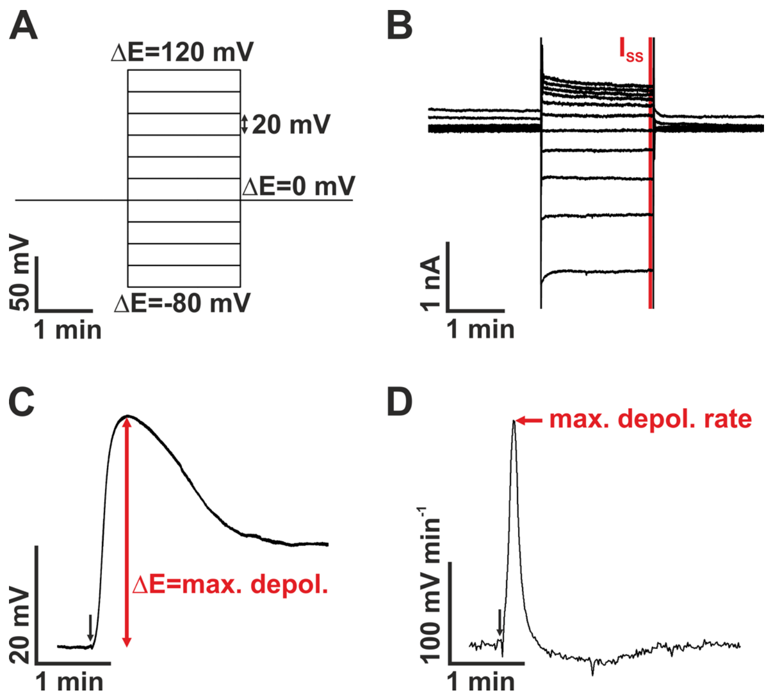

Fig. 2.5: *Arabidopsis* root hair impalement measurements and their analysis. (**A**) Bipolar voltage pulse protocol. Each cell was clamped to their respective resting potential (ΔE=0 mV), and 2 s voltage pulses with 20 mV increments were applied up to potentials 120 mV positive and 80 mV negative of the resting potential. (**B**) Exemplary intravacuolar currents triggered with the voltage-puls protocol shown in (A). For analysis, the steady-state currents (I_{SS}, red line) at the end of each voltage pulse were used. (**C**) Typical response of the PM potential to a 1 s puls of auxin (black arrow). For analysis, the difference between the resting potential before auxin application and the peak of depolarization was used (red arrow). (**D**) To obtain the velocity of the potential change before and after auxin application (black arrow) the response shown in (C) was differentiated. As a measure of the auxin response, the peak depolarization rate (red arrow) was used.

2.2.2. Non-invasive measurement of ion fluxes

Scanning ion selective microelectrodes were used to measure the H^+ and Ca^{2+} fluxes at root epidermal cells in response to externally applied auxin. This non-invasive method uses the voltage readout of oscillating ion-selective microelectrodes to estimate ion fluxes across the PM (Newman 2001).

2.2.2.1. Preparation of ion-selective microelectrodes, calibration, and experimental set-up

Borosilicate glass capillaries ($Ø_{out}$ 1.0 mm, $Ø_{in}$ 0.58 mm, w/o filament, Science Products GmbH, Germany) were used to produce H^+- and Ca^{2+}-selective microelectrodes. Glass capillaries were pulled into thin microelectrodes by using a PC-10 vertical puller (Narishige Scientific Instruments Lab, Japan). Electrode tips were broken off under microscopic inspection. The electrodes were baked overnight at 220°C, and their surface was silanized by adding N, N-Dimethyltrimethylsilylamine (Sigma-Aldrich). The electrodes were then backfilled with either 40 mM KH_2PO_4 and 15 mM NaCl (H^+-electrodes) or 500 mM $CaCl_2$ (Ca^{2+}-electrodes) and tip filled with either hydrogen ionophore I cocktail A (Sigma-Aldrich) or calcium ionophore I cocktail A (Sigma-Aldrich). For calibration and measurements of ion fluxes, the microelectrodes were connected to either a custom-built microelectrode amplifier (H^+ fluxes), or an IPA-2 Ion/Polarographic amplifier (Applicable Electronics, USA) for simultaneous H^+/Ca^{2+} flux recordings; Applicable Electronics, USA) via head stages (Applicable Electronics) and Ag/AgCl half cells. Online acquisition of raw voltage data was achieved by using an NI USB 6259 interface (National Instruments, USA) and the custom built Labview-based software “Ion flux monitor”. Ion fluxes were calculated offline from the acquired raw data. H^+-electrodes were calibrated at pH 4 and pH 7 (pH standard solutions, AppliChem) and Ca^{2+}-electrodes at 0.1, 1, and 10 mM $CaCl_2$ (**Fig. 2.6A**). Before measurements, seedling containing Petri-dishes were placed horizontally and plants were accustomed to the bath solution (**Tab. 2.5**) for at least 20 min. When needed, PAT and auxin perception inhibitors were added as shown in **Tab. 2.3**. Positioning of the ion-selective electrodes near bulging root hair cells (**Fig. 2.6B**) was achieved under microscopic inspection (Axiovert 135, Carl Zeiss AG (H^+ fluxes); Axioskop, Carl Zeiss AG (simlutaneous H^+/Ca^{2+} fluxes)) with either a PatchStar micromanipulator (Scientifica, UK) or a SM-17 micromanipulator (Narishige Scientific Instruments Lab, Japan), respectively. Electrodes were either moved by a piezo stepper (Luigs & Neumann GmbH, Germany) or a micro stepping motor driver (US Digital, USA) at 10 s intervals over distances of either 50 or 100 µm. When stable fluxes were recorded for at least 3 min, auxin was manually added to a final concentration of 10 µM.

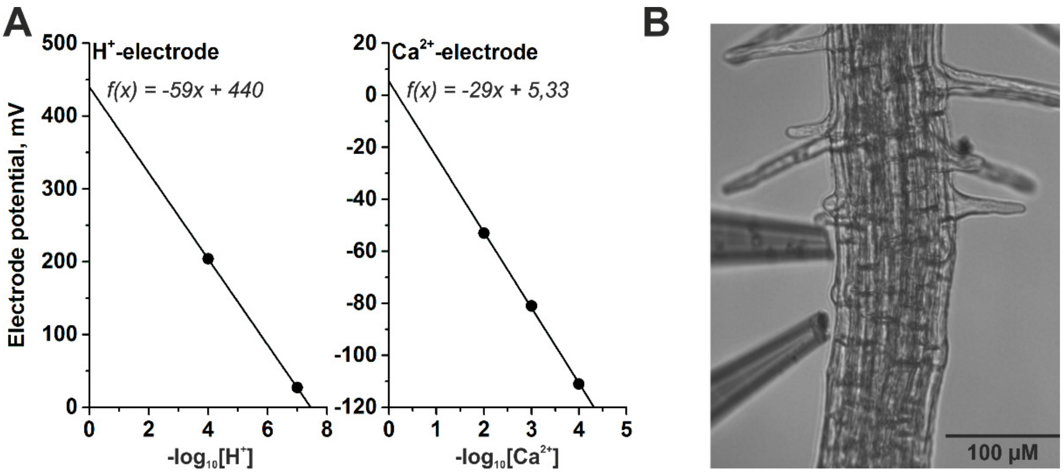

Fig. 2.6: Calibration data and position of H^+- and Ca^{2+}-selective microelectrodes near an *Arabidopsis* root. (**A**) Linear regression of a H^+ electrode calibration data, gave a Nernst slope of -59 mV/pH unit and an interception point with the y-axis at 440 mV. Calibration of the Ca^{2+}-electrode resulted in a Nernst slope of -29 mV/pCa unit and an y-axis interception point at 5.3 mV. (**B**) Before measurements, the two ion-selective electrodes were positioned close to bulging root hair cells.

Tab. 2.5: Bath solution for ion flux measurements.

Component	Concentration (µM)
KCl	100
$CaCl_2$	100
MES	100
BTP	Adjusting pH to pH 5.5

2.2.2.2. Calculation of ion fluxes

The vibrating probe technique allows the calculation of ion fluxes J_{ion}, according to Newman (2001):

$$J_{ion} = c_{ion} * \mu_{ion} * F * z_{ion} * \left(\frac{58\, mV}{Nernst\ slope}\right) * \left(\frac{V_2 - V_1}{dx_{corr}}\right)$$

Equation 2.2: **Calculation of ion fluxes**. $\mathbf{c_{ion}}$: ion concentration; $\mathbf{\mu_{ion}}$: ion mobility; **F**: Faraday constant; $\mathbf{z_{ion}}$*:* valence. The **Nernst slope** is obtained from electrode calibration. $\mathbf{V_1}$, $\mathbf{V_2}$*:* electrode potentials; $\mathbf{dx_{corr}}$: electrode traveling distance corrected for tissue geometry.

Parameters which were used for the calculation of ion fluxes are given in **Tab. 2.6**. Negative values of J_{ion} describe efflux and positive values influx of solutes. **Fig. 2.7** illustrates a circumstance where the cation (in this case H^+) concentration at the first electrode position (P1) near the root is higher than at the second position (P2).

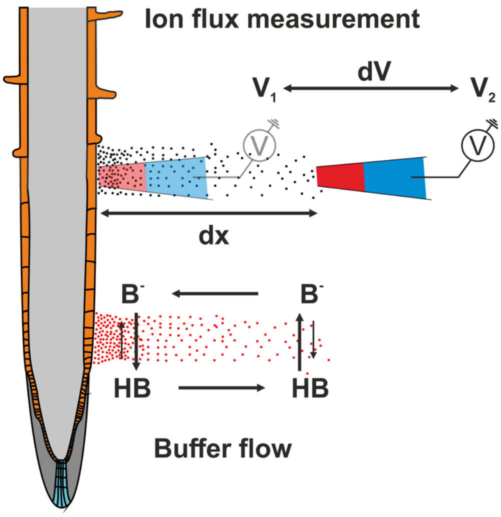

Fig. 2.7: Schematic of H^+ flux measurements at roots. Based on Newman, (2001), Arif *et al*. (1995) and Shabala *et al.* (2006). The microelectrode, filled with ionophore (red) and backfill solution (blue), scans over two positions parted by the distance *dx*. The electrode potential is recorded at both positions (V_1 *and* V_2). *dV* is the difference in potential measured by the ion-selective electrode, caused by a difference in H^+ concentration (black dots). For H^+ fluxes, the flow of conjugated buffer also must be considered. Red dots indicate H^+. At high H^+ concentrations, buffer becomes protonated (*HB*). *HB* diffuses to low H^+ concentrations where equilibrium shifts in advantage of the deprotonated buffer (B^-). The flux of the protonated buffer thus should be added to that of H^+ itself.

This concentration difference results in a higher electrode potential at P1 as compared to P2, hence *(V_2-V_1)* is negative and so is J_{ion}. Further, the geometry of plant roots has to be considered. The traveling distance of the electrode *dx* was therefore corrected for the cylindrical geometry of the root, according to Newman, (2001):

$$dx_{corr} = r_{root} * ln\left(\frac{r_{root} + x + dx}{r_{root} + x}\right)$$

Equation 2.3: Cylindrical correction of ion fluxes. $\mathbf{r_{root}}$: plant root radius; **x**: minimal electrode distance from the sample; **dx**: electrode traveling distance.

In case the ion is buffered in the bath solution, the flux of the ion can be compensated for that of the conjugated buffer with the following equation (Arif *et al.* 1995):

$$J_{H^+_{corr}} = J_{H^+} * \left[1 + \frac{\mu_{buffer}}{\mu_{H^+}} * c_{buffer} * 10^{pK} * \left(\frac{10^{pH}}{10^{pH} + 10^{pK}}\right)^2\right]$$

Equation 2.4: Buffer correction of H^+ fluxes. μ_{buffer}: mobility of the buffer; **μ_H**: mobility of protons; **c_{buffer}**: concentration of buffer in the bath; **pK**: negative $\log_{10}$ of dissociation constant of buffer; **pH**: negative $\log_{10}$ of $[H^+]$

Tab. 2.6: Parameters used in ion flux calculations.

Parameter	Value	Reference
μ_{Proton}	$37.50*10^{-13}$ (m s^{-1}) (N mol^{-1})$^{-1}$	(Wraight 2006)
$\mu_{Calcium}$	$3.19*10^{-13}$ (m s^{-1}) (N mol^{-1})$^{-1}$	(Samson *et al.* 2003)
μ_{MES}	$3.37*10^{-13}$ (m s^{-1}) (N mol^{-1})$^{-1}$	(Kunkel *et al.* 2001)
pK_{MES}	6.15	
F	96000 C mol^{-1}	
x	5 µm	
dx	100 and 50 µm	
dx_{corr}	55 and 33.8 µm	
r_{root}	57 µm	

2.2.2.3. Analysis of ion fluxes

Ion flux measurements are based on an unstirred layer at the tissue at which the fluxes occur. As auxin was pipetted into the bath solution, the unstirred layer was disrupted and measurements were perturbed for 30 to 40 s. **Fig. 2.8** illustrates how ΔJ was computed as the difference between resting fluxes (J_{rest}) and the average of the first four data points (J_{inst}) after spiking.

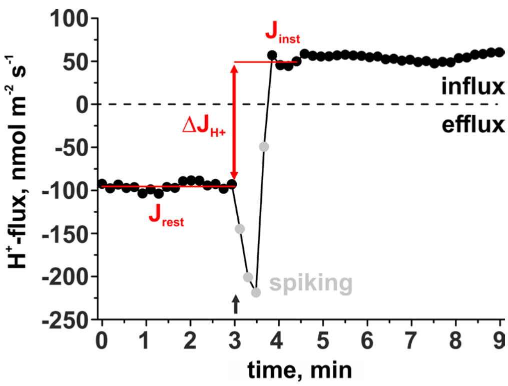

Fig. 2.8: Exemplary H^+ flux measurement with auxin response. Auxin application after 3 min of stable efflux (black arrow) resulted in spiking (gray points). J_{rest} is the average flux before auxin application (lower red line), and J_{inst} is the average of the first four points after spiking (top red line). J_{H+} was calculated as the difference between both values.

2.3. Live-cell imaging of Arabidopsis roots

The electrophysiological data were correlated to $[Ca^{2+}]_{cyt}$ signals and auxin perception with live-cell imaging experiments, using *A. thaliana* seedlings expressing fluorescent reporters. Light filters and dichroic mirrors, which are described below, were placed inside a CARV2 confocal imager (Crest Optics, Italy; see **Fig. 2.3**), with the spinning disc out of the light path. Filter selection and image acquisition with a charge multiplying CCD camera (QuantEM 512SC, Photometrics; USA; see **Fig. 2.3**) was controlled with Visiview software (Visitron, Germany). The analysis of imaging data was carried out with the free software program ImageJ (imagej.nih.gov/ij/).

2.3.1. Imaging of cytosolic Ca^{2+} levels with R-GECO1 expressing plants

The red shifted R-GECO1 Ca^{2+}-sensor has been derived from the GCaMP Ca^{2+} indicator (Nakai *et al.* 2001; Zhao *et al.* 2011). The GCaMP-related sensors are based on the same Ca^{2+} sensing mechanism. The N-terminus of a circularly permuated green fluorescent protein (cpGFP, (Nakai *et al.* 2001)) is fused to the CaM-binding domain of chicken myosin light chain kinase M13. The C-terminus of the fluorescent protein, on the other hand, is fused to a vertebrate CaM. Binding of four Ca^{2+} ions to CaM leads to an interaction between M13 and CaM resulting in conformational rearrangements within the fluorescent protein and higher fluorescence intensities (**Fig. 2.9A**). In the case of R-GECO1, GFP was replaced with the red-shifted fluorescent protein cp-mApple (Zhao *et al.* 2011) and first introduced into plants by Keinath *et al*. (2015). R-GECO1 was exposed to excitation light from a mercury lamp (LQ HXP 120; Leistungselektronik Jena, Germany) filtered at 562 nm with a Brightline single-bandpass filter (562/40 nm, Semrock, USA) and reflected with a 590 nm dichroic mirror (Zeiss). The excitation light was focused on the sample through an Achroplan 40x/0.80w objective (Zeiss) or an Achrostigmat 10x/0.25 objective (Zeiss). Light emitted by R-GECO1 was filtered at 628 nm with a Brightline single-bandpass filter (628/40 nm, Semrock).

2.3.2. Imaging of the auxin perception reporter DII-Venus

The DII-Venus reporter utilized the IAA-dependent degradation of the Aux/IAA transcription factors after IAA perception by the TIR1/AFB receptor (**Fig. 2.9B** and **Chapter 1.3.4**) and was designed by Brunoud *et al*. (2012). Venus, a fast maturing form of the yellow fluorescent protein (Nagai *et al.* 2002) was fused to the interacting domain II (DII) of IAA28. Upon auxin perception by the nuclear receptor complex $SCF^{TIR1/AFB}$ the fluorescent fusion protein is recruited for poly-ubiquitinylation by the receptor and subsequently degraded by the 26S-proteasome resulting in the loss of fluorescence. Hence, high nuclear fluorescence intensities report low auxin levels and vice versa. DII-Venus was exposed to excitation light filtered at 500 nm with a Brightline band-pass filter (500/20 nm, Semrock) and reflected with a 444/521/606 Brightline triple-edge beamsplitter (Semrock) and focused on the sample through an Achrostigmat 10x/0.25 objective (Zeiss). Light emitted by DII-Venus was filtered at 520 nm with a Brightline HC 520/35 filter (Semrock).

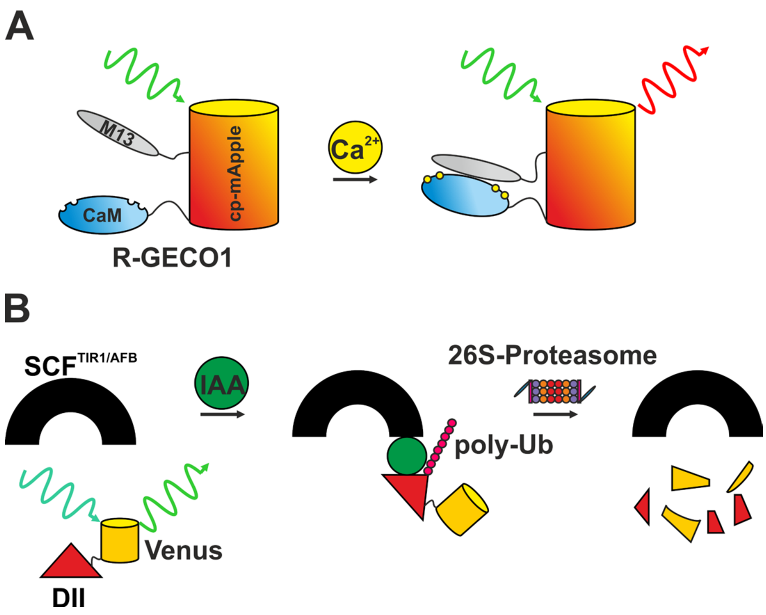

Fig. 2.9: Mechanism of Ca^{2+} and auxin sensing. (**A**) Ca^{2+}-binding by CaM induces conformational changes to R-GECO1 resulting in higher fluorescence intensities. (**B**) Venus forms a stable nuclear fluorescent fusion protein with the domain II of IAA28. The presence of auxin (green circle) facilitates interaction (middle) of DII-Venus with the auxin-receptor (black half circle) leading to the degradation of DII-Venus. Figure based on Brunoud *et al*. (2012).

2.3.3. Imaging of GFP and Lucifer Yellow

GFP was exposed to excitation light filtered at 472 nm with a Brightline single-bandpass filter (572/30 nm, Semrock, USA) and reflected with a 490 nm dichroic mirror (Zeiss). The excitation light was focused on the sample through an Achroplan 40x/0.80w objective (Zeiss). Light emitted by GFP was filtered at 520 nm with a Brightline single-bandpass filter (520/30 nm, Semrock).

LY was exposed to excitation light filtered at 430 nm with a Brightline single-bandpass filter (ET 430/24 nm, Chroma technology, USA) and passed a 490 nm dichroic mirror (Zeiss). The excitation light was focused on the sample through an Achroplan 40x/0.80w objective (Zeiss) or an Achrostigmat 10x/0.25 objective (Zeiss). Light emitted by LY was filtered at 520 nm with a Brightline single-bandpass filter (520/30 nm, Semrock).

2.4. Colorimetric detection of P_i

The residual P_i, which diffuses from the agarose-medium into the P_i-free bath solution during electrophysiological experiments was colorimetrically determined with malachite green (MG). MG detects P_i through the formation of a colored MG-phosphomolybdate complex (Baykov *et al.* 1988). The reaction was performed as described by Baykov *et al*. (1988). The reagent contained 10 ml of 0.12% MG (Sigma-Aldrich) in 3 M H_2SO_4, 2.5 ml of 64 mM $(NH_4)_6Mo_7O_{24}$ and 0.2 ml of 11% Tween-20 (AppliChem). For P_i-determination 0.8 ml of sample volume were mixed with 0.2 ml of the detection solution. The mixture was incubated for 30 min at room temperature, and the absorbance at 630 nm was measured with a NanoDrop 2000c spectrophotometer (Thermo Scientific, USA). P_i-free bath solution was supplemented with a series of defined P_i concentrations for calibration (**Fig. 2.10A**). 1 ml of growth medium was two-times overlaid with 3 ml of bath solution to simulate the conditions of electrophysiological measurements. The first equilibration was conducted over a period of 20 min. The second equilibration lasted 10 min and occurred after the first 3 ml of bath solution were removed. The P_i concentration in the bath solution after the second equilibration step were measured. Residual P_i levels in the bath solution were found to be around 1/10th of the initial P_i levels in the growth medium (**Fig. 2.10B**).

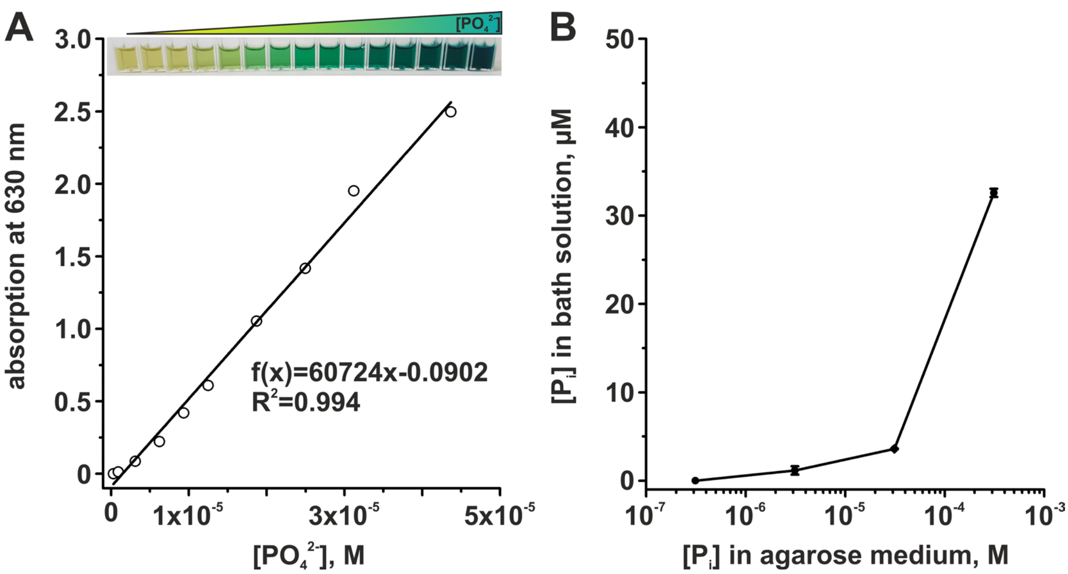

Fig. 2.10: Colorimetric P_i-detection with MG. (**A**) Calibration of the MG based assay for P_i. The black line was obtained by linear regression of all data points. The inset shows the colour of the MG assay after addition of a range of defined P_i concentrations. (**B**) Determination of residual P_i in standard bath solution after contact with P_i-containing agarose medium. Error bars show SE.

2.5. Analysis of transcript levels

Total RNA was isolated from whole *A. thaliana* seedlings after electrophysiological experiments, in order to determine the expression levels of *AUX1*, *CNGC14*, *TIR1*, *AFB2,* and *AFB3*. Approx. 3 to 10 seedlings were pooled into each sample to obtain a sufficient amount of material for subsequent RNA extraction with the NucleoSpin® RNA Plant Kit (Macherey-Nagel, Germany). Complementary DNA (cDNA) for expression analysis was synthesized from precipitated mRNA after digestion of genomic DNA, using the following procedure. 2 µg of total RNA was added to a mixture of 2 µl of 10x DNAse Buffer (Thermo Scientific), 1 µl DNAse I (Thermo Scientific, 1U/µl) and 0.5 µl RNase Inhibitor (Thermo Scientific, Ribolock 40 U/µl). The volume was adjusted to 20 µl with DEPC-H_2O, and gDNA digestion was achieved at 37°C for 45 minutes. The residual RNA was subsequently precipitated over night at -20°C. To this purpose, the volume of the gDNA digestion mixture was adjusted to 100 µl with DEPC-H_2O, and 10 µl of the following mixture was added: 5 M NH_4Ac, 1 µl of Glycogen, followed by addition of 75 µl of Isopropyl alcohol. The RNA samples were subsequently centrifuged (45 minutes at 4°C and 14000 rpm, Eppendorf Centrifuge 5430R), the RNA pellet was washed with 500 µl of 70% EtOH and centrifuged again (30 minutes at 4°C and 14000 rpm). The dry RNA pellet was finally dissolved in 7 µl DEPC-H_2O.

To generate cDNA complementary to mRNA, 6.7 µl of total RNA was added to a mixture of 0.4 µl Oligo-dT-Primer, 0.5 µl 10 µM dNTPs and 2 µl 5x M-MLV Reverse Transcriptase Buffer (Promega). Total RNA was denatured at 70°C for 2 minutes, and 0.4 µl of M-MLV Reverse Transcriptase (200 U/ µl, Promega) were subsequently added. cDNA was finally synthesized from mRNA at 42°C with a 1 h period of incubation. Transcript levels were ultimately analyzed by quantitative real-time PCR (qPCR) by adding 2 µl QPCR SYBR green capillary mix (Thermo Scientific, USA), 8 µl of each gene-specific primer (diluted to 750 nM) to 2 µl of a 1:20 dilution of cDNA. Quantitative real-time PCR was performed on a Realplex Mastercycler (epgradient S, Eppendorf, Germany). Expression levels of individual genes were calibrated with standard samples containing defined amounts of cDNA (0.02 fg to 20 fg) for each transcript and subsequently normalized to 10,000 transcripts of actin (*AtACT2/8*) under the assumption that one fg of cDNA equals 910 copies of a 1000 bp double-stranded DNA molecule. The primer pairs of genes of interest used in this work are listed in **Tab. 2.7**.

Tab. 2.7: Primer pairs used for qPCR. All primers were designed by Heike M. Müller, Research group of Peter Ache, Molecular plant physiology and biophysics, University of Wuerzburg.

Gene	Primer direction	5' to 3' sequence	T_m, °C	Fragment length, bp
AtAUX1	Forward (fwd)	GGA TGG GCT AGT GTA AC	56.5	141
	Reverse (rev)	TGA CTC GAT CTC TCA AAG	57.4	
AtCNGC14	fwd	CAG CCA AGC TAA GAC TCT	48.1	193
	rev	GTT GAA GCC TTT GCT TTA	48.5	
AtTIR1	fwd	CTT CTT GTT CCG TGA GTT	59.4	349
	rev	ATT CAA ATT ATT GGC GAC	59.4	
AtAFB2	fwd	ATG ATA ATA ACC GGA TGG A	47.5	181
	rev	TCG GGA AAG ACA CAC TAA C	50.2	
AtAFB3	fwd	GAC GTG GGT AGG TAC GAA A	52.9	267
	rev	AAA ACA CAT GAA GGT GCA A	51.6	
AtACT2/8	fwd	GGT GAT GGT GTG TCT	46.0	435
	rev	ACT GAG CAC AAT GTT AC	48.0	

3. Results

3.1. Analysis of the electrical properties of the vacuole *in planta*

In the first part of the results presented in this work, the advantages, which bulging root hair cells of *A. thaliana* provide for electrophysiological measurements (see **Chapter 1.5.**) were used to probe the VM conductivity *in planta*. In combination with live-cell imaging of genetically encoded fluorescent reporters, a first *in planta* analysis of the relationship between $[Ca^{2+}]_{cyt}$ and vacuolar ion conductivity is provided.

3.1.1. The vacuolar membrane is the limiting conductance

The work of Dr. Yi Wang (China Agricultural University), which preceded this thesis, showed that microelectrodes impaled into the vacuoles of *A. thaliana* root epidermal cells, measured electrical conductances, which differed from those that were cytosolically localized. More precisely, the vacuole localized electrodes showed a five-times lower conductance compared to those in the cytosol. Moreover, during the 2 s voltage clamp pulses, a time-dependent decrease of the current amplitude was found with electrodes localized in the vacuole, whereas cytosolically localized electrodes did not record such a decrease ((Wang *et al.* 2015); see **Chapter 1.6.**). *In planta*, however, microelectrodes can only be placed in the lumen of the vacuole, after a serial impalement of the PM and VM. Hence, any electrical currents elicited by these electrodes will be affected by the conductance of the VM as well as PM. Although the much higher conductance, i.e. lower resistance, of the PM due to the symplastical interconnection of adjacent root epidermal cells via plasmodesmata should minimize any current superposition, a direct proof of the validity of this hypothesis had to be provided.
Root hair cells offer the advantage of tolerating two simultaneously impaled microelectrodes (Lew 2004). In these cells, the polar growing tip is devoid of the vacuole, which offers the possibility of impalement into the cytosol via the tip of the hair cell. A second electrode can be impaled into the vacuole through the base of the cell. Simultaneous recordings with two electrodes in a single root hair cell, were started by Dr. Yi Wang and finished as part of the research conducted for this thesis. The illustrations in **Fig. 3.1** depict the two experimental configurations used for the analysis. In both cases, double-barrelled microelectrodes were impaled through the body of the root hair cell into the vacuole for voltage-clamp experiments. Simultaneously, voltage recording single-barrelled

microelectrodes were either impaled through the root hair tip to record the PM potential, or were also impaled into the vacuole. In the case of the first configuration, with the electrodes localized in different subcellular compartments, a significantly more positive potential (-135 mV, SE=4 mV) was measured by the microelectrode located in the vacuole, as compared to electrodes in the cytosol (-148 mV, SE=3 mV) (**Fig. 3.1A, inset**). In case that both electrodes were placed inside the vacuole, an average series potential of -139 mV was recorded (**Fig. 3.1B, inset**). The more positive serial potential of intravacuolar electrodes reflects the VM potential that superimposes the PM potential when both voltages are measured in series (see **Chapter 2.2.1.5.**). From these experiments an average VM potential of approx. -13 mV (-148 mV + 135 mV) is yielded.

In both experimental conditions shown in (**Fig. 3.1A** and **B**), the application of bipolar voltage step protocols resulted in electrical currents (**Fig. 3.1C** and **D**) similar to currents recorded via vacuolar localized microelectrodes in experiments performed by Dr. Yi Wang (see **Fig. 1.8**). Significantly, cytosolically localized single-barrelled voltage electrodes only recorded average changes of the serial potential of around 1.9 mV per 20 mV voltage pulse increment applied to the VM (**Fig. 3.1C** to **E**). Vacuolar-localized voltage electrodes, on the other hand, recorded voltage changes that appeared simultaneously and nearly showed the same voltage increments as the applied voltage pulses.

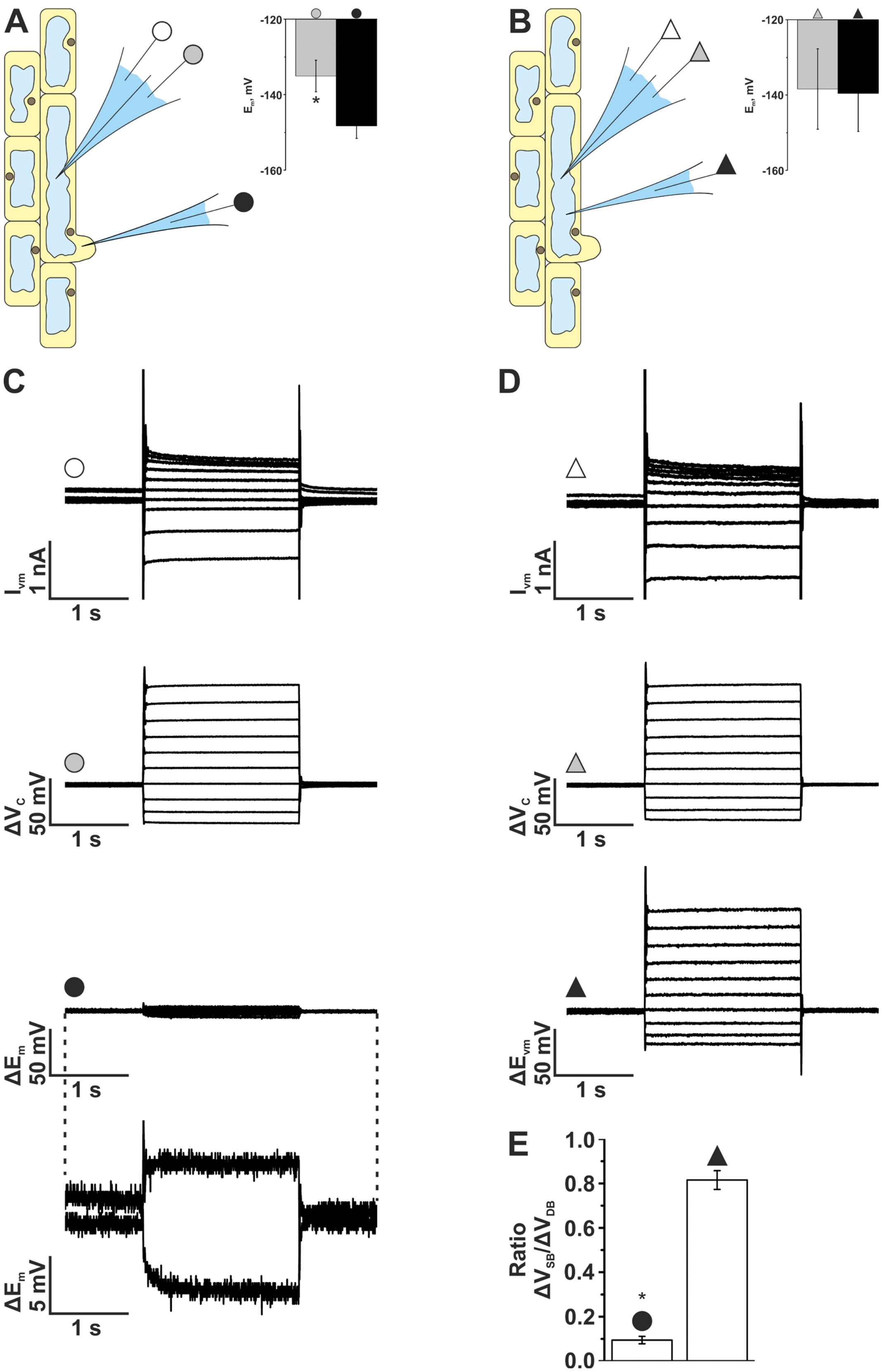
A
-120
-140
-160
E_m, mV
*
B
-120
-140
-160
E_m, mV
C
I_{vm} 1 nA
1 s
ΔV_C 50 mV
1 s
ΔE_m 50 mV
1 s
ΔE_m 5 mV
1 s
D
I_{vm} 1 nA
1 s
ΔV_C 50 mV
1 s
ΔE_{vm} 50 mV
1 s
E
Ratio $\Delta V_{SB}/\Delta V_{DB}$
1.0
0.8
0.6
0.4
0.2
0.0
*

Fig. 3.1. The VM represents the limiting conductance recorded by microelectrodes located in the vacuole. (**A**) Cartoon illustrating the localization of microelectrodes. A double-barrelled microelectrode was impaled into the vacuole of bulging *A. thaliana* root hair cells. In addition, a single-barrelled microelectrode was impaled through the root hair tip into the cytosol. The circles correspond to measurements shown in (C). The **inset** shows average resting potentials measured at the indicated electrodes (gray circle: luminal, double-barrelled electrode; black circle: cytosolic, single-barrelled electrode). Error bars indicate SE (n=6). The asterisk marks a significant difference (Student´s t-test, $p<0.05$). (**B**) Cartoon illustrating microelectrode localization. A double-barrelled microelectrode was impaled into the vacuolar lumen of bulging *A. thaliana* root hair cells. In addition, a single-barrelled microelectrode was also inserted into the vacuolar lumen. The triangles correspond to measurements shown in (D). The **inset** shows average resting potentials measured at the indicated electrodes (gray triangle: luminal, double-barrelled electrode; black triangle: luminal, single barrelled electrode). Error bars show SE (n=4). (**C**) Representative current and voltage traces measured with microelectrodes localized as indicated in (A). White circle: electrical currents measured in response to a bipolar voltage-step protocol with 20 mV increments of a duration of 2 s applied via a luminal-localized double-barrelled microelectrode. Gray circle: luminal recorded voltage pulses applied via the luminal-localized double-barrelled microelectrode. Black circle: cytosolically recorded changes of the root hair PM potential elicited via the voltage step protocol applied through the luminal-localized double-barrelled microelectrode. The lower graph shows a magnification of selected traces (**D**). Representative current and voltage traces measured with microelectrodes localized as indicated in (B). White triangle: electrical currents measured in response to a voltage-step protocol (see (C)) applied via a luminal-localized double-barrelled microelectrode. Gray triangle: luminal recorded voltage pulses applied via the luminal-localized double-barrelled microelectrode. Black triangle: luminal recorded potential changes measured via the single-barrelled microelectrode and elicited via the voltage step protocol applied through the luminal-localized double-barrelled microelectrode. (**E**) Quantification of voltage changes measured with luminal (black circle) and cytosolically (black triangle) localized single-barrelled microelectrodes. Values are given as ratios between the voltage changes measured with single-barrelled microelectrodes (ΔV_{SB}) and the voltage changes measured with a luminal localized double-barrelled microelectrode (ΔV_{DB}). Error bars show SE (n=6 and 8). The asterisk marks a significant difference (Student´s t-test, $p<0.05$). Average values which are shown in (E) combine experiments performed by Dr. Yi Wang and by the author of this work.

Together with the findings of Dr. Yi Wang the experiments with two electrodes in a single root hair cell thus show that the PM only has a minor effect on the vacuolar ion currents, due to the high electrical conductance of the PM. So far, the ion currents were shown as if the vacuolar lumen was regarded as being “inside” of the root hair cell. However, the convention of electrical measurements on endomembranes ((Bertl *et al.* 1992), see **Chapter 2.2.1.5.**) defines the vacuole as being equivalent to the “outside” of a cell. In the following, all vacuolar voltage and current traces are displayed according to this convention.

3.1.2. $[Ca^{2+}]_{cyt}$ elevations stimulate the conductivity of the vacuolar membrane

In a study that was conducted previous to that described in this thesis, Dr. Florian Rienmüller noticed a time-dependent decrease of the VM conductivity after impalement (Wang *et al.* 2015). This result led to the hypothesis that elevated cytosolic Ca^{2+} levels enhanced the conductivity of the VM shortly after impalement. Consequently, a progressive decrease of $[Ca^{2+}]_{cyt}$ to basal levels would cause the observed decrease in VM conductance. To provide evidence to this hypothesis, experiments on root hairs of *A. thaliana* seedlings expressing the genetically encoded intensiometric $[Ca^{2+}]_{cyt}$ sensor R-GECO1 were performed. In contrast to the Ca^{2+}-sensitive dye FURA-2, this approach enabled the observation of $[Ca^{2+}]_{cyt}$ before, as well as after impalement of microelectrodes (**Fig. 3.2A**). Directly after impalement, a 3.5-fold elevation of the R-GECO1 fluorescence intensity could be observed in root hairs (**Fig. 3.2B**). The signal increase was transient and returned to the basal level within three minutes. In 14 out of 26 cells, the elevation of the Ca^{2+} level was limited to the impaled root hair cell, but in the remaining 12 experiments a spread to adjacent cells could be observed. However, a wave-like transmission of Ca^{2+} signals across the root tissue, was not observed after impalement. In order to test if the R-GECO1 fluorescence intensity saturates during impalement, microelectrodes back-filled with 1 M $CaCl_2$ instead of 0.3 M KCl were used. As expected, these electrodes neither enhanced the impalement-induced fluorescence peak, nor did subsequent iontophoretic Ca^{2+} injections trigger fluorescence signals that exceeded the impalement-induced peak (**Fig. 3.2C**).

Based on the finding that the R-GECO1 signal can be stimulated 3.5-fold, a calibration procedure was developed. Purified R-GECO1 proteins have been demonstrated to show a maximum Ca^{2+}-dependent fluorescence intensity change of 10.5-fold, while they exhibit a K_d for $[Ca^{2+}]$ of 449 nM and a Hill-coefficient of 1.51 (Akerboom *et al.* 2013), the following general relationship between the R-GECO1 fluorescence signal and $[Ca^{2+}]$, deduced from the law of mass action, can be applied to estimate $[Ca^{2+}]_{cyt}$ of root hair cells (Suzuki *et al.* 2014):

$$f = f_{min} + \frac{(f_{max} - f_{min}) * [Ca^{2+}]^n}{K_d^n + [Ca^{2+}]^n}$$

Equation 3.1: Kinetics of Ca^{2+}-dependent fluorescence signals. f: fluorescence; $\mathbf{f_{min}}$: minimal fluorescence; $\mathbf{f_{max}}$: maximal fluorescence; **n**: Hill coefficient; $\mathbf{K_d}$: dissociation constant.

Provided that the impalement-induced 3.5-fold change of the R-GECO1 signal represents 95% of a saturated signal, this signal equals a $[Ca^{2+}]_{cyt}$ of 3 µM (**Fig. 3.2D**). Consequently, the $[Ca^{2+}]_{cyt}$

approximates 200 nM before impalement with microelectrodes, which is in agreement with reported values (Felle 1988a; Bethmann *et al.* 1995; Felle and Hepler 1997; Wymer *et al.* 1997).

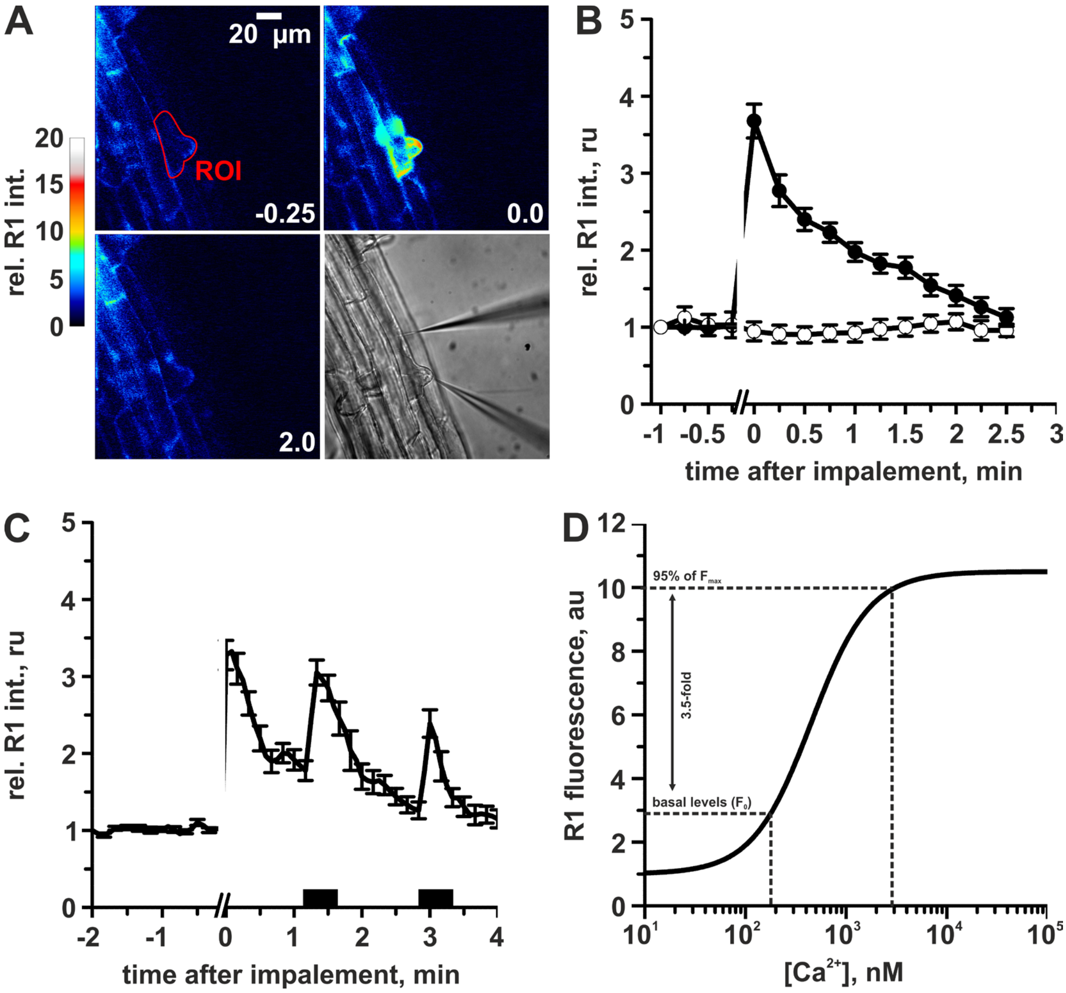

Fig. 3.2: Impalement of root hairs induces elevation of $[Ca^{2+}]_{cyt}$. (**A**) Representative images of cytosolic R-GECO1 fluorescence intensities in a bulging root hair cell of *A. thaliana*, which was impaled with two microelectrodes. The red line encircles a region of interest (ROI) from which fluorescent intensities were deduced. Relative intensities are color coded as indicated by the scale bar at the left. The average fluorescence intensity in the ROI was set to 1.0 just before impalement with the micro electrode. The time points indicated in the panels relate to the time scale in (B). The image at the right shows the corresponding brightfield picture. Note the microelectrodes impaled into the cell. (**B**) Time course of the R-GECO1 fluorescence signal during impalement with a microelectrode (closed symbols) vs. the R-GECO1 signal of root hair cells that were not subject of impalement (open symbols). Experiments are interrupted during impalement with the microelectrode. Error bars show SE (n=7 closed symbols and n=26 open symbols). (**C**) Time course of the R-GECO1 fluorescence signal during iontophoretic injection of Ca^{2+} (black bars). Experiments are interrupted during impalement with the microelectrode. Error bars show SE (n=10). (**D**) Simulation of Ca^{2+}-dependent R-GECO1 fluorescence with **Equation 3.1** (solid line). The dashed lines indicate cytosolic Ca^{2+} concentrations at 95% of maximal fluorescence and at basal fluorescence levels.

R-GECO1 expressing plants thus provide a means to test the hypothesis that $[Ca^{2+}]_{cyt}$ elevations stimulate vacuolar conductivity. For this purpose, experiments with two microelectrodes in single root hair cells were performed. A double-barrelled microelectrode was positioned in the vacuole, to probe the VM conductivity with the voltage-clamp technique, whereas a single-barrelled electrode was tip-filled with 10 mM BAPTA and impaled into the cytosol via the root hair tip. In the cell shown in **Fig. 3.3A** and **B**, iontophoretic loading of BAPTA first caused a decrease of $[Ca^{2+}]_{cyt}$ below basal levels, followed by a rapid transient elevation (**Fig. 3.3A** and **B**). During elevation of $[Ca^{2+}]_{cyt}$, a transient increase of the VM conductance could be detected, using bipolar voltage-step protocols (**Fig. 3.3C** and **D**). A correlation between the velocity of the $[Ca^{2+}]_{cyt}$ elevation and the increase in VM conductance divided the experiments into two groups (**Fig. 3.3E**). Low to modest $[Ca^{2+}]_{cyt}$ changes did not cause significant changes of the VM conductance, whereas pronounced elevations of $[Ca^{2+}]_{cyt}$, increased the VM conductance (**Fig. 3.3F** and **G**). The relationship between the imposed change of the VM potential and corresponding steady-state currents (**Fig. 3.3G**) shows that especially outward currents (i.e. cationic currents from the cytosol into the vacuole, or anion currents into the cytosol) were enhanced during elevation of the cytosolic Ca^{2+} level.

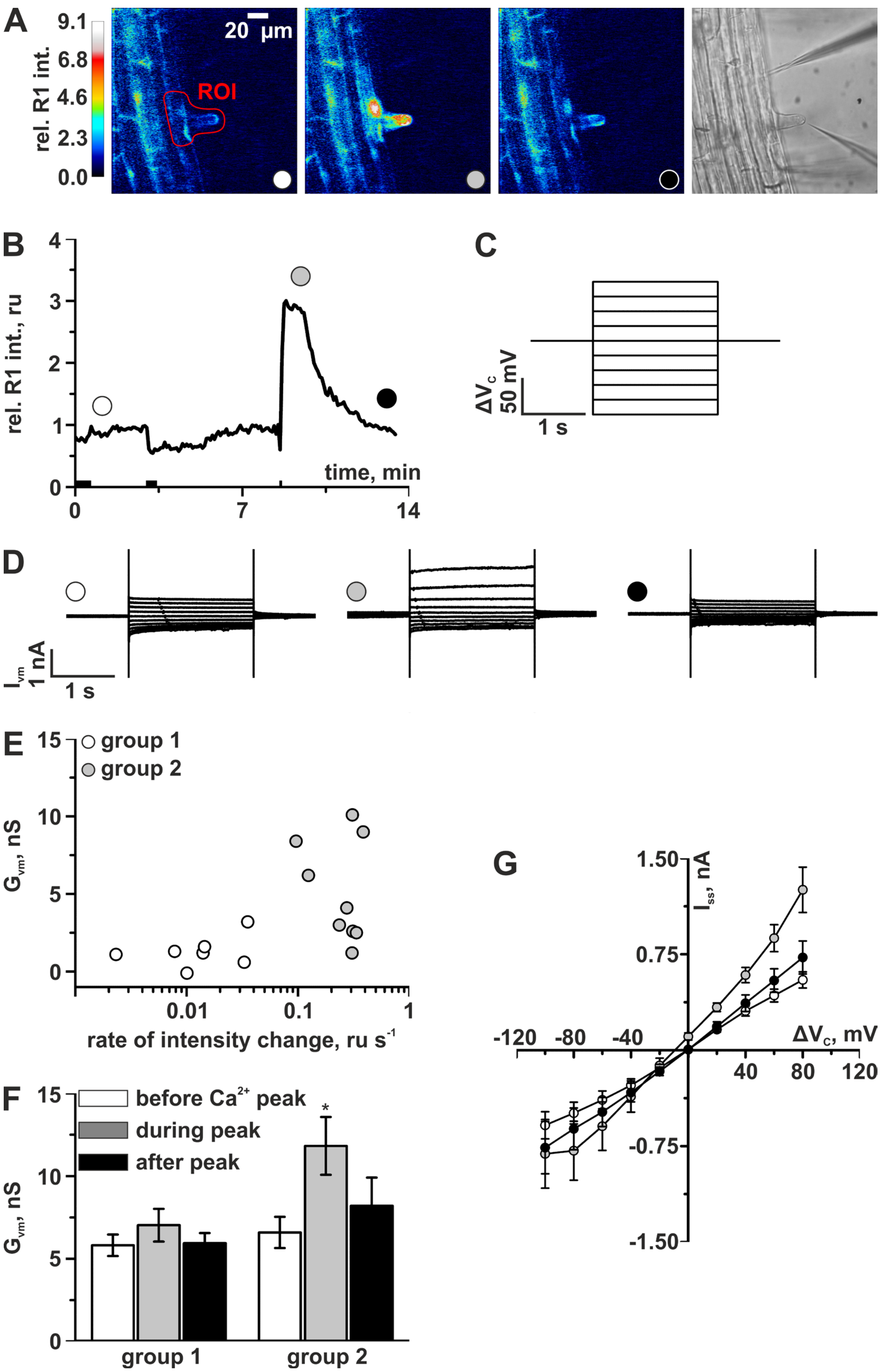
A
rel. R1 int.
9.1
6.8
4.6
2.3
0.0
20 µm
ROI
B
rel. R1 int., ru
time, min
0
7
14
C
ΔV_c 50 mV
1 s
D
I_vm 1 nA
1 s
E
G_vm, nS
group 1
group 2
rate of intensity change, ru s^-1
0.01
0.1
1
F
before Ca^2+ peak
during peak
after peak
G_vm, nS
group 1
group 2
G
I_ss, nA
1.50
0.75
-0.75
-1.50
ΔV_c, mV
-120
-80
-40
40
80
120

Fig. 3.3: $[Ca^{2+}]_{cyt}$ elevations result in increased vacuolar conductance. (**A**) Representative images of cytosolic R-GECO1 fluorescence intensities in a root hair cell of *A. thaliana* in response to iontophoretic injection of 10 mM BAPTA. The white, grey and black symbols correspond to those in (B) and (C). The red line encircles a region of interest (ROI) from which fluorescent intensity was deduced. The fluorescence intensity is given relative to the average value in the left panel, as indicated by the calibration bar at the left. The image at the right shows a brightfield image of the root hair cell. Note the microelectrodes impaled into the cell on the right. A single-barrelled microelectrode for cytosolic injection of Bapta was impaled through the tip of the root hair cell, while a double-barrelled microelectrode was impaled via the cell body into the vacuole. (**B**) Time-course of the R-GECO1 fluorescence of the cell shown in (A), symbols above the trace correlate to those in the panels. The black bars above the X-axis indicate that periods of iontophoretic loading of BAPTA. (**C**) Voltage step protocol used to probe the vacuolar conductance, the holding potential was equal to the free-running membrane potential before start of the voltage pulses. (**D**) Vacuolar current traces measured at the following time points; white circle: before a BAPTA-induced Ca^{2+} peak; gray circle: during the transient elevation of the cytosolic Ca^{2+} level; black circle: after the Ca^{2+} response. Current traces are presented according to the convention for electrical measurements at endomembranes (Bertl *et al.* 1992). (**E**) Correlation between the change in VM conductivity and the rate of R-GECO1 intensity change evoked by BAPTA injection. The experiments were grouped according to the rate of R-GECO1 fluorescence intensity changes below (group 1) or above 0.1 ru s^{-1} (group 2). (**F**) Average conductivities before (white bars), during (gray bars) and after BAPTA induced cytosolic Ca^{2+} peaks (black bars). The experiments were grouped as explained in (E). Error bars show SE (n=7 to 9). The asterisk marks a significant change (Student´s t-test; $p<0.05$). (**G**) Average current-voltage relationship of group 2 measurements. The symbols correspond to those in (A) and (B) and indicate measurements before, during and after BAPTA-induced cytosolic Ca^{2+} peaks. Error bars indicate SE (n=9).

3.1.3. Voltage-induced Ca^{2+} currents across the VM

The evidence of $[Ca^{2+}]_{cyt}$ influencing the VM conductance (see **Fig. 3.3**) made it tempting to speculate if voltage-pulses applied to the VM result in changes of $[Ca^{2+}]_{cyt}$. For this purpose, double-barrelled microelectrodes were impaled into the vacuole of bulging root hair cells of R-GECO1 expressing *A. thaliana* seedlings. In these cells, an average serial potential (E_{pm}-E_{vm}) was measured of -112 mV (SE=2 mV). In the following experiments, VMs were clamped to the free running potential, measured at the start of the experiment, and de- and hyperpolarizing voltage pulses (ΔV_c=100 mV and -80 mV) were applied for a period of 30 s. Simultaneously, the changes in the cytosolic R-GECO1 fluorescence intensity were recorded (**Fig. 3.4A** to **C**). While depolarizing VM potentials induced typical outward currents, hyperpolarizing VM potentials led to typical inward current responses (**Fig. 3.4B** and **C**). The voltage jumps applied to the VM resulted in fast changes of the R-GECO1 fluorescence intensity. Voltage steps to depolarized VM potentials induced an increase of the fluorescence intensity, whereas hyperpolarized potentials resulted in a decreased R-GECO1 signal. The changes in R-GECO1 signal were reversible, as they returned to their original values after the voltage pulse was completed. In fact, the fluorescence intensity of R-

GECO1 decreased to lower intensities as compared to basal level, after application of a depolarizing VM pulse. This drop in $[Ca^{2+}]_{cyt}$ after the voltage pulse was accompanied with a small inward current as visible from the slightly negative current response after the depolarizing voltage pulse (**Fig 3.4B**).

Prolonged clamp-currents were reported to provoke changes in the cytosolic volume of guard cells, which cause changes in the intensity of fluorescent dyes in the cytosol (Voss *et al.* 2016). In order to rule out if such changes in volume lead to false-positive signals of the single wavelength Ca^{2+} indicator R-GECO1, control experiments were conducted with seedlings that express cytosolic GFP. The vacuolar impaled microelectrodes recorded an average serial potential of -101 mV (SE=3 mV) in these seedlings. Voltage pulses applied with these electrodes caused no changes in the GFP fluorescence intensity, although the average current response was identical to R-GECO1 expressing root hair cells (**Fig. 3.4A** to **C**). The changes in R-GECO1 intensity are thus most likely caused by changes in the cytosolic free Ca^{2+} concentration.

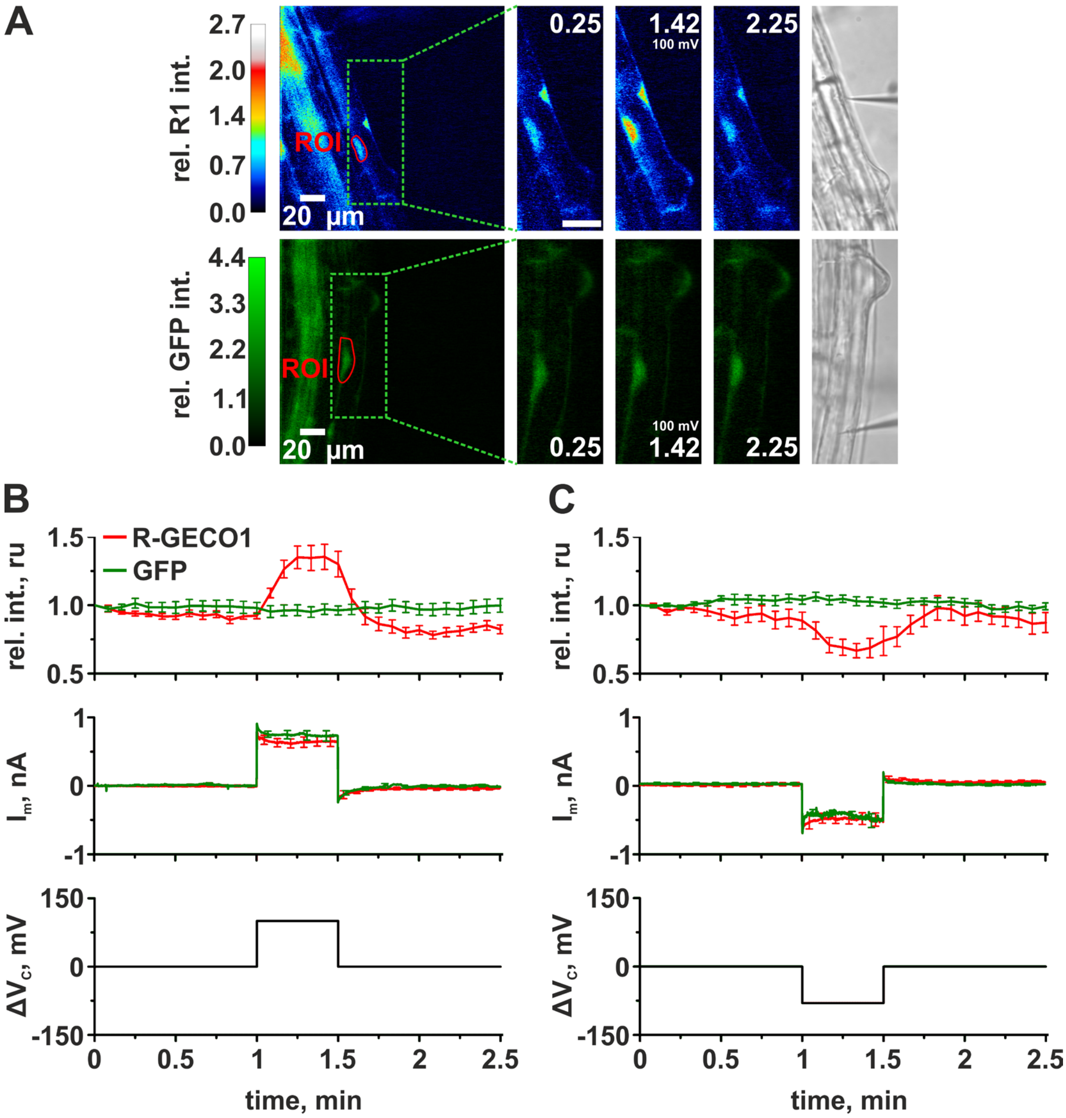

Fig. 3.4: De- and hyperpolarization of the tonoplast potential results in $[Ca^{2+}]_{cyt}$ changes. (**A**) Representative false colored images of bulging root hair cells of *A. thaliana*, which express R-GECO1 (upper panels), or GFP (lower panels). The cells were stimulated with a 100 mV depolarizing voltage pulse at the VM from 1 to 1.5 min. The region of interest (ROI) are encircled by a red line in the left panel. The panels in the middle show magnifications, as indicated by the green box in the left panel. Time points are indicated on the bottom of the middle panels (B). The panels at the right show brightfield images of the same magnification as for the middle panels. Note the microelectrodes impaled through the cell body into the vacuolar lumen. Fluorescence intensities are color coded as indicated by the calibration bars at the left. (**B** and **C**) Average values of $[Ca^{2+}]_{cyt}$ and vacuolar currents of cells stimulated either with a 100 mV depolarizing (B) or -80 mV hyperpolarizing (C) voltage pulse at the VM. **Upper panels**: average R-GECO1 (red) and GFP (green) fluorescence intensities of ROIs as indicated in (A) and (B). Error bars show SE (n=7 (GFP) and 9 (R-GECO1) in B and n=6 in C). **Middle panel**: average vacuolar current traces in response to a +100 mV, or -80 mV pulse in root hair cells that express R-GECO1 (red) or GFP (green). **Lower panel**: voltage pulse protocols applied via double-barrelled microelectrodes impaled into the vacuole.

The 100 mV depolarizing pulses applied to the VM will have resulted in hyperpolarization of the PM by approximately -10 mV (see **Fig. 3.1**). Even though these voltages are relatively small, they may have caused an increase in $[Ca^{2+}]_{cyt}$, as hyperpolarization activated Ca^{2+}-permeable channels have been described for several types of plant cells (Hamilton *et al.* 2000; Pei *et al.* 2000; Foreman *et al.* 2003; Qu *et al.* 2007). This possibility was tested with root hairs of R-GECO1 expressing seedlings, which were impaled by two single-barrelled microelectrodes (**Fig. 3.5**). Current-pulses of ± 1 nA were applied via the tip-impaled electrode, while the second electrode recorded the free running PM potential. On average the free running membrane potential was -149 mV (SE=5 mV) and electrical currents of ± 1 nA across the PM only induced absolute changes of the PM potential of 8 mV (SE=1 mV). The small voltage changes of the PM potential did not affect the R-GECO1 fluorescence intensity. Hence, the changes in R-GECO1 fluorescence intensity imposed through de- and hyperpolarization of the VM potential, are likely due to the voltage-induced Ca^{2+} currents across the VM.

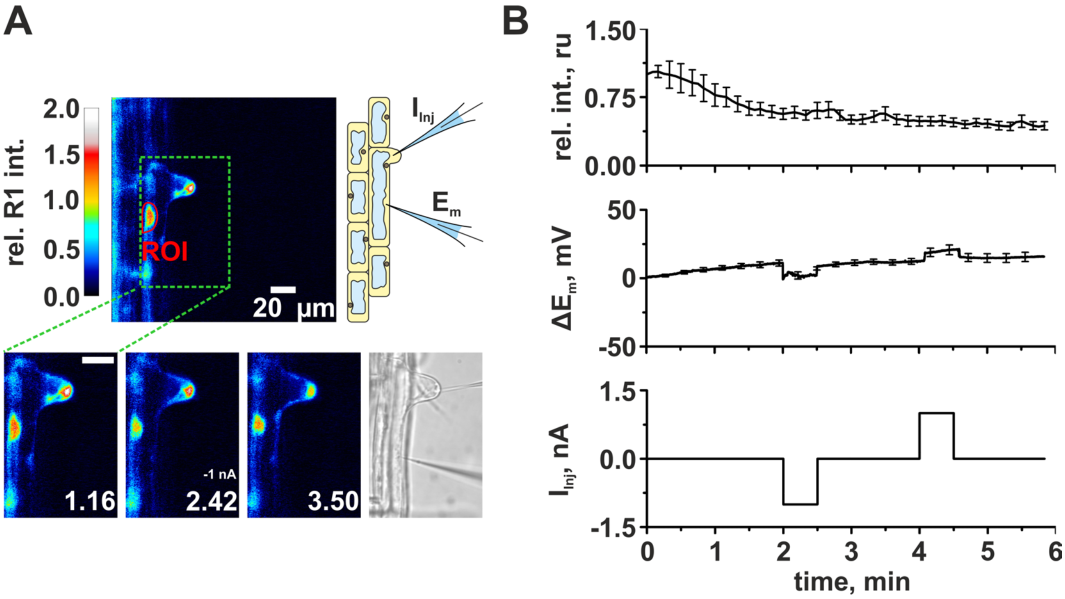

Fig. 3.5: Cytosolic current pulses of 1 nA do not provoke PM Ca^{2+} currents in root hairs. (**A**) Representative images of an *A. thaliana* bulging root hair cell that expresses R-GECO1, stimulated with a -1 nA current pulse from 2 to 2.5 min. The upper panel shows false colored images of R-GECO1 fluorescence intensity, given relative to that at the region of interest (ROI, red line) before application of the current pulse. The cartoon depicts the experimental setup in which two single-barrelled microelectrodes are impaled into a single root hair cell. The electrode impaled through the body of the cell was used as a voltage electrode, while the tip-impaled electrode was used to inject current pulses. The lower panels on the right and in the middle are magnifications of the upper panel as indicated by the green dashed lines. The time points at the bottom of the panels indicate the time after start of the experiment. The panel on the right shows the transmitted light signal at the same magnification as the other lower panels. Note the two electrodes impaled into the root hair cell on the right. (**B**) Average values of $[Ca^{2+}]_{cyt}$ and the root hair PM potential, stimulated with a -1 nA and +1 nA current pulse. **Upper panel**:

average R-GECO1 fluorescence intensities of ROIs as shown in (A). Error bars show SE (n=9). **Middle panel**: average voltage trace of the root hair serial potential. **Lower panel**: current pulse protocol applied via single-barrelled microelectrodes localized in the cytosol.

The relationship between the voltage across the VM and the cytosolic Ca^{2+} level was studied in further detail, using alternative voltage-clamp protocols. Instead of using block pulses, a voltage ramp was applied from ΔV_c = 100 mV, to the serial holding potential of -131 mV (SE=5 mV). During the slow repolarizing ramp, a steady decrease of the R-GECO1 signal was observed (**Fig. 3.6A** to **B**). The slow repolarization of the VM allowed the analysis of the correlation between $[Ca^{2+}]_{cyt}$ and the VM potential in more detail. Due to the saturation kinetics of the Ca^{2+}-dependent R-GECO1 fluorescence (see **Fig. 3.2D**), a Boltzmann function was used to describe the correlation between the applied VM potential and the R-GECO1 intensity (**Fig. 3.6C**).
The average current-voltage relationship of the VM was linear and revealed a conductance of 6 nS, which is approximatley 3 times lower as found for epidermal cells by Wang et al. (2015).

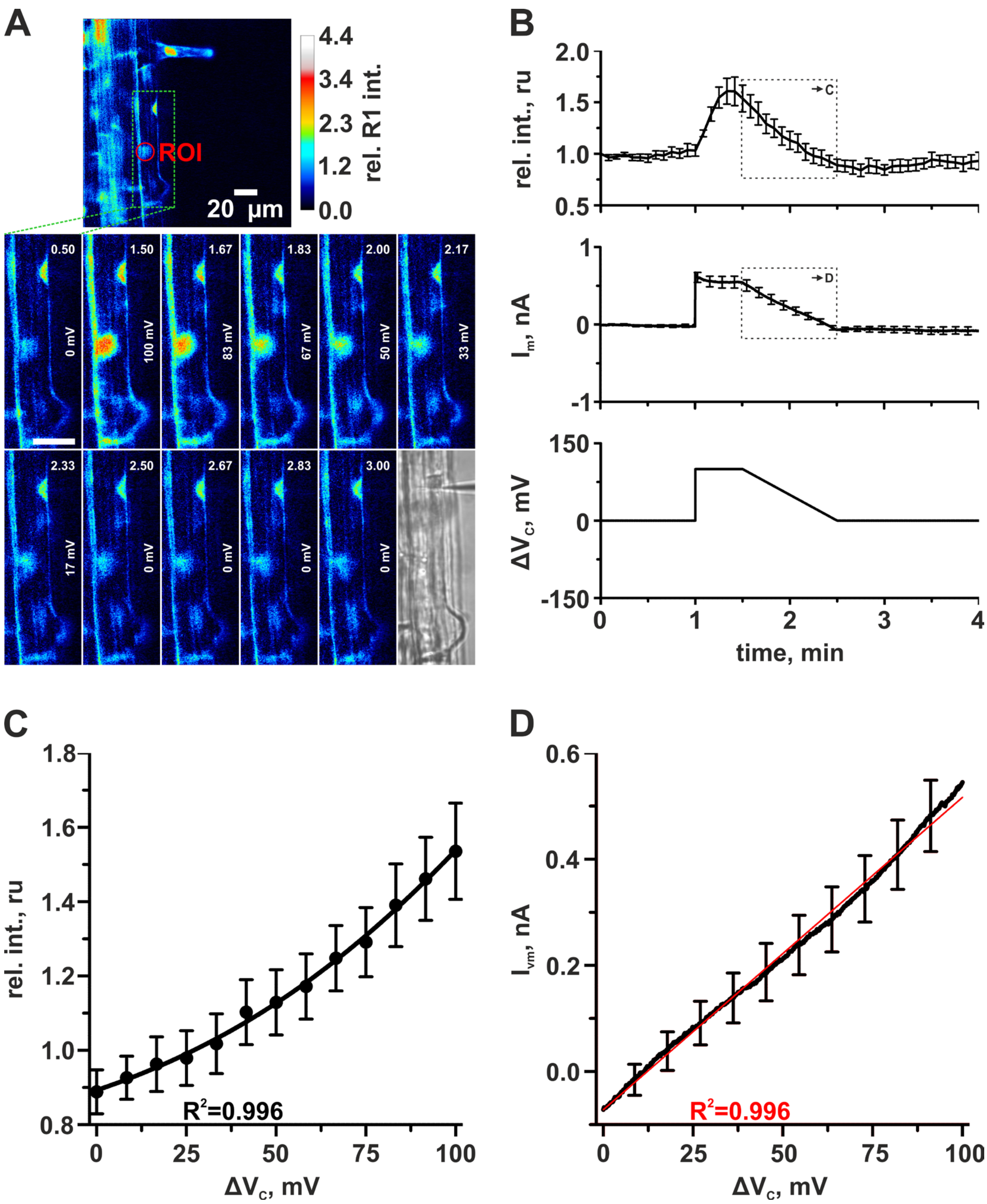

Fig. 3.6: Ca^{2+} currents across the VM strictly depend on the VM potential. (A) Representative images of an *A. thaliana* bulging root hair cell that expresses R-GECO1. The upper panel shows a false colored image of the R-GECO1 intensity relative to that in a region of interest (ROI, red line), just before application of the voltage pulse, as indicated by the calibration bar on the upper right. The panels below are magnifications as indicated by the dashed green lines. The time points after start of the experiment are given at the bottom of the lower panels. The indicated voltage values correspond to the clamp-voltage. The lower panel on the right shows a transmitted light image of the root hair cell at the same magnification as the other lower panels. All scale bars are 20 µm. (**B**) Average values of R-GECO1 fluorescence intensity and vacuolar currents, in response to a voltage ramp of ΔV_c=100 to 0 mV. **Upper panel**: average R-GECO1 fluorescence intensities measured in

the cytoplasm-rich region around the nucleus of root hair cells. Error bars show SE (n=7). The dotted squares indicate data points that were used for the analysis in (C) and (D). **Middle panel**: average vacuolar current traces of cells stimulated with a voltage ramp. **Lower panel**: voltage pulse protocol applied via double-barrelled microelectrodes impaled into the vacuole. (**C**) Average rel. R-GECO1 fluorescence intensity plotted against the potential difference at the VM. The solid line shows a Boltzmann function fitted to the data points: $\Delta F(V_c) = \frac{(0.7-3.5)}{1+e^{\frac{(V_C-149)}{58.9}}} + 3.5$. R^2 is the correlation coefficient. Error bars show SE (n=7). (**D**) The averaged current-voltage of the vauolar membrane, measured with a voltage ramp as shown in (B). The solid red line was obtained by linear regression. Error bars show SE (n=7).

In addition to the experiments with voltage ramps, shown above, the voltage dependence of Ca^{2+}-permeable transport at the VM was studied with voltage step protocols. The VMs of root hair cells that express R-GECO1 were clamped from the free running membrane potential (average serial potential = -116 mV, SE=5 mV) to depolarizing and hyperpolarizing potentials for 30 s. Consecutive depolarizing voltage pulses (ΔV_c from 100 mV to 20 mV with 20 mV increments) resulted in $[Ca^{2+}]_{cyt}$ elevations with successively lower amplitudes (**Fig. 3.7A** and **B**). The application of hyperpolarizing potentials (ΔV_c from -80 mV to -20 mV, **Fig. 3.7C**) resulted in reductions of $[Ca^{2+}]_{cyt}$ with likewise successively lower amplitudes. The correlation between the applied VM potentials and the voltage-induced changes in $[Ca^{2+}]_{cyt}$ was again found to be in agreement with a Boltzmann relationship (**Fig. 3.7D**). From the linear current-voltage regression an average VM conductance of 8 nS could be calculated (**Fig. 3.7D, inset**).

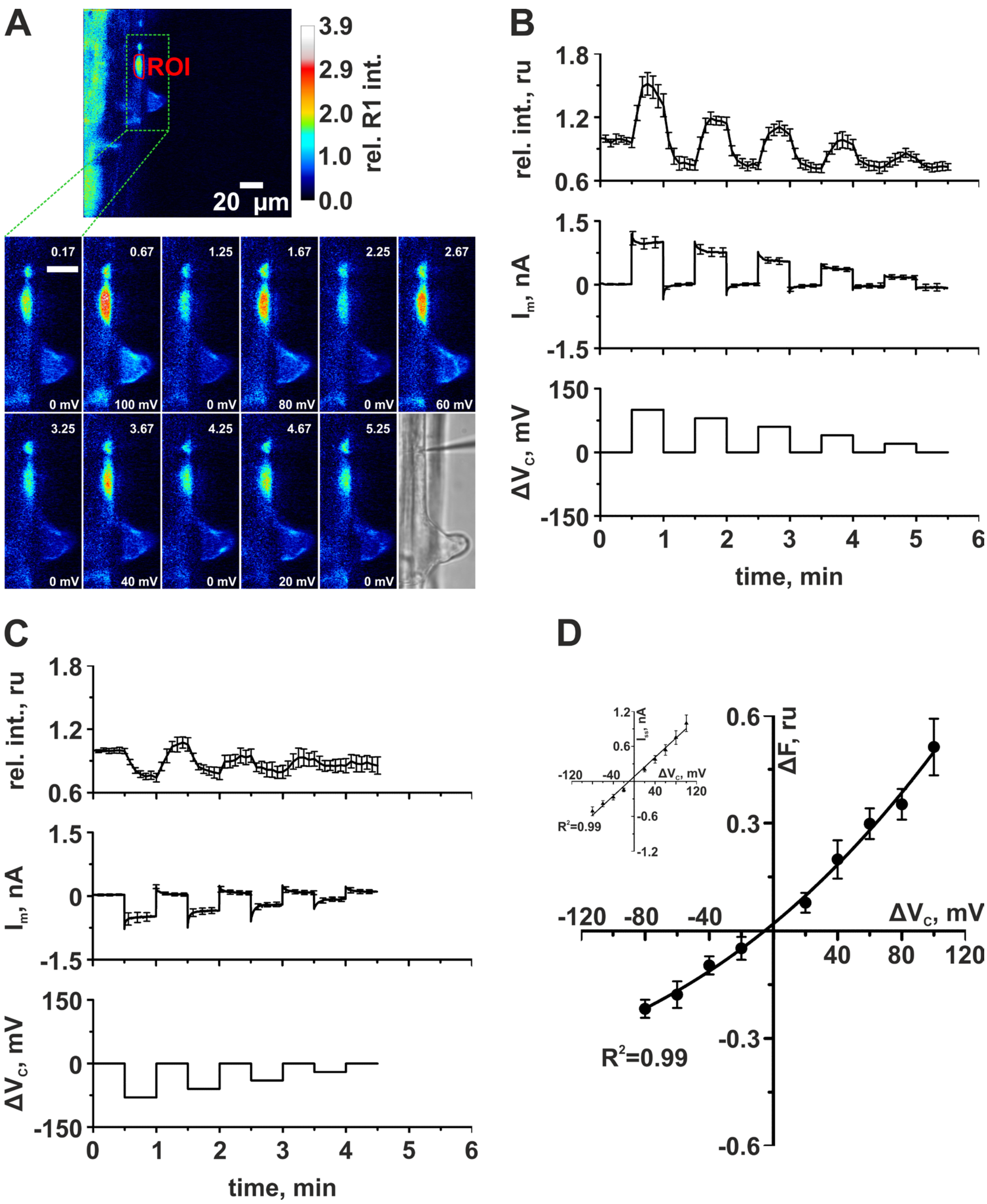

Fig. 3.7: Relationship between $[Ca^{2+}]_{cyt}$ and the voltage across the VM. (**A**) Representative images of a bulging root hair that expresses R-GECO1, stimulated with voltage pulses. The region of interest (ROI), which includes a cytoplasm-rich region around the nucleus is indicated by a red line. The panels below are magnifications as indicated by the dashed green line. The time points after start of the experiment are shown in the top and the clamp voltage on the bottom of the panels. A transmitted light image of the root hair with the same magnification is shown in the lower right panel. The calibration bar on the upper right links the relative R-GECO1 intensity to the colour code. All scale bars are 20 µm. (**B**) Impact of depolarizing voltage pulses at the VM on the average R-GECO1 fluorescence intensity and vacuolar ion currents. **Upper panel**: Average R-GECO1 fluorescence intensities measured in the cytoplasm-rich region around the nucleus of root hair cells. The cells

were stimulated with voltage pulses as shown in the lower panel. Error bars show SE (n=7). **Middle panel**: Average vacuolar current traces in response to the applied voltage pulses. **Lower panel**: Voltage pulse protocol applied via double-barrelled microelectrodes impaled into the vacuole. The amplitudes of consecutive pulses range from +100 mV to +20 mV. (**C**) Impact of hyperpolarizing voltage pulses at the VM on the average R-GECO1 fluorescence intensity and vacuolar ion currents. **Lower panel**: voltage pulse protocol applied via double-barrelled microelectrodes impaled into the vacuolar lumen. The amplitudes of consecutive pulses range from -80 mV to -20 mV. **Middle panel**: average vacuolar current traces in response to the applied voltage pulses. **Upper panel**: average R-GECO1 fluorescence intensities measured in the cytoplasm-rich region around the nucleus of root hair cells. Error bars show SE (n=7). (**D**) The relationship between average R-GECO1 fluorescence change amplitudes and the applied voltage pulses. Values are deduced from measurements shown in (A) and (B). The solid line shows a Boltzmann function fitted to the data points: $\Delta F(V_c) = \frac{(-0.54-3.5)}{1+e^{\frac{(V_c-238.6)}{130.9}}} + 3.5$. R^2 is the correlation coefficient. **The inset** gives the corresponding current-voltage relationship with linear regression. Error bars show SE (n=7).

3.2. Auxin transport and perception are integrated in a Ca^{2+}-dependent fast auxin signaling pathway

The physiological function of auxin, as a major regulator of plant development and growth is tighly linked to polar transport of this phytohormone through various tissues and organs. At the cellular level, PAT is responsible for the formation of defined auxin gradients through which auxin imposes its physiological functions during organ primordia formation or tropic responses (Benkova *et al.* 2003; Ottenschläger *et al.* 2003).

The importance of auxin transport for its function, resulted in great efforts to characterize all aspects of auxin transport (Bennett *et al.* 1996; Swarup *et al.* 2001; Friml *et al.* 2002a; Friml *et al.* 2003; Ottenschläger *et al.* 2003; Kleine-Vehn *et al.* 2006; Rutschow *et al.* 2014). Although it has long been suggested that carrier-mediated auxin uptake causes electrical signals (Felle *et al.* 1991), a thorough electrophysiological *in planta* analysis employing the advantages of an established model plant like *A. thaliana* has yet to be undertaken.

Hence, in the following part of the results presented in this work, the auxin sensitivity of *A. thaliana* bulging root hair cells is combined with their advantage for electrophysiological measurements (see **Chapter 1.5**) to analyze carrier-mediated auxin influx. Special emphasis is provided regarding its electrophysiological characteristics, genetic underlying, affinities, and specificities.

Since $[Ca^{2+}]_{cyt}$ elevation are among the first observable responses to auxin (Felle 1988a; Monshausen *et al.* 2011) a fast auxin signaling pathway that is involved in the root gravitropic response has been suggested (Shih *et al.* 2015). However, despite the identification of the putative Ca^{2+} channel CNGC14 as mediator of auxin-induced Ca^{2+} signals, other components of fast auxin signalling remain elusive (Shih *et al.* 2015). Therefore, auxin-induced Ca^{2+} signals and their interaction with auxin transport and auxin perception were analysed to gain insights into fast auxin signaling.

3.2.1. The first electrophysiological *in planta* analysis of auxin influx

Application of auxin can provoke rapid changes in the plasma membrane potential of plant cells, which have been suggested to be related to carrier-mediated auxin uptake. These studies were continued with *A. thaliana*, as the mutant collection of this model plant provides the genetic resources that allow the identification of the genes responsible for the observed responses.

Bulging root hair cells of *A. thaliana* seedlings were stimulated with 1 s pulses of auxin-containing solution supplied with pressure operated application pipettes (**Fig. 3.8A**). The membrane response was measured with single-barrelled microelectrodes impaled into the root hair tip. On average, a resting PM potential of -161 mV (SE=1 mV, n=156) was recorded. Application of 10 µM of the native auxin 3-IAA induced a rapid depolarization of the PM with an amplitude of up to 70 mV. Based on the time-course of the membrane response, five phases can be distinguished (**Fig. 3.8B**). Upon auxin application, a lag phase (**i**) can be recognized, during which the membrane potential often slightly hyperpolarized. The auxin-induced depolarization is of biphasic nature divided in an acceleration phase (**ii**), which is followed by a deceleration phase (**iii**) until the maximal depolarization is reached. Finally, a slow repolarization period (**iv**) is followed by a new steady state value (**v**). In experiments during which the bath solution was constantly exchanged, i.e. auxin applied via pipettes was rapidly washed out, showed that root hair cells show a similar response to two consecutive auxin pulses (**Fig. 3.8C**, compare to **Fig. 3.25A**).

The tissue specificity of the auxin-induced depolarization was studied by comparing the electrical responses of root hair cells and hypocotyl epidermal cells of dark-grown *A. thaliana* seedlings (**Fig. 3.8D**). Although external application of auxin to epidermal hypocotyl cells induces apoplastic acidification and cell elongation (Fendrych *et al.* 2016), only root hair cells depolarized in response to a short auxin pulse. Since both cell types showed a similar PM resting potential (**Fig. 3.8D inset**), the auxin-induced depolarization seemed to be a highly root specific response in *A. thaliana*. The immediacy of the auxin-induced depolarization thereby points towards auxin influx as the responsible process as it has already been suggested by Felle *et al*. (1991).

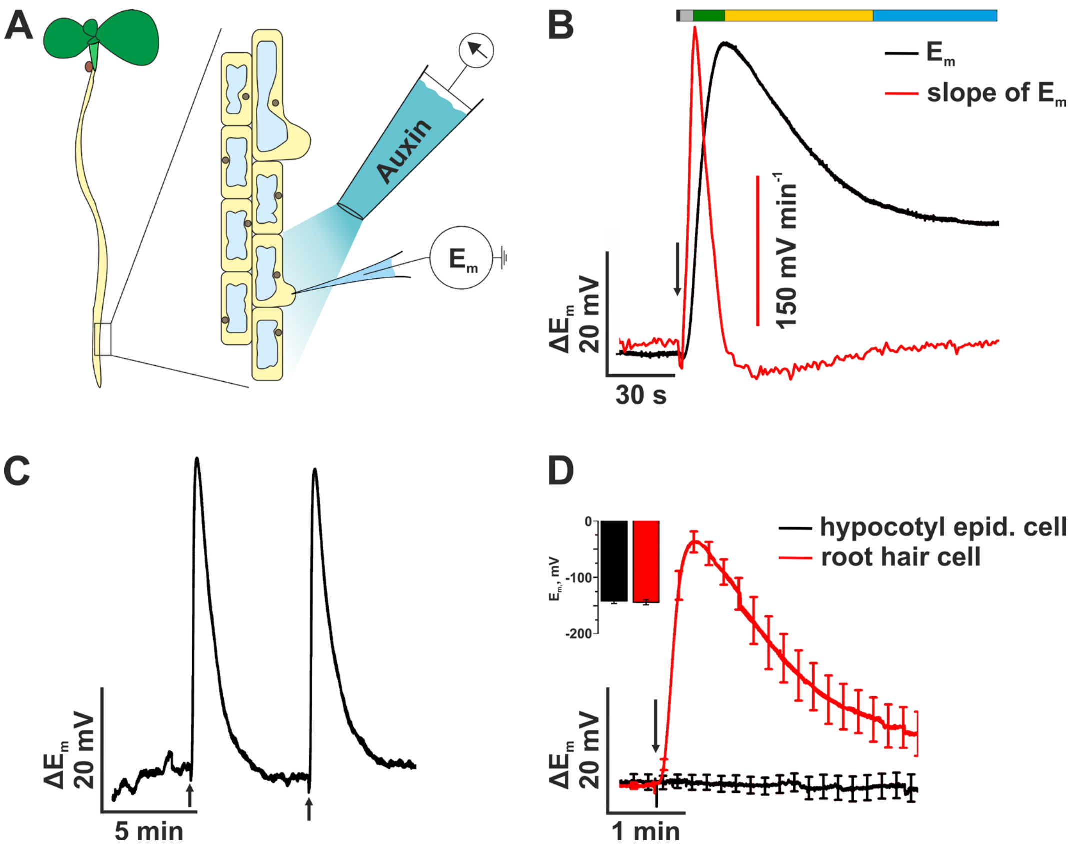

Fig. 3.8: Short auxin pulses induce a cell specific depolarization of the PM. (**A**) Cartoon illustrating the experimental set-up, in which auxin was applied to impaled bulging root hairs of *A. thaliana* seedlings, by use of backpressure operated application pipettes. (**B**) Representative PM potential trace of a root hair stimulated with auxin (black line) and a trace of the corresponding derivative that indicates the depolarization rate (red line). The arrow indicates the time point at which a 1 s pulse of 10 µM 3-IAA was applied. The colored bar above the traces indicates the five phases of the membrane response: lag phase (black); acceleration phase (gray); deceleration phase (green); slow repolarization phase (yellow); new steady state level (blue). (**C**) Representative PM potential trace of a root hair cell that was stimulated with two consecutive 1 s pulses of 1 µM 3-IAA (arrows). The bath solution was constantly perfused during the experiment. (**D**) Average PM voltage traces of root hair cells (red) and hypocotyl epidermal cells (black) of dark-grown *A. thaliana* seedlings in response to a 1 s pulse of 10 µM 3-IAA (arrow). Traces are normalized to the point of 3-IAA application. **Inset:** Average PM resting potential 5 s before 3-IAA was applied. Error bars show SE (n=16 (hypocotyl) and 9 (root hair)).

Since the efficient uptake of auxin would only be possible through H^+-coupled symport (see **Chapter 1.3.2.**), the auxin- as well as the H^+-dependency of the electrical response was investigated. The auxin-induced depolarization of the root hair cells was depended on the concentration of 3-IAA, as well as on the pH of the external medium (**Fig. 3.9**). Depolarizations were recorded if 3-IAA was applied at concentrations higher than 1 nM (**Fig. 3.9A**). Both the amplitude of the depolarization and the maximal velocity of the depolarization response increased if higher concentrations of auxin were applied (**Fig. 3.9B**). The relation between the auxin concentration, amplitude-, and velocity of the depolarization were fitted with a Michaelis-Menten equation that yielded apparent half maximal concentrations of 53 nM (SE=6 nM) and 300 nM (SE=133 nM), respectively (**Fig. 3.9B**). Likewise, the auxin-induced depolarization was enhanced at more acidic pH values of the bath solution, with 3-IAA applied at a concentration of 10 µM, as well as 0.3 µM. No auxin-induced depolarization occurred at a pH-value of 8.5 in the bath solution, although the PM potential had a similar value as at pH 5.5 (**Fig. 3.9C**). The pH-dependence of the depolarization rates at auxin concentrations of 10 and 0.3 µM were fitted with a Michaelis-Menten equation, which yielded an apparent half-maximal proton concentration of 910 nM (SE=500 nM) (i.e. pH ≈ 6) (**Fig. 3.9D**). The observation that auxin induces a depolarization of the root hair PM potential in a strictly pH-dependent manner lead to the hypothesis that an auxin-induced and inward directed H^+ flux might be responsible for the fast depolarization.

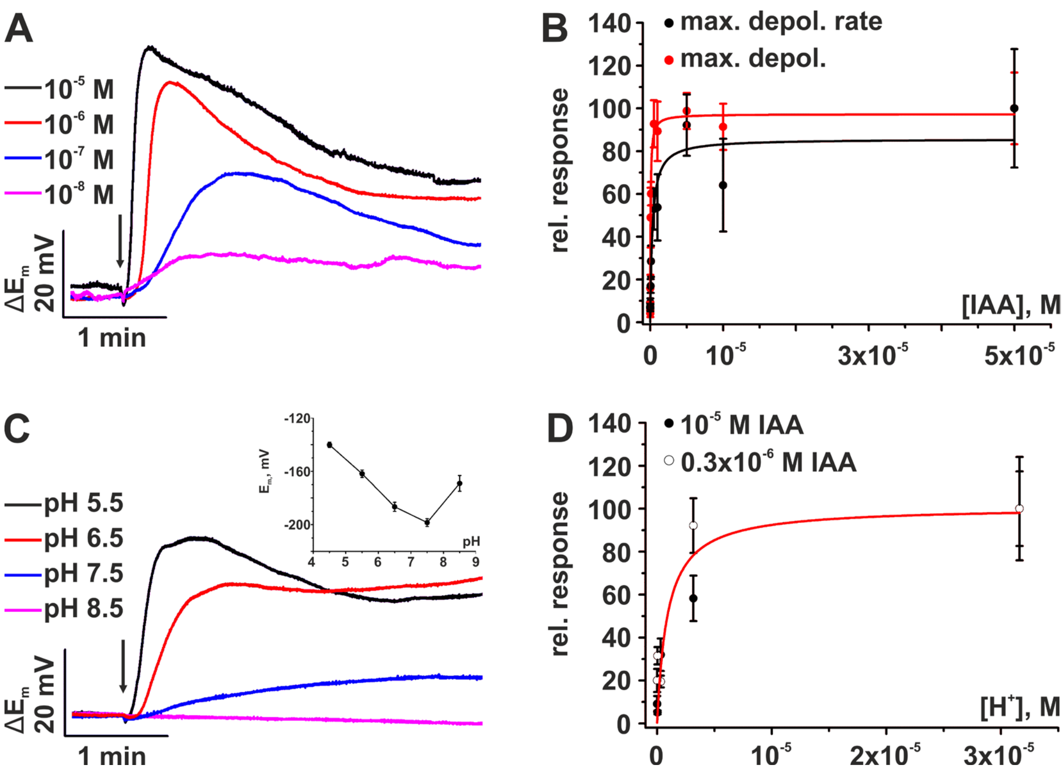

Fig. 3.9: The auxin-induced PM-depolarization of *A. thaliana Col-0* root hair cells is IAA- and pH-dependent. (**A**) Representative voltage traces of root hair PM depolarizations at pH 5.5. 3-IAA was applied at the concentrations indicated by the color code for 1 s (arrow). Traces are normalized to the point of 3-IAA application. (**B**) Dose-response curve of the auxin-dependent maximal depolarization amplitudes and –rates, deduced from experiments shown in (A) and fitted with a Michaelis-Menten equation. Error bars indicate SE (n=6) (**C**) Representative single measurements of the auxin-induced depolarization at different external pH values, as indicated by the colour-code. 10 µM 3-IAA was applied for 1 s (arrow).

Traces are normalized to the point of 3-IAA application. The **inset** shows resting PM potentials of the impaled root hair cells at the external pH values applied, 5 s before the stimulation with a 3-IAA pulse. Error bars indicate SE (n=16). (**D**) Relation between maximal depolarization rates, deduced from experiments as in (C), performed with 10 µM (closed circles) and 0.3 µM (open circles) 3-IAA. The data were fitted with a Michaelis-Menten equation. Error bars indicate SE (n=6 for 10 µM 3-IAA and n=10 for 0.3 µM 3-IAA).

The hypothesis that the depolarization is linked to carrier mediated co-transport of auxin and H^+, was tested with scanning H^+-selective microelectrodes. At control conditions, an efflux of H^+ was determined at the early differentiation zones of *A. thaliana* seedling roots, in which the first root hairs begin to differentiate (**Fig. 3.10**). The pronounced and stable H^+ efflux is most likely due to the activity of the PM H^+-ATPases in root cells. The application of 3-IAA, to a final concentration of 10 µM in the bath solution, first resulted in a reduction of the net H^+ efflux that subsequently turned into a net H^+ influx. Note that application of 3-IAA led to a short-term disturbance of the measurement, which is indicated by the interruption of the graph after 3 min. (**Fig. 3.10**).

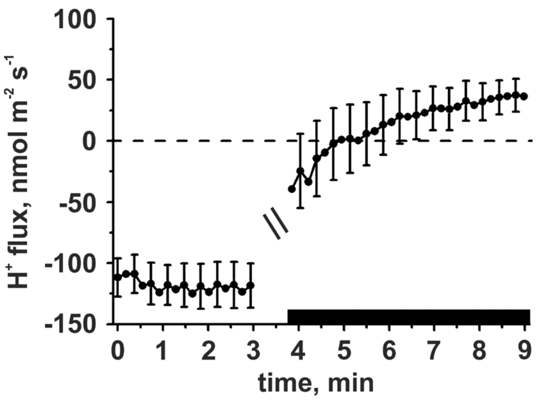

Fig. 3.10: Auxin induces H^+ influx at *A. thaliana Col-0* seedling roots. Average H^+ fluxes from root epidermal cells in the early differentiation zone, stimulated with 3-IAA at t=3min. Negative values represent efflux of H^+ from the roots and positive values influx. The application of 10 µM IAA to the bath solution is indicated by the black bar. The trace is interrupted after application of 3-IAA. Error bars show SE (n=11). The data were provided by Katharina von Meyer, Research group of Dirk Becker, Molecular plant physiology and biophysics, University of Wuerzburg.

Because of the pH-dependence of the auxin-induced depolarization and H^+ influx, it is likely that 3-IAA is taken up in symport with H^+ by a carrier protein in the PM. The main auxin uptake transporter in epidermal root cells is AUX1, which has long been proposed to be a H^+/auxin symporter, based on its similarities to amino acid permeases (Bennett *et al.* 1996). However, the putative auxin receptor ABP1 also was found to induce ion fluxes across the PM (Rück *et al.* 1993; Thiel *et al.* 1993) and thus a contribution of ABP1 to auxin-induced membrane responses had to be taken into account. For this reason, the auxin-induced depolarization of root hairs in wild type was compared with two independent ABP1 loss-of-function lines, *abp1-c1* and *abp1-TD1* (Gao *et al.* 2015) (**Fig. 3.11**). In addition, we studied a loss-of-function mutant of the auxin efflux carrier *PIN2*. This revealed that the auxin response of both *abp1* mutants was not significantly different from wild type, but a reduced response to 3-IAA was found for the *pin2* mutant. Moreover, the PM potentials at control conditions were not affected by the loss-of-function mutations in the three lines tested (**Fig. 3.11A, inset**). In contrast to PIN2, an involvement of ABP1 in PM responses, which are induced through auxin transport can thus be excluded.

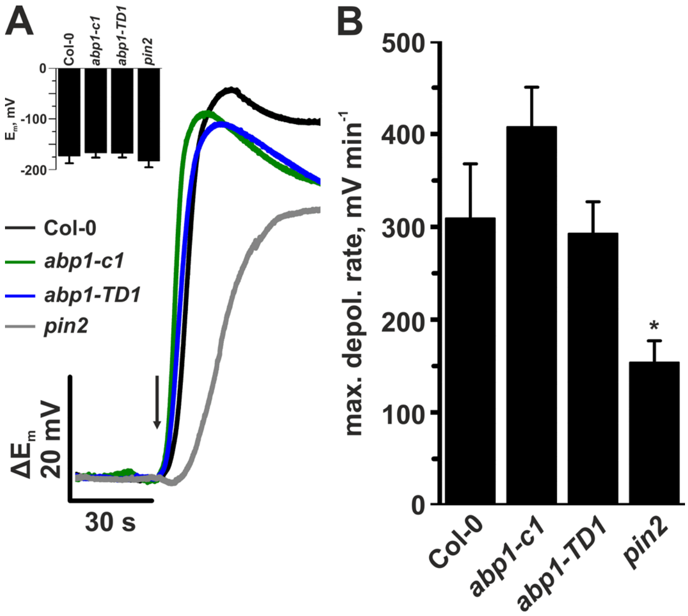

Fig. 3.11: Auxin-induced root hair depolarizations are *ABP1*-independent, but reduced in a *pin2* mutant. (**A**) Representative voltage traces of the root hair PM of *Col-0* (black) as well as *abp1* (green and blue) and *pin2* (gray) lines in response to a 1 s pulse of 10 µM 3-IAA (arrow). The **inset** shows average root hair resting potential at 5 s before auxin application Error bars show SE (n=10 to 11). (**B**) Average values of maximal depolarization rates from measurements as shown in (A). Error bars show SE (n=10 to 11). The asterisk marks a significant difference (Student's t-test, p<0.05).

In the next step, several *aux1* loss-of-function mutants (**Fig. 3.12A**) were tested to study the role of AUX1 in auxin-induced root hair depolarizations and stimulation of H^+ influx. The selected *aux1* mutants all showed a reduced gravitropic root growth (**Fig. 3.12B**), which is characteristic for a disrupted PAT due to the loss of AUX1 (Swarup *et al.* 2004). Most of the mutations in *AUX1* also impaired the auxin-induced depolarization of root hair cells, as well as H^+ influx in the most apical part of the root hair zone. Only the partial loss-of-function line *aux1-2* showed no significant reduction of the auxin-dependent H^+ influx (**Fig. 3.12C**). The null alleles *wav5-33* and *aux1-T* showed on average an 80% loss of the root hair depolarization, which clearly exceeds the phenotype of PIN2 (**Fig. 3.12C** and **D**). Moreover, the *wav5-33* and *aux1-T* mutants showed a complete loss of auxin-induced H^+ influx (**Fig. 3.12E**). These phenotypes are unlikely to be due to a general impact of the mutations on ion transport, as w*av5-33* root hair cells have on average the same PM potential as their counterparts in wild type seedlings (**Fig. 3.12D, inset**). The net contribution of AUX1 to the auxin induced depolarization and H^+ influx were calculated by subtracting the mean mutant response from that of the wild type (red curves in **Fig. 3.12D** and **E**). This analysis suggests that AUX1 is responsible for the rapid auxin-induced depolarization and H^+

influx, whereas a residual slow depolarization and H^+ influx are due to AUX1-independent auxin transport. As the slow auxin-induced root hair depolarization is likely to depend on other transport proteins as AUX1, the 3-IAA affinity of both systems was tested with a series of auxin concentrations in wild type and *wav5-33* seedlings (**Fig. 3.12F**). Whereas the half-maximal response of wild type occurred at an auxin concentration of 67 nM (SE=54 nM), this value increased to 1.7 µM (SE=1.6 µM) in the *wav5-33* mutant (red graph in **Fig. 3.12F**). These data thus suggest that AUX1 is the predominant auxin influx transporter at physiological auxin concentrations below 1 µM. At higher auxin concentrations, however, other electrogenic transporters contribute to auxin uptake, which have a much lower affinity for 3-IAA.

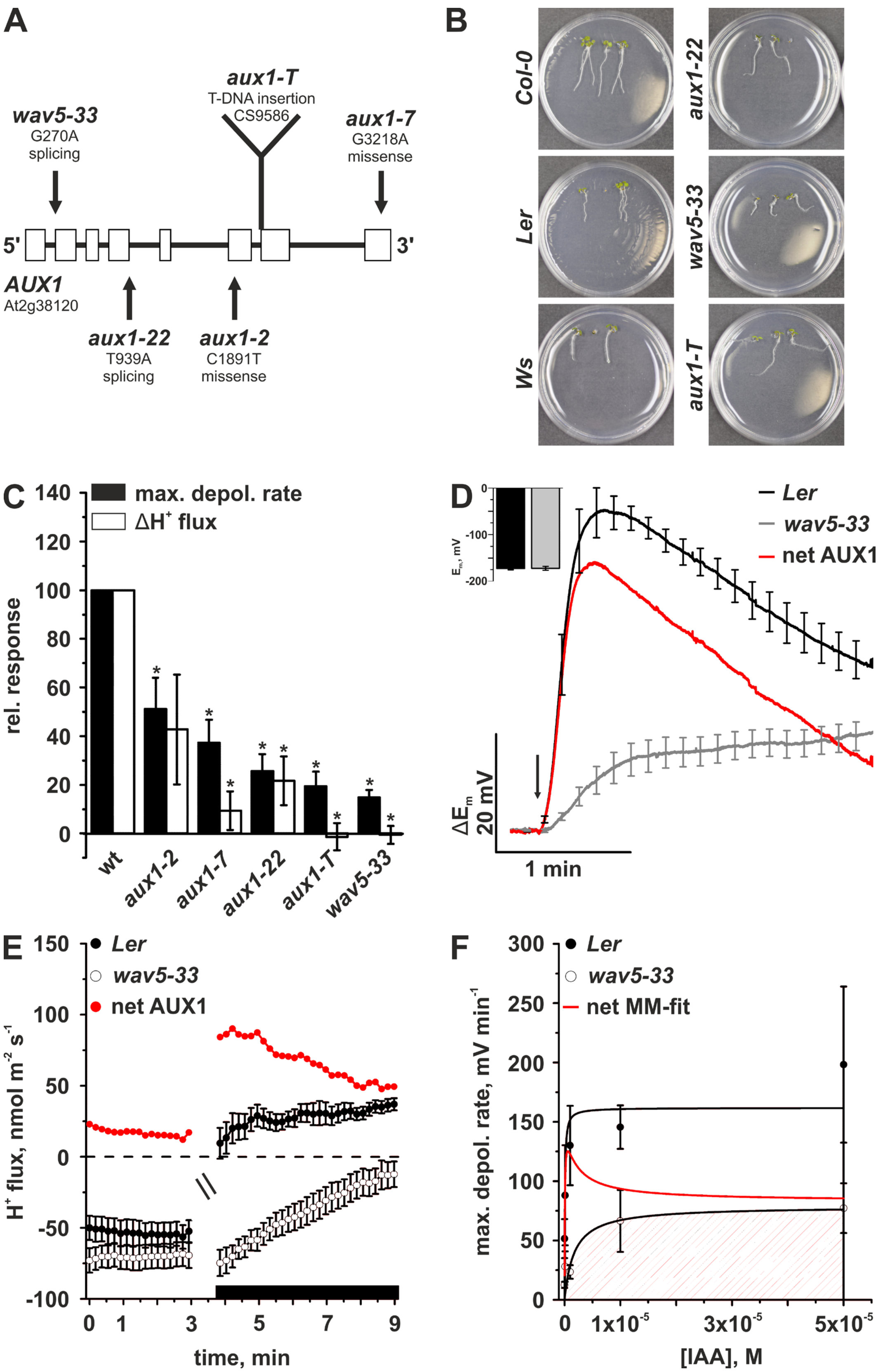
A
wav5-33
G270A
splicing
aux1-T
T-DNA insertion
CS9586
aux1-7
G3218A
missense
5'
3'
AUX1
At2g38120
aux1-22
T939A
splicing
aux1-2
C1891T
missense
B
Col-0
aux1-22
Ler
wav5-33
Ws
aux1-T
C
max. depol. rate
ΔH+ flux
rel. response
wt
aux1-2
aux1-7
aux1-22
aux1-T
wav5-33
D
Ler
wav5-33
net AUX1
ΔEm 20 mV
1 min
E
Ler
wav5-33
net AUX1
H+ flux, nmol m-2 s-1
time, min
F
Ler
wav5-33
net MM-fit
max. depol. rate, mV min-1
[IAA], M

Fig. 3.12: Auxin-induced root hair depolarization and H⁺ influx are AUX1-dependent. (**A**) Genomic model of the *AUX1* gene from the start- to the stop codon including the positions of exons (open boxes) and introns (black lines). *aux1* loss-of-function mutants used in this work are indicated at the respective position by arrows, with the underlying mutations. (**B**) Agravitropic root growth phenotypes of *aux1* mutants (right column) compared to their respective accessions (left column). (**C**) Average depolarization rates (closed bars) and the change of H^+ fluxes (open bars) in response to application of 10 µM 3-IAA. Data shows normalized values of *aux1* mutants, relative to their respective accessions. Error bars show SE (n=10 to 13). Asterisks mark significant changes to the wild type response (Student's t-test, $p<0.05$). (**D**) Average root hair depolarizations of *Ler* (black) and *wav5-33* (gray) seedlings. The red curve represents the net contribution of AUX1 calculated by subtracting the average curve of *wav5-33* from the average curve of *Ler*. IAA was applied at a concentration of 10 µM for 1 s (arrow). Traces are normalized to the point of 3-IAA application. **Inset:** Average PM resting potential 5 s before application of 3-IAA. Error bars show SE (n=11 (*Ler*) and 10 (*wav5-33*)). (**E**) Average H^+ flux from the early differentiation zone of *Ler* (closed circles) and *wav5-33* (open circles) seedlings. Red data points represent the net contribution of AUX1, calculated by subtracting the average data points of *wav5-33* from those of *Ler*. Error bars show SE (n=13 (*Ler*) and 12 (*wav5-33*)). (**F**) Maximal depolarization rates of *Ler* (closed circles) and *wav5-33* (open circles) root hairs in response to a range of IAA concentrations applied for 1 s. The shaded area beneath *wav5-33* indicates the AUX1-independent transport of IAA. The red curve shows the net AUX1 contribution, calculated by subtracting the black curves, which were obtained by fitting a Michaelis-Menten equation to the data of *wav5-33* and *Ler* wild type. Error bars indicate SE (n=6 to 8 (*Ler*) and 5 (*wav5-33*)).

AUX1 has a high affinity for the natural auxin 3-IAA, but it is unknown to which extend it can transport other auxins *in planta*. In addition to 3-IAA, the synthetic auxins 5F-IAA, 1-NAA, and 2,4-D, as well as the physiological inactive substance 2-NAA were tested for their ability to provoke a PM potential depolarization in root hair cells (**Fig. 3.13A**). Benzoic acid (BA) served as a weak organic acid control. Active auxins such as 3-IAA, 5F-IAA and 1-NAA were able to elicit a fast depolarization of the root hair PM potential when applied at a concentration of 10 µM for 1 s, but 2,4 D was not (**Fig. 3.13B**). Both, 5F-IAA and 1-NAA, caused rapid depolarization, albeit at a lesser extent as 3-IAA (**Fig. 3.13B** and **C**). However, no difference was observed between the response of wild type and *wav5-33* root hairs, which indicates that AUX1 is not involved in the transport of these synthetic auxins. Hence, AUX1 seems to display a high specificity for the natural auxin indole-3-acetic acid.

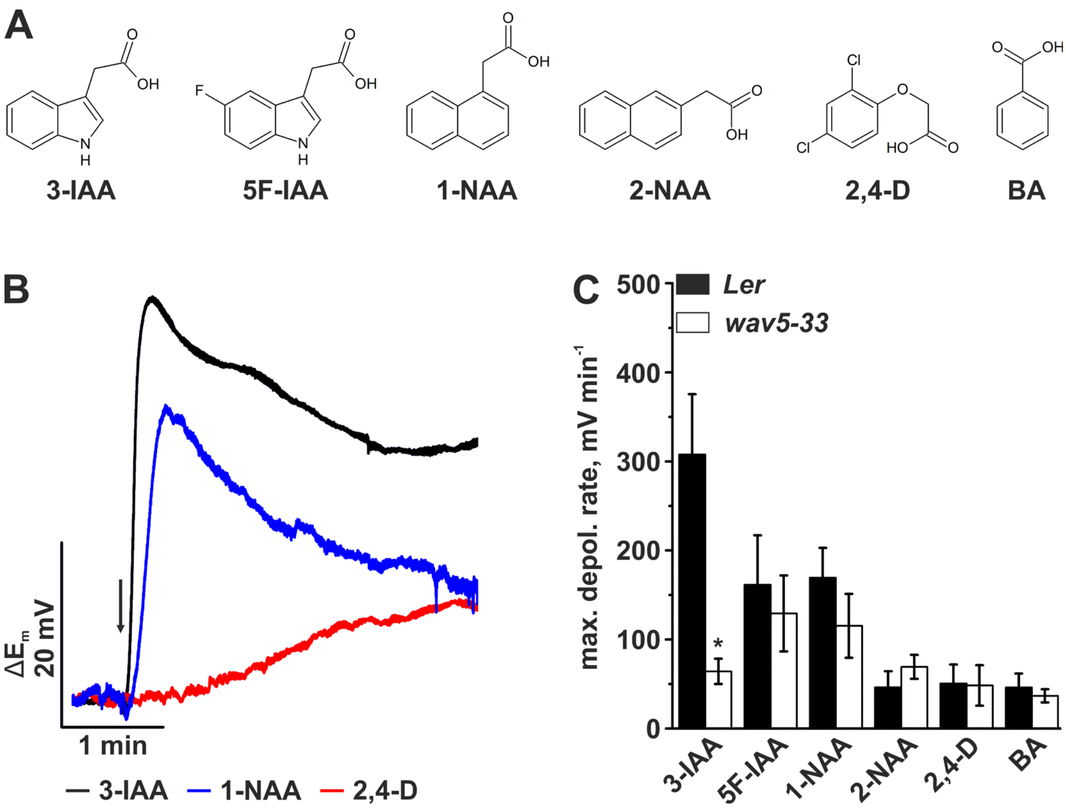

Fig. 3.13: AUX1 specifically transports indole-3-acetic acid. (**A**) Chemical structures of the auxins used in this work. Physiological active auxins are 3-IAA, 5F-IAA, 1-NAA, and 2,4-D. BA was used as a weak organic acid control. (**B**) Representative traces of PM potentials in *Ler* root hairs stimulated with native auxin 3-IAA (black) and the synthetic auxins 1-NAA (blue) and 2,4-D (red). Auxins were applied at 10 µM with a 1 s pulse from an application pipette (arrow). Traces are normalized to the point of auxin application. (**C**) Average maximal depolarization rates of bulging root hairs deduced from measurements as shown in (A). The auxins were applied to *Ler* (closed bars) and *wav5-33* (open bars) seedling root hairs. Error bars show SE (n=8 (3-IAA) and 5 (analogs)). The asterisk marks a significant difference between the groups of measurements (Student's t-test, p<0.05).

To further substantiate the genetic evidence for AUX1 causing the described PM responses of root epidermal cells in subsequent experiments it was tested whether *AUX1* expression levels affect the auxin-triggered PM potential depolarization.

Jones *et al*. (2009) reported a pronounced difference in AUX1 abundance when comparing root hair cells and non-hair epidermal root cells. Indicative for a specific expression in non-hair cells pAUX1::AUX1::YFP fusions were detectable in the PM of non-hair cells, while a fluorescent signal was absent in differentiated hair cells. However, transcriptomic approaches by Birnbaum *et al*. (2003) and Lan *et al*. (2013) (see **Fig. 1.7**) provided evidence for the presence of *AUX1* transcripts in both cell types.

To test whether the proposed difference in *AUX1* expression results in a different magnitude of auxin influx, root hair and non-hair cells were consequently compared in their auxin-induced PM potential response. Non-hair cells were found to react with a faster depolarization to 3-IAA application then root hair cells did (**Fig. 3.14A** and **B**), although both cell types shared a similar resting potential (**Fig. 3.14C**). In line with Jones *et al*. (2009) the average maximal depolarization rate of non-hair cells was found to be more than twice as high as it was found for hair cells (**Fig. 3.14B**). However, since bulging root hair cells show several advantages for experimental approaches involving live-cell imaging and electrophysiological strategies (see **Chapter 1.5.)** they can be regarded as a well-suited system to study auxin transport.

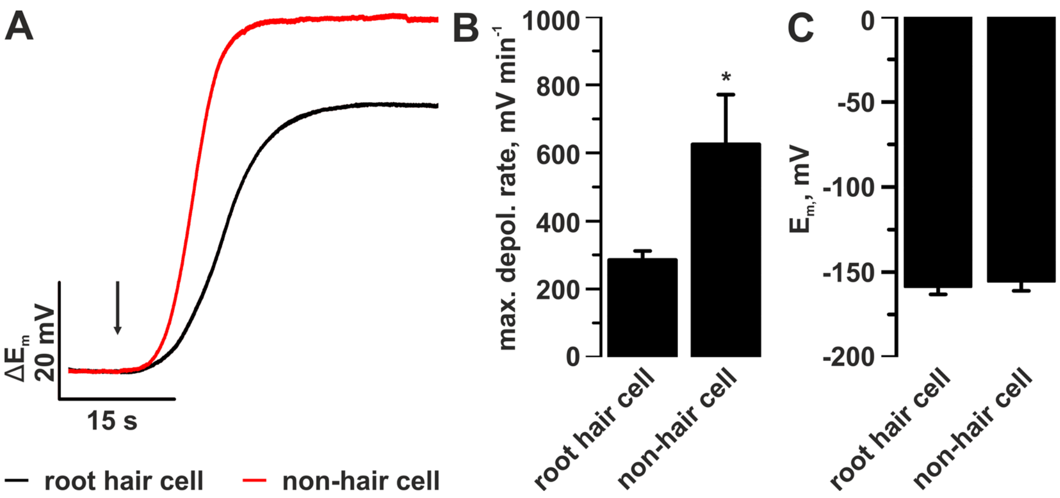

Fig. 3.14: Epidermal non-hair cells show a higher auxin sensitivity than root hair cells. (**A**) Representative voltage traces of auxin-induced PM depolarizations of *A. thaliana Col-0* root hair cells (black) and non-hair epidermal root cells (red). The arrow indicates the application of a 1 s pulse of 10 µM 3-IAA. Traces are normalized to the point of 3-IAA application. (**B**) Average maximal depolarization rates from experiments as shown in (A). Error bars show SE (n=5). (**C**) Average epidermal root cell PM resting potential within 5 s before the 3-IAA pulse from experiments as shown in (A). Error bars show SE (n=5). The asterisk marks a significant difference (Student's t-test, p=0.05)

The availability of P_i in the soil is one of the major limiting factors for plant growth and crop yield in agriculture (Peret *et al.* 2011; Elser 2012). The architecture of the root system is altered in response to P_i nutrition, which guarantees an efficient P_i supply under P_i-limiting conditions (Drew 1975). As auxin is the main hormone that affects root architecture, it is likely that auxin is involved in root response to low P_i nutrition. In line with this role, the expression *AUX1* was recently show to be enhanced under P_i-deficiency, in cells of the root elongation zone (Kumar *et al.* 2015).

Based on the reported role of P_i on *AUX1* expression, we set out to test the impact of P_i nutrition on auxin transport in root hair cells. For this purpose, wild type and *wav5-33* seedlings were grown on P_i concentrations ranging from 0.3 µM to 312 µM. A low P_i concentration in the growth medium resulted in a growth retardation of *A. thaliana* seedlings (**Fig. 3.15A**). In line with the enhanced expression of *AUX1* at low P_i nutrition, low P_i (3 and 0.3 µM) significantly enhanced the depolarization rates in response to 0.3 µM 3-IAA in wild type (**Fig. 3.15B** and **C**). In contrast, no effect of P_i supply on auxin transport could be found in the *aux1* null allele mutant. The P_i concentration in the growth medium did not affect the resting PM potential measured before 3-IAA application, neither in wild type, nor in *wav5-33* root hair cells (**Fig. 3.15C, inset**).

P_i is taken up from the soil via the H^+-coupled PHOSPHATE TRANSPORTER1 (PHT1; (Mlodzinska and Zboinska 2016)). At high external P_i concentrations, this transport mechanism should lead to a decreased electrical resistance of the root hair PM because of higher P_i uptake rates.

An unaltered H^+-coupled auxin influx current would consequently be represented by a smaller depolarization of the PM potential under high P_i than it would be under low P_i conditions. However, residual P_i in the bath solution is approx. 1/10 of its initial concentration (see **Fig. 2.10**) in the growth medium. Hence, transport of P_i should not significantly interfere with auxin transport in the described experimental system. Low P_i nutrition thus enhances the auxin-induced depolarization of root hairs, suggesting a higher rate of auxin transport via AUX1. The latter conclusion is backed up by ion flux measurements, which also revealed higher initial H^+ influx compared to seedlings grown at high P_i levels (**Fig. 3.15D**). This thus demonstrates that AUX1-mediated auxin uptake is enhanced in P_i-starved roots, most likely via an increased expression of *AUX1*.

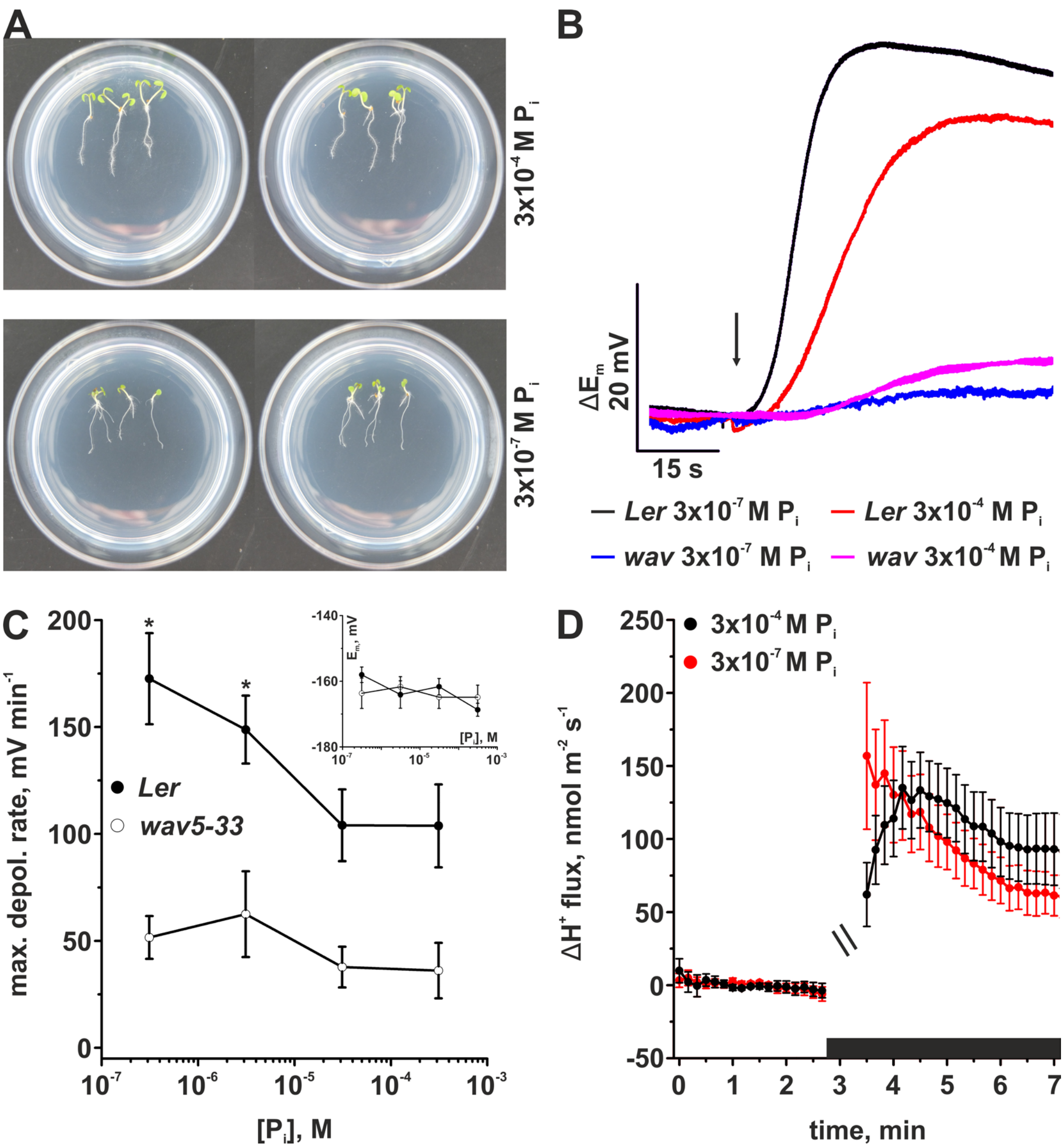

Fig. 3.15: The external phosphate availability modulates the AUX1-mediated root hair response. (**A**) Representative growth phenotype of 5-day-old *A. thaliana Ler* seedlings grown at normal P_i nutrition (upper panels) and P_i-limiting conditions (lower panels) (P_i concentrations in growth medium are indicated). (**B**) Representative membrane potential traces of *Ler* and *wav5-33* seedlings root hairs, grown under at normal and P_i limited conditions, as indicated by the clour code below the graph. The arrow indicates a 1 s pulse of 0.3 µM IAA. Traces are normalized to the point of 3-IAA application. (**C**) Average P_i-dependent peak depolarization rates of *Ler* and *wav5-33* seedling root hairs, deduced from experiments as shown in (A). The **inset** shows the corresponding averaged membrane potentials of *Ler* and *wav5-33* root hair cells within 5 s before the IAA pulse. Error bars show SE (n=14 (*Ler)* and 9 (*wav5-33*). Asterisks mark significant differences between the groups of measurements (Student's t-test, $p<0.05$). (**D**) Average net H^+ fluxes of the early differentiation zone of *Ler* wild type seedlings. Seedlings were either grown at high P_i conditions (312 µM Pi, black circles/line) or P_i starving conditions (312 nM P_i, red circles/line). The black bar indicates the presence of 10 µM 3-IAA in the bath solution. Curves are interrupted due to 3-IAA application. Error bars show SE (n=18 (300 µM P_i) and 22 (0.3 µM P_i)).

3.2.2. The PAT inhibitor TIBA interferes with the generation of the proton motive force

Auxin-induced responses at the PM may be influenced by efflux of 3-IAA, as suggested by the results with the *pin2* mutant (see **Fig. 3.11**). We therefore tested if the auxin-efflux inhibitors TIBA (Capua and Eshed 2017) or NPA (Cecchetti *et al.* 2017) affected the auxin-induced depolarization of root hairs or H^+ fluxes. To this purpose, *Col-0* seedlings were accustomed to bath solutions containing 20 µM of NPA, which had no effect on the fast root hair depolarization, whereas 20 µM of TIBA strongly reduced this response (**Fig. 3.16A** and **B**). TIBA treated seedlings, however, had a pronounced depolarized resting potential (-109 mV, SE=3 mV; **Fig. 3.16C)**, in comparison to NPA-treated (-163 mV, SE=4 mV) and control seedlings (-170 mV, SE=5 mV).
The impact of TIBA was studied in further detail with *Col-0* seedlings (**Fig. 3.16D**). Shortly after the application of 20 µM TIBA, the PM potential of root hair cells slowly depolarized, with an average amplitude of 23 mV (SE=6 mV), seven minutes after the start of TIBA exposure (**Fig. 3.16D** and **E**). Despite of the TIBA-induced depolarization, root hairs were still responsive to auxin application, although the response tended to be reduced 7 min after start of the exposure (**Fig. 3.16D** and **F**). H^+ flux measurements at the apical root differentiation zone, showed that basal H^+ efflux was absent from TIBA-treated seedling roots (**Fig. 3.16G**). Additionally, pre-incubation with TIBA, prevented the elicitation of any H^+ influx after the application of 10 µM 3-IAA (**Fig. 3.16G** and **H**). The slow TIBA-induced depolarization of root hair cells, together with the reduction of basal H^+ efflux and auxin-induced H^+ influx, suggest that TIBA affects the generation of the pmf as a driving force for auxin uptake possibly through a reduction of H^+-ATPase activity. Interestingly, the 3-IAA analogs 1-NAA and 2-NAA also triggered H^+ influx responses, which were not affected by TIBA treatment (**Fig. 3.16H**). These results strengthen the hypothesis that synthetic auxins are transported by other carriers than AUX1, while AUX1 itself is highly specific for 3-IAA. (**Fig. 3.16H**).

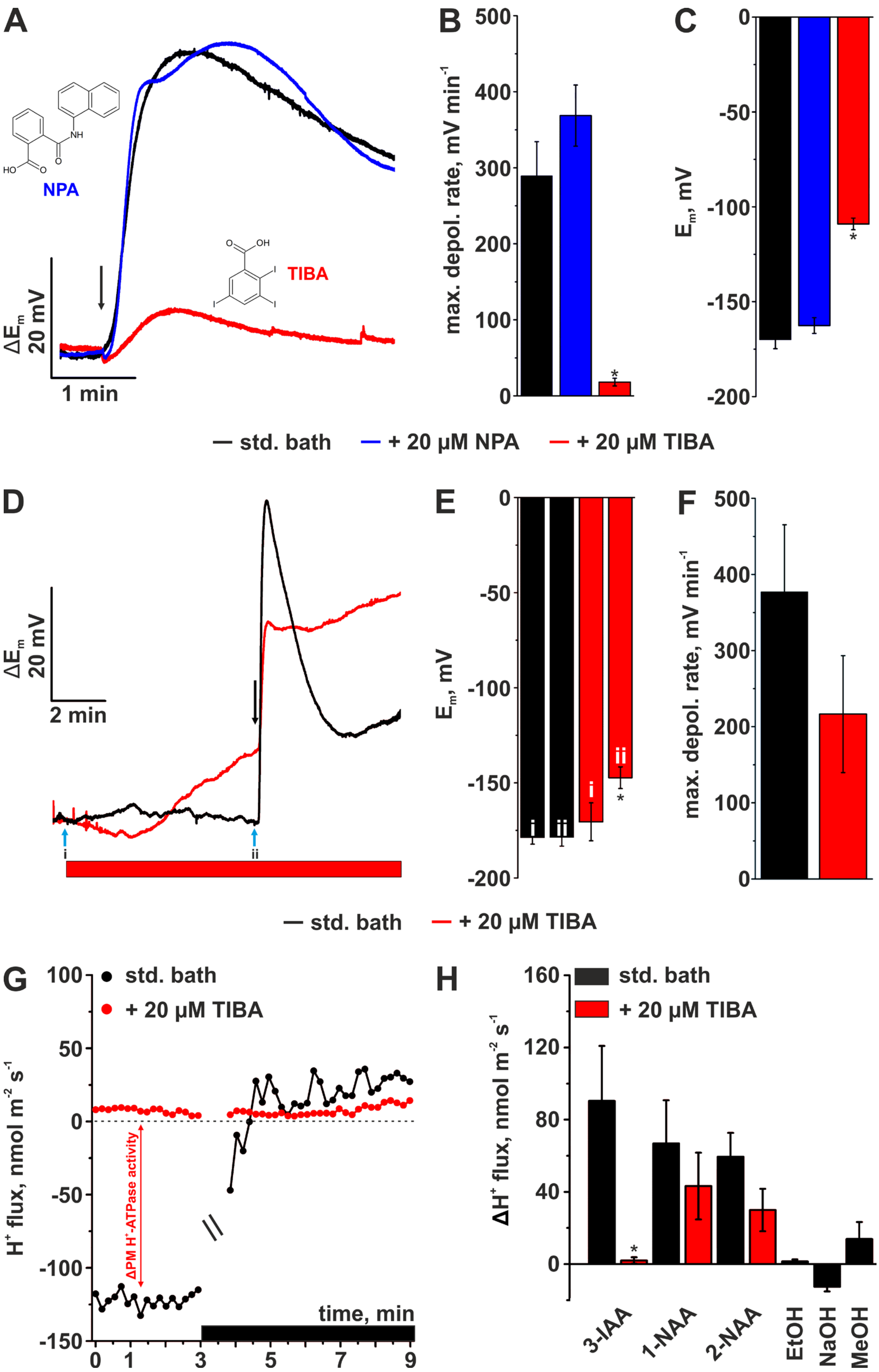
A
NPA
TIBA
ΔEm 20 mV
1 min
B
max. depol. rate, mV min-1
C
Em, mV
— std. bath — + 20 µM NPA — + 20 µM TIBA
D
ΔEm 20 mV
2 min
E
Em, mV
F
max. depol. rate, mV min-1
— std. bath — + 20 µM TIBA
G
std. bath
+ 20 µM TIBA
H+ flux, nmol m-2 s-1
ΔPM H+-ATPase activity
time, min
H
std. bath
+ 20 µM TIBA
ΔH+ flux, nmol m-2 s-1
3-IAA
1-NAA
2-NAA
EtOH
NaOH
MeOH

Fig. 3.16: The auxin efflux inhibitor TIBA reduces the pmf of root cells. (**A**) Representative voltage traces of *Col-0* root hair cells stimulated with a 1 s pulse of 10 µM IAA (arrow). Seedlings were either accustomed to the standard bath solution (black) or accustomed to a bath solution that contains 20 µM NPA (blue, structure on the left), or 20 µM TIBA (red with the chemical structure above the red curve). Traces are normalized to the point of 3-IAA application. (**B**) Average root hair PM potentials 5 s before 3-IAA application from measurements as shown in (A). The same color code as in (A) applies. Error bars show SE (n=13 (std. bath), 8 (NPA) and 5 (TIBA). (**C**) Average maximal depolarization rates in response to IAA application from measurements as shown in (A). The same color code as in (A) applies. Error bars are SE (n is as in (B)). (**D**) Representative voltage traces of *Col-0* root hair cells, perfused with standard bath solution (black) or standard bath solution supplied with 20 µM TIBA (red). The black arrow marks the time point at which a 1 s pulse of 10 µM 3-IAA was applied. The red bar indicates the period at which TIBA containing bath solution was perfused. Blue arrows mark the time points at which the PM potential was determined as shown in (E). Traces are normalized to the indicated point (i). (**E**) Average root hair PM potentials 5 s before application of TIBA containing bath solution (**i**) and 5 s before stimulation with a 3-IAA pulse (**ii**). Values were deduced from experiments as shown in (D). The same color code as in (D) applies. Error bars show SE (n=6). The asterisk marks a significant difference of the PM potential between root hairs exposed to TIBA and control (Student´s t-test, $p<0.05$). (**F**) Average maximal depolarization rates in response to 3-IAA application from measurements as shown in (D). The same color code as in (D) applies. Error bars indicate SE (n is as under (E)). (**G**) Representative H^+ flux recordings at the early differentiation zone of *Col-0* seedling roots. Seedlings were either accustomed to the standard bath solution (black, a single recording from the average response shown **Fig. 3.10**) or to the standard bath solution with 20 µM TIBA (red). The gap marks the disturbance of the measurements due to the application of 3-IAA to a final concentration of 10 µM (black bar). The red arrow indicates the change of PM H^+-ATPase activity due to TIBA treatment. (**H**) Average changes in H^+ fluxes in response to application of 10 µM of 3-IAA (values for 3-IAA w/o TIBA correspond to **Fig. 3.10**), 1-NAA and 2-NAA from measurements as shown in (G). Seedlings were either accustomed to the standard bath solution (black bars), or the standard bath solution with 20 µM TIBA (red bars). Solvent controls were conducted for 3-IAA, 1-NAA and 2-NAA for which 100 mM stock concentrations were dissolved in EtOH, 1 M NaOH and MeOH, respectively. Final concentrations during H^+ flux measurements were 0.01% EtOH, 0.01 % MeOH and 0.1 mM NaOH. Error bars show SE (n=11 (3-IAA w/o TIBA), 10 (1-NAA w/ TIBA), 9 (3-IAA w/ TIBA and 1-NAA w/o TIBA), 7 (2-NAA w/ and w/o TIBA), 4 (EtOH and NaOH) and 3 (MeOH)). The asterisk marks a significant difference between the values of data sets (Student´s t-test, $p<0.05$). Katharina von Meyer provided data from (G) and (H), Research group of Dirk Becker, Molecular plant physiology and biophysics, University of Wuerzburg.

3.2.3. Auxin induces Ca^{2+} signals that depend on the AUX1 transporter, TIR1/AFB-class F-box proteins and the putative Ca^{2+} channel CNGC14

Auxin elicits changes of $[Ca^{2+}]_{cyt}$ in roots of *A. thaliana* (Monshausen *et al.* 2011; Shih *et al.* 2015), but a correlation between the uptake of auxin and cytosolic Ca^{2+} signals has not been documented. The relation between Ca^{2+} signals and auxin transport therefore was studied with simultaneous H^+ and Ca^{2+} flux measurements, as well as with plants that expres the cytosolic Ca^{2+} reporter R-GECO1 (Keinath *et al.* 2015) (see **Fig. 2.9**). Auxin evoked a transient Ca^{2+} influx that occurred right after application of the stimulus, thereafter the Ca^{2+}-uptake decreased, but it remained well above the net efflux of Ca^{2+} before auxin application (**Fig. 3.17A**). In line with the data shown in **Fig. 3.12**, the auxin-induced Ca^{2+} flux was significantly reduced in three out of five *aux1* mutants (**Fig. 3.17B**). The influx of Ca^{2+} is linked to a transient increase of the $[Ca^{2+}]_{cyt}$, which was monitored with the cytosolic Ca^{2+} reporter R-GECO1. Local application of 3-IAA to impaled bulging root hair cells triggered a fast-occurring transient increase of the R-GECO1 fluorescence that is very similar to the response reported by Monshausen *et al*. (2011) and Shih *et al*. (2015) (**Fig. 3.17C** and **D**). The cytosolic Ca^{2+} signal was found to be tightly associated with the auxin-induced depolarization (**Fig. 3.17D, upper panel**). An even more pronounced correlation was found between rate of the voltage and Ca^{2+} signal change (**Fig. 3.17D, lower panel**). This indicates that the cytosolic Ca^{2+} response coincides with H^+-coupled auxin influx through AUX1.

Just as shown for the auxin-induced root hair depolarization, also cytosolic Ca^{2+} signals are modulated in amplitude and slope, depending on the applied 3-IAA concentration or external pH (**Fig. 3.17E** and **F**). The analysis of auxin-induced R-GECO1 signals revealed that a 3-IAA concentration of 1.6 µM (SE=0.9 µM) and pH 5.8 (1.7 µM of $[H^+]$, SE=1.4 µM) led to half maximal Ca^{2+} responses (**insets of Fig. 3.17E** and **F**).

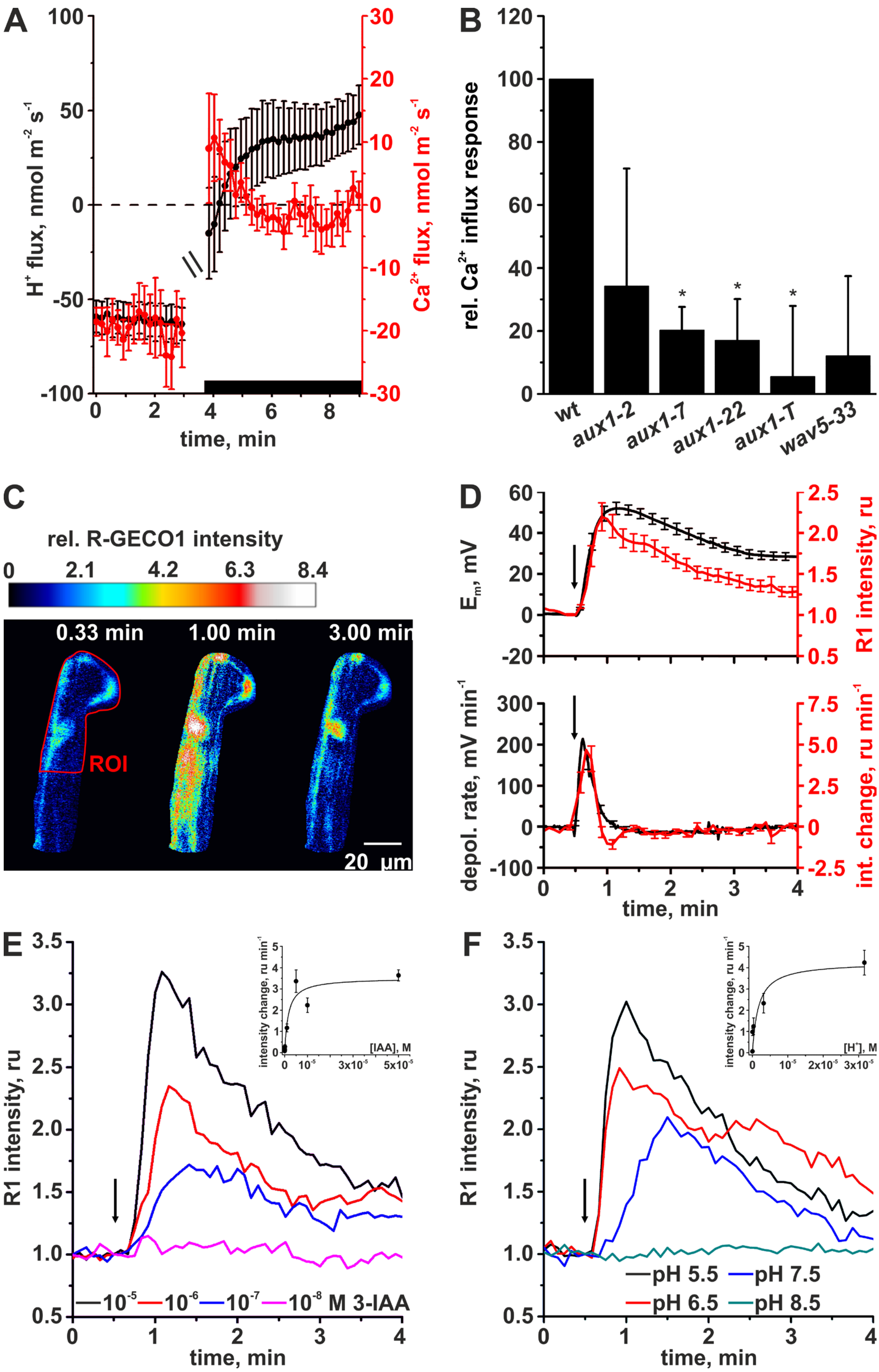

A
H+ flux, nmol m-2 s-1
Ca2+ flux, nmol m-2 s-1
time, min
B
rel. Ca2+ influx response
wt
aux1-2
aux1-7
aux1-22
aux1-T
wav5-33
C
rel. R-GECO1 intensity
0 2.1 4.2 6.3 8.4
0.33 min
1.00 min
3.00 min
ROI
20 µm
D
Em, mV
R1 intensity, ru
depol. rate, mV min-1
int. change, ru min-1
time, min
E
R1 intensity, ru
10-5 10-6 10-7 10-8 M 3-IAA
intensity change, ru min-1
[IAA], M
time, min
F
R1 intensity, ru
pH 5.5 pH 7.5
pH 6.5 pH 8.5
intensity change, ru min-1
[H+], M
time, min

Fig. 3.17: Auxin triggers AUX1-dependent Ca^{2+} influx in root epidermal cells resulting in cytosolic Ca^{2+} signals. (**A**) Average H^{+} (black circles, left axis) and Ca^{2+} fluxes (red circles, right axis) measured simultaneously at the early differentiation zone of *A. thaliana Col-0* seedling roots. The gap marks the disturbance of the measurements due to the application of 3-IAA to a final concentration of 10 µM (black bar). Error bars show SE (n=12). (**B**) Average change of Ca^{2+} fluxes of *aux1* mutants normalized to the response of their respective accessions. Error bars indicate SE (n=12 to 13 (wt) and 12 (*aux1* mutants)). Asterisks mark significant differences to the wild type response (Student's t-test, p<0,05). (**C**) Time series of images of which the colour indicates the R-GECO1 fluorescent intensities, relative to a time point right before auxin application, in a single bulging root hair. From left to right images show the $[Ca^{2+}]_{cyt}$ before, during and after application of a 10 µM 3-IAA pulse. Time points correspond to the time scale of (D). (**D**) **Upper panel:** average traces of the PM potential (black, left axis), which were simultaneously measured with the R-GECO1 intensity (red, right axis) from experiments as shown in (C). Fluorescent intensities were deduced from regions of interest (ROI, red line) as depicted in (C). The arrow marks the time point at which 1 s pulse of 10 µM 3-IAA was applied. Fluorescence values were normalized to the time point right before IAA application Error bars show SE (n=26). **Lower panel**: first derivatives derived from curves shown in the upper panel depicting the time course of the slope of the PM depolarization and $[Ca^{2+}]_{cyt}$ changes. The same color code applies as in the top panel. Error bars show SE. (**E**) Representative recordings of the R-GECO1 fluorescent intensities measured across a root of the early differentiation zone in response to a range of 3-IAA concentrations, as indicated by the different colors. The arrow marks the time point of application of 3-IAA pulses. Fluorescence values were normalized to the time point right before 3-IAA application. The **inset** shows the 3-IAA concentration-dependence of the R-GECO1 signal change fitted with a Michaelis-Menten function. Error bars in the inset show SE (n=7). Measurements were performed in the standard bath solution. (**F**) Representative recordings of the R-GECO1 fluorescent intensities measured across a root section of the early differentiation zone in response to 3-IAA measured in standard bath solutions adjusted to a range of pH values, as indicated by the color code. The arrow marks the time point of a 1 s pulse of 10 µM 3-IAA. Fluorescence values were normalized to the time point right before IAA application. The **inset** shows the pH-dependence of the R-GECO1 signal slope fitted with a Michaelis-Menten function. Error bars in the inset show SE (n=6).

The putative Ca^{2+} channel CNGC14 has been identified as an important mediator for auxin signaling events that are associated with gravitropic root bending (Shih *et al.* 2015). In line with the reported absence of any auxin-induced cytosolic Ca^{2+} signals in roots of the *cngc14* loss-of-function mutant, application of 3-IAA did not trigger the influx of Ca^{2+} into root epidermal cells of this mutant (**Fig. 3.18A**). Moreover, the auxin-induced depolarization was strongly impaired in the *cngc14-2* mutant (**Fig. 3.18B**). This phenotype could be due to transcriptional regulation of *AUX1* and we therefore determined the expression level of *AUX1* in whole seedlings (**Fig. 3.18C**). This revealed that the expression level of *AUX1* was unaffected in the *cngc14* mutant. In addition, the expression of genes coding for F-box proteins in the auxin receptor complex was probed, but also the transcript numbers of *TIR1*, *AFB2 and AFB3* were unaffected by the loss of CNGC14.

Taken together the *cngc14-2* mutant did not provide a tool to separate fast electrical response from the fast elevation of $[Ca^{2+}]_{cyt}$, but supported the close association of $[Ca^{2+}]_{cyt}$ and AUX1 activity, probably through a post-translational regulation of AUX1, with even more evidence.

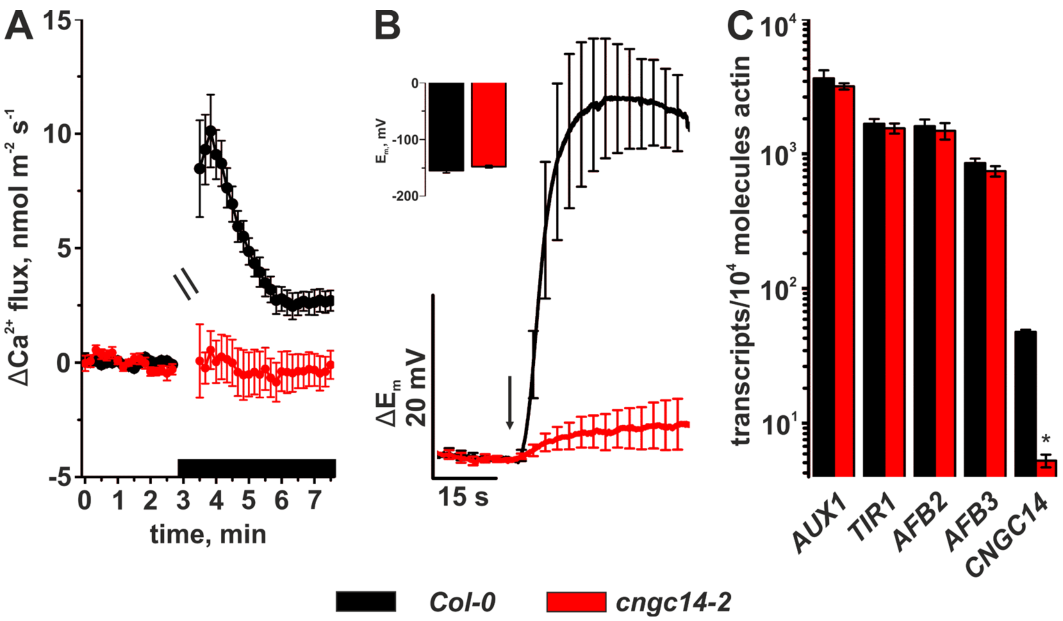

Fig. 3.18: The Ca^{2+} channel CNGC14 is essential for the auxin-induced Ca^{2+} influx and root hair depolarization. (**A**) Average net Ca^{2+} flux measurements at the apical root differentiation zone near bulging root hair cells of *Col-0* (black) and *cngc14-2* (red) seedlings. The black bar indicates the time point of application of 10 µM 3-IAA to the bath solution. Measurements are interrupted because of disturbance of the measurement, due to auxin application. Fluxes were normalized to the values just before IAA application. Error bars show SE, n=10 (*Col-0*) and 11 (*cngc14-2*). (**B**) Average voltage traces of the root hair PM potential of *Col-0* (black) and *cngc14-2* (red) seedlings. Traces were normalized to the time point of 3-IAA application. The arrow marks a 1 s pulse of 10 µM 3-IAA. Error bars show SE, n=6 (*Col-0*) and 7 (*cngc14-2*). **Inset**: Average root hair PM resting potentials 5 s before application of the 3-IAA pulse. Error bars show SE. (**C**) Relative expression levels of *AUX1*, *TIR1*, *AFB2/3* and *CNGC14* in whole *Col-0* (black) and *cngc14-2* (red) seedlings. Error bars show SE (n=5). Heike M. Müller and Pamela Korte (research group of Peter Ache, Molecular plant physiology and biophysics, University of Wuerzburg) provided qPCR data.

The $SCF^{TIR1/AFB}$ auxin receptor complex is known to affect the degradation of transcriptional repressors and thus gene expression, but it is unknown if this receptor complex is important for fast auxin responses that occur within seconds. For this reason, a pharmacological approach was chosen to analyze a potential role of $SCF^{TIR1/AFB}$-mediated auxin perception in the auxin-dependent depolarization of root hair cells, as well as H^+ and Ca^{2+} fluxes. Several substances, which were designed to bind to the auxin receptor and to block the formation of the $SCF^{TIR1/AFB}$-IAA-Aux/IAA interacting complex (Hayashi *et al.* 2012), were tested (**Fig. 3.19A**). In addition, the impact of the benzoic acid derivative p-amino-benzoic acid, (pABA), a putative AUX1 inhibitor was tested. When seedlings were pre-treated with 10 µM of either pABA, PEO-IAA, N-ethoxy-ethyl-PEO-IAA, N-ethyl-PEO-IAA, or 2,4-dimethylphenylethyl-2-oxo-IAA (hereafter auxinole), only auxinole had the ability to inhibit the auxin-induced root hair PM depolarizations, as well as H^+ and Ca^{2+} influx (**Fig. 3.19B** to **E**). Although auxinole repressed the auxin-induced PM responses, no effect on the root hair PM resting potential was observed (**Fig. 3.19E, inset**). Compared to auxinole, PEO-IAA and its derivatives were less effective in inhibiting auxin responses. The latter inhibitors also affected the membrane potential at control conditions, whereas PEO-IAA hyperpolarized the root hair PM potential by -18 mV (SE=3 mV), its derivatives N-ethoxy-ethyl-PEO-IAA and N-ethyl-PEO-IAA depolarized the PM potential by 35 mV (SE=7 mV) and 26 mV (SE=5 mV), respectively. The putative AUX1-inhibitor pABA had no significant impact on the auxin responses.

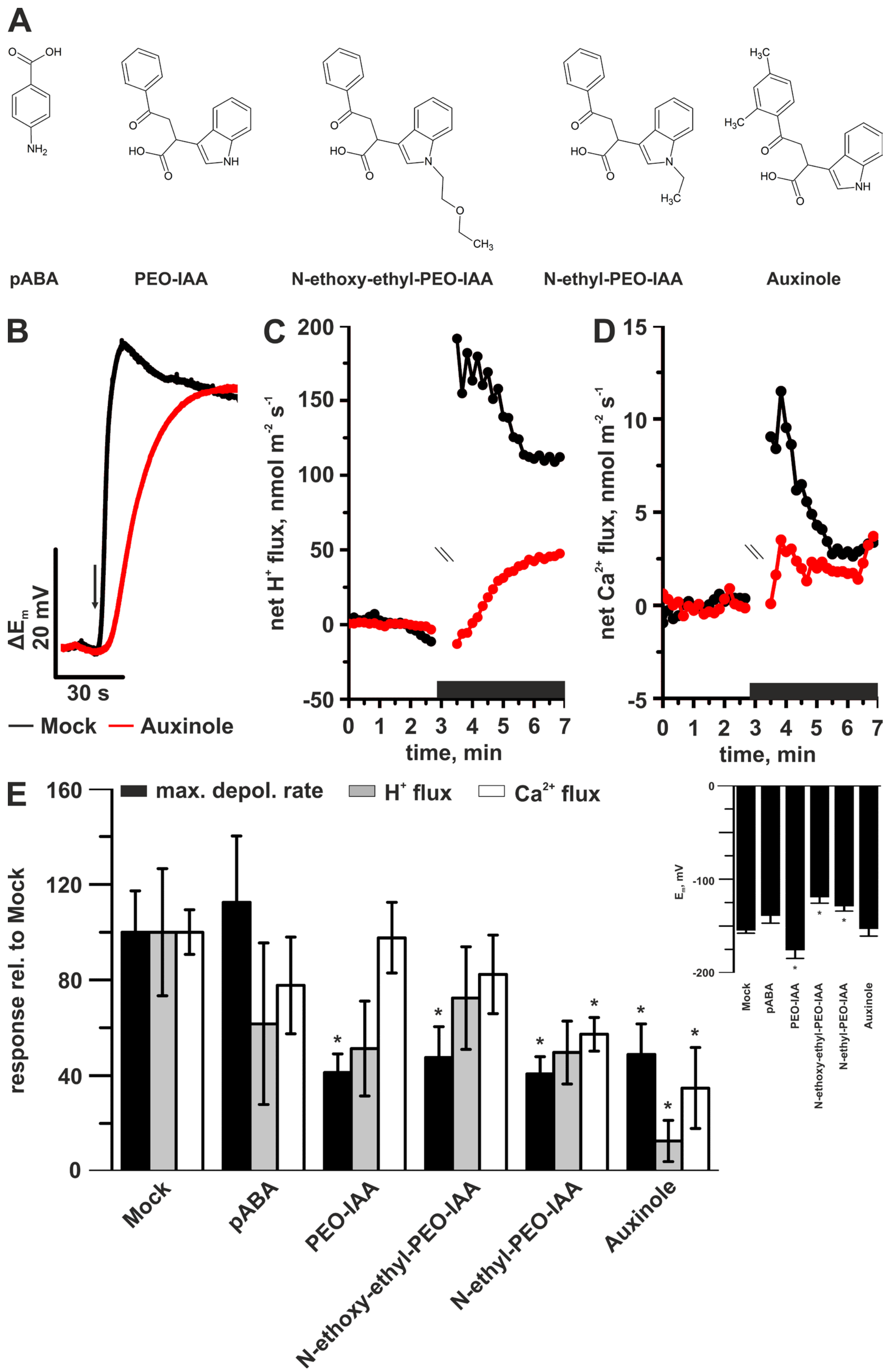
A
pABA
PEO-IAA
N-ethoxy-ethyl-PEO-IAA
N-ethyl-PEO-IAA
Auxinole
B
ΔE_m 20 mV
30 s
Mock
Auxinole
C
net H+ flux, nmol m-2 s-1
time, min
D
net Ca2+ flux, nmol m-2 s-1
time, min
E
max. depol. rate
H+ flux
Ca2+ flux
response rel. to Mock
Mock
pABA
PEO-IAA
N-ethoxy-ethyl-PEO-IAA
N-ethyl-PEO-IAA
Auxinole
E_m, mV

Fig. 3.19: Auxinole is a potent inhibitor of auxin-induced PM-responses. (**A**) Structures of AUX1 (pABA) and TIR1-inhibitors. (**B**) Representative voltage traces of the *Col-0* root hair PM in response to a 1 s pulse of 10 µM 3-IAA (arrow) in the absence (mock (0.02% DMSO), black trace) or presence (red trace) of 10 µM auxinole. (**C**) Representative net H^+ flux measurements in response to application of 10 µM 3-IAA (indicated by horizontal black bar) in the absence (mock, black trace) or presence (red trace) of 10 µM auxinole. Measurements are interrupted after application of 3-IAA. (**D**) Representative net Ca^{2+} flux measurements in response to application of 10 µM 3-IAA (black bar) in the absence (mock, black trace) or presence (red trace) of 10 µM auxinole. Measurements are interrupted due to application of 3-IAA. (**E**) Average values of the maximal depolarization rate (black bars) and initial changes in H^+ (gray bars) and Ca^{2+} (white bars) fluxes in response to TIR1-inhibitors. Error bars show SE (n=7 to 14). Asterisks mark significant differences to mock treatment (Student's t-test, p<0.05). The **inset** shows average root hair PM potentials 5 s prior to the 3-IAA pulse. Error bars show SE (n=7 to 14). Asterisks mark significant differences to mock treatment (Student's t-test, p<0.05).

Despite of the clear impact of auxinole on auxin-induced PM responses, a residual response was still found at a concentration of 10 µM (see **Fig.3.19**). The concentration of auxinole was therefore increased to 20 µM, which caused a block of the 3-IAA-induced $[Ca^{2+}]_{cyt}$ elevations in bulging root hair cells, as well as a further reduction of the auxin-induced depolarization (**Fig. 3.20A** and **B**). In comparison, treatment with the auxin efflux inhibitor TIBA also reduced the auxin-induced depolarization but did not block the auxin-induced $[Ca^{2+}]_{cyt}$ elevation to the same extent as auxinole (**Fig. 3.20A** and **B**). Both TIBA and auxinole, at concentrations of 20 µM, depolarized the root hair PM resting potential (**Fig. 3.20A** and **C**). Whereas TIBA depolarized the root hairs cells on average by 67 mV (SE=2 mV), auxinole only caused a change of 30 mV (SE=3 mV). Apparently, the tested PEO-IAA derivatives all have the ability to depolarize the PM potential of root hair cells.

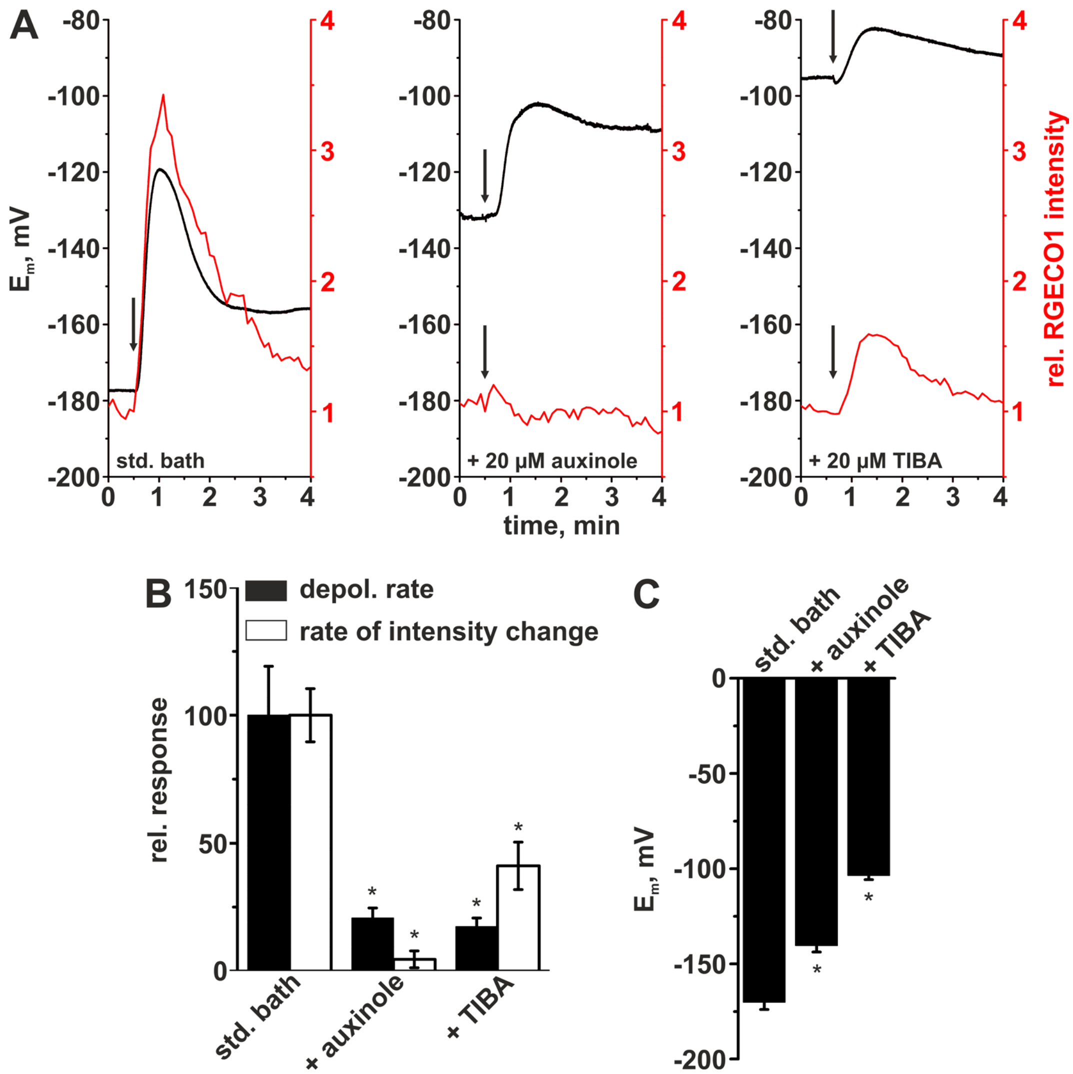

Fig. 3.20: The SCF$^{TIR1/AFB}$-inhibitor auxinole and the auxin-efflux inhibitor TIBA inhibit auxin-induced PM responses. (**A**) Representative simultaneous recordings of the PM potential (black, left axis) and the cytosolic R-GECO1 intensity of an impaled root hair cell (red, right axis), measured in standard bath solution (left panel), standard bath solution supplied with 20 µM auxinole (middle panel) and standard bath solution supplied with 20 µM TIBA (right panel). The arrows mark a 1 s pulse of 10 µM 3-IAA. Fluorescence values were normalized (fluorescence intensity = 1), to the value 5 s before IAA application. (**B**) Average depolarization rates (black bars) and rates of R-GECO1 intensity change (white bars) deduced from measurements as shown in (A). Values were normalized to experiments performed in the standard bath solution. Error bars show SE (n=10 (std. bath), 11 (auxinole) and 9 (TIBA)). Asterisks mark significant changes to control conditions (Student's t-test, $p<0.05$). (**C**) Average resting PM potentials of root hair cells 5 s before the 3-IAA pulse. Values are deduced from measurements as shown in (A). Error bars indicate SE (n as under (B)). Asterisks mark significant changes to control conditions (Student's t-test, $p<0.05$).

As auxins other than 3-IAA can elicit PM potential responses (see **Fig. 3.13** and **3.16**), it was tempting to speculate that these auxins may differ in their ability to evoke Ca^{2+} signals. 5F-IAA, 1-NAA, and the inactive 2-NAA were therefore compared to 3-IAA for their ability to trigger $[Ca^{2+}]_{cyt}$ elevations in root hair cells. In addition to measurements in standard bath solution at pH 5.5, experiments were also performed at an external pH of 7.5. The physiological active auxins 5F-IAA and 1-NAA triggered cytosolic Ca^{2+} signals similar to those induced by 3-IAA, although they had less effect on the PM potential (**Fig. 3.21A** and **B**). Provided that the auxin-induced PM depolarization correlates with auxin transport, Ca^{2+} signals thus are not closely related to the auxin uptake rate. As expected, the physiologically inactive 2-NAA hardly affected the $[Ca^{2+}]_{cyt}$ level and the PM potential. A trait common to all auxins tested is the pH-dependence of both the root hair depolarization and the increase in $[Ca^{2+}]_{cyt}$. At an external pH of 7.5 the auxin-induced root hair depolarizations, as well as $[Ca^{2+}]_{cyt}$ elevations were both found to be heavily reduced for all auxins tested (**Fig. 3.21A** and **B**), although the higher pH hyperpolarized root hair cells in comparison to an external pH of 5.5 (**Fig. 3.21B inset**, compare to **Fig. 3.9C inset**).

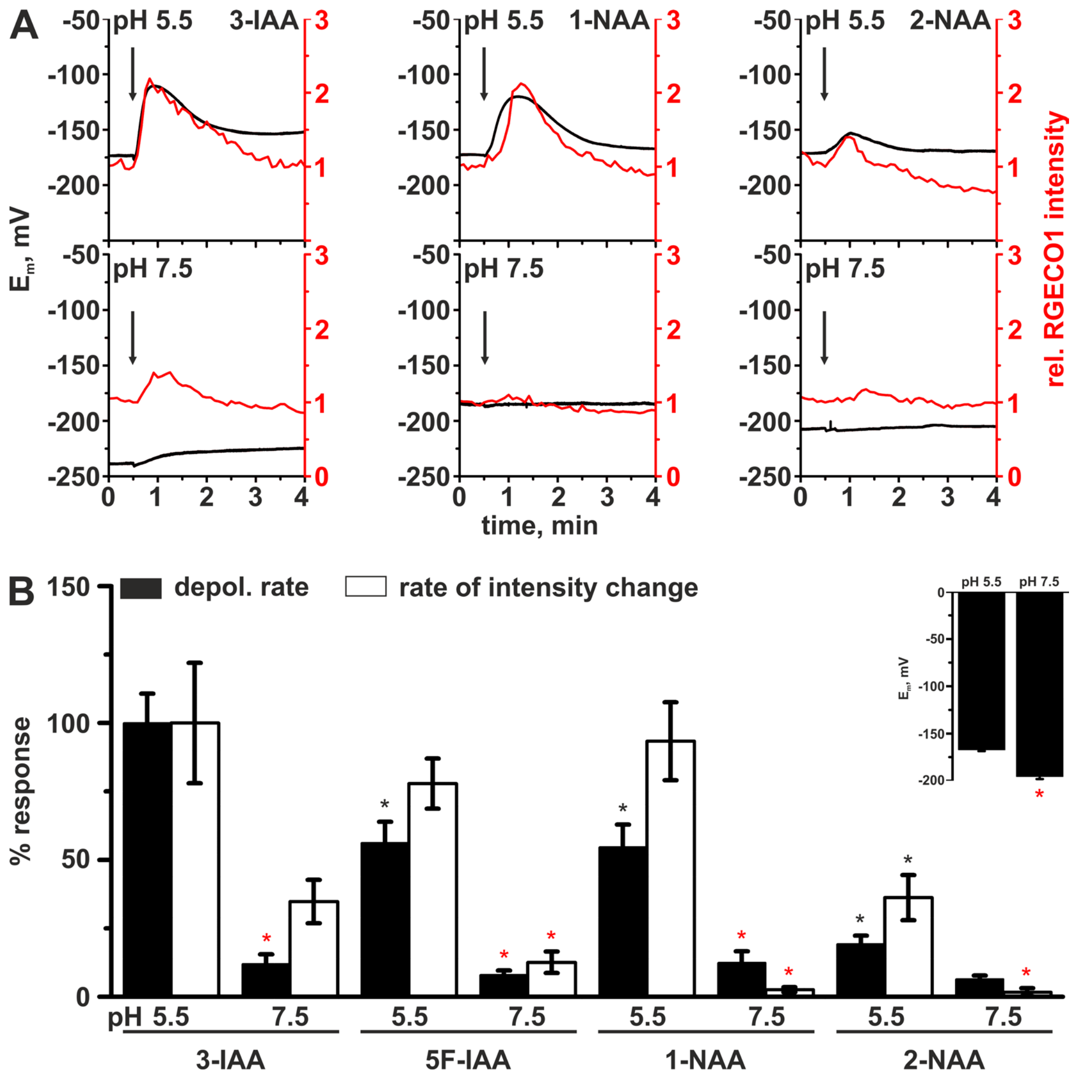

Fig. 3.21: Physiological active auxins induce $[Ca^{2+}]_{cyt}$ elevations. (**A**) Representative simultaneous recordings of the PM potential (black, left axis) and the cytosolic R-GECO1 intensity of impaled root hair cells (red, right axis) in response to stimulation with 3-IAA (left panel), 1-NAA (middle panel) and 2-NAA (right panel). Responses to all auxins were measured at external pH values of 5.5 (upper graphs) and 7.5 (lower graphs). The arrows mark the time point at which a 1 s pulse of 10 µM of the auxin was applied. Fluorescence values were normalized (fluorescence intensity = 1) to the values measured just before IAA application. (**B**) Average depolarization rates (black bars) and rates of R-GECO1 intensity change (white bars) deduced from measurements as shown in (A). Values are given relative to 3-IAA at pH 5.5. Error bars indicate SE (n=16, pH 5.5) and (n=8, pH 7.5)). The **inset** shows average resting PM potentials of root hair cells at external pH values of 5.5 and 7.5, the values were determined 5 s before application of auxins. Error bars indicate SE (n=64, pH 5.5) and (n=32, pH 7.5). Asterisks mark significant differences compared to 3-IAA (black asterisks) or compared to pH 5.5 of the same auxin (red asterisks, Student's t-test, p<0.05).

Auxinole inhibits PM responses to 3-IAA, suggesting that the SCF$^{TIR1/AFB}$ auxin receptor complex is important for these responses. However, because of potential side effects of auxinole (see **Fig. 3.20**), it was important to back up these data with genetic evidence. The *tir1-1* single loss-of-function mutant (Ruegger *et al.* 1998), as well as the *tir1-1afb2-3afb3-4* triple mutant line (Parry *et al.* 2009) were tested for auxin-induced PM responses (**Fig. 3.22**). Experiments in which the auxin-induced root hair PM potential depolarization, as well as the H^+ influx response, were tested (**Fig. 3.22A, C,** and **E**) revealed the combined loss of TIR1, AFB2, and AFB3 but not of TIR1 alone to be sufficient for mimicking the auxinole-induced loss of AUX1 activity. However, it should be noted that the depolarization-response of the triple mutant varied from completely unresponsive to a rather strong response (**Fig. 3.22A, inset**). These varying responses are, however, in line with the reported root growth phenotype of this line that shows variations from an aborted growth after germination to rather wild type-like root growth (Parry *et al.* 2009). Further, root hair cells of the triple mutant did not show the reduced resting potential as auxinole treated wild type cells did (**Fig. 3.22B**), thus again highlighting the unspecific side-effect caused by auxinole treatment.
In the absence of a genetically encoded $[Ca^{2+}]_{cyt}$ sensor in the F-box loss-of-function mutant lines auxin-induced Ca^{2+} fluxes into root epidermal cells were observed with scanning ion selective microelectrodes. Like the treatment with auxinole, the combined absence of the three F-box proteins TIR1, AFB2 and AFB3 again resulted in the loss of the initial CNGC14-mediated Ca^{2+} influx response (**Fig. 3.22D** and **E**). Again, the loss of TIR1 alone turned out to be insufficient for a significant reduction of the initial response. The apparent absence of auxin-induced Ca^{2+} influxes thus underpins the necessity of a functional F-box protein-mediated auxin perception for the fast activation of Ca^{2+} influx with genetic evidence. The observed auxin-insensitivities of the auxin-perception mutant could be due to an altered expression of *AUX1* and/or *CNGC14*. However, real time PCR studies showed that *AUX1* and *CNGC14* expression is unaltered in the receptor mutant lines, as well as in auxinole treated wild type seedlings (**Fig. 3.22F**). Please note that *tir1-1* is an EMS generated point mutant and that the expression of the mutated *TIR1* transcript can be detected in the mutant lines (Ruegger *et al.* 1998; Parry *et al.* 2009).

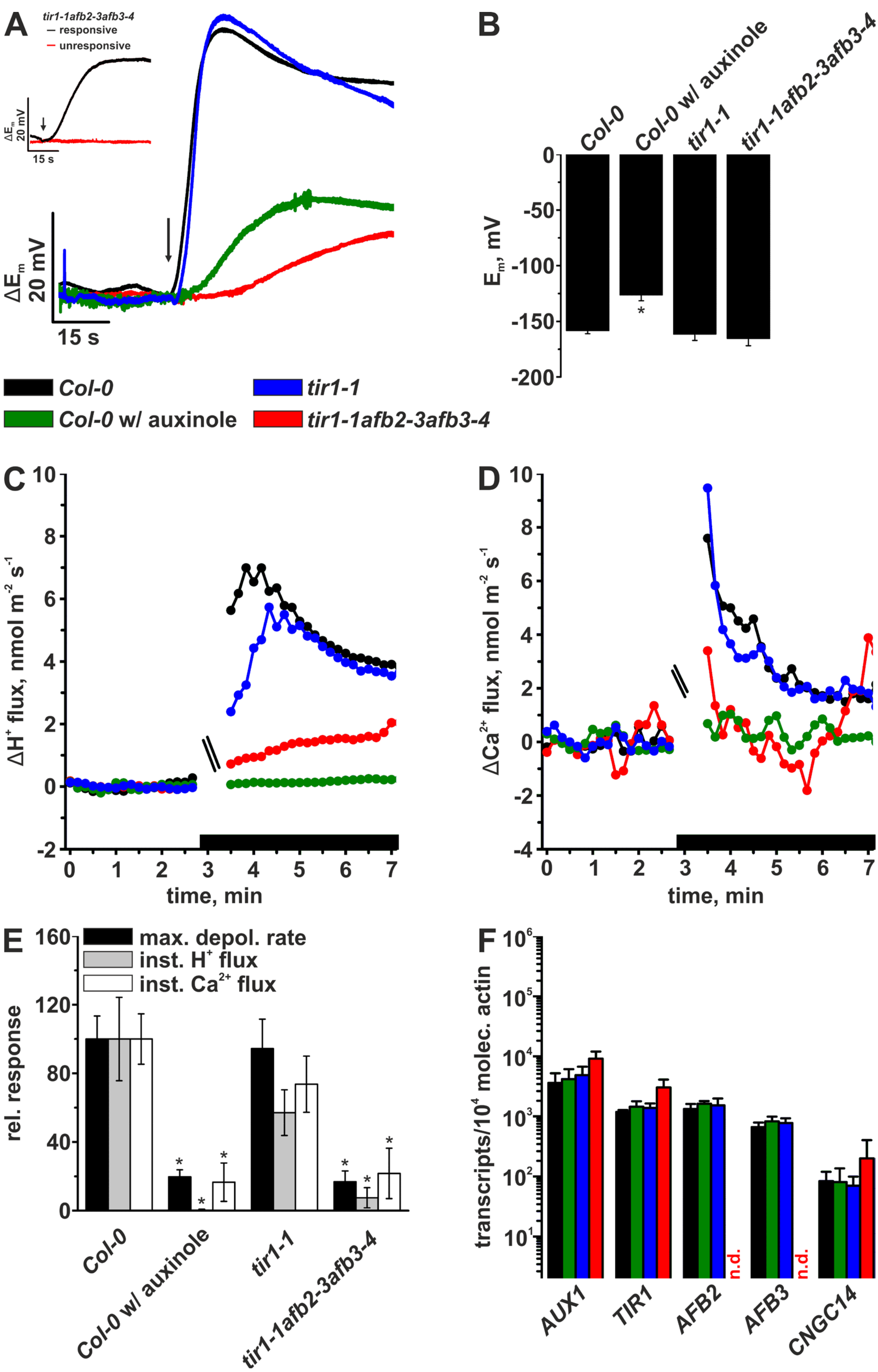
A
tir1-1afb2-3afb3-4
responsive
unresponsive
ΔEm 20 mV
15 s
B
Col-0
Col-0 w/ auxinole
tir1-1
tir1-1afb2-3afb3-4
Em, mV
0
-50
-100
-150
-200
Col-0
tir1-1
Col-0 w/ auxinole
tir1-1afb2-3afb3-4
C
ΔH+ flux, nmol m-2 s-1
time, min
D
ΔCa2+ flux, nmol m-2 s-1
time, min
E
max. depol. rate
inst. H+ flux
inst. Ca2+ flux
rel. response
Col-0
Col-0 w/ auxinole
tir1-1
tir1-1afb2-3afb3-4
F
transcripts/10^4 molec. actin
n.d.
n.d.
AUX1
TIR1
AFB2
AFB3
CNGC14

Fig. 3.22: The auxin receptor complex SCF$^{TIR1/AFB}$ is a mediator of AUX1 activity and auxin-induced Ca^{2+} influx. (**A**) Representative voltage traces of the root hair PM potential of *Col-0* in the absence (black trace) or presence (green trace) of 20 µM auxinole, the *tir1-1* (blue trace) and *tir1-1afb2-3afb3-4* (red trace) loss-of-function mutants in response to a 1 s pulse of 10 µM 3-IAA (arrow). Traces are normalized to the values measured just before 3-IAA application. The **inset** shows voltage traces of the *tir1-1afb2-3afb3-4* mutant that are exemplary for a seedling that responded (black trace) and one that did not (red trace). (**B**) Average PM potential from experiments shown in (A) measured 5 s before application of the 3-IAA pulse. Error bars show SE (n=14, *Col-0*; n=6, *Col-0* with auxinole; n= 8, *tir1-1*; n=6, *tir1-1afb2-3afb3-4*). The asterisk marks a significant difference in comparison with *Col-0* (Student's t-test, $p<0.05$). (**C** and **D**) Representative net H^+ (C) and Ca^{2+} (D) fluxes in the early root differentiation zone of *Col-0* in the absence, or presence, of 20 µM auxinole, as well as of the *tir1-1* and *tir1-1afb2-3afb3-4* loss-of-function mutants evoked by application of 3-IAA. The same color code as in (A) applies. The horizontal black bar marks the presence 10 µM 3-IAA in the bath solution. Graphs are interrupted after the time point of application of 3-IAA. Fluxes are normalized to the values just before 3-IAA application. (**E**) Quantification of the auxin-induced PM responses. Shown are average values of the maximal depolarization rates (black bars), as well as the change in H^+ fluxes (gray bars) and Ca^{2+} fluxes (white bars). Error bars show SE of *Col-0*, n=14 and 10, for depolarization and ion fluxes, respectively; *Col-0* with auxinole, n=6 and 10 for depolarization and ion fluxes, respectively; *tir1-1*, n=8 and 16, for depolarization ion fluxes, respectively; *tir1-1afb2-3afb3-4*, n=6 and 9 for depolarization ion fluxes, respectively. Asterisks mark significant differences to Col-0 in the absence of auxinole (Student's t-test, $p<0.05$). (**F**) Relative expression levels of *AUX1*, *TIR1*, *AFB2/3* and *CNGC14* in whole seedlings. The same color code as shown in (A) applies. Error bars show SD (n=4 (*Col-0, tir1-1, tir1-1afb2-3afb3-4*) and 3 (*Col-0* w/ auxinole)). Transcript levels marked with n.d. were below the detection limit. qPCR data were provided by Heike M. Müller, Research group of Peter Ache, Molecular plant physiology and biophysics, University of Wuerzburg. Ion flux data were provided by Dr. Sönke Scherzer, Molecular plant physiology and biophysics, University of Wuerzburg.

The apparent reduction or absence of AUX1-mediated H^+-coupled auxin influx in root hair cells of plants either lacking the F-box proteins needed for auxin perception or the channel necessary for auxin-induced Ca^{2+} influx prompted the idea that $[Ca^{2+}]_{cyt}$ feeds back into AUX1 activity. To gain further insights into the propagation of auxin-induced cytosolic Ca^{2+} signals, we studied Ca^{2+} signals in root tips with plants expression R-GECO1. In these experiments, the cytosol of single root hair cells was iontophoretically stimulated with the hormone. The first barrel of double-barrelled microelectrodes was tip-filled with the injection mixture containing auxin and the fluorescent dye LY as a loading control, while the second barrel served as the voltage recording electrode (**Fig. 3.23A).**

This experimental approach offered the possibility to stimulate a single cell, while propagation of the Ca^{2+} signal could be monitored in the root tissue. The cytosolic injection of 3-IAA with an electrical current of -1 nA, applied for one minute, was reported by LY appearing at cytosol rich regions like the root hair tip and around the nucleus as well as at the rim of the cell (**Fig. 3.23B**). Cytosolic stimulation with 3-IAA lead to the immediate induction of a local $[Ca^{2+}]_{cyt}$ elevation in the injected root hair cells (**Fig. 3.23B** and **C**). Those Ca^{2+} signals were not restricted to the site of auxin stimulation but rather propagated with 5 mm/h (SE=0.8 mm/h) towards the opposite lateral root side. During propagation, the Ca^{2+} signal was enhanced, since its amplitude was higher on the opposite site of the root, as in the stimulated root hair cells (**Fig. 3.23B** and **C**). Simultaneous to the Ca^{2+} wave, injection of 3-IAA induced a slow and transient depolarization of the injected root hair cell which reached an average maximal amplitude of 18 mV (SE=2 mV, **Fig. 3.23C** and **D**). This response differs from that triggered by externally applied auxin with regard to the velocity of the voltage change as well as with regard to the maximal amplitudes (compare to **Fig. 3.8**). The depolarization as well as the lateral moving Ca^{2+} wave evoked by intracellular injection of 3-IAA were inhibited in seedlings pre-treated with auxinole (**Fig. 3.23C** to **E**). Moreover, injection of the inactive 2-NAA did neither cause a slow root hair PM depolarization, nor a $[Ca^{2+}]_{cyt}$ response (**Fig. 3.23C** to **E**), suggeting that the relatively slow depolarizaton induced by injection of auxin requires a functional auxin perception module.

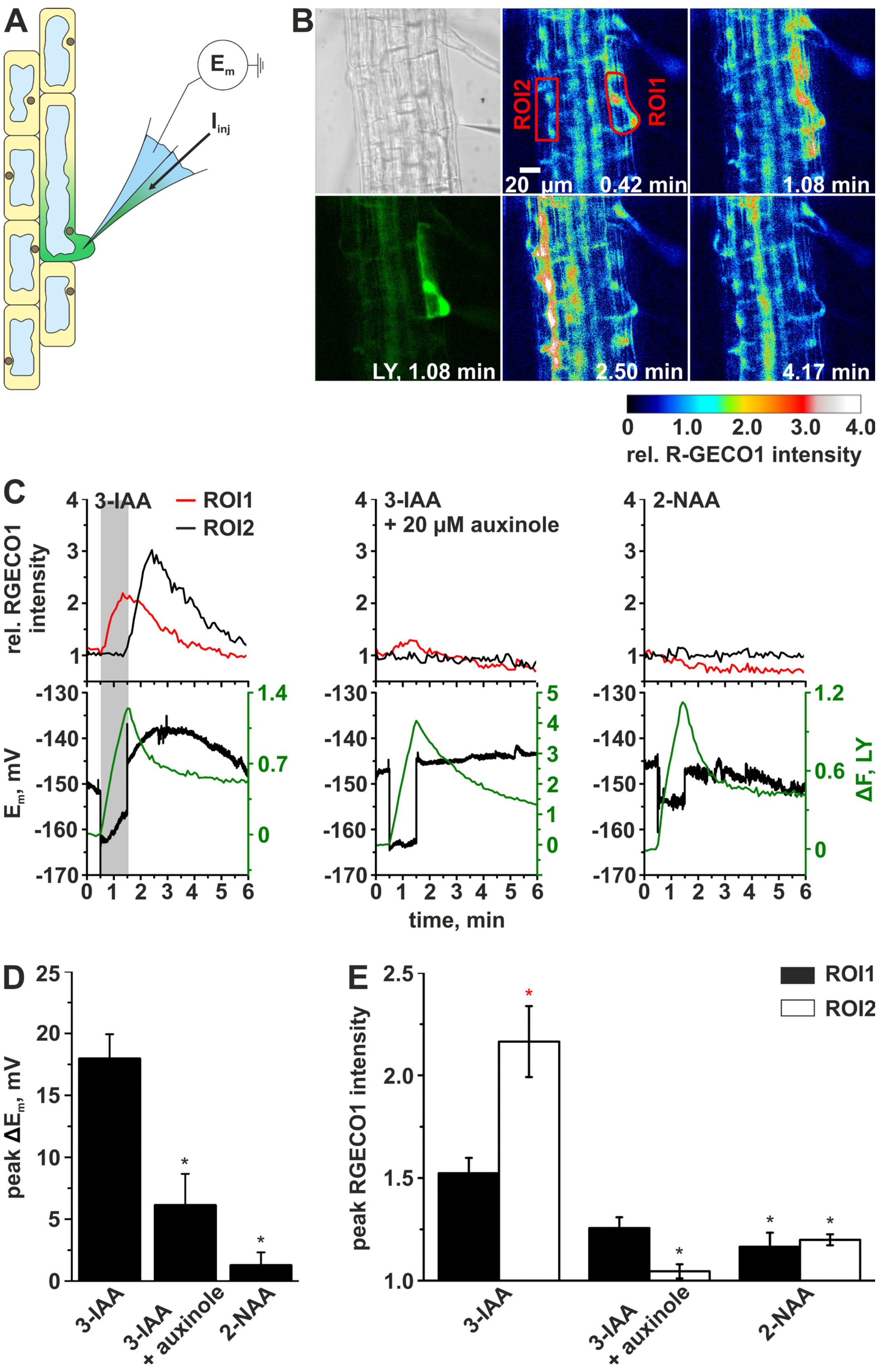
A
Em
Iinj
B
ROI2
ROI1
20 µm
0.42 min
1.08 min
LY, 1.08 min
2.50 min
4.17 min
0 1.0 2.0 3.0 4.0
rel. R-GECO1 intensity
C
3-IAA
ROI1
ROI2
rel. RGECO1 intensity
3-IAA + 20 µM auxinole
2-NAA
Em, mV
ΔF, LY
time, min
D
peak ΔEm, mV
3-IAA
3-IAA + auxinole
2-NAA
E
peak RGECO1 intensity
ROI1
ROI2
3-IAA
3-IAA + auxinole
2-NAA

Fig. 3.23: Cytosolic injection of 3-IAA into single bulging root hair cells induces propagating Ca^{2+} waves. (**A**) Cartoon illustrating iontophoretic auxin injection into the cytosol of a bulging root hair cell with the simultaneous recording of the PM potential via double-barrelled microelectrodes. (**B**) Imaging of $[Ca^{2+}]_{cyt}$ in R-GECO1 expressing seedling roots in response to cytosolic 3-IAA injection. **Upper left panel**: brightfield image of an *A. thaliana* seedling root with a bulging root hair impaled by a microelectrode. **Lower left panel**: Cytosolic localization of the iontophoretically injected dye LY. **Middle and right panels**: False coloured images, indicating the R-GECO1 fluorescent intensity. 3-IAA was injected with a current of -1 nA, in the period of t=30 to 90 s, into the root hair of ROI1 (compare to LY distribution, lower left panel). The colour code indicates the R-GECO1 intensity relative to a time point before auxin injection as shown in the calibration bar below the panels. Time points correspond to the time scale of (C). (**C**) Representative measurements of iontophoretic injection of auxin into bulging root hair cells. From left to right panels show data for 3-IAA injection in seedling roots kept in standard bath solution, 3-IAA injection in roots pre-treated with bath solution supplemented with 20 µM auxinole and injection of the physiological inactive 2-NAA. **Lower graphs:** the response of the PM potential (black line, left axis) to auxin injection together with the fluorescence intensity of the control dye LY (green line, right axis). Note the relaxation of LY fluorescence after the end of injection due to the translocation of the dye into the vacuolar lumen. **Upper graphs:** corresponding response of the R-GECO1 fluorescence intensities of ROI1 (red line) and ROI2 (black line) as indicated in (B). Intensities were normalized to the time point before the start of injection (equal to 1.0). The gray bar in the first panel indicates the period of auxin injection, which is the same in all three panels observable by the voltage jump to hyperpolarized potentials. (**D**) Average maximal depolarization of root hair cells, in response to cytosolic auxin injection. Error bars show SE (n=20 for 3-IAA, n=6 for 3-IAA in the presence of auxinole, n=11 for injection of 2-NAA). Asterisk mark significant differences compared to 3-IAA (Student's t-test, $p<0.05$). (**E**) Average maximal change of the R-GECO1 fluorescence intensities of ROI1 (black bars) and ROI2 (white bars), relative to the time point before the start of auxin injection (equal to 1.0). Error bars show SE (n is as under (D)). Asterisks mark significant differences (Student's t-test, $p<0.05$) between ROI1 and ROI2 in the case of 3-IAA (red asterisk) as well as in comparison to the respective ROI of experiments with 3-IAA (black asterisks).

Intracellular injection of auxin into single root hair cells triggered a slow depolarization and Ca^{2+} signals that were apparently $SCF^{TIR1/AFB}$-dependent. Since CNGC14 mediates Ca^{2+} influx in response to external auxin application, it was tested if the responses to a cytosolic auxin application require the putative Ca^{2+} channel CNGC14 as well. For this purpose, 3-IAA was iontophoretically loaded into root hair cells of wild type and *cngc14-2* seedlings (**Fig. 3.24**). Wild type root hairs showed an average maximal depolarization amplitude of the PM potential of 19 mV (SE=4 mV) in response to cytosolic application of 3-IAA, while root hairs of *cngc14-2* showed no depolarization. Hence, the putative Ca^{2+}-permeable channel CNGC14 is apparently required for the auxinole-sensitive responses to cytosolically applied 3-IAA.

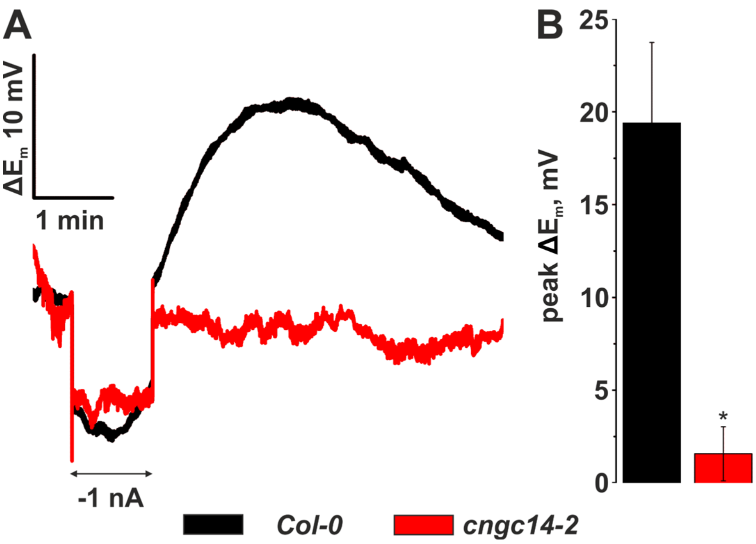

Fig. 3.24: CNGC14 is responsible for the Ca^{2+} influx in response to cytosolic auxin application. (**A**) Representative voltage traces of the root hair PM potential of *Col-0* (black) and *cngc14-2* (red) seedlings in response to iontophoretic loading of 3-IAA into the cytosol. Traces were normalized to values measured right before the start of 3-IAA injection. The double headed arrow marks the time frame of cytosolic loading of 3-IAA with a current of -1 nA. (**B**) Average peak PM potential depolarization caused by iontophoretic 3-IAA loading into root hair cells of *Col-0* (black) and *cngc14-2* (red) seedlings. Values were obtained from measurement as shown in (A). Error bars show SE (n= 7). The asterisk marks a significant difference (Student's t-test, $p<0.05$).

Since the loss of auxin and Ca^{2+} influx activity in the *cngc14-2* mutant led to the hypothesis that auxin-induced cytosolic Ca^{2+} signals feed back into AUX1 activity (see **Fig. 3.18**) a closer look at this relationship became necessary. Shih *et al.* (2015) showed that the broad range Ca^{2+} channel blocker Lanthanum (La^{3+}) causes an auxin-insensitive primary root growth phenotype, similar as observed in *cngc14* mutants. La^{3+} was therefore used to inhibit the auxin-induced responses of root hairs. A range of La^{3+} concentrations was tested to find the minimal concentration that inhibits the auxin-induced depolarization (**Fig. 3.25A** to **C**). The treatment with La^{3+}, three minutes before stimulation with a 1 µM 3-IAA pulse, did not inhibit the depolarization of root hair cells (**Fig. 3.25A** and **B**). However, a consecutive 3-IAA pulse, which was applied after La^{3+} had been washed out, was strongly reduced after pre-treatment with 64 µM or 128 µM La^{3+}, respectively (**Fig. 3.25A** and **B**). Please note, that the pre-treatment with La^{3+}, at concentrations up to 128 µM, imposed no effect on the root hair PM potential (**Fig. 3.25C**). As depicted in **Fig. 3.25D** and **E** external application of 64 µM La^{3+} gradually blocked the AUX1-dependent fast root hair PM potential depolarization reaching an effective block after nine minutes into La^{3+} exposure.

La^{3+} thus clearly inhibits the auxin-induced depolarization of roots hairs, but only after cells have been exposed to the inhibitor for more than 5 min. These results raised the question, how La^{3+} affects the cytosolic Ca^{2+} concentration of root hair cells. Therefore the auxin-induced elevations of $[Ca^{2+}]_{cyt}$ in roots of R-GECO1 expressing seedlings were probed (**Fig. 3.25F**). In accordance with the observations for the PM potential, a first auxin stimulation was observed to be La^{3+} insensitive, while a second 3-IAA pulse triggered a strongly reduced $[Ca^{2+}]_{cyt}$ elevation after the root hair cells were treated with 128 µM La^{3+}. In cases seedlings were exposed to 128 µM La^{3+}, $[Ca^{2+}]_{cyt}$ failed to return to low basal levels after the first auxin-induced elevation, thus indicating a severe effect of La^{3+} on cytosolic Ca^{2+} homeostasis.

These experiments revealed a short-term effect of La^{3+} which supports the hypothesis of a Ca^{2+}-dependent post-translational regulation of AUX1. A possible explanation for the effect that only the second auxin stimulus turned out to be La^{3+}-sensitive could be an open channel block of CNGC14 by La^{3+}, which is either achieved by an initial forced channel activation through auxin application or, in the case of the time-dependent block, through stochastic channel activation events and its effect on Ca^{2+}-homeostasis. The apparent effect La^{3+} has on $[Ca^{2+}]_{cyt}$ homeostasis might point towards La^{3+} entering the cells and affecting the activities of Ca^{2+}-ATPase and H^+/Ca^{2+} exchangers, which are discussed to be involved in maintaining low basal $[Ca^{2+}]_{cyt}$ (Roelfsema and Hedrich 2010; Schönknecht 2013).

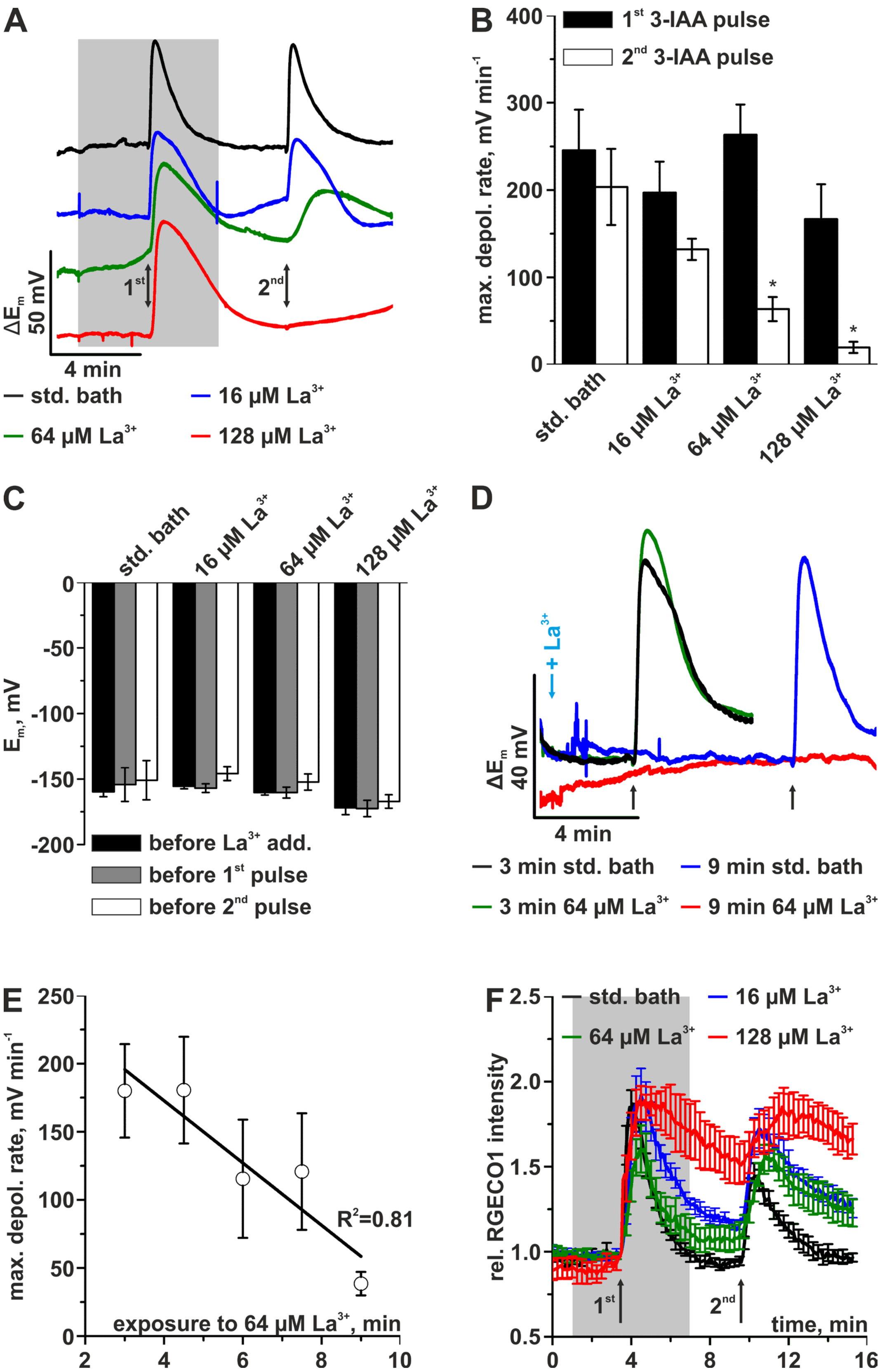
A
1st
2nd
ΔEm 50 mV
4 min
std. bath
16 µM La3+
64 µM La3+
128 µM La3+
B
1st 3-IAA pulse
2nd 3-IAA pulse
max. depol. rate, mV min-1
400
300
200
100
0
*
*
std. bath
16 µM La3+
64 µM La3+
128 µM La3+
C
std. bath
16 µM La3+
64 µM La3+
128 µM La3+
Em, mV
0
-50
-100
-150
-200
before La3+ add.
before 1st pulse
before 2nd pulse
D
+ La3+
ΔEm 40 mV
4 min
3 min std. bath
9 min std. bath
3 min 64 µM La3+
9 min 64 µM La3+
E
max. depol. rate, mV min-1
250
200
150
100
50
0
R2=0.81
exposure to 64 µM La3+, min
2
4
6
8
10
F
std. bath
16 µM La3+
64 µM La3+
128 µM La3+
rel. RGECO1 intensity
2.5
2.0
1.5
1.0
0.5
1st
2nd
time, min
0
4
8
12
16

Fig. 3.25: Treatment with La^{3+} mimics the auxin-insensitive phenotype of the *cngc14-2* mutant. (**A**) Representative voltage traces of the root hair PM potential of seedlings exposed to 16 µM (blue trace), 64 µM (green trace), 128 µM (red trace) La^{3+} and in the absence of this Ca^{2+} channel blocker (black trace, see **Fig. 3.8C**). The bath solution was constantly perfused during measurements. The gray box below the graph indicates exposure to the La^{3+} containing solutions. 3-IAA was applied in two consecutive 1 s pulses of 1 µM, with an application pipette (double-headed arrows). Traces are displayed on top of each other for clarity. (**B**) Average maximal depolarization rates determined for the first (closed bars) and second 3-IAA pulse (open bars), in the absence, or presence of La^{3+} at a range of concentrations as shown in (A). Error bars show SE (n=7, with La^{3+}) and n=10 without La^{3+}). Asterisks mark significant differences between values measured in the first and second 3-IAA pulse (Student's t-test, $p<0.05$). (**C**) Average root hair PM potential within 5 s before La^{3+} was applied (black bars) and before the first (gray bars) and the second (white bars) 3-IAA pulses from experiments as shown in (A). Error bars show SE (n as under (B)). (**D**) Representative voltage traces of the root hair PM potential of seedlings, exposed for 3 min (green), or 9 min (red) to 64 µM La^{3+}, before stimulation with a 1 s pulse of 1 µM of 3-IAA (arrows). Control experiments (black and blue) were performed with the standard bath solution. The bath solutions were constantly exchanged during experiments. The blue arrow marks the time point, at which the perfusion with solutions containing La^{3+} was started. Traces are normalized to the points of 3-IAA application. (**E**) Average maximal depolarization rates in response to the 1 s pulse of 1 µM 3-IAA plotted against the duration of exposure to 64 µM La^{3+}, as shown in (D). Error bars show SE (n=7 to 8). The black line was calculated by linear regression ($R^2=0.81$). (**F**) Average R-GECO1 fluorescence intensities measured in a region of interest across a seedling root in response to two consecutive 1 s pulses of 1 µM 3-IAA (arrows), in the absence (black), or presence of 16 µM (blue), 64 µM (green), or 128 µM (red) La^{3+}. The gray box indicates the time frame at which La^{3+} containing bath solutions were applied. Values are normalized to the point right before the first 3-IAA application. Error bars show SE (n=6, 128 µM La^{3+} and 64 µM La^{3+}, n=8, 16 µM La^{3+} and n=9, std. bath).

The ability of moderate La^{3+} concentrations to block auxin-induced Ca^{2+} influx was an essential prerequisite to directly address the hypothesis of a fast Ca^{2+}-dependent regulation of auxin transport. The following questions remained to be addressed: (**i**) does the lateral Ca^{2+} wave, induced through a single cell stimulation with auxin (see **Fig. 3.23**), also has a longitudinal component and (**ii**) if this is the case, do these Ca^{2+} signals affect auxin transport and signaling in cells not directly stimulated by auxin application?

The $[Ca^{2+}]_{cyt}$ of the apical part of the root, including the meristematic and elongation zones, was observed in seedlings that express R-GECO1 (**Fig. 3.26A**). Root epidermal cells were impaled with single-barrelled microelectrodes and stimulated by iontophoretic injection of 3-IAA for five minutes. Auxin triggered a Ca^{2+} wave that traversed the root acropetally from the side of auxin stimulation to a more apical root zone over distances of approx. 440 µm with an average velocity of 39 mm/h (SE=10 mm/h, **Fig. 3.26A** and **B**). In line with the data shown in **Fig. 3.23**, cytosolic injection of 2-NAA did not elicit such Ca^{2+} signals (**Fig. 3.26B**).

The ability of local auxin stimuli to trigger tip-directed Ca^{2+} waves together with a possible Ca^{2+}-dependent regulation of particular auxin-transporters made it tempting to analyze, in how far these auxin-induced Ca^{2+} waves interfere with the auxin gradients at the root tip. Therefore, seedlings, expressing the fluorescent auxin perception reporter DII-Venus ((Brunoud *et al.* 2012), see **Chapter 2.3.2.** for details) were used to investigate such a possible signaling over greater distances. In the case of the root tip, DII-Venus fluorescence can be observed in the meristematic zone and in parts of the adjoining root cell elongation zone where cells rely on a relatively low auxin concentration to undergo a high mitotic activity and elongation, respectively (**Fig. 3.26C**). 3-IAA was iontophoretically injected together with LY for five minutes into the cytosol of a single epidermal root cell, approx. 400 µm above the meristematic zone (**Fig. 3.26C**, **upper left panel**). The DII-Venus fluorescence intensity started to decrease, without an apparent lag-time, after stimulation with 3-IAA (**Fig. 3.26C** and **D**). A remaining level of the fluorescence signal intensity, at approximately 30% of the initial value, was reached roughly 25 minutes after the start of injection (**Fig. 3.26D**). Cytosolic injection of the inactive auxin 2-NAA had no effect on the time-dependent decrease in DII-Venus fluorescence intensity. In the presence of 128 µM La^{3+}, which was applied ten minutes before stimulation with 3-IAA, the degradation rate of DII-Venus was reduced and new steady-state levels of DII-fluorescence were higher than in the absence of La^{3+}.

As explained in **Chapter 2.3.2**, the DII-Venus fluorescence is an indirect reciprocal measure for the intracellular auxin concentration. Hence, the loss of this signal in cells distant to the site of local auxin stimulation can be interpreted as an accumulation of auxin and the onset of auxin signaling in these cells. From the time-courses of the acropetal Ca^{2+} wave and DII-Venus degradation, it seems that the Ca^{2+} signal coincides with the onset of degradation in these distant cells (**Fig. 3.26B** and **D**), which indicates that the auxin-induced Ca^{2+} signals feed back into auxin transport resulting in the indirectly observed accumulation of auxin.

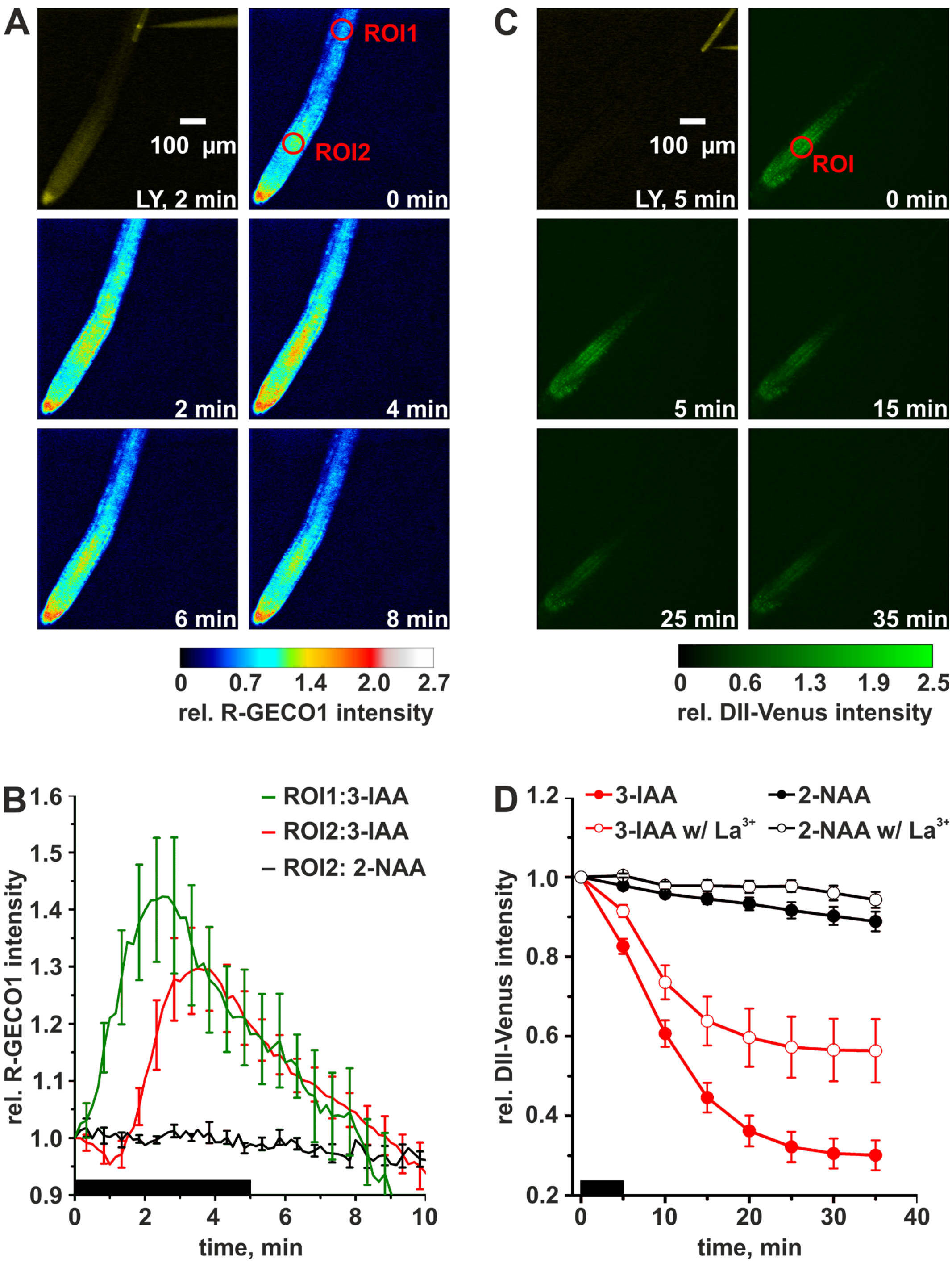

Fig. 3.26: Local application of auxin evokes responses in distant apical root tissues. (**A**) Intensiometric R-GECO1-based imaging of $[Ca^{2+}]_{cyt}$ in apical parts of the root. The upper left panel shows the injection of 3-IAA together with the fluorescent dye LY into the cytosol of a root epidermal cell, in the border region between elongation and differentiation zone, two minutes after the start of injection. The remaining panels show a representative time series of false coloured R-GECO1 fluorescence images. The colors are linked to the R-GECO1 intensity relative to the start of the experiment (equal to 1.0), as indicated by the calibration bar below the panels. The indicated time points correspond to the time scale shown in (B).

(**B**) Average traces of relative R-GECO1 fluorescence intensities of a ROI near the injected epidermal cell (ROI1 in (A), green line) and an ROI at the meristematic root zone (ROI2 in (A), red line). An epidermal cell in ROI1 was stimulated by 3-IAA injection, as indicated by the horizontal black bar below the graph. As a control, the inactive 2-NAA was injected, and the fluorescence time-course of ROI2 is shown in black. R-GECO1 fluorescence data are normalized as explained for (A). Error bars show SE (n=8). (**C**) Intensiometric DII-Venus imaging in apical parts of the root. The upper left panel shows the injection of the 3-IAA together with LY into the cytosol of a root epidermal cell in the border region between elongation and differentiation zone five minutes after the start of injection. The remaining panels show a representative time series of changes in the DII-Venus fluorescence intensity, relative to the intensity at start of injection (equal to 1.0), as indicated by the calibration bar shown below the panels. The indicated time points correspond to the time scale shown in (D). (**D**) Average time-course of DII-Venus fluorescence intensities in the meristematic root zone. Epidermal cells were stimulated by injection of 3-IAA (red), or the inactive 2-NAA (black), in the absence (closed circles), or presence of 128 µM La^{3+} (open circles). Fluorescence intensities are normalized to the time point at the start of the experiment. The black bar above the time axis indicates the time frame of iontophoretic auxin injection. Error bars show SE (n=14, without La^{3+}, n=6 with La^{3+}).

4. Discussion

4.1. Intracellular measurements of the vacuolar conductivity

Vacuoles are essential for plants, because of their ability to store high amounts of inorganic ions, metabolites, proteins, and water. Because of the important role of vacuoles in plant physiology, there is a need to analyse transport processes across the VM. The patch-clamp technique (Neher *et al.* 1978) enabled the characterization of many individual transport processes at isolated vacuoles (Hedrich *et al.* 1986; Peiter *et al.* 2005; De Angeli *et al.* 2013; Jaslan *et al.* 2016). However, most cytosolic factors that regulate vacuolar transport processes *in vivo* are lost during vacuole isolation. To overcome this drawback of the patch-clamp technique, an experimental approach was developed to measure the electrical properties of vacuoles in intact *A. thaliana* root hair cells, with intravacuolar microelectrodes. Since cytosolic Ca^{2+} is known to regulate the activity of vacuolar transporters (Becker *et al.* 2004; Bihler *et al.* 2005; Meyer *et al.* 2011; Latz *et al.* 2013; Tang *et al.* 2015) the correlation between the electrical conductivity of the VM and cytosolic Ca^{2+} was analysed in detail.

The movement of Ca^{2+} across the VM is assumed to be of importance for cytosolic signaling (Roelfsema and Hedrich 2010; Schönknecht 2013). However, the ion-conductances that facilitate the release of Ca^{2+} from the vacuole remain elusive and the active transporters that mediate Ca^{2+} uptake into vacuoles, have not yet been characterized with electrophysiological techniques. Hence, intracellular microelectrodes provide a unique opportunity to test if the $[Ca^{2+}]_{cyt}$ depends on the voltage across the VM and to provide insights into the properties of the ionic conductances that are involved.

4.1.1. The VM conductance can be measured with electrodes in the vacuole of root cells

In this work, it is demonstrated that voltage pulses applied to the VM do not elicit significant changes in the PM potential (see **Fig. 3.1**). Hence, the VM represents the highest resistance for ionic currents elicited between a microelectrode in the vacuole of root hair cells and an extracellular reference electrode. The experiments shown in **Fig. 3.1** clearly demonstrate that intravacuolar microelectrodes record ion currents that depend on the conductance of the VM of *A. thaliana* root hair cells, even though the PM and the VM are impaled in series.

These findings are in line with earlier work by Goldsmith and Cleland (1978) who reported that the VM is the limiting electrical conductance, of symplastically connected *Avena sativa* coleoptile cells. The relatively high conductance of the PM, in comparison with the conductance of the VM, is most likely due to symplastic connections between adjacent cells through plasmodesmata. The symplastic connections cause electrical coupling between root cells (Spanswick 1972; Zhu *et al.* 1998) and as a result, impaled microelectrodes record an electrical continuum of many epidermal root cells. However, vacuoles are electrically isolated and therefore a much lower conductance is recorded by microelectrodes positioned in the vacuole.

The work of Dr. Yi Wang and Dr. Florian Rienmüller, together with the results presented in this thesis, demonstrate that the electrical conductance of the *A. thaliana* epidermal root cell vacuole varies between 5 and 20 nS. The conductance of the PM, in conjuncture with the plasmodesmatal connections to neighbouring cells, on the other hand, is approx. 100 nS. A value of similar range for the electrical conductance of the PM and plasmodesmata of *A. thaliana* epidermal root cells was measured by Roger R Lew, who reported approximately 172 nS (Lew 1996). However, in a later study he found a much higher VM conductance of 589 nS, which he regarded: "*indicative of large ion fluxes between the vacuole and the cytoplasm*" (Lew 2004). The author used a double-impalement approach through which the cytosol of root hair cells was kept as a virtual ground. Through this, the electrical properties of the VM could be separated from those of the PM. Voltage-clamp experiments revealed vacuolar ionic currents with amplitudes of 50 nA at a VM potential 50 mV negative or 90 mV positive of the serial holding potential. The reason why such high vacuolar currents, causing the high VM conductance, were recorded cannot be determined.

Under consideration of a root hair cells dimensions (cylindrical geometry of the cell body: 12.5 by 87.5 µm) Lew (2004), gives a specific VM conductance of 160 S m^{-2}. If the cell dimensions given by Lew (2004) are applied to an electrical conductance of epidermal root cell vacuoles of 20 nS (Wang *et al.* 2015), a specific VM conductance of approx. 5 S m^{-2} is yielded. The vacuolar conductance of root hair cells presented by Wang et al. (2015) and herein are thus two orders of magnitude smaller than the value given by Lew (2004).

However, such a small value of 5 S m^{-2} is just in the range of the various VM conductances of different giant algae species compiled by Tester *et al.* (1987). Values reported therein are mostly < 10 S m^{-2}. Moreover, the conductance of the VM reported by Wang *et al*. (2015) and herein is in line with PM conductances of not symplastically connected and thus electrical isolated cells like *A. thaliana* pollen tubes (approx. 10 to 20 nS, deduced from Gutermuth *et al*. 2013). An example showcasing that the VM conductance is much smaller than the conductance of the PM was reported to be *Avena sativa* coleoptile cells (Goldsmith and Cleland 1978). While the authors demonstrated the electrical resistance of the VM to be approx. 30 MΩ (corresponding to a conductance of 33 nS), the electrical resistance of the PM, on the other hand, was found to be approx. 8 MΩ (corresponding to a conductance of 125 nS). The electrical conductances deduced from *Avena* coleoptile cells by Goldsmith and Cleland (1978) thus are very similar to the values obtained from epidermal root cells of *A.thaliana* presented by Wang *et al*. (2015) and herein.

4.1.2. The VM conductance is regulated by cytosolic Ca^{2+}

In this work, a positive correlation between the VM conductance and $[Ca^{2+}]_{cyt}$ is shown. As a first line of evidence, a time-dependent decrease of the root hair VM conductance after microelectrode impalement (Wang *et al.* 2015) is shown to coincide with the return of the $[Ca^{2+}]_{cyt}$ to basal levels (see **Fig. 3.2**). In conjunction with experiments performed by Dr. Florian Rienmüller (Wang *et al.* 2015) a second line of evidence was obtained by cytosolic injection of Ca^{2+} chelating substances, which can induce transient elevation of $[Ca^{2+}]_{cyt}$ that are associated with an increase of the VM conductance (see **Fig. 1.8** and **Fig. 3.3**).
In general, such a close relationship between the VM conductance and $[Ca^{2+}]_{cyt}$ is supported by the findings of Lew (2004). Although the absolute values of the VM conductance reported therein are not in agreement with the literature consensus, Lew (2004) showed that application of a hyperosmotic shock to root hair cells increased the VM conductance while the PM hyperpolarized. Such osmotic shocks generate mechanical forces at the PM (Monshausen and Gilroy 2009; Monshausen and Haswell 2013; Peyronnet *et al.* 2014). Since such forces are believed to activate PM-localized mechanosensitive channels of high conductance facilitating the movement of osmolytes to minimize these forces (Peyronnet *et al.* 2014), these fluxes have to be compensated to maintain cytosolic ion homeostasis. Moreover, mechanical stimulation was shown to be closely associated with the induction of $[Ca^{2+}]_{cyt}$ elevations. For example, local elevations are provoked through the mechanical stimulation of growing root hairs (Bibikova *et al.* 1997; Monshausen *et al.* 2009) and hyperosmotic treatments were shown to elicit $[Ca^{2+}]_{cyt}$ elevations in whole *A. thaliana* seedlings (Knight *et al.* 1997; Yuan *et al.* 2014). The subsequent stimulation of VM conductances through these mechanically induced Ca^{2+} signals could thus act to maintain cytosolic ion homeostasis at the expense of the vacuole. Through such a mechanism the tugor-dependent polar growth of root hairs could be maintained in cases mechanical forces are encountered as it is to be expected when they grow in soil. Moreover, since the polar growth of root hairs is dependent on

a tip-focused Ca^{2+} gradient (Zhang *et al.* 2017b), it is conceivable that this local $[Ca^{2+}]_{cyt}$ elevation provides the means for tugor maintenance through the vacuole during fast root hair growth independent from external stimuli.

But of what is the nature of those apparently Ca^{2+} regulated vacuolar ion conductances? Intravacuolar microelectrodes record a population of ion conductances in the VM. However, several vacuolar ion channels have been characterized with the patch-clamp technique and their potential contribution to the Ca^{2+}-stimulated VM conductance is discussed in the following.

TPC1 - K^+ is the most abundant cation in plant cells and it is likely to contribute to the VM conductance. The K^+-permeable channel TPC1 has the intrinsic ability to directly sense $[Ca^{2+}]_{cyt}$ via EF-hand motifs (Schulze *et al.* 2011). A hallmark of the TPC1 channel is its activation upon depolarization of the VM (outward rectification). The voltage threshold for TPC1 activation is shifted to more negative potentials (closer to physiological VM potentials) by high Ca^{2+} levels in the cytosol, as well as low Ca^{2+} levels in the lumen (Hedrich and Neher 1987; Pottosin *et al.* 1997; Pottosin *et al.* 2004; Beyhl *et al.* 2009). TPC1 is not only regulated by Ca^{2+}, but also can conduct Ca^{2+} currents, albeit at conditions that are unlikely to occur in intact cells (Ward and Schroeder 1994; Pottosin *et al.* 1997; Beyhl *et al.* 2009; Rienmüller *et al.* 2010; Hedrich and Marten 2011). Nevertheless, TPC1 was suggested to mediate Ca^{2+}-induced Ca^{2+}-release from the vacuole during stress-induced signaling events (Ward and Schroeder 1994; Pottosin *et al.* 2009; Schönknecht 2013; Choi *et al.* 2014; Evans *et al.* 2016).

TPC1 may contribute to the observed Ca^{2+}-dependent changes of the VM conductance in root hair cells. It is most likely to conduct K^+ currents, as TPC1 has highest permeability for K^+ (Ward and Schroeder 1994) and K^+ is present in high concetrations in the vacuole (Wang and Wu 2013). Because of the small electrochemical gradient of K^+ ($[K^+]_{lum}/[K^+]_{cyt} \approx 1$; Wang and Wu, 2013), TPC1-mediated K^+ fluxes into the vacuole, activated through a $[Ca^{2+}]_{cyt}$-dependent shift of the activation threshold, could contribute to the observed changes of the VM conductance in root hair cells. However, patch-clamp experiments show that TPC1-mediated ionic currents are typical being only slowly activated under depolarising VM potentials (Hedrich and Neher 1987). This characteristic feature of TPC1 neither was found for vacuolar currents of stimulated (i.e. high $[Ca^{2+}]_{cyt}$), nor unstimulated root hair cells. This finding thus indicates that SV channels are to a large extend in an inactivated state in root hair cells. Activation may occur when plants encounter larger stress stimuli. A role of TPC1 was shown for the propagation Ca^{2+} and ROS waves in roots, after stimulation with high salt concentrations (Choi *et al.* 2014; Evans *et al.* 2016) and for the biosynthesis of the wound hormone jasmonic acid (Bonaventure *et al.* 2007).

TPK1 - Members of the TPK family have been shown to function as voltage-independent K^+-selective channels (Becker *et al.* 2004; Latz *et al.* 2007; Carraretto *et al.* 2013). TPK1 is located in the VM and is activated through the interaction with 14-3-3 proteins as well as through a direct EF-hand motif-mediated Ca^{2+} sensing. An additional layer of regulation is provided by the Ca^{2+}-dependent phosphorylation of the 14-3-3 interaction domain of TPK1 by CPK3 (Latz *et al.* 2007; Latz *et al.* 2013). Because of the voltage-independent characteristic, and because of its sensitivity to cytosolic Ca^{2+}, TPK1 is very likely to contribute to the Ca^{2+}-stimulated VM conductivity that was observed in this study.

Anion channels - The VM of root hair cells also harbours several anion channels from which the P_i channel PHT5.1 (Liu *et al.* 2015; Liu *et al.* 2016), and the Cl^--permeable channels ALMT9 (De Angeli *et al.* 2013) and DTX33/35 (Zhang *et al.* 2017a) are highly expressed and well characterized (see **Fig. 1.6**). These channels are of outward (into the vacuole) rectifying manner and thus could facilitate vacuolar currents measured in root hair cells at hyperpolarizing VM potentials. However, no Ca^{2+}-dependent regulation was found for ALMT9 in isolated vacuoles, while the Ca^{2+}-dependent regulation was neither studied for PHT5.1 (Liu *et al.* 2015), nor for DTX33/35 (Zhang *et al.* 2017a).

Transporter - In addition to ion channels, several carriers may contribute to the conductance of the VM. The anion/H^+ exchanger of the ClC family are promising candidates. Recently published patch-clamp experiments on isolated mesophyll vacuoles of *A. thaliana* showed vacuolar current kinetics to depend on the presence of the phosphatidylinositol-3,5-bisphosphate-regulated ClCa with respect to an instantaneous activation and slow time-dependent deactivation (Carpaneto *et al.* 2017). Thus far, no evidence for the absence or presence of a Ca^{2+}-dependent regulation of ClCs has been brought forward.

The cation/H^+ exchangers of the NHX and CAX family may be active in the VM and at least NHX1 and CAX2 could be present at the VM in a high copy number, since both their genes are among the more highly abundant transcripts encoding vacuolar transporters in root hair cells (see **Fig. 1.6**). These secondary active transporters can significantly contribute to vacuolar currents in root hair cells, provided they operate in an electrogenic manner.

Both NHX1 and CAX2 are likely to be controlled by Ca^{2+}. In the case of NHX1, regulation through luminal Ca^{2+} via luminal-localized CaM15 has been shown in the heterologous system of yeast cells (Yamaguchi *et al.* 2005). Although no regulation through Ca^{2+} has been brought forward in the case of CAX2 so far, a search for putative physical CAX2 interaction partners on the ARAPORT database (https://www.araport.org/) revealed at least four CaMs (CaM1/4/7/10), a 14-3-3 protein

(AT5G38480) and two CaM interacting proteins (AT2G41090 and AT2G41100). These putative interactions strongly point towards a Ca^{2+}-dependent regulation of CAX2.

4.1.3. A tool to study H^+-coupled vacuolar Ca^{2+} import

The results presented in this work unequivocally demonstrate that the movement of calcium ions across the VM is regulated by the electrical potential across this endomembrane. While depolarization of the VM led to elevations of $[Ca^{2+}]_{cyt}$, hyperpolarizing VM potentials caused a drop of $[Ca^{2+}]_{cyt}$ below basal levels (see **Fig. 3.4** to **3.7**). The observed relationship between the changes in $[Ca^{2+}]_{cyt}$ and the VM potential is in contrast to the impact that the electrochemical gradient is supposed to have on Ca^{2+} currents. The ideal thermodynamic behaviour of passive Ca^{2+} movement across the VM can be calculated by **Equation 4.1** (compare to **Equation 1.1;** (Christensen 1975)):

$$\Delta G = \left[R * T * ln\left(\frac{[Ca^{2+}]_{lum}}{[Ca^{2+}]_{cyt}}\right) - z_{Ca^{2+}} * F * \Delta E_{VM} \right]$$

Equation 4.1: Thermodynamic simulation of passive Ca^{2+} movement across the VM. **ΔG**: free energy, **R**: universal gas constant, **T**: absolute temperature (293 K), **z**: charge of the ion, **F**: Faraday constant, **ΔE_{VM}** as the VM potential at the cytosolic side.

Since the luminal/cytosolic Ca^{2+} gradient in root hair cells of *A. thaliana* can be assumed to be in the range of 10^3 to 10^4, **Equation 4.1** results in reversal potentials for Ca^{2+} of 87 mV and 116 mV, respectively (**Fig. 4.1**). As it is apparent from **Fig. 4.1**, a passive release of Ca^{2+} from the vacuole is thus facilitated at all experimentally tested VM potentials. The depolarization of the VM, i.e. a shift to more positive potentials at the cytosolic side, represents a decrease of the electrochemical gradient and passive Ca^{2+} fluxes into the cytosol should consequently be reduced. Hence, a decrease of $[Ca^{2+}]_{cyt}$ should be the expected outcome. The same relation holds true for a hyperpolarized VM potential, which should enhance the passive release of Ca^{2+} from the vacuole and thus should lead to $[Ca^{2+}]_{cyt}$ elevations.

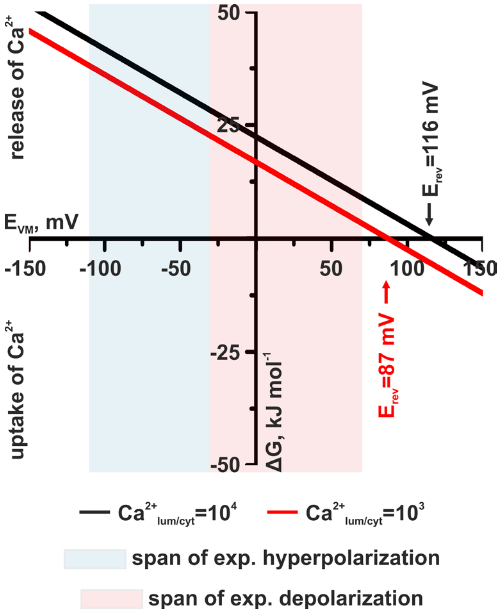

Fig. 4.1: Thermodynamics of Ca^{2+} movement across the VM. The change in free energy of Ca^{2+} is plotted against the VM potential. Calculations were performed for luminal/cytosolic Ca^{2+} gradients of 10^3 (red) and 10^4 (black). The span of hyper- and depolarizing voltage pulses applied to the VM during voltage-clamp experiments are indicated by light colored areas. Negative ΔG values represent uptake of Ca^{2+} into the vacuole, while positive values indicate the release of Ca^{2+} into the cytosol.

How can the experimentally observed voltage-induced change in the cytosolic Ca^{2+} level, opposite from the expected outcome be explained? The considerations shown above exclude that a Ca^{2+}-permeable vacuolar ion channel is involved. Instead, active Ca^{2+} transporters may explain the outcome of the voltage clamp experiments.

Whereas vacuolar Ca^{2+}-ATPases like ACA11 (see **Fig. 1.6**) use ATP to pump Ca^{2+} into the vacuole, cation/H^+ exchangers of the CAX family rely on the pmf. Even though Ca^{2+}-ATPases and CAXs transporters were not yet characterized with electrophysiological techniques, the CAX family was studied extensively at the molecular and biochemical level. CAXs from *A. thaliana* were able to rescue cation sensitive growth phenotypes in yeast and *in planta*, as well as a reduced pH-dependent vacuolar Ca^{2+} uptake in *A. thaliana cax* loss-of-function mutants (Hirschi *et al.* 1996; Hirschi *et al.* 2000; Cheng *et al.* 2002; Cheng *et al.* 2003; Cheng *et al.* 2004). The functions of the two vacuolar Ca^{2+}-ATPases in *A. thaliana* have been deduced in a similar approach, by a study that revealed their ability to rescue the growth of Ca^{2+} transport deficient yeast strains. (Geisler *et al.* 2000; Lee *et al.* 2007). In these Ca^{2+} pumps, the hydrolysis of one molecule of ATP is likely to drive the uphill transport of two Ca^{2+} in exchange of two H^+ (Yu *et al.* 1993; Olesen *et al.* 2007). Both, Ca^{2+}-ATPases and H^+/Ca^{2+} exchanger are likely to have a significant influence on shaping cytosolic Ca^{2+} signatures and in maintaining low basal $[Ca^{2+}]_{cyt}$ (Roelfsema and Hedrich 2010; Bose *et al.* 2011; Schönknecht 2013).

Thermodynamic considerations of active Ca^{2+} transport across the VM may help to interpret the presented experimental data. **Equation 4.2** describes the ideal thermodynamic behaviour of vacuolar Ca^{2+} uptake via a H^+-coupled transport process. For this purpose, **Equation 4.1** was expanded through the expression describing the pmf across the VM.

$$\Delta G = n_{Ca^{2+}} * \left[R * T * ln\left(\frac{[Ca^{2+}]_{lum}}{[Ca^{2+}]_{cyt}}\right) - z_{Ca^{2+}} * F * \Delta E_{VM}\right] + n_{H^+} * \left[R * T * ln\left(\frac{[H^+]_{cyt}}{[H^+]_{lum}}\right) + z_{H^+} * F * \Delta E_{VM}\right]$$

Equation 4.2: Thermodynamic simulation of a H^+/Ca^{2+} exchanger. Symbols are as defined for **Equation 4.1**. **n:** H^+/Ca^{2+} coupling ratio.

Calculations displayed in **Fig. 4.2A** were performed for a luminal/cytosolic Ca^{2+} gradient of 10^4, four different H^+/Ca^{2+} coupling ratios as well as several pH gradients across the VM.

Based on this model, an efficient uptake of Ca^{2+} into the vacuole is only possible at electrogenic H^+/Ca^{2+} coupling ratios of three or four. Moreover, at a ΔpH of 1 unit, uptake can only occur at VM potentials at or negative of the free running value (approx. -30 mV, **Fig. 4.2A**). A ΔpH of 1.5 or 2 pH units, however, is sufficient to enable vacuolar Ca^{2+} uptake at VM potentials positive of the free running value as well. Depending on the Ca^{2+} gradient, the ΔpH_{VM} and the exact transport stoichiometry, a depolarization of the VM potential should thus lead to a reduced activity of H^+/Ca^{2+} exchanger, while hyperpolarizing VM potentials should have the opposite effect.

The pmf also will affect the activity of Ca^{2+}-ATPases. As Ca^{2+}-ATPases are likely to act as ATP-driven electrogenic H^+/Ca^{2+} exchanger working with a 1:1 stoichiometry the ideal thermodynamic behaviour of a Ca^{2+} pump can be simulated by expanding **Equation 4.2** through an expression describing the energy liberated from cytosolic ATP-hydrolysis (**Equation 4.3;** (Lodish *et al.* 2008))

$$\Delta G = n_{Ca^{2+}} * \left[R * T * ln\left(\frac{[Ca^{2+}]_{lum}}{[Ca^{2+}]_{cyt}}\right) - z_{Ca^{2+}} * F * \Delta E_{VM}\right] + n_{H^+} * \left[R * T * ln\left(\frac{[H^+]_{cyt}}{[H^+]_{lum}}\right) + z_{H^+} * F * \Delta E_{VM}\right] + \left[\Delta G_{0,ATP} + R * T * ln\left(\frac{[ADP]_{cyt}}{[ATP]_{cyt}} * [P_i]_{cyt}\right)\right]$$

Equation 4.3: Thermodynamic simulation of a Ca^{2+}-ATPase. Symbols are as defined for **Equations 4.1** and **4.2**. **$\Delta G_{0,ATP}$:** Energy liberated from ATP hydrolysis at standard conditions.

The calculations presented in **Fig. 4.2B** presumed a conservative cytosolic ATP/ADP ratio of 1 (Gardestrom and Igamberdiev 2016), a cytosolic [P_i] of 70 µM (Pratt *et al.* 2009) and three different pH gradients across the VM. The additional energy provided by ATP hydrolysis ensures the uptake of Ca^{2+} into the vacuole at virtually all VM potentials displayed in **Fig. 4.2B**, except for those negative of -100 mV. A depolarization of the VM potential leads to a higher activity of Ca^{2+}-ATPases, because a net positive load (2Ca^{2+} in versus 2H^+ out) has to be transported against a smaller electrical potential.

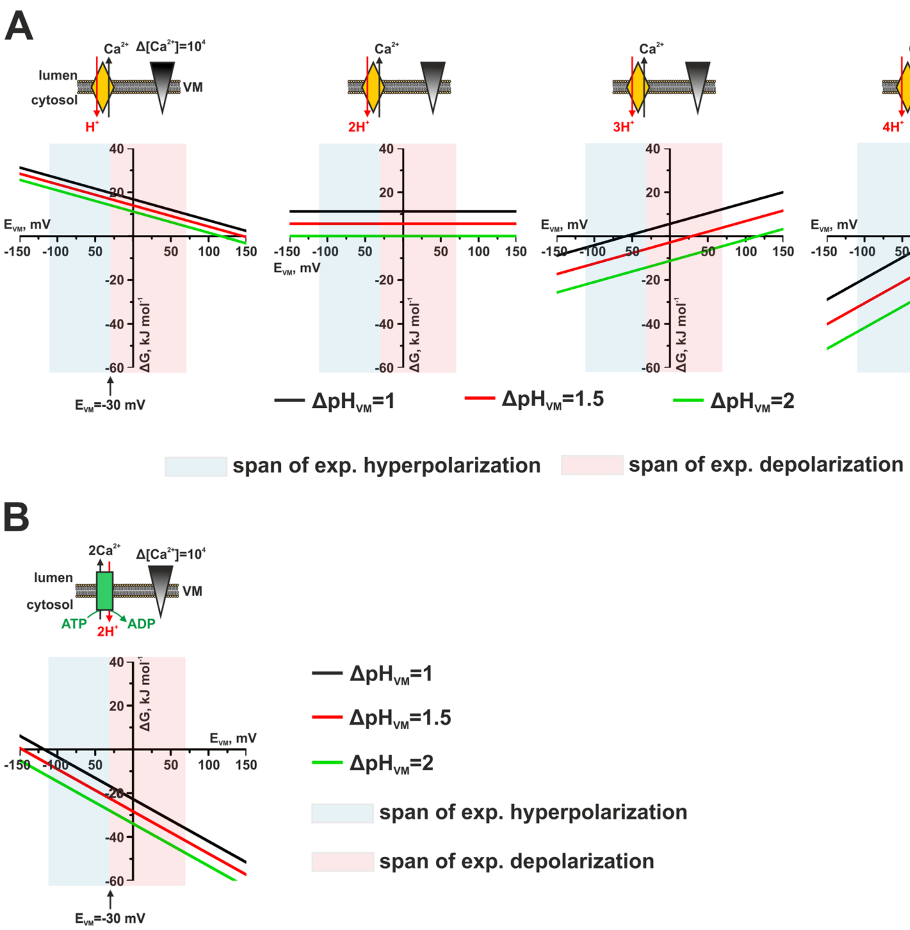

Fig. 4.2: Thermodynamic simulation of vacuolar Ca^{2+} uptake via H^+/Ca^{2+} exchangers and Ca^{2+}-ATPases. (**A**) H^+/Ca^{2+} antiport. The cartoons above the graphs illustrate the transport mechanism and the Ca^{2+} gradient used in the calculations (black triangle). Calculations were performed for different coupling ratios (from left to right: 1, 2, 3 and 4) as indicated by the cartoons, as well as for different trans-VM pH differences as indicated by the different colours. The luminal/cytosolic Ca^{2+} gradient of 10^4 was constant for all calculations. The light-coloured areas show the span of hyper (up to -80 mV)- and depolarizations (up to +100 mV) from the free running VM potential of -30 mV. (**B**) Simulation of a Ca^{2+}-ATPase. Calculations were performed for different trans-VM pH differences as indicated by the different colours. The luminal/cytosolic Ca^{2+} gradient of 10^4, the cytosolic ADP/ATP ratio of 1 and the cytosolic [Pi] at 70 µM were constant for all calculations. The light-

coloured areas show the span of hyper (up to -80 mV)- and depolarizations (up to +100 mV) from the free running VM potential of -30 mV.

From the thermodynamic considerations explained above, the model displayed in **Fig. 4.3** can be deduced, which explains the relationship that was experimentally observed between $[Ca^{2+}]_{cyt}$ and the VM potential (**Fig 4.3**). At a ground state defined through a free running VM potential of approximately -30 mV, a ΔpH_{VM} of 1.5 units and a luminal/cytosolic Ca^{2+} gradient of 10^4 (Bibikova *et al.* 1998; Bassil *et al.* 2011; Martinoia *et al.* 2012; Schönknecht 2013), the Ca^{2+}-ATPases and H^+/Ca^{2+} exchanger transport Ca^{2+} into the vacuole to compensate for Ca^{2+} release into the cytosol, via non-selective cation channels.

The ideal thermodynamic behavior of vacuolar Ca^{2+}-ATPases in this model is dominated by the electrochemical gradient of Ca^{2+}. Hence, a positively shifted VM potential would enhance vacuolar Ca^{2+} import together with cytosolic ATP/ADP ratios > 1. This opposing behaviour excludes Ca^{2+}-ATPases from being responsible for the $[Ca^{2+}]_{cyt}$ changes observed in voltage-clamp experiments.

However, since the pmf across the VM is the sum of the ΔpH_{VM} and the VM potential, it is enhanced, or reduced, through hyper- and depolarization of the VM, respectively. In the model depicted in **Fig. 4.3** the pmf in the ground state has a value of -120 mV. A hyperpolarization of the VM potential by -80 mV will shift the pmf to -200 mV. A depolarization by 100 mV, on the other hand, will lower the pmf across the VM to -20 mV. Because of these voltage-dependent changes in the pmf, Ca^{2+} is less efficiently imported into the vacuole by H^+/Ca^{2+} exchangers upon depolarization of the VM and *vice versa*. Voltage-induced changes in the activity of H^+/Ca^{2+} exchanger thus are likely the cause of the changes in $[Ca^{2+}]_{cyt}$, monitored in vacuolar voltage-clamp experiments.

In this model, Ca^{2+}-ATPases would counteract the activity of H^+/Ca^{2+} exchangers. However, since the experimental evidence shows $[Ca^{2+}]_{cyt}$ changes matching the described ideal thermodynamics of H^+/Ca^{2+} exchanger, Ca^{2+}-ATPases with their high affinity but low turnover rates (Lodish *et al.* 2008) seem to have only negligible contributions.

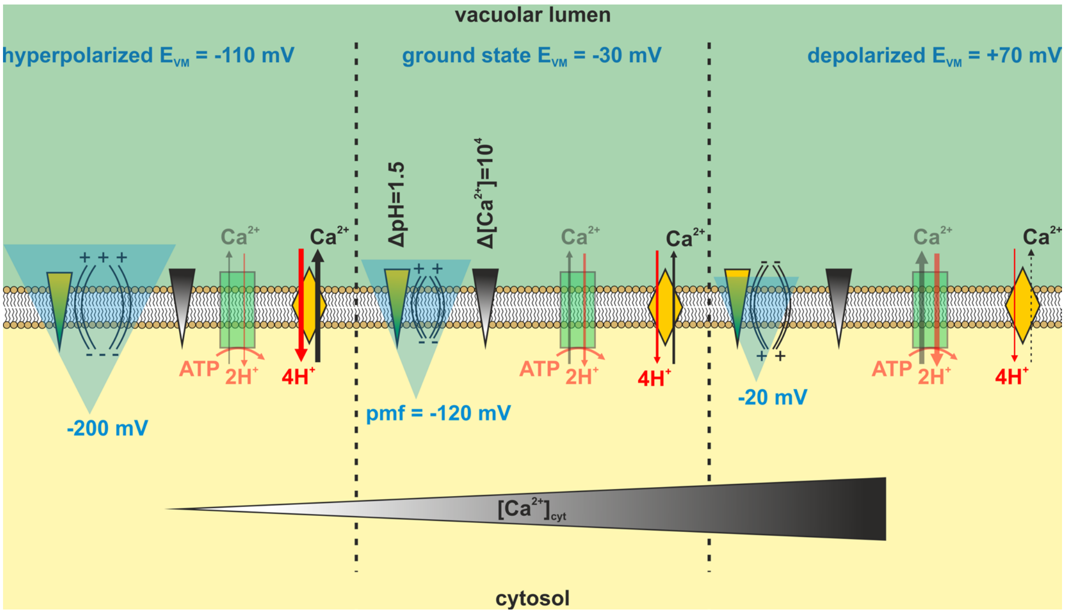

Fig. 4.3: Model for VM potential-mediated changes of $[Ca^{2+}]_{cyt}$. The close correlation between $[Ca^{2+}]_{cyt}$ and the VM potential can be explained by the changes to the pmf (light blue triangle) which enhance or decrease the ability of H^+/Ca^{2+} exchanger (yellow diamond) to transport Ca^{2+} into the vacuole at hyper- or depolarized membrane potentials. The size of the arrows is relative to transport activity. Although H^+ influx is still possible at depolarized potentials, the energy liberated through this is not sufficient for the uphill transport of Ca^{2+} (dashed arrow). Ca^{2+}-ATPases counteract antiport activity but are expected to have negligible contributions (transparent appearance).

The experimentally acquired data, together with thermodynamic reflections explained above, firmly point towards a major role of vacuolar H^+/Ca^{2+} exchangers in VM potential-induced changes of $[Ca^{2+}]_{cyt}$. In the family of so far identified vacuolar H^+/Ca^{2+} exchangers, only CAX2 seems significantly expressed in root hair cells (see **Fig.1.6A**), which makes it the prime candidate for further analysis. The presented experimental approach offers a tool to study the role of CAX2 in regulating $[Ca^{2+}]_{cyt}$ and characterize its transport properties and regulation mechanisms in the *in planta* system of bulging root hair cells. As mentioned in **Chapter 4.1.2.**, CAX2 possibly interacts with Ca^{2+} sensing CaMs. This possibility could explain the observed drop of the $[Ca^{2+}]_{cyt}$ below basal levels which was observed when the VMs were returned to their resting potentials after highly depolarizing voltage pulses (see **Fig. 3.4**). The elevations of the $[Ca^{2+}]_{cyt}$ during such voltage pulses could potentially lead to an activation of CAX2 through the Ca^{2+}-dependent interaction with CaMs. Whereas depolarizing potentials would mask such an activation by diminishing the pmf, a persistent Ca^{2+}-dependent increase of the activity of CAX2 could be responsible for the post-depolarization drop in $[Ca^{2+}]_{cyt}$. Since H^+-coupled vacuolar Ca^{2+} uptake into the vacuole would require the net movement of positive charges into the cytosol, the small inward current response observed after depolarizing voltage pulses supports the hypothesis of a Ca^{2+}-dependent activation of the responsible H^+/Ca^{2+} exchanger.

4.1.4. Outlook and open questions for intracellular vacuolar measurements

Whereas the ion conductivity of the VM apparently is regulated by cytosolic Ca^{2+} signals, the membrane potential of the VM may affect the shaping of cytosolic Ca^{2+} signatures. Although the results presented in this work point to such a mutual interaction of the VM and $[Ca^{2+}]_{cyt}$, it remains to be investigated in much more detail, in order to get answers to the following outstanding questions:

(i) Which vacuolar ion channels, or transporters, are dominating the vacuolar conductance *in planta*?

The vacuolar currents measured during voltage-clamp experiments *in planta* will likely represent the superposition of various active conductances. So far, a strong statement regarding the contribution of specific ion channels or transporters cannot be made. Analysis of loss-of-function mutants, however, could potentially provide such data. Prime candidates would be null alleles of TPK K^+ channels and anion channels, like ALMT9 and PHT5.1 or secondary active transporter like ClC-a and CAX2. Besides their influence on the VM conductance under control conditions, their contribution to an elevated conductance under high $[Ca^{2+}]_{cyt}$ would be of special interest.

(ii) Which physiological relevant signals trigger Ca^{2+} signals in root hairs cells?

So far, the cytosolic Ca^{2+} signals, which were shown to the enhance the VM conductivity, were induced by impalement and current injection of Ca^{2+} chelators. A prime goal for future research will be to study which physiologically more relevant signals trigger Ca^{2+} signals can enhance the VM conductivity. The fast occurring Ca^{2+} signals induced by the growth hormone auxin would be worthwhile to test in this respect. Auxin-induced Ca^{2+} signals were shown to solely depend on CNGC14-mediated Ca^{2+} influx across the PM (see **Fig. 3.18**, (Shih *et al.* 2015)). Provided that vacuolar Ca^{2+} release does not contribute to auxin-induced elevations of the $[Ca^{2+}]_{cyt}$, an enhanced VM conductivity during auxin-induced signaling could point to a Ca^{2+}-dependent regulation of other transport processes like the vacuolar uptake of excess cytosolic Ca^{2+}.

(iii) Are Ca^{2+}/H^+ transporters responsible for VM potential-induced changes in the $[Ca^{2+}]_{cyt}$ and are these transporters encoded by *CAX* genes?

Plant lines expressing genetically encoded cytosolic Ca^{2+} reporter in the background of loss-of-function mutants of genes like *CAX2* can be used to study if these transporters contribute to the experimentally observed voltage-induced $[Ca^{2+}]_{cyt}$ changes. Moreover, the ΔpH_{VM} could be altered in order to provide insights into the H^+-dependency of Ca^{2+} transport in root hair cells. In a pharmacological approach the vacuolar H^+-ATPase could be specifically inhibited with bafilomycin (Rienmüller *et al.* 2012) or the ΔpH_{VM} could be increased through overexpression of vacuolar H^+-pumps (V-ATPases and V-PPases).

The experimentally applied range of VM potentials is, of course, unphysiological, since the VM, resting at around -30 mV, is unlikely to change by 80 or even 100 mV in response to a physiological trigger. However, the data presented in **Fig. 3.7** show that also smaller changes of the VM voltage can affect $[Ca^{2+}]_{cyt}$. The intracellular localization of the vacuole complicates long-time measurements of the VM potential since double-impalement experiments are necessary to correct the VM potential for the PM potential. A statistical approach, however, in which a sufficient number of PM potential measurements are compared to measurements of the serial potential measured through intravacuolar electrodes ($E_{VM} = E_{PM} - E_T$) could gain insights into the response of the VM potential to different elicitors and if those changes are sufficient to influence the activity of H^+/Ca^{2+} exchanger.

4.2. Analysis of auxin transport and membrane-localized signaling

The second part of this work aimed at a comprehensive understanding of the earliest auxin-induced responses in the root of the model plant *A. thaliana*. Such fast auxin responses that occur within seconds after application of an external auxin stimulus, include a depolarization of the PM potential, an apoplastic alkalinization, as well as cytosolic Ca^{2+} signals mediated by a PM-localized putative Ca^{2+}-permeable ion channel (Felle *et al.* 1991; Monshausen *et al.* 2011; Shih *et al.* 2015).
Although the rapid depolarization of the PM potential already had been suggested to represent electrogenic H^+-coupled auxin influx, the electrical signals were so far not used to provide a detailed characterization of auxin transport *in vivo*.
Recently a model has been proposed that links auxin-induced $[Ca^{2+}]_{cyt}$ elevations and fast alkalinization of the apoplast to the establishment of the root gravitropic response (Shih *et al.* 2015). However, the role and interaction of the single components within this model, including auxin perception, Ca^{2+} signals, and the conductance that mediates apoplastic alkalinization, still remained elusive.

4.2.1. The first *in vivo* characterization of carrier-mediated auxin influx

Local short-term application of auxin induces fast and high-amplitude PM potential depolarizations in root hair cells of *A. thaliana* (see **Fig. 3.8**). The characteristics of the membrane depolarization, like a half-maximal response at 300 nM auxin, as well as the strict dependence on an apoplastic pH < 7, are in line with previous reported properties of auxin influx transporters. Rubery and Sheldrake (1974) first proposed the existence of a saturable, carrier-mediated, uptake mechanism of IAA^-. They showed that auxin-uptake has an optimum at pH 6 and a half-maximal response at 1-5 µM IAA, by examining auxin-uptake in crown gall suspension cells. Felle *et al.* (1991) described the characteristics of the auxin-induced electrical response of maize coleoptiles and found that it is also dependent on an acidic pH and displays a half-maximal value at 490 nM IAA.
In addition to the depolarization of the root hair PM, auxin was also shown to trigger a rapid influx of H^+ across the PM of root epidermal cells (see **Fig. 3.10**). If the IAA- and pH-dependence of the root hair depolarization, as well as the auxin-induced H^+ influx are taken into account, it is likely that these responses represent real-time observations of a secondary active auxin uptake machinery. In this regard, Felle *et al.* (1991) were the first to suggest a $2H^+/IAA^-$ stoichiometry for carrier-mediated auxin-uptake that gives rise to a depolarizing positive inward current.

Subsequently, protein sequence homologies between amino acid permeases and the putative auxin-uptake facilitator AUX1, suggested such a H^+-coupled auxin transport mechanism for AUX1 (Bennett *et al.* 1996). The hypothesis, that the depolarization of the root hair PM is caused by AUX1-mediated H^+-coupled auxin uptake, was indeed confirmed in this thesis, based on experiments with a series of *aux1* loss-of-function mutants, which were tested for their auxin-induced root hair depolarization and stimulation of H^+ influx (see **Fig. 3.12**). The fast component of the depolarization and the rapid induction of H^+ influx were reduced, or absent, in the tested *aux1* loss-of-function mutants. The apparent absence of auxin influx in *aux1* mutants is in accordance with a phenotypic analysis of root agravitropism in the same mutant lines (Swarup *et al.* 2004), as well as with an impaired ^{3}H-IAA uptake in oocytes expressing mutated versions of *AUX1* (Yang *et al.* 2006). Significantly, Yang and co-workers found AUX1-mediated ^{3}H-IAA uptake into oocytes to be half-maximal at an applied concentration of 800 nM. Furthermore, the experiments by Yang *et al*. (2006) demonstrated the activity of AUX1 to be highest at pH 6. The oocyte experiments are thus in accordance with the *in planta* experiments presented herein that characterized auxin transport via AUX1 with apparent K_m values for the applied auxin and H^+ concentration of 300 nM and pH 6, respectively (see **Fig. 3.9**).

A comparison between wild type and the *aux1* mutants provided evidence that AUX1 is solely responsible for the electrogenic auxin uptake into roots at physiological relevant concentrations (< 1 µM) (see **Fig. 3.12**). However, at higher auxin concentrations (> 1 µM) a considerable fraction of the fast root hair PM depolarization was caused by AUX1-independent auxin transport processes. An explanation for the AUX1-independent auxin uptake is given by Rutschow *et al*. (2014). They analysed auxin-uptake into *A. thaliana* mesophyll protoplasts that transiently expressed *AUX1*. Rutschow *et al*. (2014) reported that a saturable, but unspecified, transporter caused 20% of the IAA uptake. It is thus likely that the AUX1-independent responses represent auxin uptake by transporters of lower auxin affinity, compared to AUX1. These might be other members of the class of amino acid permeases, sharing a H^+-coupled transport mechanism with AUX1 (Fischer *et al.* 2002) and which might have affinity to Tryptophane-derived IAA (Woodward and Bartel 2005).

Besides the high affinity for the native auxin, AUX1 also shows a high specificity for 3-IAA when compared to other physiological active, but synthetic auxin analogs (see **Fig. 3.13**). At this point, a significant discrepancy with the results shown in **Fig. 3.13** to the literature must be discussed. The active synthetic auxins 1-NAA and 2,4-D are widely used in auxin in research (Ottenschläger *et al.* 2003; Dharmasiri *et al.* 2005a; Dharmasiri *et al.* 2005b; Parry *et al.* 2009; Shih *et al.* 2015) and it is supposed that the lipophilic nature of 1-NAA enables it to passively enter cells via diffusion, whereas 2,4-D was shown to be a substrate for carrier-mediated influx via AUX1 (Delbarre *et al.* 1996; Yang *et al.* 2006; Swarup and Peret 2012). By analyzing uptake of radiolabelled auxins into suspension-cultured tobacco cells, Delbarre *et al*. (1996) reported a saturable 2,4-D influx component with a fourfold lower affinity than it was obtained for 3-IAA. Yang *et al*. (2006) heterologously expressed *A.thaliana AUX1* in *Xenopus* oocytes and found that 2,4-D, but not 1-NAA, inhibits the uptake of ^{3}H-IAA. Based on these results they concluded that 2,4-D is a substrate for uptake via AUX1.

However, the hypothesis of Yang *et al*. (2006) is not in line with the electrical responses of root hair cells to 2,4-D and 1-NAA presented in this work and those recorded by Felle *et al*. (1991).

In accordance with the electrical measurements of Felle *et al*. (1991) this work showed that 2,4-D is unable to elicit strong electrical responses in root hair cells (see **Fig. 3.13**). This observation led to the conclusion that 2,4-D is not a major substrate for active uptake via AUX1.

In the case of 1-NAA, a fast depolarization of the PM potential with an amplitude that reached approx. 50 % of the response induced by 3-IAA was consistently observed by this work and by Felle *et al*. (1991). Significantly, while 1-NAA was shown to induce the influx of H^+ (see **Fig. 3.16**), the fast depolarization of root hair cells induced through this synthetic auxin was found to be independent from AUX1 (see **Fig. 3.13**). This is in support of a model in which synthetic auxins are actively transported albeit via unspecified transporters.

The immediate auxin-induced depolarization of the PM of *A. thaliana* root hair cells presented here, of maize coleoptiles reported by Felle *et al*. (1991) and of *Sinapis alba* root hairs reported by Felle and Hepler (1997) can be safely regarded as direct observations of an electrogenic auxin-influx. Experimental approaches that monitor the uptake of radiolabelled auxins in hetero- as well as homologous expression systems, however, might underestimate the contribution of AUX1-independent and non-characterized transport to the influx of auxins over time.

In contrast to root hair cells, epidermal hypocotyl cells of etiolated *A. thaliana* seedlings were found not to show a fast auxin-induced depolarization of the PM potential (see **Fig. 3.8**). The absence of an electrical response in the hypocotyl was unexpected, since the elongation of this organ is considered to be highly auxin-responsive (Friml *et al.* 2002b; Fendrych *et al.* 2016). Moreover, the involvement of AUX1 in the formation of the apical hook clearly demonstrates the importance of AUX1 outside root tissues (Vandenbussche *et al.* 2010). Additional functions of AUX1 in aerial organs encompass vascular patterning (Fabregas *et al.* 2015) and phyllotaxis (Reinhardt *et al.* 2003). How can the absence of an electrical response and thus auxin influx in the hypocotyl be explained?

The auxin-induced influx of H^+ into root cells presented in this work is synonymous with the apoplastic or root surface alkalinisation shown by Monshausen *et al*. (2011), Shih *et al*. (2015) and Barbez *et al*. (2017). In accordance with the absent depolarization shown in this work, Fendrych *et al*. (2016) did not report such an auxin-induced alkalinisation of the apoplastic space in the hypocotyl. Hence, the active uptake of auxin seems not to be a major form of auxin influx in hypocotyl cells. Since root cells are more auxin sensitivity than shoot tissues (Thimann 1938), it is conceivable that this is partially related to the apparent higher activity of AUX1 in this cell type as compared to hypocotyl cells. The reason why AUX1 seems to be more active in root tissues than in the shoot, however, needs to be studied in more detail. Apart from AUX1, also the influence of tissue- and organ-dependent $SCF^{TIR1/AFB}$ receptor compositions and their specific affinities to different target AUX/IAA repressors (29 members in *A. thaliana*) has also to be considered as a possible reason (Dreher *et al.* 2006; Weijers and Wagner 2016; Winkler *et al.* 2017).

Membrane potential measurements not only revealed differences in the auxin-induced depolarization between root and shoot tissues, but also between cell types of the root epidermis. Non-hair cells were found to show a faster auxin-induced PM depolarization than root hair cells (see **Fig. 3.14**). As explained above, such an enhanced response may be the result of a higher activity of AUX1 in non-hair cells as compared to root hair cells. With respect to the occurrence of AUX1, contradictory statements are found in the literature. Jones *et al*. (2009) described the absence of any fluorescent signal in root hair cells that were transformed with an AUX1::YFP fusion protein, driven by its native promotor, whereas a fluorescence signal was detectable from the PM of non-hair cells. They concluded that the low cytosolic auxin levels caused by the absence of AUX1 from root hair cells are necessary for hair cell differentiation and subsequent root hair growth. However, *AUX1* transcripts were found by a transcriptomics approach in isolated root hair protoplasts (Lan *et al.* 2013). The results presented in this work support both findings. Root hair cells were chosen as model cell type, because of their advantages for electrophysiological measurements (see **Chapter 1.5.**) and they proved to be very much suitable for the analysis of AUX1-mediated auxin transport. Root epidermal cells are electrically coupled, and the electrical signal, i.e. the depolarization of the PM potential, generated by auxin uptake does not necessarily represent the AUX1-activity in the impaled cell, but it rather represents the response of a series of symplastically connected cells. Consequently, a statement concerning the absence or presence of AUX1 in root hair cells cannot be made based solely on the membrane potential responses measured with root hair cells.

4.2.2. AUX1-mediated auxin uptake is important for the low P_i-adaptive response of root hair cells

Plants adapt to low external P_i concentrations by altering the architecture of their root system, which leads to an increased resorptive surface that exploits surface near soil layers. Since root growth is regulated through PAT, the P_i-dependence of AUX1-mediated auxin influx was studied. These experiments revealed that the strength of AUX1-mediated H^+-coupled auxin influx was negatively correlated with the availability of P_i (see **Fig. 3.15**). Significantly, AUX1, PIN2, and TIR1 were already shown to have roles in the low P_i adaptive response of the root. Whereas P_i starvation has been reported to impair auxin efflux (Kumar *et al.* 2015), the transcription of *TIR1* and *AUX1* seems to be positively regulated by low P_i (Perez-Torres *et al.* 2008; Kumar *et al.* 2015). Taken together, low P_i levels thus induce an increased auxin responsiveness of root cells resulting in the above-described RSA alterations (Lopez-Bucio *et al.* 2002; Al-Ghazi *et al.* 2003; Nacry *et al.* 2005). Regarding root hairs, *AUX1* was recently shown to be essential for growth promotion under P_i-limiting conditions. Both in *Oryza sativa* and *A. thaliana* AUX1-mediated transport of auxin from the root apex to the differentiation zone was demonstrated to be of critical importance for the root hair adaptive response to low P_i (Bhosale *et al.* 2017; Giri *et al.* 2017). The observed amplification of auxin-induced membrane responses at low P_i conditions fits very well with the P_i-adaptive response of roots. A transcriptional upregulation of *AUX1* as it has been reported by Kumar *et al*. (2015) based on an increased AUX1::YFP fluorescence signal in the root elongation zone can be regarded as the most likely reason for the increased auxin influx observed under low P_i.

4.2.3. Drawbacks of experimental approaches based on pharmacology

Chemical inhibitors have been used intensively to study auxin transport and signaling (Morris and Thomas 1978; Benkova *et al.* 2003; Friml *et al.* 2003; Ottenschläger *et al.* 2003; Hayashi *et al.* 2012; Fendrych *et al.* 2016). Among them, TIBA and NPA are potent auxin efflux inhibitors that interfere with the intracellular trafficking of PM-localized PIN proteins (Geldner *et al.* 2001).
TIBA, in contrast to NPA, led to a severely diminished auxin influx response (see **Fig. 3.16**). Addtionally, TIBA, but not NPA, caused a severe positive shift of the resting PM potential and the inhibition of basal H^+ efflux (see **Fig. 3.16**). These PM responses point towards the inhibition of the root H^+-ATPases by TIBA. This process should lead to a reduction of the pmf needed for AUX1-

dependent auxin influx and thus explains the lack of the auxin-induced electrical responses in the presence of TIBA. How could it be possible that TIBA, an auxin efflux inhibitor, interferes with the activity of the PM H^+-ATPase?

An explanation is provided by Geldner *et al*. (2001). They showed that the inhibitory effect of auxin efflux inhibitors on the subcellular trafficking of PINs is not restricted to the PIN proteins but is a general effect. For example, the authors also found the subcellular cycling of the PM H^+-ATPase to be sensitive to TIBA. From this it seems apparent that the observed TIBA-induced root cell depolarization and the absence of basal H^+-efflux in TIBA treated roots is indeed caused through the impairment of the subcellular cycling and thus inhibition of the PM H^+-ATPase. The absence of a NPA-induced depolarization can be explained through the different effective concentrations reported by Geldner *et al*. (2001). In this study, TIBA and NPA were used at 20 µM. However, Geldner *et al.* (2001) reported an effective concentration for TIBA of 25 µM, whereas for NPA this concentration was 200 µM. NPA-treatment, as performed in this study, was thus one order of magnitude below the effective concentration and could therefore not interfere with subcellular protein cycling.

Besides TIBA, several $SCF^{TIR1/AFB}$ inhibitors, among them auxinole, were also found to influence the resting root cell PM potential (see **Fig. 3.19** and **Fig.3.20**). Especially PEO-IAA, N-ethyl- as well as N-ethoxy-ethyl-PEO-IAA and auxinole severely affected the resting PM potential of root hair cells. Apart from a transcriptional auxin response suppressed through auxinole (Hayashi *et al.* 2012) only limited data on the effects of these auxin antagonists is available and so far, their effects on the subcellular cycling of PM-localized proteins has not been analysed. However, PEO-IAA was shown to suppress the basal, as well as the auxin-induced expression of *KAT1*, which encodes an inward-rectifying K^+ channel (Philippar *et al.* 2004; Takahashi *et al.* 2012). Although not emphasized by Takahashi *et al*. (2012), the effect of PEO-IAA on basal *KAT1* expression might explain the hyperpolarization of the root cells observed for this auxin antagonist. However, *KAT1* is not significantly expressed in root tissues (Philippar *et al.* 2004). Therefore, a similar effect of PEO-IAA on the expression of K^+-inward rectifying channels present in root cells, like AKT1 (Ivashikina *et al.* 2001), could potentially explain the observed hyperpolarization.

Concerning the root hair PM potential depolarizations induced through the other auxin antagonists, especially through auxinole, further research is needed.

4.2.4. A new Ca^{2+}-dependent and membrane-localized fast auxin signaling pathway

4.2.4.1. The current model

External application of auxin to *A. thaliana* roots triggers Cytosolic Ca^{2+} elevations (Monshausen *et al.* 2011). With CNGC14, a PM-localized and presumably Ca^{2+}-permeable ion channel, has been identified to be responsible for those auxin-related Ca^{2+} signals (Shih *et al.* 2015). However, the molecular mechanism that connects auxin transport and auxin perception to the Ca^{2+} influx has not been uncovered. A possible model has been brought forward by Monshausen *et al*. (2011) and especially by Shih *et al*. (2015). This model postulates that auxin perception by an unknown apoplastic auxin receptor results in CNGC14-mediated Ca^{2+} influx. Elevations of the $[Ca^{2+}]_{cyt}$ subsequently lead to the stimulation of not further described membrane processes responsible for the alkalinization of the cell wall and the subsequent inhibition root cell elongation during the gravitropic response (**Fig 4.4**).

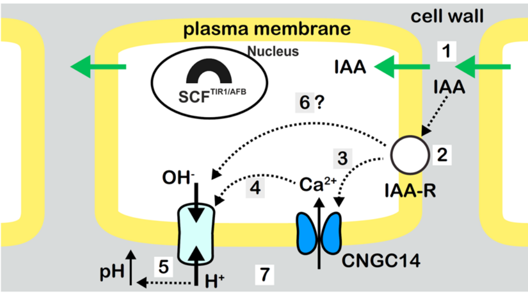

Fig. 4.4: Model of Ca^{2+}-dependent auxin signaling published by Shih *et al.* (2015). External auxin (1) is perceived by an unknown receptor (2), and CNGC14 mediates cytosolic Ca^{2+} signals (3). Ca^{2+} signals activate unknown membrane processes (4) leading to cell wall alkalinization (5). Ca^{2+}-independent processes, as well as other not further described processes, might result in alkalinization through activation of a H^+/OH^--conductance (6, 7). Modified and reused with permission from Elsevier.

Shih *et al.* (2015) derived this model from the following observations. They demonstrated that both the external application of auxin as well as a stimulation by gravity induce the rapid alkalinization of the root surface and $[Ca^{2+}]_{cyt}$ elevations. In case of the gravistimulus, both signals were shown to occur at the lower site of the root where increased auxin levels inhibit cell elongation. The auxin-induced change in root surface pH was found to be impaired in the *cngc14* loss-of-function mutant (Shih *et al.* 2015). Importantly, the surface pH change was also found to be independent of the nuclear $SCF^{TIR1/AFB}$-complex for auxin perception as it still occurred in the *tir1afb2afb3* triple loss-of-function mutant (Monshausen *et al.* 2011). Those findings point towards a fast auxin signaling pathway, which includes the activation of PM-localized Ca^{2+} channels and which is independent of the well-known $SCF^{TIR1/AFB}$-IAA-Aux/IAA perception complex

4.2.4.2. AUX1 is the PM-localized H^+ conductance

Although the model by Shih *et al*. (2015) is compelling and complementing the mechanism of root gravitropism, it relies on the assumption of a yet to be discovered H^+/OH^- conductance responsible for apoplastic alkalinisation. Responsible for this suggestion could be a possible misinterpretation of surface pH changes. A comparison of the data from Shih *et al*. (2015) with the data presented in this work revealed the kinetic correlation between the auxin-induced processes of surface pH changes and AUX1-dependent root cell PM depolarization as well as H^+ influx (**Fig. 4.5,** see **Chapter 4.2.1.**). By taking this close correlation into account, the auxin-induced surface pH change is apparently caused by the AUX1-mediated H^+-coupled uptake of auxin and not by an unknown PM-associated ion signaling process. In accordance with this assumption, Monshausen *et al*. (2011) already reported an absent auxin-induced alkalinization of the root surface of the *aux1-21* loss-of-function mutant. However, the authors still concluded that an unspecified H^+/OH^- PM conductance is responsible for the auxin-induced apoplastic alkalinization.

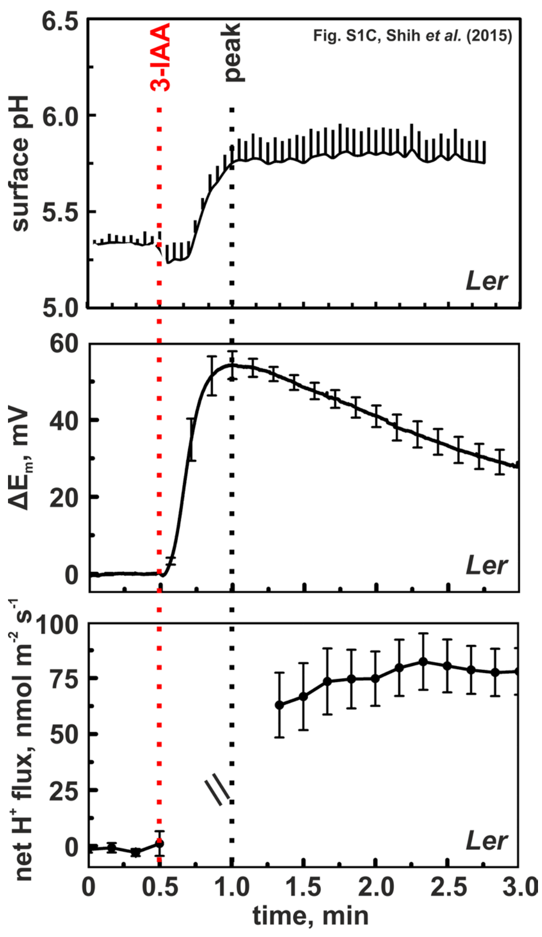

Fig. 4.5: Correlation between auxin-induced root responses. The graph at the top shows a modified version of Fig. S1C from Shih *et al*. (2015) displaying wild type root surface pH in response to 3-IAA application (red dotted line). The graphs in the middle and at the bottom show results from this work. Being at the same time scale (see bottom graph) as the upper graph, the graphs show the auxin-induced wild type root hair PM potential depolarization (middle) and H^+ influx response (bottom). All graphs were aligned to the point of 3-IAA application. The black dotted line marks the peak response in surface pH and membrane potential change. H^+-flux data are interrupted due to the application of 3-IAA. In all graphs, data of the wild type accession *Ler* are depicted. Top panel reused with permission from Elsevier.

4.2.4.3. Fast auxin signaling depends on TIR1/AFB-mediated auxin perception

The model by Shih *et al*. (2015) additionally assumes a yet to be discovered auxin receptor, capable of sensing extracellular auxin. The extracellular auxin receptor was long thought to by ABP1, but this protein was recently shown to have no auxin-related physiological function, despite of its auxin binding capacity (Woo *et al.* 2002; Gao *et al.* 2015). In line with the recent results of Gao *et al*. (2015), the loss of ABP1 did not affect the auxin-induced depolarization of the root hair PM potential (see **Fig. 3.11**) and Shih *et al*. (2015) excluded a contribution of ABP1 to the auxin-dependent change in surface pH.

Experiments, in which the AUX1-dependent root hair depolarization and H^+ influx were probed in *tir1afb2afb3* triple mutant and auxinole treated wild type roots, showed a strong reduction of both responses. Significantly, the expression levels of *AUX1* were neither affected by the absence of the F-box proteins nor through auxinole treatment (see **Fig. 3.22**). The data provided by this thesis thus shows a clear posttranscriptional downregulation of AUX1-mediated auxin uptake through the loss of $SCF^{TIR1/AFB}$ functionality.

In roots and the hypocotyl auxin-induced, apoplastic pH changes were shown to occur simultaneously with modifications in the rate of cell elongation (Evans *et al.* 1994; Scheitz *et al.* 2013; Shih *et al.* 2015; Fendrych *et al.* 2016). Ruegger *et al*. (1998) and Scheitz *et al*. (2013) further demonstrated that auxin-sensitive root and hypocotyl growth depends on a functional auxin perception system involving TIR1/AFB-class F-box proteins. In contrast to this, Monshausen *et al*. (2011) reported auxin-induced apoplastic alkalinization to be independent of these F-box proteins. Unfortunately, Monshausen and co-workers did not provide a quantification or statistical analysis of their data regarding the *tir1afb2afb3* mutant, but under consideration of the described variations of auxin-induced responses in this mutant ((Parry *et al.* 2009); see **Fig. 3.22**), it is possible that their measurement ranks at the more wild type-like end of the scale.

4.2.4.4. CNGC14-mediated cytosolic Ca^{2+} signals feed back into AUX1 activity

The AUX1-dependent depolarization of the root hair PM potential was shown to co-occur with $[Ca^{2+}]_{cyt}$ elevations (see **Fig 3.17**). This is in accordance with the results of Monshausen *et al*. (2011) and Shih *et al*. (2015) who showed that externally applied auxin, as well as gravitropic stimulation, induce apoplastic alkalinization, $[Ca^{2+}]_{cyt}$ elevations and inhibition of cell elongation.

The dependency of auxin-induced $[Ca^{2+}]_{cyt}$ elevations on auxin perception by TIR1-like receptors is shown in multiple approaches in this work. First of all, it is shown that only physiological active auxins are able to trigger cytosolic Ca^{2+} signals (see **Fig. 3.21**). Secondly, a chemical block of TIR1 by auxinole suppresses the auxin-induced Ca^{2+} signals (see **Fig. 3.19**, **Fig. 3.20** and **Fig. 3.22**), as well as the induction of wave-like propagating Ca^{2+} signals upon cytosolic injection of auxin (see **Fig. 3.23**). Finally, the auxin-induced Ca^{2+} influx in stongly impaired in the *tir1afb2afb3* triple mutant (see **Fig. 3.22**).

Shih *et al.* (2015) were the first to show that CNGC14 is the sole responsible Ca^{2+} channel for auxin-induced $[Ca^{2+}]_{cyt}$ elevations. In accordance with their work, responses like Ca^{2+} influx and the Ca^{2+} influx-associated PM depolarization through cytosolic auxin application were absent in the *cngc14* mutant (see **Fig. 3.19** and **Fig. 3.24**). In contrast to the results by Monshausen *et al*. (2011) this work demonstrated the necessity of TIR1-like auxin receptors for fast auxin signaling. Those results thus place CNGC14 downstream of an established auxin perception mechanism, rather than of an unknown apoplastic receptor. It is unclear how F-box-mediated auxin perception could lead to the activation of Ca^{2+} channels like CNGC14. However, a protein phosphatase or kinase linking auxin perception with the activation of CNGC14 would be in analogy with the fast ABA signaling pathway, which links cytosolic ABA perception by RCAR/PYR/PYL receptors with the activation of the anion channel SLAC1 in guard cells (Geiger *et al.* 2009; Geiger *et al.* 2010).

It is likely that auxin does not only regulate CNGC14, but also that CNGC14 has an impact on auxin uptake by regulating AUX1, since the *cngc14* mutant also showed no auxin uptake activity as observed by the absent AUX1-dependent root hair PM depolarization. Because the expression of AUX1 in the *cngc14* loss-of-function mutant is not different from the wild type a post-translational regulation of AUX1 through CNGC14-mediated Ca^{2+} signals seems conceivable.

Further support for a Ca^{2+}-dependent regulation of AUX1 was obtained through experiments in which the broad range Ca^{2+} channel blocker La^{3+} was not only able to block auxin-induced cytosolic $[Ca^{2+}]_{cyt}$ elevations but also AUX1-mediated auxin transport (see **Fig. 3.25**).

In line with these results, La^{3+} has already been shown to mimic the reduced auxin-sensitivity of root growth of the *cngc14* mutant in wild type roots (Shih *et al.* 2015). Moreover, La^{3+} should be able to block CNGC14 directly, since the *A. thaliana* CNGCs 5, 6, and 18 were reported to be blocked in the presence of La^{3+} in patch-clamp experiments (Wang *et al.* 2013b; Gao *et al.* 2014).

Importantly, auxin-induced $[Ca^{2+}]_{cyt}$ elevations lost their transient nature and were prolonged in the presence of La^{3+} (see **Fig. 3.25**). Such an effect might point towards a severe interference of La^{3+} with Ca^{2+} homeostasis. Since H^+/Ca^{2+} exchanger and Ca^{2+}-ATPases are suggested to be responsible for maintaining low basal $[Ca^{2+}]_{cyt}$ (Roelfsema and Hedrich 2010; Schönknecht 2013), a negative regulation of active Ca^{2+} transport through La^{3+} could explain the observed prolonged $[Ca^{2+}]_{cyt}$ elevations. Because the La^{3+}-induced loss of AUX1-mediated auxin uptake coincides with a supposedly disturbed Ca^{2+} homeostasis, those findings substantiate the crucial role of fast Ca^{2+} signaling as well as the importance of Ca^{2+} homeostasis for the activity of AUX1.

4.2.4.5. Auxin-induced Ca^{2+} waves regulate auxin transport over greater distances

Auxin-induced Ca^{2+} signals are not locally restricted to the site of auxin-stimulation, but instead are transmitted as waves through root tissues after an auxin-stimulus has been locally applied via intracellular microelectrodes (see **Fig. 3.23** and **Fig. 3.26**). In order to propose that those auxin-triggered Ca^{2+} signals represent self-sustained long distance signals, diffusion of auxin and PAT have to be excluded as possible reasons of an auxin stimulation that would not be restricted to a single root cell.

Concerning diffusion, the complete deprotonation of auxin at the cytosolic pH should lead to the trapping of the anion inside the cell (see **Fig. 1.3**). Hence, apart from efflux carriers, only leakage through a rapture of the PM (e.g. at the site of impalement) could lead to diffusion of auxin to neighbouring cells. Although the co-injected dye LY was rapidly taken up into the vacuole, it did not indicate a major leakage in the beginning of experiments.

Concerning the possibility of PAT as the cause of the propagating Ca^{2+} signals the velocity of the Ca^{2+} wave can be compared to known *in planta* auxin transport rates. The propagation rate of the lateral transmitted Ca^{2+} wave of 5 mm/h is well within compiled auxin transport rates in plant roots of up to 12 mm/h (Kramer *et al.* 2011). The strong effect of amplification of the Ca^{2+} signal observable at the opposite site of injection, however, cannot be explained by auxin transport. Concerning the longitudinal wave, the speed of this Ca^{2+} wave (40 mm/h) is much greater than any reported velocities for auxin transport (Kramer *et al.* 2011). *In silico* simulations of auxin transport out of a biosynthesis maximum in a single epidermal cell of the root elongation zone, however, showed the generation of an auxin maximum at the quiescent center within two minutes (Grieneisen *et al.* 2007). However, the authors employed a permeability of basal-localized PIN efflux carriers of 20 µm/s (72 mm/h) which is much faster than any experimentally determined value for auxin transport. Moreover, a diffusion constant for IAA (600 $\mu m^2/s$) was employed which was originally defined in an aqueous solution (Robinson *et al.* 1990). In the gel-like viscosity of the extra- and intracellular matrix, however, this coefficient should be significantly lower.

Although the distribution of auxin from a cellular maximum throughout the tissues of the root cannot be unequivocally excluded by the experimental data presented herein, both the lateral as well as the acropetal component of the auxin injection-induced Ca^{2+} wave are still likely to be propagated independently from the movement of auxin. Provided that this is indeed the case a mechanism that could underlie the propagation of such Ca^{2+} waves could potentially be their connection to the parallel propagation of ROS signals ((Kimura *et al.* 2012; Dubiella *et al.* 2013); see **Chapter 1.4.2.**).

Significantly, the decay of the DII-Venus signal in apical root parts correlates with the speed at which the longitudinal Ca^{2+} wave propagates (see **Fig. 3.26**). A possible connection between both signals is substantiated through the impaired decay of DII-Venus in La^{3+} treated roots in which the induction and propagation of a Ca^{2+} wave should be likewise impaired. Since, the DII-Venus signal is a reciprocal measure of cytosolic auxin levels, the auxin-induced Ca^{2+} waves can be assumed to trigger the cytosolic accumulation of auxin in cells, that are at distance from the locally applied auxin stimulus. As discussed above, La^{3+} inhibits AUX1 possibly through an inhibition of CNGC14-mediated Ca^{2+} signaling and/or a deregulation of Ca^{2+} homeostasis that are integrated into a Ca^{2+}-dependent post-translational modification of the auxin influx transporter. Hence, in the presence of La^{3+}, the Ca^{2+}-dependent cytosolic accumulation of auxin would be impaired.

Together with the obviously important role of CNGC14 in fast auxin signalling, the above described La^{3+}-sensitive correlation between Ca^{2+} signals and cellular auxin levels make it thus likely that the cytosolic accumulation of auxin in root cells is under the control of a Ca^{2+}-dependent regulation of auxin transporters, especially of AUX1.

4.2.4.6. A new model for fast Ca^{2+}-dependent and membrane-localized auxin signaling

In summary, the findings of this work substantiate, adapt and expand the Ca^{2+}-dependent fast auxin signaling model of Shih *et al*. (2015) on three major points: (**i**) the activation of CNGC14 does not require an unknown apoplastic auxin receptor, but rather relies on the described auxin perception by $SCF^{TIR1/AFB}$ complexes; (**ii**) auxin-induced $[Ca^{2+}]_{cyt}$ elevations do not activate unknown H^+/OH^- PM conductances, but instead seem to target AUX1-mediated H^+-coupled auxin uptake and (**iii**) auxin-induced cytosolic Ca^{2+} signals can propagate over longer distances in plant tissues and organs and are likely to influence auxin transport and physiology distant from a local auxin stimulus. Hence, a model (**Fig. 4.6**) arises in which the cytosolic perception of IAA activates CNGC14-mediated Ca^{2+} influx. The signature of the Ca^{2+} signals thereby seems to be integrated into auxin transport. Whereas a proper CNGC14 functionality appears to be necessary for AUX1 activity, a disturbance of the Ca^{2+} homeostasis by the block of Ca^{2+} channels (and possibly Ca^{2+} transporters) through La^{3+} seems to have a negative influence on AUX1. Additionally, two feedback loops regulating CNGC14 are possible.

Several CNGCs from *A. thaliana*, including CNGC14, are known to interact with Ca^{2+} sensing proteins of the CaM family (DeFalco *et al.* 2016; Fischer *et al.* 2017). Concerning a diverse regulation of CNGCs, DeFalco *et al.* (2016) proposed a model in which the activity of CNGC12 is regulated by CaM interaction at their C- and N-terminal domains. Whereas a Ca^{2+}-facilitatet binding of CaMs to the C-terminal domain positively regulates channel function, a CaM binding domain at the N-terminus might be involved in a negative feedback inhibition of the channel.

A second possible feed back loop regulating the activity of CNGC14 is based on three reported observations. (**i**) The activities of ROS-producing NADPH oxidases like RBOHD are apparently Ca^{2+}-regulated via a direct integration of Ca^{2+} signals through EF-hand motifs as well as indirectly through N-terminal phosphorylation sites (Foreman *et al.* 2003; Ogasawara *et al.* 2008; Kimura *et al.* 2012; Dubiella *et al.* 2013). (**ii**) ROS stimulate Ca^{2+} influx through hyperpolarization activated Ca^{2+} channels in root epidermal protoplasts (Foreman *et al.* 2003) and (**iii**) root hair tip-localized CNGC14 promotes $[Ca^{2+}]_{cyt}$ fluctuations and root hair growth (Zhang *et al.* 2017b).

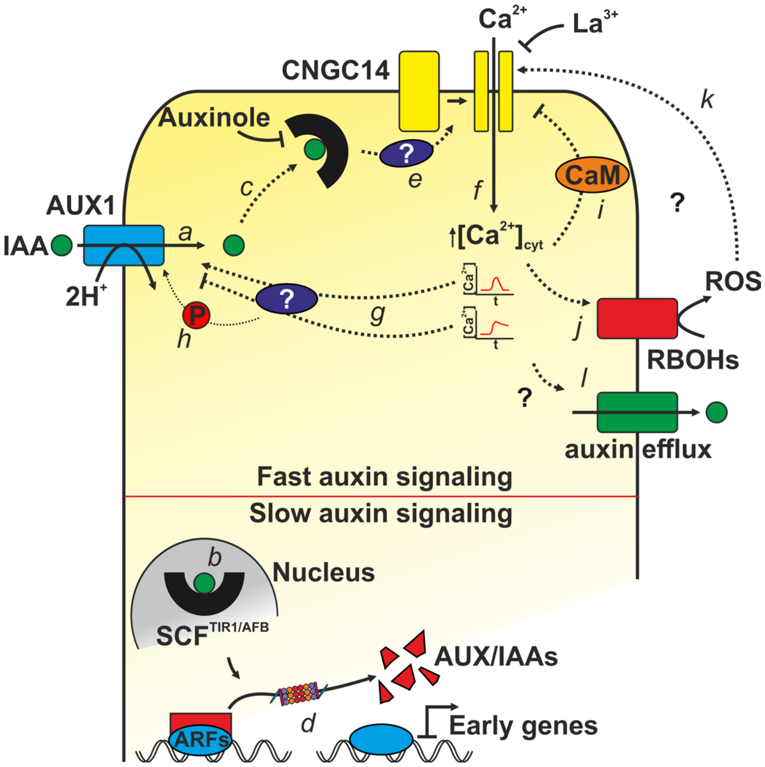

Fig 4.6: Model of Fast Ca^{2+}-dependent auxin signaling. H^+/IAA symport via AUX1 (**a**) results in IAA perception by nuclear (**b**) and cytosolic (**c**) receptors. Nuclear perception activates slow auxin signaling via degradation of AUX/IAA TFs leading to ARF-promoted transcriptional changes (**d**). Auxinole-sensitive cytosolic perception activates CNGC14 through so far unknown factors (**e**). The La^{3+}-sensitive Ca^{2+} influx results in $[Ca^{2+}]_{cyt}$ elevations (**f**), $[Ca^{2+}]_{cyt}$ regulates AUX1 (**g**). Phosphorylation of AUX1 is a possible target for Ca^{2+}-dependent kinases (**h**). Ca^{2+} might also feedback into CNGC14 through the interaction with CaMs (**i**). CNGC14-mediated Ca^{2+} signals might additionally stimulate the production of ROS (**j**) which might positively feedback into CNGC14 activity (**k**). Additionally, auxin efflux might also be regulated through CNGC14 mediated Ca^{2+}-signals (**l**).

Four major so far unknown factors persist in this model.

(**i**) Ubiquitylation-dependent proteasomal degradation of target transcription factors so far represents the only established mechanism of $SCF^{TIR1/AFB}$-mediated perception of auxin. Thus, it remains to be tested how this receptor complex can trigger the fast activation of CNGC14. An example for regulation of a Ca^{2+} channel by a PM bound ubiquitin ligase exists, since the E3-type ubiquitin ligase THERMAL RESISTANCE1 (TR1) from *Brassica napus* was found to regulate this class of ion channels (Liu *et al.* 2014). The fast induction of $[Ca^{2+}]_{cyt}$ elevations in response to auxin, however, argues against a nuclear perception mechanism, or a role for poly-ubiquitinylation of target proteins, as these possibilities normally would require a much longer time. TIR1/AFB-class F-box proteins have been reported to be localized to the nucleus in homo- and heterologous expression systems (Dharmasiri *et al.* 2005b; Dezfulian *et al.* 2016; Wang *et al.* 2016). In the case of AFB2, however, a considerable proportion of the proteins was shown to have cytosolic localization (Wang *et al.* 2016; Katz and Chamovitz 2017). Possibly, AFB2 or AFB3 are crucial for cytosolic perception of auxin and CNGC14 activation. A functional complex consisting of an auxin binding F-box protein, a kinase or phosphatase, and CNGC14 thus seems conceivable. AUX1 might be a part of such complex since a physical interaction with at least TIR1 has been shown (Yu *et al.* 2013). Such a complex would account for the immediate auxin-induced activation of CNGC14. Other mechanisms that cause elevated $[Ca^{2+}]_{cyt}$ might be the direct activation of CNGC14 through the auxin-induced PM potential depolarization, or through the associated H^+ influx. These options could be studied through the analysis of CNGC14 in patch-clamp or oocyte experiments, which can gain insights into regulation mechanisms of the channel.

(**ii**) So far, there is no direct evidence for a Ca^{2+}-dependent regulation of auxin transporters. As outlined in **Chapter 1.4.3.**, the integration of Ca^{2+} signals into the phosphorylation of PIN efflux carriers by members of the PID and D6PK subfamilies of AGCVIII class protein kinases is discussed but not yet proven. PID and D6PK kinases itself are not discussed to be Ca^{2+}-dependent (Zourelidou *et al.* 2009; Zourelidou *et al.* 2014), however, a possible integration of Ca^{2+} signals might occur via the interaction of PID with the Ca^{2+} binding proteins PID BINDING PROTEIN1 (PBP1) and TOUCH3 (TCH3; (Benjamins *et al.* 2003)).

In the case of AUX1, no post-translational regulation apart from its subcellular trafficking is known. Potential phosphorylation sites of AUX1 were determined with the PhosPhAt database (PhosPhAt 4.0; http://phosphat.uni-hohenheim.de/; (Heazlewood *et al.* 2008)). This approach revealed that AUX1 has eight putative phosphorylation sites at cytosolic loops, from which three reside within the N-terminal domain (**Fig 4.7**). These residues represent possible targets for protein kinases and phosphatases, which may act in a fast Ca^{2+}-dependent manner.

AUX1

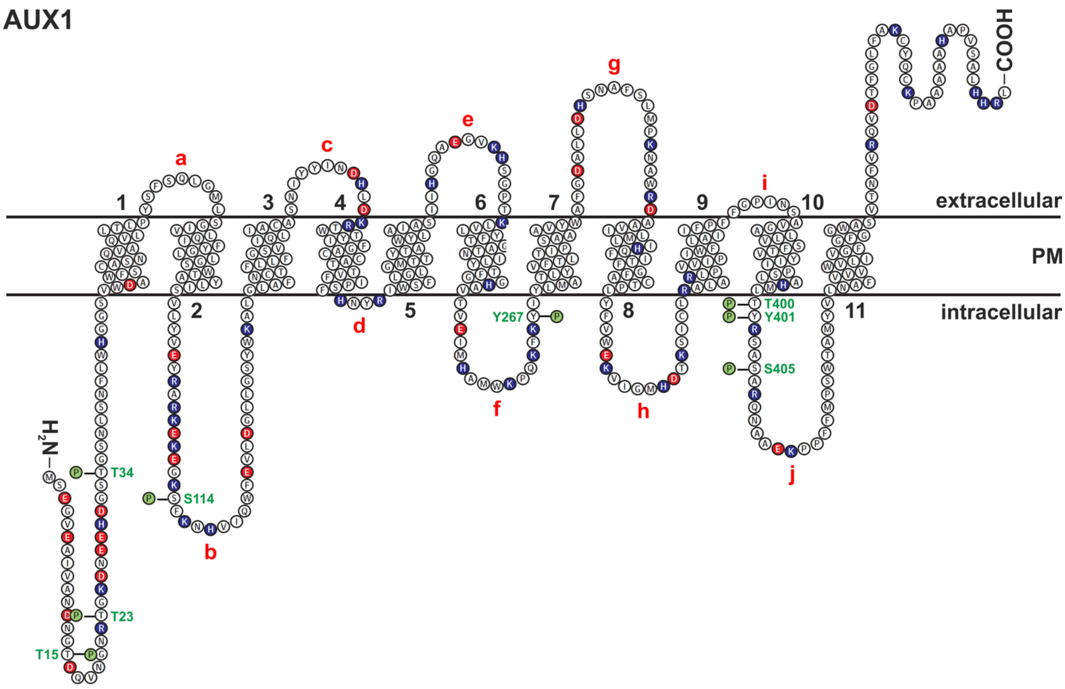

Fig. 4.7: Topology model of AUX1 with putative cytosolic phosphorylation sites. The sequence of extra- and intracellular loops (a-j) and transmembrane domains (1-11) is based on the Aramemnon consensus topology prediction for AUX1 (http://aramemnon.uni-koeln.de/) with phosphorylation sites (green) as predicted by the PhosPhAt 4.0 database (http://phosphat.uni-hohenheim.de/). Blue circles represent basic amino acid residues, and red circles show acidic amino acids. The model was generated using the LaTeX application TeXtopo by Dirk Becker, Molecular plant physiology, and biophysics, University of Wuerzburg.

(**iii**) Besides the contribution of AUX1, this work also showed that the loss of the auxin efflux carrier PIN2 has a negative influence on the auxin-induce PM depolarization (see **Fig. 3.11**). The efflux of the IAA anion would, of course, result in a depolarization of the PM. Therefore, it remains to be tested if the reduced response of the *pin2* loss-of-function mutant is due to a lack of auxin efflux or if the loss of PIN2 has repercussions on the activity of AUX1. The loss of PINs was shown to result in enhanced transcriptional auxin responses (Friml *et al.* 2002a; Benkova *et al.* 2003; Blilou *et al.* 2005). As this observations is likely caused by elevated cytosolic auxin levels, those could potentially negatively feedback into auxin influx via a Ca^{2+}-dependent regulation of AUX1, thus explaining the reduced PM depolarization in the *pin2* mutant.

(**iv**) In general, the integration of ROS signals into auxin physiology is elusive, and this work does not provide new findings related to this subject. An integration of ROS signals into the fast auxin signaling pathway is nevertheless very likely based on the apparent inter-dependency of RBOHD-dependent ROS production and CNGC14-mediated Ca^{2+} oscillations during root hair growth

(Foreman *et al.* 2003; Ogasawara *et al.* 2008; Kimura *et al.* 2012; Dubiella *et al.* 2013; Zhang *et al.* 2017b). Although this hypothesis remains to be investigated, ROS were shown to occur during the gravitropic root response in maize (Joo *et al.* 2001). Additionally, ROS seem to be involved in the auxin-directed alteration of the *A. thaliana* RSA during P_i-starvation (Tyburski *et al.* 2009).

The addition of ROS expands the model of fast auxin signaling because it provides additional possibilities for a fine-tuned regulation of CNGC14 and auxin transport. If RBOHs are components of fast auxin signaling and in which way the production of reactive oxygen species influences the other components remains to be investigated.

4.2.4.7. Consequences that arise for auxin physiology from the new model

The importance of fast Ca^{2+}-dependent signaling during the root gravitropic response has already been highlighted by Shih *et al*. (2015). However, the supplements to this model described in this work provide novel insight on auxin-sensitive root and root hair growth.

4.2.4.7.1. Gravitropism and auxin-induced root growth inhibition

A shift of the gravitational vector leads to the redirection of root apical auxin fluxes due to the change in the polar localization of PIN3 at the PM of gravity sensing columella cells (Friml *et al.* 2002b). Auxin now preferentially flows through cells of the lateral root cap and epidermis at the new physiologically lower site of the root (Ottenschläger *et al.* 2003). As this redirection of auxin fluxes should result in a wave-like pattern, it is accompanied by a likewise basipetally propagating Ca^{2+} wave and ROS signals (Joo *et al.* 2001; Monshausen *et al.* 2011; Shih *et al.* 2015). Those cytosolic Ca^{2+} signals could feed back to an enhanced auxin transport capacity through the stimulation of AUX1. Additionally, Ca^{2+} and ROS signals could result from a self-sustaining activation loop. Such a loop could be responsible for signal propagation as auxin-induced CNGC14 activation could result in RBOH-mediated ROS production which in turn might feed back into cytosolic Ca^{2+} signals stimulating AUX1. This kind of propagation could potentially support the basipetal flow of auxin as the continuous stimulation of auxin transport in adjacent cells could be decoupled from the auxin threshold needed for CNGC14 activation. Successively, this signaling loop would reach the cells of the root elongation zone faster as predicted for an auxin transport based mechanism.

Based on the coincidence of auxin-induced apoplastic alkalinization and TIR1/AFB-dependent root growth inhibition (Monshausen *et al.* 2011; Scheitz *et al.* 2013; Shih *et al.* 2015) two possibilities explaining the inhibition of cell elongation in the context of the acid growth theory arise.

(**i**) As it was shown for the root, the auxin-induced Ca^{2+} signals are possibly integrated in a CBL2/CIPK11-dependent downregulation of the PM H^+-ATPase activity thus causing apoplastic alkalinization (Fuglsang *et al.* 2007). The promotion of root growth, on the other hand, through low auxin levels was shown to result from the SAUR19-dependent inhibition of PP2C-D-mediated dephosphorylation of the PM H^+-ATPase (Spartz *et al.* 2014). The same mechanism was reported to induce cell elongation in the hypocotyl with a lag time of 20 minutes after auxin application (Fendrych *et al.* 2016). Therefore, it seems unlikely that the deactivation of the H^+ pump with the successive creeping cell wall alkalinization can account for the immediate responses observed in roots after external auxin application.

(**ii**) Monshausen *et al*. (2011) and Shih *et al*. (2015) suggested an unknown H^+/OH^- PM conductance activated by auxin-induced Ca^{2+} signals to cause rapid cell wall alkalinization. The results presented in this work, however, unequivocally showed this conductance to be the AUX1-mediated H^+/IAA symport. Through this, AUX1 is placed at a central position to explain the high auxin-sensitivity of the root in general and in particular the gravitropic root response, as it is the AUX1 mediated H^+ influx which seems to cause the alkalinization of the cell wall and the subsequent fast inhibition of cell elongation.

Within this model the PM H^+-ATPase would have a role as a counterbalancing factor as its deactivation upon increasing auxin levels would prevent the pmf, which was reduced through H^+ and Ca^{2+} influx, to return to pre-existing levels rapidly. Through a more alkaline apoplastic pH and a reduced capacity for osmolyte uptake, a prolonged reduced pmf would consequently inhibit cell elongation as well as auxin uptake, thus balancing both against each other.

4.2.4.7.2. Root hair growth

The polar growth of root hairs is another auxin sensitive process. Like in pollen tubes, a tip-focused $[Ca^{2+}]_{cyt}$ gradient which regulates the stability of actin filaments, H^+ extrusion and ROS generation is essential for the polar growth of root hairs (Mendrinna and Persson 2015). The $[Ca^{2+}]_{cyt}$ of root hairs undergoes periodic fluctuations, which are paralleled by changes in growth rate, pH and ROS (Monshausen *et al.* 2007; Monshausen *et al.* 2008). ROS were further found to induce Ca^{2+} influx into root hair cells, thus supporting a positive feedback loop between the two signaling molecules

(Foreman *et al.* 2003). Significantly, CNGC14 was found to be localized at the root hair tip, and since the *cngc14* mutant showed a short root hair phenotype and reduced $[Ca^{2+}]_{cyt}$ fluctuations, CNGC14 seems to be responsible for the growth directing Ca^{2+} influx (Zhang *et al.* 2017b).

Auxin is also involved in root hair development, because PAT seems to be organized in a way that the maintenance of relatively low auxin levels in root hair cells is necessary for their differentiation and outgrowth (Jones *et al.* 2009). Consequently, the absence of AUX1, PIN2 or of the auxin perceiving TIR1-like F-box proteins results in a short root hair phenotype (Dharmasiri *et al.* 2005b; Jones *et al.* 2009; Rigas *et al.* 2013).

Moreover, the herein described close interaction between auxin transport, perception and Ca^{2+} influx seems to be essential for the maintenance of root hair growth during P_i starvation. AUX1 was recently shown to be necessary for the root hair adaptive response to low P_i (Bhosale *et al.* 2017; Giri *et al.* 2017). Prolonged higher cytosolic auxin levels resulting from a low P_i-induced upregulation of AUX1 abundance (Kumar *et al.* 2015) could lead to a likewise higher activity of CNGC14, which could additionally be amplified and sustained through the involvement of RBOHD-dependent ROS production. Ultimately, this could help to maintain the apical $[Ca^{2+}]_{cyt}$ maximum necessary for the coordination of root hair growth during nutrient foraging under P_i starving conditions.

In support for this connection between $[Ca^{2+}]_{cyt}$ and auxin, with CPK11 a Ca^{2+}-dependent protein kinase was found to be a downstream target of the auxin-inducible transcription factor RSL4 (Vijayakumar *et al.* 2016). A role of CPK11 in an auxin- and Ca^{2+}-dependent signaling pathway regulating root hair elongation especially under low P_i conditions seems conceivable because the loss of RSL4 disrupts the root hair adaptive response to low P_i (Bhosale *et al.* 2017).

This signaling network maintaining the $[Ca^{2+}]_{cyt}$ gradient in response to low P_i further describes that the connection between AUX1 and CNGC14 is seemingly not limited to fast auxin signaling. It seems further able to mediate slow signaling processes such as the response to a gradual depletion of the available P_i in the surrounding soil.

4.2.5. Outlook and open questions for the analysis of fast auxin signaling

Although the results of this work have been included into the new model for fast Ca^{2+}-dependent auxin signaling, some major questions remain to be addressed in future studies.

(i) What is the exact mechanism of AUX1-mediated H^+/IAA^- symport?

Although auxin uptake occurs by electrogenic transport mechanism, the exact stoichiometry of auxin uptake is still elusive. As the simultaneous influx of Ca^{2+}, as well as the PIN-mediated efflux of the IAA anion will also cause a root hair PM depolarization, it would be of major advantage to know the transport mechanism of AUX1. Functional expression of AUX1, in a system that is suitable for two electrode voltage-clamp, or patch-clamp experiments, like pollen tubes, oocytes or mesophyll protoplasts would help to deduce the stoichiometry of H^+/IAA^- symport. Moreover, such an expression system can be used to assess the influence of H^+- and IAA- concentrations, as well as the membrane voltage-dependence on AUX1 activity. These studies could be complemented by structure-function analysis, in which certain protein domains of AUX1 are mutated or exchanged with those of related proteins, like LAX1/2/3. In addition, modelling the three-dimensional structure of AUX1, either by crystallization of the protein, or based on the homology to other amino acid permeases, could gain information on the transport mechanism of this auxin transporter.

(ii) Is AUX1 a target for Ca^{2+}-dependent protein kinases or phosphatases?

AUX1 seems to be a target for post-transcriptional regulation, since putative phosphorylation sites reside in cytoplasmic loops, as well as in the N-terminal domain. In this regard, a database search for AUX1 interacting proteins on ARAPORT (https://www.araport.org/) revealed that at least three putative protein kinases, AT1G07860, AT5G16590, and AT5G59650 as well as the CaM-binding IQ-domain protein AT2G26180 are interacting with AUX1. This information thus offers a possibility to study the Ca^{2+}-dependent regulation of AUX1. Other candidate interaction partners can be identified using co-immunoprecipitation and mass spectrometry with AUX1 as a bait protein. Subsequent yeast-two hybrid screens and phosphorylation assays may verify interacting kinases or phosphatases, as well as the putative phosphorylation sites. In addition, modulating the putative phosphorylation sites of AUX1 by exchanging the respective amino acid residues through phospho- and dephosphomimetic substitutions would gain further insights into the role of $[Ca^{2+}]_{cyt}$

signatures in regulating auxin transport. Phenotypic analysis of loss-of-function mutants of putative interaction partners could also give insights into the mechanisms by which regulation of AUX1 affects auxin-mediated responses, like the root gravitropic response, or root hair growth under low P_i.

(iii) How does auxin perception result in the activation of CNGC14?

Auxin-perception and the downstream processes that lead to changes in gene transcription are well described. However, components of this mechanism have so far not been included in a fast signaling pathway. As the fast activation of CNCG14 is dependent on the presence of auxin-binding F-Box proteins, some fast signal must be transmitted between the receptor molecule and the Ca^{2+} channel. It is unlikely that the 26S-proteasome-dependent pathway will lead to CNGC14 activation, but this could be tested with the 26S-proteasome inhibitor MG132.
Alternative pathways that activate CNGC14 might be the direct physical interaction between auxin-perceiving F-box proteins and the channel protein, or its activation via a mobile signal like a protein kinase or phosphatase. Candidate kinases or phosphatases could be identified in a similar way like those with AUX1 as a target. A subsequent mutant analysis in *A. thaliana*, as well as transient expression in tobacco leaves of AUX1, CNGC14, F-box proteins as well as candidate kinases/phosphatases labelled with fluorescent proteins, could clarify possible interactions through colocalization analysis, Förster resonance energy transfer (FRET) experiments and bimolecular fluorescence complementation (BiFC) analysis. Of particular interest would be the identification of the associated F-box protein responsible for auxin perception and its localization. Transient and heterologous expression in tobacco leaves and oocytes offers the possibility for a functional reconstitution of the fast auxin signaling pathway with PM potential recordings, live-cell imaging of $[Ca^{2+}]_{cyt}$ reporters, ion flux measurements and TEVC recordings as possible output signals. The apparent involvement of this signaling pathway in the root hair adaptive response to low P_i offers the possibility to test participation and connection of single components in the easily accessible system of *A. thaliana* root hairs. In this regard, CNGC14 and CPK11 would be primary targets for an investigation of their role and connection. Moreover, a detailed analysis of the homo- or heterologous expressed CNGC14 channel through patch-clamp or TEVC measurements could provide the necessary insights to determine its biophysical properties concerning voltage-, Ca^{2+}-, cyclic nucleotide-, and pH-dependent activation or deactivation, respectively.

(iv) Does the receptor-like kinase FERONIA have a role in fast auxin signaling

FERONIA is a PM-localized receptor-like kinase that is involved in cell elongation, and that constitutes an important signaling hub for hormonal crosstalk (Liao *et al.* 2017). Recently, an impaired auxin-induced apoplastic alkalinization in roots of the *fer-4* loss-of-function mutant was reported (Barbez *et al.* 2017). Provided that H^+-coupled auxin uptake via AUX1 is responsible for the fast auxin-induced alkalinization of the apoplastic space of root cells, FERONIA should be required for AUX1 to be active. As explained above, the presence of TIR1-like auxin receptors and CNGC14 are also necessary for AUX1 activity. The question arises, which role FERONIA could have in the above-described model of fast auxin signaling? A hint may be obtained from the recently discovered function of FERONIA in plant immunity. Here, FERONIA was shown to provide the scaffold for the interaction between the receptor-like kinase FLS2 and its coreceptor BAK1 after PAMP-perception (Stegmann *et al.* 2017). A similar scaffold-providing role of FERONIA for mediating the interaction of AUX1, TIR1/AFB-class F-box proteins and CNGC14 is thus conceivable and would help to explain the fast activation of CNGC14. To test the contribution of FERONIA in fast auxin signaling, the loss-of-fuction mutant should be examined for auxin-induced root hair PM depolarization, as well as H^+ and Ca^{2+} fluxes. Because of the potential scaffolding function of FERONIA it might be worthwhile to study its interaction with AUX1, CNGC14 and F-box proteins.

(v) Constitute CNGC14-mediated Ca^{2+} fluxes and RBOHD-dependent production of ROS a positive feedback loop involved in fast auxin signaling?

Apparently, the Ca^{2+}-dependent production of ROS through RBOHD forms a positive feedback loop through stimulation of Ca^{2+} influx at the apex of growing root hairs (Foreman *et al.* 2003). Since CNGC14 is localized at the root hair tip and is involved in Ca^{2+}-directed polar growth (Zhang *et al.* 2017b) an ROS-dependent regulation is very likely. Moreover, local auxin stimuli can induce Ca^{2+} waves that propagate through the root. It is discussed that the propagation of Ca^{2+} waves in plant tissues is intimately linked with the co-transmission of other long-range signals like ROS and electrical signals (Gilroy *et al.* 2014; Choi *et al.* 2016; Evans *et al.* 2016; Gilroy *et al.* 2016; Choi *et al.* 2017). Therefore, future *in planta* analysis should focus on whether auxin induces the production of ROS simultaneously to the well-described cytosolic Ca^{2+} signals in *A. thaliana* roots. Genetically encoded ROS-sensitive fluorescent probes like HyPerRed (Ermakova *et al.* 2014) or externally applied ROS-sensitive fluorescent dyes like H_2DCFDA (Arnaud *et al.* 2017) could be used to monitor ROS production, $[Ca^{2+}]_{cyt}$ elevations and auxin uptake in parallel to determine a possible sequence of events. External and cytosolic application of auxin in the *cngc14* and *rbohd* mutant background could show if potential ROS signals are induced and transmitted and if they depend on CNGC14-mediated Ca^{2+} influx or *vice versa*. These experiments could be supplemented by the analysis of AUX1-mediated auxin uptake in the presence of H_2O_2. Furthermore, in a heterologous characterization of CNGC14, its potential ROS-dependent regulation could be elucidated.

Another possible feedback loop involving CNGC14 is based on its interaction with $[Ca^{2+}]_{cyt}$-sensing CaMs (DeFalco *et al.* 2016; Fischer *et al.* 2017). Therefore, a Ca^{2+}-dependent regulation of CNGC14 is likely. Transient co-expression of both components in protoplast or oocytes could show a CaM-dependent regulation of CNGC14-mediated Ca^{2+} fluxes. The importance of this interaction for fast auxin signaling must be additionally investigated *in planta*. As such interaction can also be expected to deactivate CNGC14 after it has been stimulated through auxin, the transient nature of Ca^{2+} influx and $[Ca^{2+}]_{cyt}$ elevations should be affected in appropriate CaM loss-of-function mutant lines.

Ca^{2+} and ROS accompanying electric waves would be harder to observe. In the case of external auxin application diffusion of auxin would be a major obstacle, but could be monitored with the simultaneous application of a fluorescent dye like LY if the PM potential is to be recorded at increasing distances to the site of application. The transmission of the electrical signal induced through cytosolic auxin application could be observed in the same way. In both cases, the propagation of $[Ca^{2+}]_{cyt}$ and ROS signals could be monitored in parallel in wild type and loss-of-function mutant lines. The dependence of the propagation of possible auxin induced electrical signals on CNGC14 and RBOHD could additionally be investigated in the roots of *A. thaliana* loss-of-function mutants or in a heterologous system in which the fast auxin signaling pathway has been successfully reconstituted.

4.3. Auxin and the vacuole

Can the vacuole have a role in fast auxin signaling? The experimental data presented herein demonstrated how PM-localized auxin transport, Ca^{2+} influx, and perception constitute a fast auxin signaling pathway in *A. thaliana* root cells (see **Fig. 4.6**). This pathway might also include several processes at the VM.

(**i**) The vacuole can occupy over 90% of a root cells volume. Consequently, the VM and PM are often very close to each other and due to the high electrical resistance of the VM large ionic fluxes across the PM would also affect the VM potential. The auxin-coupled influx of H^+ and the following depolarization of the root cell PM would thus depolarize the VM, this, in turn, could activate voltage-dependent channels like TPC1 (Hedrich and Marten 2011) or increase the conductance of voltage-independent cation channels like TPK1 (Gobert *et al.* 2007). The depolarization of the VM would additionally contribute to auxin-induced cytosolic Ca^{2+} signals via the above-described deactivation of the H^+/Ca^{2+} exchanger.

(**ii**) Auxin uptake via AUX1 is coupled to the influx of H^+. The cytosolic processes, however, rely on a rather constant pH (Casey *et al.* 2010). H^+ pumps at both the PM and the VM fulfill essential functions in maintaining cytosolic pH (Rienmüller *et al.* 2012; Inoue *et al.* 2016). Therefore, the pump activity of the V-ATPase and PPase may get increased together with the PM H^+-ATPase to counteract cytosolic H^+ influx across the PM.

(**iii**) Since auxin influx is closely linked to the activation of CNGC14 and subsequent transient $[Ca^{2+}]_{cyt}$ elevations, the ion conductivity of the VM is likely to be increased through these Ca^{2+} signals. Vacuolar Ca^{2+} transporter like CAX2 or the Ca^{2+}-ATPase ACA11 are probably involved in returning high auxin-induced $[Ca^{2+}]_{cyt}$ back to basal levels (Roelfsema and Hedrich 2010; Schönknecht 2013) and could therefore act in concert with CNGC14 in shaping auxin-induced Ca^{2+} signals.

(**iv**) Subcellular compartments like the ER are proposed to be important for cytosolic auxin homeostasis. Therefore, the ER membrane is equipped with efflux carriers of the PIN and PILS-family, which supposedly compartmentalize auxin and thereby withdraw it from the cytosol and nuclear signaling (Mravec *et al.* 2009; Dal Bosco *et al.* 2012; Ding *et al.* 2012). With WAT1, the first vacuolar auxin transporter was identified. Analogous to AUX1, WAT1 was suggested to mediate the influx of IAA into the cytosol in symport with H^+ (Ranocha *et al.* 2013). However, the presence of such a transporter would only make sense if there are also transporters present which facilitate uptake of auxin into the vacuole. Since IAA is almost completely dissociated in its anionic form at the cytosolic pH, it cannot diffuse across the VM but needs a transport protein. Given the ΔpH across the VM and its negative polarization at the cytosolic side, vacuolar auxin uptake would be thermodynamically downhill and thus would not require a coupling to protons or ATP. So far, no such transporter has been identified, but provided that it would fulfil a function similar to the ER-localized PINs and PILs a high structural similarity with those intracellular auxin efflux carriers can be expected.

List of Figures

List of Tables

List of Equations

Abbreviations

$[Ca^{2+}]_{cyt}$	Cytosolic free Calcium ion concentration
Δ	Delta (difference / gradient)
Ω	Ohm, electrical resistance
µ	Micro / mobility
1-NAA	1-Naphthaleneacetic acid
2,4-D	2,4-Dichlorophenoxyacetic acid
2-NAA	2-Naphthaleneacetic acid
3-IAA	3-indole acetic acid
5F-IAA	5-fluoro-indoleacetic acid
A	Ampere
ABA	Abscisic acid
Ag	Silver
AP	Action potential
A. thaliana	Arabidopsis thaliana
ATP	Adenosine triphosphate
BA	Benzoic acid
BiFC	Bi-molecular fluorescence complementation
bp	Base pairs
Br^-	Bromide ions
BTP	Bis-tris propane
C	Capacity
c	Concentration / centi
CAM	Crassulacean acid metabolism
CaM	Calmodulin
cDNA	Complementary deoxyribonucleic acid
CICR	Ca^{2+}-induced Ca^{2+}-release
Cl^-	Chloride ions
Col-0	Columbia-0
CRISP/CAS	Clustered Regularly Interspaced Short Palindromic Repeats/CRISPR-associated
E	Membrane voltage
E_{rev}	Reversal potential
EMS	Ethyl methanesulfonate
ER	Endoplasmic reticulum
EtOH	Ethanol
f	Fluorescence / femto
F	Faraday constant
FRET	Förster-resonance energy transfer
FURA-2	Ratiometric Ca^{2+} dye
G	Gibbs free energy

g	Gram
GFP	Green fluorescent protein
H^+	Proton(s)
h	hour
HEPES	Hydroxyethyl piperazineethanesulfonic acid
Hz	Hertz, frequency
I	Electrical current
I^-	Iodine ions
J	Ion flux / Joule
k	kilo
K^+	Potassium ions
l	liter
La^{3+}	Lanthanum ions
Ler	Landsberg erecta
LY	Lucifer yellow
M	Molar
m	Milli / meter
MES	Morpholinoethanesulfonic acid
MeOH	Methanol
Mg^{2+}	Magnesium ions
min	Minutes
MS-medium	Murashige & Skoog medium
n	Nano / stoichiometric quantity / Hill coefficient
n.d.	Not detectable
NO_3^-	Nitrate
NPA	Naphthylphthalamic acid
pABA	Para-aminobenzoic acid
PAT	Polar auxin transport
PEO-IAA	Phenylethyl-2-oxo-IAA
pH	Negative logarithm of H^+ concentration
P_i / PO_4^{2-}	Inorganic phosphate
pK_a	Negative logarithm of the dissociation constant of an acid
PM	Plasma membrane
pmf	Proton motif force
PP_i	Pyrophosphate
qPCR	Quantitative polymerase chain reaction
R	Universal Gas constant / electrical resistance
RAM	Root apical meristem
R-GECO1	Red shifted – genetically encoded Ca^{2+} indicator for optical imaging
ROS	Reactive oxygen species
ru	Relative units

S	Siemens
s	Seconds
SAM	Shoot apical meristem
SD	Standard deviation
SE	Standard error
SO_4^{2-}	Sulphate
ss	Steady state
T	Absolute temperature
T-DNA	Transfer-DNA
TEVC	Two-electrode voltage-clamp technique
TIBA	Triiodobenzoic acid
TRIS	Tris-hydroxymethyl-aminomethane
V	Voltage
VM	Vacuolar membrane
Ws	Wassilewskija
x	Distance
YFP	Yellow fluorescent protein
z	Valence

References

Abel S, Theologis A (1996) Early genes and auxin action. Plant Physiol 111 (1):9-17.

Akerboom J, Carreras Calderon N *et al.* (2013) Genetically encoded calcium indicators for multi-color neural activity imaging and combination with optogenetics. Front Mol Neurosci 6:2.

Al-Ghazi Y, Muller B *et al.* (2003) Temporal responses of Arabidopsis root architecture to phosphate starvation: evidence for the involvement of auxin signalling. Plant Cell and Environment 26 (7):1053-1066.

Allen GJ, Chu SP *et al.* (2000) Alteration of stimulus-specific guard cell calcium oscillations and stomatal closing in Arabidopsis det3 mutant. Science 289 (5488):2338-2342.

Allen GJ, Chu SP *et al.* (2001) A defined range of guard cell calcium oscillation parameters encodes stomatal movements. Nature 411 (6841):1053-1057.

Alvarez ME, Pennell RI *et al.* (1998) Reactive oxygen intermediates mediate a systemic signal network in the establishment of plant immunity. Cell 92 (6):773-784.

Andres Z, Perez-Hormaeche J *et al.* (2014) Control of vacuolar dynamics and regulation of stomatal aperture by tonoplast potassium uptake. Proc Natl Acad Sci U S A 111 (17):E1806-1814.

Apse MP, Aharon GS *et al.* (1999) Salt tolerance conferred by overexpression of a vacuolar Na+/H+ antiport in Arabidopsis. Science 285 (5431):1256-1258.

Arif I, Newman IA *et al.* (1995) Proton Flux Measurements from Tissues in Buffered Solution. Plant Cell and Environment 18 (11):1319-1324.

Armengaud P, Breitling R *et al.* (2004) The potassium-dependent transcriptome of Arabidopsis reveals a prominent role of jasmonic acid in nutrient signaling. Plant Physiol 136 (1):2556-2576.

Arnaud D, Lee S *et al.* (2017) Cytokinin-Mediated Regulation of Reactive Oxygen Species Homeostasis Modulates Stomatal Immunity in Arabidopsis. Plant Cell 29 (3):543-559.

Bainbridge K, Guyomarc'h S *et al.* (2008) Auxin influx carriers stabilize phyllotactic patterning. Genes Dev 22 (6):810-823.

Baldwin IT, Halitschke R *et al.* (2006) Volatile signaling in plant-plant interactions: "talking trees" in the genomics era. Science 311 (5762):812-815.

Barbez E, Kubes M *et al.* (2012) A novel putative auxin carrier family regulates intracellular auxin homeostasis in plants. Nature 485 (7396):119-122.

Barbez E, Dunser K *et al.* (2017) Auxin steers root cell expansion via apoplastic pH regulation in Arabidopsis thaliana. Proc Natl Acad Sci U S A 114 (24):E4884-E4893.

Barbosa IC, Zourelidou M *et al.* (2014) D6 PROTEIN KINASE activates auxin transport-dependent growth and PIN-FORMED phosphorylation at the plasma membrane. Dev Cell 29 (6):674-685.

Barragan V, Leidi EO *et al.* (2012) Ion exchangers NHX1 and NHX2 mediate active potassium uptake into vacuoles to regulate cell turgor and stomatal function in Arabidopsis. Plant Cell 24 (3):1127-1142.

Bassil E, Tajima H *et al.* (2011) The Arabidopsis Na+/H+ antiporters NHX1 and NHX2 control vacuolar pH and K+ homeostasis to regulate growth, flower development, and reproduction. Plant Cell 23 (9):3482-3497.

Bates TR, Lynch JP (1996) Stimulation of root hair elongation in Arabidopsis thaliana by low phosphorus availability. Plant Cell and Environment 19 (5):529-538.

Bates TR, Lynch JP (2000) The efficiency of Arabidopsis thaliana (Brassicaceae) root hairs in phosphorus acquisition. Am J Bot 87 (7):964-970.

Batistic O, Kudla J (2012) Analysis of calcium signaling pathways in plants. Biochim Biophys Acta 1820 (8):1283-1293.

Baykov AA, Evtushenko OA *et al.* (1988) A malachite green procedure for orthophosphate determination and its use in alkaline phosphatase-based enzyme immunoassay. Anal Biochem 171 (2):266-270.

Becker D, Geiger D *et al.* (2004) AtTPK4, an Arabidopsis tandem-pore K+ channel, poised to control the pollen membrane voltage in a pH- and Ca2+-dependent manner. Proc Natl Acad Sci U S A 101 (44):15621-15626.

Benjamins R, Ampudia CS *et al.* (2003) PINOID-mediated signaling involves calcium-binding proteins. Plant Physiol 132 (3):1623-1630.

Benkova E, Michniewicz M *et al.* (2003) Local, efflux-dependent auxin gradients as a common module for plant organ formation. Cell 115 (5):591-602.

Bennett MJ, Marchant A *et al.* (1996) Arabidopsis AUX1 gene: a permease-like regulator of root gravitropism. Science 273 (5277):948-950.

Bertl A, Blumwald E *et al.* (1992) Electrical Measurements on Endomembranes. Science 258 (5084):873-874.

Bethmann B, Thaler M *et al.* (1995) Electrochemical Potential Gradients of H+, K+, Ca2+, and Cl- across the Tonoplast of the Green Alga Eremosphaera Viridis. Plant Physiol 109 (4):1317-1326.

Bewell MA, Maathuis FJ *et al.* (1999) Calcium-induced calcium release mediated by a voltage-activated cation channel in vacuolar vesicles from red beet. FEBS Lett 458 (1):41-44.

Beyhl D, Hortensteiner S *et al.* (2009) The fou2 mutation in the major vacuolar cation channel TPC1 confers tolerance to inhibitory luminal calcium. Plant J 58 (5):715-723.

Bhosale R, Giri J *et al.* (2017) A mechanistic framework for auxin dependent Arabidopsis root hair elongation in response to low external phosphate.

Bibikova TN, Zhigilei A *et al.* (1997) Root hair growth in Arabidopsis thaliana is directed by calcium and an endogenous polarity. Planta 203 (4):495-505.

Bibikova TN, Jacob T *et al.* (1998) Localized changes in apoplastic and cytoplasmic pH are associated with root hair development in Arabidopsis thaliana. Development 125 (15):2925-2934.

Bihler H, Eing C *et al.* (2005) TPK1 is a vacuolar ion channel different from the slow-vacuolar cation channel. Plant Physiol 139 (1):417-424.

Birnbaum K, Shasha DE *et al.* (2003) A gene expression map of the Arabidopsis root. Science 302 (5652):1956-1960.

Bjorkman T, Leopold AC (1987) Effect of inhibitors of auxin transport and of calmodulin on a gravisensing-dependent current in maize roots. Plant Physiol 84:847-850.

Blakely LM, Evans TA (1979) Cell Dynamics Studies on the Pericycle of Radish Seedling Roots. Plant Sci Lett 14 (1):79-83.

Blilou I, Xu J *et al.* (2005) The PIN auxin efflux facilitator network controls growth and patterning in Arabidopsis roots. Nature 433 (7021):39-44.

Bonaventure G, Gfeller A *et al.* (2007) A gain-of-function allele of TPC1 activates oxylipin biogenesis after leaf wounding in Arabidopsis. Plant J 49 (5):889-898.

Bose J, Pottosin, II *et al.* (2011) Calcium efflux systems in stress signaling and adaptation in plants. Front Plant Sci 2:85.

Boysen-Jensen P (1913) Über die Leitung des phototropischen Reizes in der Avenakoleoptile. Berichte der Deutschen Botanischen Gesellschaft 31 (10):559-566.

Brunoud G, Wells DM *et al.* (2012) A novel sensor to map auxin response and distribution at high spatio-temporal resolution. Nature 482 (7383):103-106.

Cambridge AP, Morris DA (1996) Transfer of exogenous auxin from the phloem to the polar auxin transport pathway in pea (Pisum sativum L). Planta 199 (4):583-588.

Capua Y, Eshed Y (2017) Coordination of auxin-triggered leaf initiation by tomato LEAFLESS. Proc Natl Acad Sci U S A 114 (12):3246-3251.

Carpaneto A, Boccaccio A *et al.* (2017) The signaling lipid phosphatidylinositol-3,5-bisphosphate targets plant CLC-a anion/H+ exchange activity. EMBO Rep 18 (7):1100-1107.

Carraretto L, Formentin E *et al.* (2013) A thylakoid-located two-pore K+ channel controls photosynthetic light utilization in plants. Science 342 (6154):114-118.

Carrier DJ, Bakar NT *et al.* (2008) The binding of auxin to the Arabidopsis auxin influx transporter AUX1. Plant Physiol 148 (1):529-535.

Carter C, Pan S *et al.* (2004) The vegetative vacuole proteome of Arabidopsis thaliana reveals predicted and unexpected proteins. Plant Cell 16 (12):3285-3303.

Casey JR, Grinstein S *et al.* (2010) Sensors and regulators of intracellular pH. Nat Rev Mol Cell Biol 11 (1):50-61.

Casimiro I, Marchant A *et al.* (2001) Auxin transport promotes Arabidopsis lateral root initiation. Plant Cell 13 (4):843-852.

Cecchetti V, Celebrin D *et al.* (2017) An auxin maximum in the middle layer controls stamen development and pollen maturation in Arabidopsis. New Phytol 213 (3):1194-1207.

Chardon F, Bedu M *et al.* (2013) Leaf Fructose Content Is Controlled by the Vacuolar Transporter SWEET17 in Arabidopsis. Current Biology 23 (8):697-702.

Charpentier M, Sun J *et al.* (2016) Nuclear-localized cyclic nucleotide-gated channels mediate symbiotic calcium oscillations. Science 352 (6289):1102-1105.

Cheng NH, Pittman JK *et al.* (2002) Characterization of CAX4, an Arabidopsis H(+)/cation antiporter. Plant Physiol 128 (4):1245-1254.

Cheng NH, Pittman JK *et al.* (2003) The Arabidopsis cax1 mutant exhibits impaired ion homeostasis, development, and hormonal responses and reveals interplay among vacuolar transporters. Plant Cell 15 (2):347-364.

Cheng NH, Pittman JK *et al.* (2004) The protein kinase SOS2 activates the Arabidopsis H(+)/Ca(2+) antiporter CAX1 to integrate calcium transport and salt tolerance. J Biol Chem 279 (4):2922-2926.

Cheng Y, Dai X *et al.* (2006) Auxin biosynthesis by the YUCCA flavin monooxygenases controls the formation of floral organs and vascular tissues in Arabidopsis. Genes Dev 20 (13):1790-1799.

Cheong YH, Pandey GK *et al.* (2007) Two calcineurin B-like calcium sensors, interacting with protein kinase CIPK23, regulate leaf transpiration and root potassium uptake in Arabidopsis. Plant J 52 (2):223-239.

Cho M, Lee SH *et al.* (2007) P-glycoprotein4 displays auxin efflux transporter-like action in Arabidopsis root hair cells and tobacco cells. Plant Cell 19 (12):3930-3943.

Choi WG, Toyota M *et al.* (2014) Salt stress-induced Ca2+ waves are associated with rapid, long-distance root-to-shoot signaling in plants. Proc Natl Acad Sci U S A 111 (17):6497-6502.

Choi WG, Hilleary R *et al.* (2016) Rapid, Long-Distance Electrical and Calcium Signaling in Plants. Annu Rev Plant Biol 67:287-307.

Choi WG, Miller G *et al.* (2017) Orchestrating Rapid Long-Distance Signaling in Plants with Ca2+ , ROS, and Electrical Signals. Plant J.

Cholodny NG (1927) Wuchshormone und Tropismen bei den Pflanzen. Biol Zentralbl 47:604-626.

Chopin F, Orsel M *et al.* (2007) The Arabidopsis ATNRT2.7 nitrate transporter controls nitrate content in seeds. Plant Cell 19 (5):1590-1602.

Christensen HN (1975) Biological transport. 2d edn. W. A. Benjamin, Reading, Mass.,

Christensen SK, Dagenais N *et al.* (2000) Regulation of auxin response by the protein kinase PINOID. Cell 100 (4):469-478.

Corbesier L, Vincent C *et al.* (2007) FT protein movement contributes to long-distance signaling in floral induction of Arabidopsis. Science 316 (5827):1030-1033.

Dal Bosco C, Dovzhenko A *et al.* (2012) The endoplasmic reticulum localized PIN8 is a pollen-specific auxin carrier involved in intracellular auxin homeostasis. Plant Journal 71 (5):860-870.

Darwin C, Darwin F *et al.* (1880) The power of movement in plants. First edition edn. John Murray, London

De Angeli A, Monachello D *et al.* (2006) The nitrate/proton antiporter AtCLCa mediates nitrate accumulation in plant vacuoles. Nature 442 (7105):939-942.

De Angeli A, Moran O *et al.* (2009) ATP binding to the C terminus of the Arabidopsis thaliana nitrate/proton antiporter, AtCLCa, regulates nitrate transport into plant vacuoles. J Biol Chem 284 (39):26526-26532.

De Angeli A, Zhang JB *et al.* (2013) AtALMT9 is a malate-activated vacuolar chloride channel required for stomatal opening in Arabidopsis. Nature Communications 4.

DeFalco TA, Marshall CB *et al.* (2016) Multiple Calmodulin-Binding Sites Positively and Negatively Regulate Arabidopsis CYCLIC NUCLEOTIDE-GATED CHANNEL12. Plant Cell 28 (7):1738-1751.

Dela Fuente RK, Leopold AC (1970) Time course of auxin stimulations of growth. Plant Physiol 46 (2):186-189.

Dela Fuente RK, Leopold AC (1973) A role for calcium in auxin transport. Plant Physiol 51 (5):845-847.

Dela Fuente RK (1984) Role of calcium in the polar secretion of indoleacetic Acid. Plant Physiol 76 (2):342-346.

Delbarre A, Muller P *et al.* (1996) Comparison of mechanisms controlling uptake and accumulation of 2,4-dichlorophenoxy acetic acid, naphthalene-1-acetic acid, and indole-3-acetic acid in suspension-cultured tobacco cells. Planta 198 (4):532-541.

Demidchik V, Bowen HC *et al.* (2002) Arabidopsis thaliana root non-selective cation channels mediate calcium uptake and are involved in growth. Plant J 32 (5):799-808.

Denninger P, Bleckmann A *et al.* (2014) Male-female communication triggers calcium signatures during fertilization in Arabidopsis. Nat Commun 5:4645.

Dezfulian MH, Jalili E *et al.* (2016) Oligomerization of SCFTIR1 Is Essential for Aux/IAA Degradation and Auxin Signaling in Arabidopsis. Plos Genetics 12 (9).

Dharmasiri N, Dharmasiri S *et al.* (2005a) The F-box protein TIR1 is an auxin receptor. Nature 435 (7041):441-445.

Dharmasiri N, Dharmasiri S *et al.* (2005b) Plant development is regulated by a family of auxin receptor F box proteins. Dev Cell 9 (1):109-119.

Dhonukshe P, Huang F *et al.* (2010) Plasma membrane-bound AGC3 kinases phosphorylate PIN auxin carriers at TPRXS(N/S) motifs to direct apical PIN recycling. Development 137 (19):3245-3255.

Dietrich P, Anschutz U *et al.* (2010) Physiology and biophysics of plant ligand-gated ion channels. Plant Biol (Stuttg) 12 Suppl 1:80-93.

Ding Z, Wang B *et al.* (2012) ER-localized auxin transporter PIN8 regulates auxin homeostasis and male gametophyte development in Arabidopsis. Nat Commun 3:941.

Dobritzsch M, Lubken T *et al.* (2016) MATE Transporter-Dependent Export of Hydroxycinnamic Acid Amides. Plant Cell 28 (2):583-596.

Dodd AN, Kudla J *et al.* (2010) The language of calcium signaling. Annu Rev Plant Biol 61:593-620.

Dreher KA, Brown J *et al.* (2006) The Arabidopsis Aux/IAA protein family has diversified in degradation and auxin responsiveness. Plant Cell 18 (3):699-714.

Drew MC (1975) Comparison of the effects of a localised supply of phosphate, nitrate, ammonium and potassium on the growth of the seminal root system, and the shoot, in barley. New Phytologist 75 (3):479-490.

Dubiella U, Seybold H *et al.* (2013) Calcium-dependent protein kinase/NADPH oxidase activation circuit is required for rapid defense signal propagation. Proc Natl Acad Sci U S A 110 (21):8744-8749.

Dunlop J, Bowling DJF (1971) The Movement of Ions to the Xylem Exudate of Maize RootsI. PROFILES OF MEMBRANE POTENTIAL AND VACUOLAR POTASSIUM ACTIVITY ACROSS THE ROOT. Journal of Experimental Botany 22 (2):434-444.

Durrett TP, Gassmann W *et al.* (2007) The FRD3-mediated efflux of citrate into the root vasculature is necessary for efficient iron translocation. Plant Physiol 144 (1):197-205.

Ehrhardt DW, Wais R *et al.* (1996) Calcium spiking in plant root hairs responding to Rhizobium nodulation signals. Cell 85 (5):673-681.

Elser JJ (2012) Phosphorus: a limiting nutrient for humanity? Curr Opin Biotechnol 23 (6):833-838.

Epstein E, Rains DW *et al.* (1963) Resolution of Dual Mechanisms of Potassium Absorption by Barley Roots. Proc Natl Acad Sci U S A 49 (5):684-692.

Ermakova YG, Bilan DS *et al.* (2014) Red fluorescent genetically encoded indicator for intracellular hydrogen peroxide. Nat Commun 5:5222.

Escalante-Perez M, Krol E *et al.* (2011) A special pair of phytohormones controls excitability, slow closure, and external stomach formation in the Venus flytrap. Proc Natl Acad Sci U S A 108 (37):15492-15497.

Evans MJ, Choi WG *et al.* (2016) A ROS-Assisted Calcium Wave Dependent on the AtRBOHD NADPH Oxidase and TPC1 Cation Channel Propagates the Systemic Response to Salt Stress. Plant Physiol 171 (3):1771-1784.

Evans ML, Ishikawa H *et al.* (1994) Responses of Arabidopsis Roots to Auxin Studied with High Temporal Resolution - Comparison of Wild-Type and Auxin-Response Mutants. Planta 194 (2):215-222.

Fabregas N, Formosa-Jordan P *et al.* (2015) Auxin influx carriers control vascular patterning and xylem differentiation in Arabidopsis thaliana. PLoS Genet 11 (4):e1005183.

Farmer EE, Gasperini D *et al.* (2014) The squeeze cell hypothesis for the activation of jasmonate synthesis in response to wounding. New Phytol 204 (2):282-288.

Felle H (1988a) Auxin Causes Oscillations of Cytosolic Free Calcium and Ph in Zea-Mays Coleoptiles. Planta 174 (4):495-499.

Felle H (1988b) Cytoplasmic free calcium in Riccia fluitans L. and Zea mays L.: Interaction of Ca(2+) and pH? Planta 176 (2):248-255.

Felle H, Peters W *et al.* (1991) The electrical response of maize to auxins. Biochim Biophys Acta 1064 (2):199-204.

Felle HH, Hepler PK (1997) The Cytosolic Ca2+ Concentration Gradient of Sinapis alba Root Hairs as Revealed by Ca2+-Selective Microelectrode Tests and Fura-Dextran Ratio Imaging. Plant Physiol 114 (1):39-45.

Fendrych M, Leung J *et al.* (2016) TIR1/AFB-Aux/IAA auxin perception mediates rapid cell wall acidification and growth of Arabidopsis hypocotyls. Elife 5.

Ferreira PC, Hemerly AS *et al.* (1994) Developmental expression of the arabidopsis cyclin gene cyc1At. Plant Cell 6 (12):1763-1774.

Fischer C, DeFalco TA *et al.* (2017) Calmodulin as a Ca2+-sensing subunit of Arabidopsis cyclic nucleotide-gated channel complexes. Plant Cell Physiol.

Fischer WN, Loo DD *et al.* (2002) Low and high affinity amino acid H+-cotransporters for cellular import of neutral and charged amino acids. Plant J 29 (6):717-731.

Foreman J, Demidchik V *et al.* (2003) Reactive oxygen species produced by NADPH oxidase regulate plant cell growth. Nature 422 (6930):442-446.

Friml J, Benkova E *et al.* (2002a) AtPIN4 mediates sink-driven auxin gradients and root patterning in Arabidopsis. Cell 108 (5):661-673.

Friml J, Wisniewska J *et al.* (2002b) Lateral relocation of auxin efflux regulator PIN3 mediates tropism in Arabidopsis. Nature 415 (6873):806-809.

Friml J, Vieten A *et al.* (2003) Efflux-dependent auxin gradients establish the apical-basal axis of Arabidopsis. Nature 426 (6963):147-153.

Fromm J, Lautner S (2007) Electrical signals and their physiological significance in plants. Plant Cell and Environment 30 (3):249-257.

Fuglsang AT, Visconti S *et al.* (1999) Binding of 14-3-3 protein to the plasma membrane H(+)-ATPase AHA2 involves the three C-terminal residues Tyr(946)-Thr-Val and requires phosphorylation of Thr(947). J Biol Chem 274 (51):36774-36780.

Fuglsang AT, Guo Y *et al.* (2007) Arabidopsis protein kinase PKS5 inhibits the plasma membrane H+ -ATPase by preventing interaction with 14-3-3 protein. Plant Cell 19 (5):1617-1634.

Fukaki H, Tameda S *et al.* (2002) Lateral root formation is blocked by a gain-of-function mutation in the SOLITARY-ROOT/IAA14 gene of Arabidopsis. Plant Journal 29 (2):153-168.

Furuichi T, Cunningham KW *et al.* (2001) A putative two pore channel AtTPC1 mediates Ca(2+) flux in Arabidopsis leaf cells. Plant Cell Physiol 42 (9):900-905.

Gajdanowicz P, Michard E *et al.* (2011) Potassium (K plus) gradients serve as a mobile energy source in plant vascular tissues. P Natl Acad Sci USA 108 (2):864-869.

Gälweiler L, Guan C *et al.* (1998) Regulation of polar auxin transport by AtPIN1 in Arabidopsis vascular tissue. Science 282 (5397):2226-2230.

Ganguly A, Lee SH *et al.* (2010) Differential auxin-transporting activities of PIN-FORMED proteins in Arabidopsis root hair cells. Plant Physiol 153 (3):1046-1061.

Gao QF, Fei CF *et al.* (2014) Arabidopsis CNGC18 is a Ca(2)(+)-permeable channel. Mol Plant 7 (4):739-743.

Gao QF, Gu LL *et al.* (2016) Cyclic nucleotide-gated channel 18 is an essential Ca2+ channel in pollen tube tips for pollen tube guidance to ovules in Arabidopsis. P Natl Acad Sci USA 113 (11):3096-3101.

Gao Y, Zhang Y *et al.* (2015) Auxin binding protein 1 (ABP1) is not required for either auxin signaling or Arabidopsis development. Proc Natl Acad Sci U S A 112 (7):2275-2280.

Gardestrom P, Igamberdiev AU (2016) The origin of cytosolic ATP in photosynthetic cells. Physiol Plant 157 (3):367-379.

Geelen D, Lurin C *et al.* (2000) Disruption of putative anion channel gene AtCLC-a in Arabidopsis suggests a role in the regulation of nitrate content. Plant J 21 (3):259-267.

Gehring CA, Irving HR *et al.* (1990) Effects of auxin and abscisic acid on cytosolic calcium and pH in plant cells. Proc Natl Acad Sci U S A 87 (24):9645-9649.

Geiger D, Scherzer S *et al.* (2009) Activity of guard cell anion channel SLAC1 is controlled by drought-stress signaling kinase-phosphatase pair. Proc Natl Acad Sci U S A 106 (50):21425-21430.

Geiger D, Scherzer S *et al.* (2010) Guard cell anion channel SLAC1 is regulated by CDPK protein kinases with distinct Ca2+ affinities. P Natl Acad Sci USA 107 (17):8023-8028.

Geisler M, Frangne N *et al.* (2000) The ACA4 gene of Arabidopsis encodes a vacuolar membrane calcium pump that improves salt tolerance in yeast. Plant Physiol 124 (4):1814-1827.

Geisler M, Blakeslee JJ *et al.* (2005) Cellular efflux of auxin catalyzed by the Arabidopsis MDR/PGP transporter AtPGP1. Plant J 44 (2):179-194.

Geldner N, Friml J *et al.* (2001) Auxin transport inhibitors block PIN1 cycling and vesicle trafficking. Nature 413 (6854):425-428.

Gierth M, Maser P *et al.* (2005) The potassium transporter AtHAK5 functions in K(+) deprivation-induced high-affinity K(+) uptake and AKT1 K(+) channel contribution to K(+) uptake kinetics in Arabidopsis roots. Plant Physiol 137 (3):1105-1114.

Gigolashvili T, Kopriva S (2014) Transporters in plant sulfur metabolism. Front Plant Sci 5:442.

Gilroy S, Suzuki N *et al.* (2014) A tidal wave of signals: calcium and ROS at the forefront of rapid systemic signaling. Trends Plant Sci 19 (10):623-630.

Gilroy S, Bialasek M *et al.* (2016) ROS, Calcium, and Electric Signals: Key Mediators of Rapid Systemic Signaling in Plants. Plant Physiol 171 (3):1606-1615.

Giri J, Bhosale R *et al.* (2017) The rice auxin influx carrier *OsAUX1* facilitates root hair elongation in response to low external phosphate.

Gobert A, Isayenkov S *et al.* (2007) The two-pore channel TPK1 gene encodes the vacuolar K+ conductance and plays a role in K+ homeostasis. Proc Natl Acad Sci U S A 104 (25):10726-10731.

Goldsmith MH, Cleland RE (1978) The contribution of tonoplast and plasma membrane to the electrical properties of a higher-plant cell. Planta 143 (3):261-265.

Goldsmith MHM (1977) The Polar Transport of Auxin. Annu Rev Plant Phys 28:439-478.

Grabov A, Blatt MR (1998) Membrane voltage initiates Ca2+ waves and potentiates Ca2+ increases with abscisic acid in stomatal guard cells. P Natl Acad Sci USA 95 (8):4778-4783.

Gray WM, del Pozo JC *et al.* (1999) Identification of an SCF ubiquitin-ligase complex required for auxin response in Arabidopsis thaliana. Genes Dev 13 (13):1678-1691.

Gray WM, Kepinski S *et al.* (2001) Auxin regulates SCF(TIR1)-dependent degradation of AUX/IAA proteins. Nature 414 (6861):271-276.

Grieneisen VA, Xu J *et al.* (2007) Auxin transport is sufficient to generate a maximum and gradient guiding root growth. Nature 449 (7165):1008-1013.

Guilfoyle TJ, Key JL (1986) Auxin-Regulated Gene-Expression in Higher-Plants. Critical Reviews in Plant Sciences 4 (3):247-276.

Guilfoyle TJ, Hagen G (2007) Auxin response factors. Curr Opin Plant Biol 10 (5):453-460.

Guo WJ, Nagy R *et al.* (2014) SWEET17, a facilitative transporter, mediates fructose transport across the tonoplast of Arabidopsis roots and leaves. Plant Physiol 164 (2):777-789.

Gutermuth T, Lassig R *et al.* (2013) Pollen tube growth regulation by free anions depends on the interaction between the anion channel SLAH3 and calcium-dependent protein kinases CPK2 and CPK20. Plant Cell 25 (11):4525-4543.

Haagen-Smit AJ, Dandliker WB *et al.* (1946) Isolation of 3-Indoleacetic Acid from Immature Corn Kernels. Am J Bot 33 (2):118-120.

Hamilton DWA, Hills A *et al.* (2000) Ca2+ channels at the plasma membrane of stomatal guard cells are activated by hyperpolarization and abscisic acid. P Natl Acad Sci USA 97 (9):4967-4972.

Hardtke CS, Berleth T (1998) The Arabidopsis gene MONOPTEROS encodes a transcription factor mediating embryo axis formation and vascular development. EMBO J 17 (5):1405-1411.

Hashimoto K, Kudla J (2011) Calcium decoding mechanisms in plants. Biochimie 93 (12):2054-2059.

Hatsugai N, Hara-Nishimura I (2010) Two vacuole-mediated defense strategies in plants. Plant Signal Behav 5 (12):1568-1570.

Hayashi K, Neve J *et al.* (2012) Rational design of an auxin antagonist of the SCF(TIR1) auxin receptor complex. ACS Chem Biol 7 (3):590-598.

Heazlewood JL, Durek P *et al.* (2008) PhosPhAt: a database of phosphorylation sites in Arabidopsis thaliana and a plant-specific phosphorylation site predictor. Nucleic Acids Res 36 (Database issue):D1015-1021.

Hedrich R, Flugge UI *et al.* (1986) Patch-Clamp Studies of Ion-Transport in Isolated Plant Vacuoles. Febs Letters 204 (2):228-232.

Hedrich R, Neher E (1987) Cytoplasmic Calcium Regulates Voltage-Dependent Ion Channels in Plant Vacuoles. Nature 329 (6142):833-836.

Hedrich R, Marten I (2011) TPC1-SV channels gain shape. Mol Plant 4 (3):428-441.

Hedrich R (2012) Ion channels in plants. Physiol Rev 92 (4):1777-1811.

Heisler MG, Ohno C *et al.* (2005) Patterns of auxin transport and gene expression during primordium development revealed by live imaging of the Arabidopsis inflorescence meristem. Curr Biol 15 (21):1899-1911.

Henrichs S, Wang B *et al.* (2012) Regulation of ABCB1/PGP1-catalysed auxin transport by linker phosphorylation. EMBO J 31 (13):2965-2980.

Herdean A, Nziengui H *et al.* (2016) The Arabidopsis Thylakoid Chloride Channel AtCLCe Functions in Chloride Homeostasis and Regulation of Photosynthetic Electron Transport. Front Plant Sci 7:115.

Herman EM, Larkins BA (1999) Protein storage bodies and vacuoles. Plant Cell 11 (4):601-614.

Hirsch RE, Lewis BD *et al.* (1998) A role for the AKT1 potassium channel in plant nutrition. Science 280 (5365):918-921.

Hirschi KD, Zhen RG *et al.* (1996) CAX1, an H+/Ca2+ antiporter from Arabidopsis. P Natl Acad Sci USA 93 (16):8782-8786.

Hirschi KD, Korenkov VD *et al.* (2000) Expression of arabidopsis CAX2 in tobacco. Altered metal accumulation and increased manganese tolerance. Plant Physiol 124 (1):125-133.

Ho CH, Lin SH *et al.* (2009) CHL1 Functions as a Nitrate Sensor in Plants. Cell 138 (6):1184-1194.

Holdaway-Clarke TL, Walker NA *et al.* (1996) Measurement of the electrical resistance of plasmodesmata and membranes of corn suspension-culture cells. Planta 199 (4):537-544.

Hou C, Tian W *et al.* (2014) DUF221 proteins are a family of osmosensitive calcium-permeable cation channels conserved across eukaryotes. Cell Res 24 (5):632-635.

Hurth MA, Suh SJ *et al.* (2005) Impaired pH homeostasis in Arabidopsis lacking the vacuolar dicarboxylate transporter and analysis of carboxylic acid transport across the tonoplast. Plant Physiol 137 (3):901-910.

Inoue SI, Takahashi K *et al.* (2016) Auxin Influx Carrier AUX1 Confers Acid Resistance for Arabidopsis Root Elongation Through the Regulation of Plasma Membrane H+-ATPase. Plant Cell Physiol 57 (10):2194-2201.

Ivashikina N, Becker D *et al.* (2001) K(+) channel profile and electrical properties of Arabidopsis root hairs. FEBS Lett 508 (3):463-469.

Jammes F, Hu HC *et al.* (2011) Calcium-permeable channels in plant cells. FEBS J 278 (22):4262-4276.

Jaslan D, Mueller TD *et al.* (2016) Gating of the two-pore cation channel AtTPC1 in the plant vacuole is based on a single voltage-sensing domain. Plant Biol (Stuttg) 18 (5):750-760.

Jeworutzki E, Roelfsema MRG *et al.* (2010) Early signaling through the Arabidopsis pattern recognition receptors FLS2 and EFR involves Ca2+-associated opening of plasma membrane anion channels. Plant Journal 62 (3):367-378.

Jiang X, Leidi EO *et al.* (2010) How do vacuolar NHX exchangers function in plant salt tolerance? Plant Signaling & Behavior 5 (7):792-795.

Jones AR, Kramer EM *et al.* (2009) Auxin transport through non-hair cells sustains root-hair development. Nature Cell Biology 11 (1):78-U156.

Joo JH, Bae YS *et al.* (2001) Role of auxin-induced reactive oxygen species in root gravitropism. Plant Physiol 126 (3):1055-1060.

Jossier M, Kroniewicz L *et al.* (2010) The Arabidopsis vacuolar anion transporter, AtCLCc, is involved in the regulation of stomatal movements and contributes to salt tolerance. Plant J 64 (4):563-576.

Jung B, Ludewig F *et al.* (2015) Identification of the transporter responsible for sucrose accumulation in sugar beet taproots. Nat Plants 1:14001.

Kagale S, Rozwadowski K (2011) EAR motif-mediated transcriptional repression in plants: an underlying mechanism for epigenetic regulation of gene expression. Epigenetics 6 (2):141-146.

Kamimoto Y, Terasaka K *et al.* (2012) Arabidopsis ABCB21 is a facultative auxin importer/exporter regulated by cytoplasmic auxin concentration. Plant Cell Physiol 53 (12):2090-2100.

Kataoka T, Watanabe-Takahashi A *et al.* (2004) Vacuolar sulfate transporters are essential determinants controlling internal distribution of sulfate in Arabidopsis. Plant Cell 16 (10):2693-2704.

Katz E, Chamovitz DA (2017) Wounding of Arabidopsis leaves induces indole-3-carbinol-dependent autophagy in roots of Arabidopsis thaliana. Plant J.

Keinath NF, Waadt R *et al.* (2015) Live Cell Imaging with R-GECO1 Sheds Light on flg22- and Chitin-Induced Transient [Ca(2+)]cyt Patterns in Arabidopsis. Mol Plant 8 (8):1188-1200.

Kepinski S, Leyser O (2005) The Arabidopsis F-box protein TIR1 is an auxin receptor. Nature 435 (7041):446-451.

Kerk NM, Feldman LJ (1995) A Biochemical-Model for the Initiation and Maintenance of the Quiescent Center - Implications for Organization of Root-Meristems. Development 121 (9):2825-2833.

Kiep V, Vadassery J *et al.* (2015) Systemic cytosolic Ca(2+) elevation is activated upon wounding and herbivory in Arabidopsis. New Phytol 207 (4):996-1004.

Kim J, Harter K *et al.* (1997) Protein-protein interactions among the Aux/IAA proteins. P Natl Acad Sci USA 94 (22):11786-11791.

Kimura S, Kaya H *et al.* (2012) Protein phosphorylation is a prerequisite for the Ca2+-dependent activation of Arabidopsis NADPH oxidases and may function as a trigger for the positive feedback regulation of Ca2+ and reactive oxygen species. Bba-Mol Cell Res 1823 (2):398-405.

Kleine-Vehn J, Dhonukshe P *et al.* (2006) Subcellular trafficking of the Arabidopsis auxin influx carrier AUX1 uses a novel pathway distinct from PIN1. Plant Cell 18 (11):3171-3181.

Kleine-Vehn J, Huang F *et al.* (2009) PIN Auxin Efflux Carrier Polarity Is Regulated by PINOID Kinase-Mediated Recruitment into GNOM-Independent Trafficking in Arabidopsis. Plant Cell 21 (12):3839-3849.

Klemens PA, Patzke K *et al.* (2013) Overexpression of the vacuolar sugar carrier AtSWEET16 modifies germination, growth, and stress tolerance in Arabidopsis. Plant Physiol 163 (3):1338-1352.

Knight H, Trewavas AJ *et al.* (1997) Calcium signalling in Arabidopsis thaliana responding to drought and salinity. Plant J 12 (5):1067-1078.

Kögl F, Haagen-Smit AJ *et al.* (1934) Über ein neues Auxin („Hetero-auxin") aus Harn. 11. Mitteilung über pflanzliche Wachstumsstoffe. bchm 228 (1-2):90.

Köhler B, Blatt MR (2002) Protein phosphorylation activates the guard cell Ca2+ channel and is a prerequisite for gating by abscisic acid. Plant J 32 (2):185-194.

Kovermann P, Meyer S *et al.* (2007) The Arabidopsis vacuolar malate channel is a member of the ALMT family. Plant Journal 52 (6):1169-1180.

Kramer EM, Bennett MJ (2006) Auxin transport: a field in flux. Trends Plant Sci 11 (8):382-386.

Kramer EM, Rutschow HL *et al.* (2011) AuxV: a database of auxin transport velocities. Trends Plant Sci 16 (9):461-463.

Krebs M, Beyhl D *et al.* (2010) Arabidopsis V-ATPase activity at the tonoplast is required for efficient nutrient storage but not for sodium accumulation. Proc Natl Acad Sci U S A 107 (7):3251-3256.

Krouk G, Lacombe B *et al.* (2010) Nitrate-regulated auxin transport by NRT1.1 defines a mechanism for nutrient sensing in plants. Dev Cell 18 (6):927-937.

Kudla J, Batistic O *et al.* (2010) Calcium signals: the lead currency of plant information processing. Plant Cell 22 (3):541-563.

Kumar M, Pandya-Kumar N *et al.* (2015) Arabidopsis response to low-phosphate conditions includes active changes in actin filaments and PIN2 polarization and is dependent on strigolactone signalling. J Exp Bot 66 (5):1499-1510.

Kunkel J, Lin L *et al.* (2001) The strategic use of good buffers to measure proton gradients around growing pollen tubes. CELL BIOLOGY OF PLANT AND FUNGAL TIP GROWTH 328:81-94.

Kutschera U (1994) The current status of the acid-growth hypothesis. New Phytologist 126 (4):549-569.

Kwak JM, Mori IC *et al.* (2003) NADPH oxidase AtrbohD and AtrbohF genes function in ROS-dependent ABA signaling in Arabidopsis. EMBO J 22 (11):2623-2633.

Lan P, Li WF *et al.* (2013) Mapping gene activity of Arabidopsis root hairs. Genome Biol 14 (6).

Latz A, Becker D *et al.* (2007) TPK1, a Ca(2+)-regulated Arabidopsis vacuole two-pore K(+) channel is activated by 14-3-3 proteins. Plant J 52 (3):449-459.

Latz A, Mehlmer N *et al.* (2013) Salt stress triggers phosphorylation of the Arabidopsis vacuolar K+ channel TPK1 by calcium-dependent protein kinases (CDPKs). Mol Plant 6 (4):1274-1289.

Lavy M, Estelle M (2016) Mechanisms of auxin signaling. Development 143 (18):3226-3229.

Lee JS, Mulkey TJ *et al.* (1983a) Reversible loss of gravitropic sensitivity in maize roots after tip application of calcium chelators. Science 220 (4604):1375-1376.

Lee JS, Mulkey TJ *et al.* (1983b) Gravity-Induced Polar Transport of Calcium across Root Tips of Maize. Plant Physiol 73 (4):874-876.

Lee SM, Kim HS *et al.* (2007) Identification of a calmodulin-regulated autoinhibited Ca2+-ATPase (ACA11) that is localized to vacuole membranes in Arabidopsis. FEBS Lett 581 (21):3943-3949.

Leidi EO, Barragan V *et al.* (2010) The AtNHX1 exchanger mediates potassium compartmentation in vacuoles of transgenic tomato. Plant J 61 (3):495-506.

Leigh RA, Jones RGW (1984) A Hypothesis Relating Critical Potassium Concentrations for Growth to the Distribution and Functions of This Ion in the Plant-Cell. New Phytologist 97 (1):1-13.

Lew RR (1996) Pressure regulation of the electrical properties of growing Arabidopsis thaliana L. root hairs. Plant Physiol 112 (3):1089-1100.

Lew RR (2004) Osmotic effects on the electrical properties of Arabidopsis root hair vacuoles in situ. Plant Physiol 134 (1):352-360.

Li F, Wang J *et al.* (2013) Glutamate Receptor-Like Channel3.3 Is Involved in Mediating Glutathione-Triggered Cytosolic Calcium Transients, Transcriptional Changes, and Innate Immunity Responses in Arabidopsis. Plant Physiology 162 (3):1497-1509.

Li J, Yang H *et al.* (2005) Arabidopsis H+-PPase AVP1 regulates auxin-mediated organ development. Science 310 (5745):121-125.

Li L, He Z *et al.* (2002) Functional cloning and characterization of a plant efflux carrier for multidrug and heavy metal detoxification. J Biol Chem 277 (7):5360-5368.

Liao HD, Tang RJ *et al.* (2017) FERONIA Receptor Kinase at the Crossroads of Hormone Signaling and Stress Responses. Plant and Cell Physiology 58 (7):1143-1150.

Liu J, Yang L *et al.* (2015) A vacuolar phosphate transporter essential for phosphate homeostasis in Arabidopsis. Proc Natl Acad Sci U S A 112 (47):E6571-6578.

Liu TY, Huang TK *et al.* (2016) Identification of plant vacuolar transporters mediating phosphate storage. Nat Commun 7:11095.

Liu ZB, Wang JM *et al.* (2014) A novel membrane-bound E3 ubiquitin ligase enhances the thermal resistance in plants. Plant Biotechnol J 12 (1):93-104.

Ljung K, Bhalerao RP *et al.* (2001) Sites and homeostatic control of auxin biosynthesis in Arabidopsis during vegetative growth. Plant J 28 (4):465-474.

Ljung K, Hull AK *et al.* (2005) Sites and regulation of auxin biosynthesis in Arabidopsis roots. Plant Cell 17 (4):1090-1104.

Lodish H, Berk A *et al.* (2008) Molecular Cell Biology. 6th edn. W. H. Freeman,

Lomax TL, Mehlhorn RJ *et al.* (1985) Active Auxin Uptake by Zucchini Membrane-Vesicles - Quantitation Using Electron-Spin-Resonance Volume and Delta-Ph Determinations. P Natl Acad Sci USA 82 (19):6541-6545.

Long JA, Ohno C *et al.* (2006) TOPLESS regulates apical embryonic fate in Arabidopsis. Science 312 (5779):1520-1523.

Lopez-Bucio J, Hernandez-Abreu E *et al.* (2002) Phosphate availability alters architecture and causes changes in hormone sensitivity in the Arabidopsis root system. Plant Physiol 129 (1):244-256.

Lopez-Bucio J, Cruz-Ramirez A *et al.* (2003) The role of nutrient availability in regulating root architecture. Curr Opin Plant Biol 6 (3):280-287.

Love J, Dodd AN *et al.* (2004) Circadian and diurnal calcium oscillations encode photoperiodic information in Arabidopsis. Plant Cell 16 (4):956-966.

Lynch JP, Brown KM (2001) Topsoil foraging - an architectural adaptation of plants to low phosphorus availability. Plant Soil 237 (2):225-237.

Lynch JP (2011) Root phenes for enhanced soil exploration and phosphorus acquisition: tools for future crops. Plant Physiol 156 (3):1041-1049.

Ma Z, Bielenberg DG *et al.* (2001) Regulation of root hair density by phosphorus availability in Arabidopsis thaliana. Plant Cell and Environment 24 (4):459-467.

Malekpoor Mansoorkhani F, Seymour GB *et al.* (2014) Environmental, developmental, and genetic factors controlling root system architecture. Biotechnol Genet Eng Rev 30 (1-2):95-112.

Manzoor H, Kelloniemi J *et al.* (2013) Involvement of the glutamate receptor AtGLR3.3 in plant defense signaling and resistance to Hyaloperonospora arabidopsidis. Plant J 76 (3):466-480.

Mao J, Manik SM *et al.* (2016) Mechanisms and Physiological Roles of the CBL-CIPK Networking System in Arabidopsis thaliana. Genes (Basel) 7 (9).

Marinova K, Pourcel L *et al.* (2007) The Arabidopsis MATE transporter TT12 acts as a vacuolar flavonoid/H+ -antiporter active in proanthocyanidin-accumulating cells of the seed coat. Plant Cell 19 (6):2023-2038.

Martinoia E, Maeshima M *et al.* (2007) Vacuolar transporters and their essential role in plant metabolism. Journal of Experimental Botany 58 (1):83-102.

Martinoia E, Meyer S *et al.* (2012) Vacuolar Transporters in Their Physiological Context. Annu Rev Plant Biol 63:183-213.

Marty F (1999) Plant vacuoles. Plant Cell 11 (4):587-599.

Mason MG, Ross JJ *et al.* (2014) Sugar demand, not auxin, is the initial regulator of apical dominance. Proc Natl Acad Sci U S A 111 (16):6092-6097.

Masucci JD, Schiefelbein JW (1994) The rhd6 Mutation of Arabidopsis thaliana Alters Root-Hair Initiation through an Auxin- and Ethylene-Associated Process. Plant Physiol 106 (4):1335-1346.

McClintock M, Higinbotham N *et al.* (1982) Active, Irreversible Accumulation of Extreme Levels of H(2)SO(4) in the Brown Alga, Desmarestia. Plant Physiol 70 (3):771-774.

McQueen-Mason S, Durachko DM *et al.* (1992) Two endogenous proteins that induce cell wall extension in plants. Plant Cell 4:1425-1433.

Mendrinna A, Persson S (2015) Root hair growth: it's a one way street. F1000Prime Rep 7:23.

Meyer S, De Angeli A *et al.* (2010) Intra- and extra-cellular excretion of carboxylates. Trends Plant Sci 15 (1):40-47.

Meyer S, Scholz-Starke J *et al.* (2011) Malate transport by the vacuolar AtALMT6 channel in guard cells is subject to multiple regulation. Plant J 67 (2):247-257.

Michard E, Lima PT *et al.* (2011) Glutamate Receptor-Like Genes Form Ca2+ Channels in Pollen Tubes and Are Regulated by Pistil D-Serine. Science 332 (6028):434-437.

Michniewicz M, Brewer PB *et al.* (2007a) Polar auxin transport and asymmetric auxin distribution. Arabidopsis Book 5:e0108.

Michniewicz M, Zago MK *et al.* (2007b) Antagonistic regulation of PIN phosphorylation by PP2A and PINOID directs auxin flux. Cell 130 (6):1044-1056.

Miller G, Schlauch K *et al.* (2009) The Plant NADPH Oxidase RBOHD Mediates Rapid Systemic Signaling in Response to Diverse Stimuli. Sci Signal 2 (84).

Miller ND, Durham Brooks TL *et al.* (2010) Detection of a gravitropism phenotype in glutamate receptor-like 3.3 mutants of Arabidopsis thaliana using machine vision and computation. Genetics 186 (2):585-593.

Mirza JI, Olsen GM *et al.* (1984) The Growth and Gravitropic Responses of Wild-Type and Auxin-Resistant Mutants of Arabidopsis-Thaliana. Physiol Plantarum 60 (4):516-522.

Mithofer A, Boland W (2012) Plant defense against herbivores: chemical aspects. Annu Rev Plant Biol 63:431-450.

Mittler R, Vanderauwera S *et al.* (2011) ROS signaling: the new wave? Trends Plant Sci 16 (6):300-309.

Miwa H, Sun J *et al.* (2006) Analysis of calcium spiking using a cameleon calcium sensor reveals that nodulation gene expression is regulated by calcium spike number and the developmental status of the cell. Plant Journal 48 (6):883-894.

Mlodzinska E, Zboinska M (2016) Phosphate Uptake and Allocation - A Closer Look at Arabidopsis thaliana L. and Oryza sativa L. Front Plant Sci 7:1198.

Monshausen GB, Bibikova TN *et al.* (2007) Oscillations in extracellular pH and reactive oxygen species modulate tip growth of Arabidopsis root hairs. Proc Natl Acad Sci U S A 104 (52):20996-21001.

Monshausen GB, Messerli MA *et al.* (2008) Imaging of the Yellow Cameleon 3.6 indicator reveals that elevations in cytosolic Ca2+ follow oscillating increases in growth in root hairs of Arabidopsis. Plant Physiol 147 (4):1690-1698.

Monshausen GB, Bibikova TN *et al.* (2009) Ca2+ regulates reactive oxygen species production and pH during mechanosensing in Arabidopsis roots. Plant Cell 21 (8):2341-2356.

Monshausen GB, Gilroy S (2009) Feeling green: mechanosensing in plants. Trends Cell Biol 19 (5):228-235.

Monshausen GB, Miller ND *et al.* (2011) Dynamics of auxin-dependent Ca2+ and pH signaling in root growth revealed by integrating high-resolution imaging with automated computer vision-based analysis. Plant J 65 (2):309-318.

Monshausen GB, Haswell ES (2013) A force of nature: molecular mechanisms of mechanoperception in plants. J Exp Bot 64 (15):4663-4680.

Morris DA, Kadir GO (1972) Pathways of auxin transport in the intact pea seedling (Pisum sativum L.). Planta 107 (2):171-182.

Morris DA, Thomas AG (1978) A Microautoradiographic Study of Auxin Transport in the Stem of Intact Pea Seedlings (Pisum sativum L.). Journal of Experimental Botany 29 (1):147-157.

Mousavi SA, Chauvin A *et al.* (2013) GLUTAMATE RECEPTOR-LIKE genes mediate leaf-to-leaf wound signalling. Nature 500 (7463):422-426.

Mravec J, Skupa P *et al.* (2009) Subcellular homeostasis of phytohormone auxin is mediated by the ER-localized PIN5 transporter. Nature 459 (7250):1136-1140.

Müller A, Guan C *et al.* (1998) AtPIN2 defines a locus of Arabidopsis for root gravitropism control. EMBO J 17 (23):6903-6911.

Müller M, Schmidt W (2004) Environmentally induced plasticity of root hair development in Arabidopsis. Plant Physiol 134 (1):409-419.

Nacry P, Canivenc G *et al.* (2005) A role for auxin redistribution in the responses of the root system architecture to phosphate starvation in Arabidopsis. Plant Physiol 138 (4):2061-2074.

Nagai T, Ibata K *et al.* (2002) A variant of yellow fluorescent protein with fast and efficient maturation for cell-biological applications. Nat Biotechnol 20 (1):87-90.

Nakai J, Ohkura M *et al.* (2001) A high signal-to-noise Ca2+ probe composed of a single green fluorescent protein. Nat Biotechnol 19 (2):137-141.

Neher E, Sakmann B *et al.* (1978) The extracellular patch clamp: a method for resolving currents through individual open channels in biological membranes. Pflugers Arch 375 (2):219-228.

Newman IA (2001) Ion transport in roots: measurement of fluxes using ion-selective microelectrodes to characterize transporter function. Plant Cell Environ 24 (1):1-14.

Nguyen CT, Agorio A *et al.* (2016) Characterization of the Chloride Channel-Like, AtCLCg, Involved in Chloride Tolerance in Arabidopsis thaliana. Plant Cell Physiol 57 (4):764-775.

Nieves-Cordones M, Aleman F *et al.* (2010) The Arabidopsis thaliana HAK5 K+ transporter is required for plant growth and K+ acquisition from low K+ solutions under saline conditions. Mol Plant 3 (2):326-333.

Noh B, Murphy AS *et al.* (2001) Multidrug resistance-like genes of Arabidopsis required for auxin transport and auxin-mediated development. Plant Cell 13 (11):2441-2454.

Noh B, Bandyopadhyay A *et al.* (2003) Enhanced gravi- and phototropism in plant mdr mutants mislocalizing the auxin efflux protein PIN1. Nature 423 (6943):999-1002.

Ogasawara Y, Kaya H *et al.* (2008) Synergistic activation of the Arabidopsis NADPH oxidase AtrbohD by Ca2+ and phosphorylation. J Biol Chem 283 (14):8885-8892.

Okada K, Shimura Y (1990) Reversible root tip rotation in Arabidopsis seedlings induced by obstacle-touching stimulus. Science 250 (4978):274-276.

Okada K, Ueda J *et al.* (1991) Requirement of the Auxin Polar Transport System in Early Stages of Arabidopsis Floral Bud Formation. Plant Cell 3 (7):677-684.

Olesen C, Picard M *et al.* (2007) The structural basis of calcium transport by the calcium pump. Nature 450 (7172):1036-1042.

Ottenschläger I, Wolff P *et al.* (2003) Gravity-regulated differential auxin transport from columella to lateral root cap cells. Proc Natl Acad Sci U S A 100 (5):2987-2991.

Parry G, Calderon-Villalobos LI *et al.* (2009) Complex regulation of the TIR1/AFB family of auxin receptors. Proc Natl Acad Sci U S A 106 (52):22540-22545.

Pei ZM, Murata Y *et al.* (2000) Calcium channels activated by hydrogen peroxide mediate abscisic acid signalling in guard cells. Nature 406 (6797):731-734.

Peiter E, Maathuis FJ *et al.* (2005) The vacuolar Ca2+-activated channel TPC1 regulates germination and stomatal movement. Nature 434 (7031):404-408.

Penny MG, Bowling DJ (1975) Direct Determination of pH in the stomatal complex of Commelina. Planta 122 (2):209-212.

Peret B, Clement M *et al.* (2011) Root developmental adaptation to phosphate starvation: better safe than sorry. Trends Plant Sci 16 (8):442-450.

Peret B, Swarup K *et al.* (2012) AUX/LAX genes encode a family of auxin influx transporters that perform distinct functions during Arabidopsis development. Plant Cell 24 (7):2874-2885.

Perez-Torres CA, Lopez-Bucio J *et al.* (2008) Phosphate availability alters lateral root development in Arabidopsis by modulating auxin sensitivity via a mechanism involving the TIR1 auxin receptor. Plant Cell 20 (12):3258-3272.

Perez Torres CA, Lopez Bucio J *et al.* (2009) Low phosphate signaling induces changes in cell cycle gene expression by increasing auxin sensitivity in the Arabidopsis root system. Plant Signal Behav 4 (8):781-783.

Petrasek J, Mravec J *et al.* (2006) PIN proteins perform a rate-limiting function in cellular auxin efflux. Science 312 (5775):914-918.

Petrasek J, Friml J (2009) Auxin transport routes in plant development. Development 136 (16):2675-2688.

Peyronnet R, Tran D *et al.* (2014) Mechanosensitive channels: feeling tension in a world under pressure. Front Plant Sci 5:558.

Philippar K, Ivashikina N *et al.* (2004) Auxin activates KAT1 and KAT2, two K+-channel genes expressed in seedlings of Arabidopsis thaliana. Plant J 37 (6):815-827.

Pickett FB, Wilson AK *et al.* (1990) The Aux1 Mutation of Arabidopsis Confers Both Auxin and Ethylene Resistance. Plant Physiology 94 (3):1462-1466.

Pierson ES, Miller DD *et al.* (1996) Tip-localized calcium entry fluctuates during pollen tube growth. Dev Biol 174 (1):160-173.

Pinon V, Prasad K *et al.* (2013) Local auxin biosynthesis regulation by PLETHORA transcription factors controls phyllotaxis in Arabidopsis. Proc Natl Acad Sci U S A 110 (3):1107-1112.

Pitts RJ, Cernac A *et al.* (1998) Auxin and ethylene promote root hair elongation in Arabidopsis. Plant J 16 (5):553-560.

Plieth C, Sattelmacher B *et al.* (1998) The action potential in Chara: Ca2+ release from internal stores visualized by Mn2+-induced quenching of fura-dextran. Plant Journal 13 (2):167-175.

Pottosin, II, Martinez-Estevez M *et al.* (2004) Mechanism of luminal Ca2+ and Mg2+ action on the vacuolar slowly activating channels. Planta 219 (6):1057-1070.

Pottosin I, Wherrett T *et al.* (2009) SV channels dominate the vacuolar Ca2+ release during intracellular signaling. FEBS Lett 583 (5):921-926.

Pottosin II, Tikhonova LI *et al.* (1997) Slowly activating vacuolar channels can not mediate Ca2+-induced Ca2+ release. Plant Journal 12 (6):1387-1398.

Pourcel L, Irani NG *et al.* (2010) The formation of Anthocyanic Vacuolar Inclusions in Arabidopsis thaliana and implications for the sequestration of anthocyanin pigments. Mol Plant 3 (1):78-90.

Pratt J, Boisson AM *et al.* (2009) Phosphate (Pi) starvation effect on the cytosolic Pi concentration and Pi exchanges across the tonoplast in plant cells: an in vivo 31P-nuclear magnetic resonance study using methylphosphonate as a Pi analog. Plant Physiol 151 (3):1646-1657.

Qi Z, Stephens NR *et al.* (2006) Calcium entry mediated by GLR3.3, an Arabidopsis glutamate receptor with a broad agonist profile. Plant Physiol 142 (3):963-971.

Qin T, Li J *et al.* (2012) Characterization of the role of calcium in regulating the microtubule-destabilizing activity of MDP25. Plant Signal Behav 7 (7):708-710.

Qu HY, Shang ZL *et al.* (2007) Identification of hyperpolarization-activated calcium channels in apical pollen tubes of Pyrus pyrifolia. New Phytol 174 (3):524-536.

Ranocha P, Dima O *et al.* (2013) Arabidopsis WAT1 is a vacuolar auxin transport facilitator required for auxin homoeostasis. Nature Communications 4.

Ranty B, Aldon D *et al.* (2016) Calcium Sensors as Key Hubs in Plant Responses to Biotic and Abiotic Stresses. Frontiers in Plant Science 7.

Raven JA (1975) Transport of Indoleacetic-Acid in Plant-Cells in Relation to Ph and Electrical Potential Gradients, and Its Significance for Polar Iaa Transport. New Phytologist 74 (2):163-172.

Rayle DL, Cleland R (1977) Control of plant cell enlargement by hydrogen ions. Curr Top Dev Biol 11:187-214.

Reid DE, Ferguson BJ *et al.* (2011) Inoculation- and nitrate-induced CLE peptides of soybean control NARK-dependent nodule formation. Mol Plant Microbe Interact 24 (5):606-618.

Reinhardt D, Pesce ER *et al.* (2003) Regulation of phyllotaxis by polar auxin transport. Nature 426 (6964):255-260.

Rienmüller F, Beyhl D *et al.* (2010) Guard cell-specific calcium sensitivity of high density and activity SV/TPC1 channels. Plant Cell Physiol 51 (9):1548-1554.

Rienmüller F, Dreyer I *et al.* (2012) Luminal and cytosolic pH feedback on proton pump activity and ATP affinity of V-type ATPase from Arabidopsis. J Biol Chem 287 (12):8986-8993.

Rigas S, Ditengou FA *et al.* (2013) Root gravitropism and root hair development constitute coupled developmental responses regulated by auxin homeostasis in the Arabidopsis root apex. New Phytol 197 (4):1130-1141.

Robinson D, Anderson JE *et al.* (1990) Measurement of Diffusion-Coefficients of Some Indoles and Ascorbic-Acid by Flow-Injection Analysis. J Phys Chem-Us 94 (2):1003-1005.

Rocchetti A, Sharma T *et al.* (2012) The putative K(+) channel subunit AtKCO3 forms stable dimers in Arabidopsis. Front Plant Sci 3:251.

Roelfsema MR, Hedrich R (2010) Making sense out of Ca(2+) signals: their role in regulating stomatal movements. Plant Cell Environ 33 (3):305-321.

Roman G, Lubarsky B *et al.* (1995) Genetic analysis of ethylene signal transduction in Arabidopsis thaliana: five novel mutant loci integrated into a stress response pathway. Genetics 139 (3):1393-1409.

Rubery PH, Sheldrake AR (1974) Carrier-Mediated Auxin Transport. Planta 118 (2):101-121.

Rück A, Palme K *et al.* (1993) Patch-Clamp Analysis Establishes a Role for an Auxin-Binding Protein in the Auxin Stimulation of Plasma-Membrane Current in Zea-Mays Protoplasts. Plant Journal 4 (1):41-46.

Ruegger M, Dewey E *et al.* (1998) The TIR1 protein of Arabidopsis functions in auxin response and is related to human SKP2 and yeast grr1p. Genes Dev 12 (2):198-207.

Rutschow HL, Baskin TI *et al.* (2014) The carrier AUXIN RESISTANT (AUX1) dominates auxin flux into Arabidopsis protoplasts. New Phytologist 204 (3):536-544.

Sabatini S, Beis D *et al.* (1999) An auxin-dependent distal organizer of pattern and polarity in the Arabidopsis root. Cell 99 (5):463-472.

Sagi M, Fluhr R (2001) Superoxide production by plant homologues of the gp91(phox) NADPH oxidase. Modulation of activity by calcium and by tobacco mosaic virus infection. Plant Physiol 126 (3):1281-1290.

Salvador-Recatala V, Tjallingii WF *et al.* (2014) Real-time, in vivo intracellular recordings of caterpillar-induced depolarization waves in sieve elements using aphid electrodes. New Phytol 203 (2):674-684.

Salvador-Recatala V (2016) New roles for the GLUTAMATE RECEPTOR-LIKE 3.3, 3.5, and 3.6 genes as on/off switches of wound-induced systemic electrical signals. Plant Signal Behav 11 (4):e1161879.

Samson E, Marchand J *et al.* (2003) Calculation of ionic diffusion coefficients on the basis of migration test results. Mater Struct 36 (257):156-165.

Sanchez-Calderon L, Lopez-Bucio J *et al.* (2005) Phosphate starvation induces a determinate developmental program in the roots of Arabidopsis thaliana. Plant Cell Physiol 46 (1):174-184.

Sanders D, Pelloux J *et al.* (2002) Calcium at the crossroads of signaling. Plant Cell 14:S401-S417.

Santner A, Calderon-Villalobos LI *et al.* (2009) Plant hormones are versatile chemical regulators of plant growth. Nat Chem Biol 5 (5):301-307.

Scheitz K, Luthen H *et al.* (2013) Rapid auxin-induced root growth inhibition requires the TIR and AFB auxin receptors. Planta 238 (6):1171-1176.

Scherzer S, Bohm J *et al.* (2015) Calcium sensor kinase activates potassium uptake systems in gland cells of Venus flytraps. Proc Natl Acad Sci U S A 112 (23):7309-7314.

Schönknecht G (2013) Calcium Signals from the Vacuole. Plants (Basel) 2 (4):589-614.

Schulz A, Beyhl D *et al.* (2011) Proton-driven sucrose symport and antiport are provided by the vacuolar transporters SUC4 and TMT1/2. Plant J 68 (1):129-136.

Schulze C, Sticht H *et al.* (2011) Differential contribution of EF-hands to the Ca(2)(+)-dependent activation in the plant two-pore channel TPC1. Plant J 68 (3):424-432.

Schwarz W, Rettinger J (2003) Foundations of Electrophysiology. 2nd Edition edn. Shaker Verlag,

Serrano M, Wang B *et al.* (2013) Export of salicylic acid from the chloroplast requires the multidrug and toxin extrusion-like transporter EDS5. Plant Physiol 162 (4):1815-1821.

Sharma SS, Dietz KJ *et al.* (2016) Vacuolar compartmentalization as indispensable component of heavy metal detoxification in plants. Plant Cell and Environment 39 (5):1112-1126.

Sharma T, Dreyer I *et al.* (2013) The role of K(+) channels in uptake and redistribution of potassium in the model plant Arabidopsis thaliana. Front Plant Sci 4:224.

Shigaki T, Hirschi KD (2006) Diverse functions and molecular properties emerging for CAX cation/H+ exchangers in plants. Plant Biol (Stuttg) 8 (4):419-429.

Shih HW, DePew CL *et al.* (2015) The Cyclic Nucleotide-Gated Channel CNGC14 Regulates Root Gravitropism in Arabidopsis thaliana. Curr Biol 25 (23):3119-3125.

Shishova M, Lindberg S (2004) Auxin induces an increase of Ca2+ concentration in the cytosol of wheat leaf protoplasts. J Plant Physiol 161 (8):937-945.

Simon S, Skupa P *et al.* (2016) PIN6 auxin transporter at endoplasmic reticulum and plasma membrane mediates auxin homeostasis and organogenesis in Arabidopsis. New Phytol 211 (1):65-74.

Spanswick RM, Williams EJ (1964) Electrical Potentials + Na K + Cl Concentrations in Vacuole + Cytoplasm of Nitella Translucens. Journal of Experimental Botany 15 (44):193-&.

Spanswick RM (1972) Electrical Coupling between Cells of Higher-Plants - Direct Demonstration of Intercellular Communication. Planta 102 (3):215-+.

Spartz AK, Ren H *et al.* (2014) SAUR Inhibition of PP2C-D Phosphatases Activates Plasma Membrane H+-ATPases to Promote Cell Expansion in Arabidopsis. Plant Cell 26 (5):2129-2142.

Stegmann M, Monaghan J *et al.* (2017) The receptor kinase FER is a RALF-regulated scaffold controlling plant immune signaling. Science 355 (6322):287-289.

Steinhorst L, Kudla J (2013) Calcium and reactive oxygen species rule the waves of signaling. Plant Physiol 163 (2):471-485.

Stetter MG, Schmid K *et al.* (2015) Uncovering genes and ploidy involved in the high diversity in root hair density, length and response to local scarce phosphate in Arabidopsis thaliana. PLoS One 10 (3):e0120604.

Stoelzle S, Kagawa T *et al.* (2003) Blue light activates calcium-permeable channels in Arabidopsis mesophyll cells via the phototropin signaling pathway. Proc Natl Acad Sci U S A 100 (3):1456-1461.

Suzuki J, Kanemaru K *et al.* (2014) Imaging intraorganellar Ca2+ at subcellular resolution using CEPIA. Nat Commun 5:4153.

Suzuki N, Miller G *et al.* (2013) Temporal-Spatial Interaction between Reactive Oxygen Species and Abscisic Acid Regulates Rapid Systemic Acclimation in Plants. Plant Cell 25 (9):3553-3569.

Swarbreck SM, Colaco R *et al.* (2013) Plant calcium-permeable channels. Plant Physiol 163 (2):514-522.

Swarup K, Benkova E *et al.* (2008) The auxin influx carrier LAX3 promotes lateral root emergence. Nat Cell Biol 10 (8):946-954.

Swarup R, Friml J *et al.* (2001) Localization of the auxin permease AUX1 suggests two functionally distinct hormone transport pathways operate in the Arabidopsis root apex. Genes Dev 15 (20):2648-2653.

Swarup R, Kargul J *et al.* (2004) Structure-function analysis of the presumptive Arabidopsis auxin permease AUX1. Plant Cell 16 (11):3069-3083.

Swarup R, Kramer EM *et al.* (2005) Root gravitropism requires lateral root cap and epidermal cells for transport and response to a mobile auxin signal. Nat Cell Biol 7 (11):1057-1065.

Swarup R, Peret B (2012) AUX/LAX family of auxin influx carriers-an overview. Frontiers in Plant Science 3.

Szemenyei H, Hannon M *et al.* (2008) TOPLESS mediates auxin-dependent transcriptional repression during Arabidopsis embryogenesis. Science 319 (5868):1384-1386.

Taiz L (1992) The Plant Vacuole. J Exp Biol 172:113-122.

Takahashi K, Hayashi K *et al.* (2012) Auxin activates the plasma membrane H+-ATPase by phosphorylation during hypocotyl elongation in Arabidopsis. Plant Physiol 159 (2):632-641.

Tang RJ, Zhao FG *et al.* (2015) Tonoplast CBL-CIPK calcium signaling network regulates magnesium homeostasis in Arabidopsis. Proc Natl Acad Sci U S A 112 (10):3134-3139.

Tester M, Beilby MJ *et al.* (1987) Electrical Characteristics of the Tonoplast of Chara-Corallina - a Study Using Permeabilized Cells. Plant and Cell Physiology 28 (8):1555-1568.

Theologis A (1986) Rapid Gene-Regulation by Auxin. Annu Rev Plant Phys 37:407-438.

Thiel G, Blatt MR *et al.* (1993) Modulation of K+ channels in Vicia stomatal guard cells by peptide homologs to the auxin-binding protein C terminus. Proc Natl Acad Sci U S A 90 (24):11493-11497.

Thimann KV, Koepfli JB (1935) Identity of the growth-promoting and root-forming substances of plants. Nature 135:101.

Thimann KV (1938) Hormones and the Analysis of Growth. Plant Physiol 13 (3):437-449.

Tiwari SB, Wang XJ *et al.* (2001) AUX/IAA proteins are active repressors, and their stability and activity are modulated by auxin. Plant Cell 13 (12):2809-2822.

Toyota M, Furuichi T *et al.* (2008) Cytoplasmic calcium increases in response to changes in the gravity vector in hypocotyls and petioles of Arabidopsis seedlings. Plant Physiol 146 (2):505-514.

Tsurumi S, Ohwaki Y (1978) Transport of C-14-Labeled Indoleacetic-Acid in Vicia Root Segments. Plant and Cell Physiology 19 (7):1195-1206.

Tuteja N, Mahajan S (2007) Calcium signaling network in plants: an overview. Plant Signal Behav 2 (2):79-85.

Tyburski J, Dunajska K *et al.* (2009) Reactive oxygen species localization in roots of Arabidopsis thaliana seedlings grown under phosphate deficiency. Plant Growth Regul 59 (1):27-36.

Ulmasov T, Hagen G *et al.* (1997a) ARF1, a transcription factor that binds to auxin response elements. Science 276 (5320):1865-1868.

Ulmasov T, Murfett J *et al.* (1997b) Aux/IAA proteins repress expression of reporter genes containing natural and highly active synthetic auxin response elements. Plant Cell 9 (11):1963-1971.

Vandenbussche F, Petrasek J *et al.* (2010) The auxin influx carriers AUX1 and LAX3 are involved in auxin-ethylene interactions during apical hook development in Arabidopsis thaliana seedlings. Development 137 (4):597-606.

Vanneste S, Friml J (2013) Calcium: The Missing Link in Auxin Action. Plants (Basel) 2 (4):650-675.

Venema K, Quintero FJ *et al.* (2002) The arabidopsis Na+/H+ exchanger AtNHX1 catalyzes low affinity Na+ and K+ transport in reconstituted liposomes. J Biol Chem 277 (4):2413-2418.

Very AA, Davies JM (2000) Hyperpolarization-activated calcium channels at the tip of Arabidopsis root hairs. Proc Natl Acad Sci U S A 97 (17):9801-9806.

Vijayakumar P, Datta S *et al.* (2016) ROOT HAIR DEFECTIVE SIX-LIKE4 (RSL4) promotes root hair elongation by transcriptionally regulating the expression of genes required for cell growth. New Phytol 212 (4):944-953.

Vincill ED, Bieck AM *et al.* (2012) Ca(2+) conduction by an amino acid-gated ion channel related to glutamate receptors. Plant Physiol 159 (1):40-46.

Viotti C (2014) ER and vacuoles: never been closer. Frontiers in Plant Science 5.

Voelker C, Schmidt D *et al.* (2006) Members of the Arabidopsis AtTPK/KCO family form homomeric vacuolar channels in planta. Plant J 48 (2):296-306.

von der Fecht-Bartenbach J, Bogner M *et al.* (2010) CLC-b-mediated NO-3/H+ exchange across the tonoplast of Arabidopsis vacuoles. Plant Cell Physiol 51 (6):960-968.

Voss LJ, Hedrich R *et al.* (2016) Current Injection Provokes Rapid Expansion of the Guard Cell Cytosolic Volume and Triggers Ca(2+) Signals. Mol Plant 9 (3):471-480.

Walker DJ, Leigh RA *et al.* (1996) Potassium homeostasis in vacuolate plant cells. Proc Natl Acad Sci U S A 93 (19):10510-10514.

Wang B, Bailly A *et al.* (2013a) Arabidopsis TWISTED DWARF1 functionally interacts with auxin exporter ABCB1 on the root plasma membrane. Plant Cell 25 (1):202-214.

Wang R, Zhang Y *et al.* (2016) HSP90 regulates temperature-dependent seedling growth in Arabidopsis by stabilizing the auxin co-receptor F-box protein TIR1. Nat Commun 7:10269.

Wang Y, Wu WH (2013) Potassium transport and signaling in higher plants. Annu Rev Plant Biol 64:451-476.

Wang Y, Dindas J *et al.* (2015) Cytosolic Ca(2+) Signals Enhance the Vacuolar Ion Conductivity of Bulging Arabidopsis Root Hair Cells. Mol Plant 8 (11):1665-1674.

Wang YF, Munemasa S *et al.* (2013b) Identification of cyclic GMP-activated nonselective Ca2+-permeable cation channels and associated CNGC5 and CNGC6 genes in Arabidopsis guard cells. Plant Physiol 163 (2):578-590.

Ward JM, Schroeder JI (1994) Calcium-Activated K+ Channels and Calcium-Induced Calcium Release by Slow Vacuolar Ion Channels in Guard Cell Vacuoles Implicated in the Control of Stomatal Closure. Plant Cell 6 (5):669-683.

Webb AAR, McAinsh MR *et al.* (1996) Calcium Ions as Intracellular Second Messengers in Higher Plants. In: Callow JA (ed) Advances in Botanical Research, vol Volume 22. Academic Press, pp 45-96

Weijers D, Wagner D (2016) Transcriptional Responses to the Auxin Hormone. Annu Rev Plant Biol 67:539-574.

Went FW (1926) On Growth-accelerating Substances in the Coleoptile of Avena Sativa. Proc Kon Ned Akad Wetensch 30:10-19.

Whalley HJ, Sargeant AW *et al.* (2011) Transcriptomic analysis reveals calcium regulation of specific promoter motifs in Arabidopsis. Plant Cell 23 (11):4079-4095.

White PJ, Smith JAC (1989) Proton and Anion Transport at the Tonoplast in Crassulacean-Acid-Metabolism Plants - Specificity of the Malate-Influx System in Kalanchoe-Daigremontiana. Planta 179 (2):265-274.

Williamson LC, Ribrioux SP *et al.* (2001) Phosphate availability regulates root system architecture in Arabidopsis. Plant Physiol 126 (2):875-882.

Willige BC, Chory J (2015) A current perspective on the role of AGCVIII kinases in PIN-mediated apical hook development. Front Plant Sci 6:767.

Winkler M, Niemeyer M *et al.* (2017) Variation in auxin sensing guides AUX/IAA transcriptional repressor ubiquitylation and destruction. Nat Commun 8:15706.

Wisniewska J, Xu J *et al.* (2006) Polar PIN localization directs auxin flow in plants. Science 312 (5775):883-883.

Woo EJ, Marshall J *et al.* (2002) Crystal structure of auxin-binding protein 1 in complex with auxin. EMBO J 21 (12):2877-2885.

Woodward AW, Bartel B (2005) Auxin: regulation, action, and interaction. Ann Bot 95 (5):707-735.

Wraight CA (2006) Chance and design - Proton transfer in water, channels and bioenergetic proteins. Bba-Bioenergetics 1757 (8):886-912.

Wymer CL, Bibikova TN *et al.* (1997) Cytoplasmic free calcium distributions during the development of root hairs of Arabidopsis thaliana. Plant J 12 (2):427-439.

Yadav SK (2010) Heavy metals toxicity in plants: An overview on the role of glutathione and phytochelatins in heavy metal stress tolerance of plants. S Afr J Bot 76 (2):167-179.

Yamada K, Osakabe Y *et al.* (2010) Functional analysis of an Arabidopsis thaliana abiotic stress-inducible facilitated diffusion transporter for monosaccharides. J Biol Chem 285 (2):1138-1146.

Yamaguchi T, Aharon GS *et al.* (2005) Vacuolar Na+/H+ antiporter cation selectivity is regulated by calmodulin from within the vacuole in a Ca2+- and pH-dependent manner. Proc Natl Acad Sci U S A 102 (44):16107-16112.

Yamamoto M, Yamamoto KT (1998) Differential effects of 1-naphthaleneacetic acid, indole-3-acetic acid and 2,4-dichlorophenoxyacetic acid on the gravitropic response of roots in an auxin-resistant mutant of Arabidopsis, aux1. Plant and Cell Physiology 39 (6):660-664.

Yang H, Murphy AS (2009) Functional expression and characterization of Arabidopsis ABCB, AUX 1 and PIN auxin transporters in Schizosaccharomyces pombe. Plant J 59 (1):179-191.

Yang Y, Hammes UZ *et al.* (2006) High-affinity auxin transport by the AUX1 influx carrier protein. Curr Biol 16 (11):1123-1127.

Yoo BC, Kragler F *et al.* (2004) A systemic small RNA signaling system in plants. Plant Cell 16 (8):1979-2000.

Yoshioka K, Moeder W *et al.* (2006) The chimeric Arabidopsis CYCLIC NUCLEOTIDE-GATED ION CHANNEL11/12 activates multiple pathogen resistance responses. Plant Cell 18 (3):747-763.

Yu H, Moss BL *et al.* (2013) Mutations in the TIR1 auxin receptor that increase affinity for auxin/indole-3-acetic acid proteins result in auxin hypersensitivity. Plant Physiol 162 (1):295-303.

Yu X, Carroll S *et al.* (1993) H+ countertransport and electrogenicity of the sarcoplasmic reticulum Ca2+ pump in reconstituted proteoliposomes. Biophys J 64 (4):1232-1242.

Yuan F, Yang H *et al.* (2014) OSCA1 mediates osmotic-stress-evoked Ca2+ increases vital for osmosensing in Arabidopsis. Nature 514 (7522):367-371.

Zhang H, Zhu H *et al.* (2014) A DTX/MATE-type transporter facilitates abscisic acid efflux and modulates ABA sensitivity and drought tolerance in Arabidopsis. Mol Plant 7 (10):1522-1532.

Zhang H, Zhao FG *et al.* (2017a) Two tonoplast MATE proteins function as turgor-regulating chloride channels in Arabidopsis. Proc Natl Acad Sci U S A.

Zhang S, Pan Y *et al.* (2017b) Arabidopsis CNGC14 Mediates Calcium Influx Required for Tip Growth in Root Hairs. Mol Plant.

Zhang Y, Zhu H *et al.* (2009) Phospholipase dalpha1 and phosphatidic acid regulate NADPH oxidase activity and production of reactive oxygen species in ABA-mediated stomatal closure in Arabidopsis. Plant Cell 21 (8):2357-2377.

Zhao YX, Araki S *et al.* (2011) An Expanded Palette of Genetically Encoded Ca2+ Indicators. Science 333 (6051):1888-1891.

Zhou L, Lan W *et al.* (2014) A calcium-dependent protein kinase interacts with and activates a calcium channel to regulate pollen tube growth. Mol Plant 7 (2):369-376.

Zhu T, Lucas WJ *et al.* (1998) Directional cell-to-cell communication in the Arabidopsis root apical meristem - I. An ultrastructural and functional analysis. Protoplasma 203 (1-2):35-47.

Zimmermann MR, Maischak H *et al.* (2009) System potentials, a novel electrical long-distance apoplastic signal in plants, induced by wounding. Plant Physiol 149 (3):1593-1600.

Zourelidou M, Muller I *et al.* (2009) The polarly localized D6 PROTEIN KINASE is required for efficient auxin transport in Arabidopsis thaliana. Development 136 (4):627-636.

Zourelidou M, Absmanner B *et al.* (2014) Auxin efflux by PIN-FORMED proteins is activated by two different protein kinases, D6 PROTEIN KINASE and PINOID. Elife 3.

Affidavit

I hereby declare that my thesis entitled: „**Cytosolic Ca^{2+}, a master regulator of vacuolar ion conductance and fast auxin signaling in *Arabidopsis thaliana***” is the result of my own work.

I did not receive any help or support from commercial consultants. All sources and / or materials applied are listed and specified in the thesis.

Furthermore, I verify that the thesis has not been submitted as part of another examination process neither in identical nor in similar form.

Eidesstattliche Erklärung

Hiermit erkläre ich an Eides statt, die Dissertation: „**Cytosolic Ca^{2+}, a master regulator of vacuolar ion conductance and fast auxin signaling in *Arabidopsis thaliana***“, eigenständig, d. h. insbesondere selbständig und ohne Hilfe eines kommerziellen Promotionsberaters, angefertigt und keine anderen, als die von mir angegebenen Quellen und Hilfsmittel verwendet zu haben.

Ich erkläre außerdem, dass die Dissertation weder in gleicher noch in ähnlicher Form bereits in einem anderen Prüfungsverfahren vorgelegen hat.

Würzburg, __________

____

Unterschrift/Signature

Publications

Publications <u>not</u> associated with this doctoral thesis

2015 *Dissection of jasmonate functions in tomato stamen development by transcriptome and metabolome analyses.* Dobritzsch, S; Weyhe, M; Schubert, R; **Dindas, J**; Hause, G; Kopka, J; Hause, B. BMC Biology (2015) 13:28

Publications that have arisen during this work

<u>First authorships</u>

2015 *Cytosolic Ca^{2+} signals enhance the vacuolar ion conductivity of buldging Arabidopsis root hair cells*. Wang, Y; **Dindas, J**; Rienmüller, F; Krebs, M; Waadt, R; Schumacher, K; Wu, WH; Hedrich, R; Roelfsema, MR. Molecular Plant (2015), doi:10.1016/j.molp.2015.07.009.

Equally contributing first author.

Contribution: Experiments with R-GECO1 expressing root hairs. Double-impalement experiments to verify the VM has the highest electrical resistance during serial impalement.

2017 *AUX1-mediated root hair auxin influx governs $SCF^{TIR1/AFB}$-type Ca^{2+} signaling*. **Dindas J**, Scherzer S, Roelfsema MRG, von Meyer K, Müller HM, Al-Rasheid KAS, Palme K, Dietrich P, Becker D, Bennett MJ ,Hedrich R.

Sole first author.

Status: under revision at Nature Communications

<u>Co-authorships</u>

2017 *Poly(A) ribonuclease controls cellotriose-based interaction of Piriformospora indica and its host Arabidopsis.* Joy M. Johnson, Johannes Thürich, Elena K. Petutschnig, Lothar Altschmied, Doreen Meichsner, Irena Sherameti, **Julian Dindas**, Anna Mrozinska, Christian Paetz, Sandra S. Scholz, Alexandra C. U. Furch, Volker Lipka, Rainer Hedrich, Bernd Schneider, Aleš Svatoš, Ralf Oelmüller

Status: under revision at Plant Physiology

Contribution: Measurement of cellotriose-induced root hair plasma membrane potential depolarizations in the *A. thaliana* Col-0 wild type and *cycam1-1* loss-of-function mutant.

Posters

2014:	International School of Biophysics course on Channels and Transporters, Erice, Sicily, Italy
Poster titel:	Analysis of the electrical properties of vacuoles *in planta*